UNIVERSITY OF SOUTHAMPTON

FACULTY OF ENGINEERING AND APPLIED SCIENCE
SCHOOL OF ENGINEERING SCIENCES

Electrochemical analysis of the erosion-corrosion of HVOF aluminium bronze coatings

KengSoong Tan

Thesis submitted for the degree of Doctor of Philosophy

June 2003

UNIVERSITY OF SOUTHAMPTON

ABSTRACT

FACULTY OF ENGINEERING AND APPLIED SCIENCE
SCHOOL OF ENGINEERING SCIENCES

Doctor of Philosophy

ELECTROCHEMICAL ANALYSIS OF THE EROSION-CORROSION OF HVOF ALUMINIUM BRONZE COATINGS

By KengSoong Tan

Modern industries such as marine, oil and gas production, and power plants require cooling systems for their generators and reactors. Seawater is often used for this purpose due to the location of these industries and its abundance. The entrainment of sand particles in seawater can result in simultaneous erosion and corrosion attacks on metallic components such as pipes and valves, resulting in enhanced material removal (synergy). The present work is interested in quantifying the synergy that occurs when High Velocity Oxy-Fuel (HVOF) aluminium bronze (AB) and nickel aluminium bronze (NAB) coatings are subjected to erosion-corrosion conditions. Estimation of the synergy was based on mass loss and electrochemical measurements obtained from erosion, flow corrosion and erosion-corrosion experiments.

Due to a porous microstructure, the erosion mechanism of the ductile HVOF coatings was shown to be different from bulk ductile materials. Cracking at the brittle splat boundary under normal impingement angle resulted in coating splat removal. Wear maps based on volume loss and kinetic energy and dimensional analysis were investigated. Surface filming occurred on the AB and NAB coatings under flowing conditions. Imperfections such as open pores on the coating surface resulted in flaws in the surface film which reduced its corrosion resistance. Permeation of electrolyte into the coating/substrate interface via the pore network resulted in its delamination. Under erosion-corrosion, material removal was enhanced by increased mass transfer (associated with protective layer removal) and corrosion at the work hardened lips of erosion scars. The open pores were possibly sealed by plastically deformed lips and electrolyte permeation was minimised. When the coating perforates, the active steel substrate was polarised anodically by the noble coating, resulting in coating delamination at the vicinity of the perforation site. A novel method of estimating the extent of synergy based on mass loss measurement was proposed, it involves determining the ratio between erosion mass loss and erosion-corrosion mass loss. A ratio that is lower than 0.83 will result in positive synergy and vice versa. Electrochemical noise measurements were used for monitoring localised corrosion events such as depassivation and repassivation and corrosion occurring at the pore network and coating/substrate interface. It was also found useful for detecting coating perforation under erosion-corrosion. Analysis of the electrochemical current noise by standard deviation and time-frequency methods (DWT – Discrete Wavelets Transform and EMD – Empirical Mode Decomposition) revealed a transition region defined by a shift in synergy from negative to positive values. This transition is associated the loss of protective layers due to the critical flow velocity being surpassed and increased erosion by higher sand particle kinetic energies.

The contribution of a synergistic constant and the determination of an electrochemical transition between positive and negative synergy based on critical velocity and kinetic energy can provide guidance to engineers when specifying materials/coatings for use under erosion-corrosion conditions.

To Katrin Topsch

ACKNOWLEDGEMENTS

I would like to thank Mr. Keith Stokes (Dstl) for supplying the HVOF aluminium bronze coatings used in the current work and for his general advice on the behaviour of copper based alloys. I would also like to express my gratitude to the Centre of Thermal Spray Technology, University of Barcelona for their help in spraying the hybrid nickel aluminium bronze coatings.

I am especially grateful to Dr. Robert Wood and Dr. Julian Wharton for their excellent supervision and technical discussions throughout the duration of this project. Thanks also to my other colleagues, particularly Dr. Sebastian Morris and Dr. Andrew Speyer for their support, general advice and cheerful moments.

I am particularly grateful to the Surface Engineering and Tribology Group technicians: Mr. Steven Pilcher and Mr. Robert Barnes for their assistance in the construction and maintenance of the jet impingement rig.

Finally, I am indebted to my parents and also Dr. Katrin Topsch for their love and constant moral support throughout the length of my stay in Southampton.

Table of contents

List of figures

List of Tables

Chapter 1 Introduction

Modern industries such as marine, oil and gas production, and power plants require cooling systems for their generators and reactors. Seawater is often used for this purpose due to the location of the industries and its abundance. However, sand particles can be entrained in the seawater, which will reduce the design life of metal components such as pipes and valves by a combination of erosion and corrosion. The entrainment of sand particles results in mechanical damage of metallic components, through cutting and ploughing processes. The seawater is similarly destructive, causing pitting, crevice corrosion, de-alloying and stress corrosion cracking. Often in a multiphase system, erosion and corrosion attack occurs simultaneously and this can enhance the overall material wastage due to a coupling between the erosion, a mechanical process, and the electrochemical process of corrosion (synergy).

In order to reduce material wastage and prolong component life, expensive alloys such as cupro-nickel and titanium based alloy were produced. However, these alloys are not extensively used or developed due to their high cost of production. Consequently, organic and metallic coatings systems were developed because of their many inherent advantages: expensive materials could be applied on a relatively low cost substrate, in addition to providing a surface that offers the excellent mechanical properties of the coating material. Other advantages of coatings include the ease of application and the reclamation of components which have been subjected to erosion or corrosion. However, factors such as grain size, chemical properties and application processes need to be considered carefully because they can ultimately affect the performance of coatings, possible factors include porosity, grain boundary corrosion, stress etc.

Electrochemical techniques were developed to provide information of corrosion processes for coatings under erosion and corrosion conditions because conventional gravimetric measurements and visual examinations have a number of limitations. The advantages of electrochemical techniques such as potentiodynamic polarisation and electrochemical noise methods include ease of data acquisition, handling, and storage. By proper interpretation of the data obtained, it is possible to predict the kinetics of corrosion processes so that replacement parts can be fabricated prior to total component failure.

1.1 Objectives

The objective of this work is to investigate the behaviour of High Velocity Oxy-Fuel (HVOF) aluminium bronze (AB) and nickel aluminium bronze (NAB) coatings under erosion, corrosion and erosion-corrosion conditions. Experimental means to elucidate the behaviour of the coating include a slurry jet impingement erosion rig, static corrosion experiments and the jet impingement erosion-corrosion apparatus. Conventional mass loss measurements were used for quantifying the rate of the coating removal and identification of synergy. Potentiodynamic polarisation experiments were carried out to understand the corrosion behaviour of the coating. Complimentary techniques such as scanning electron microscopy, surface profilometry and microhardness tester helped in characterising the morphology, chemistry and mechanism of erosion and corrosion of the coating.

The secondary objective is to gain a further understanding in the interpretation of electrochemical noise data in both time and frequency domain for the complex metallic coating system. Electrochemical potential and current noise measurements were collected and subsequently analysed in MATLAB using statistical methods, discrete wavelets transform (DWT) and empirical mode decomposition (EMD). The analysed noise signals were linked to the erosion rates and the extent of synergy.

1.2 Thesis structure

The thesis consists of four parts, containing seven chapters. The first part is the literature review, introducing the subject area, its background and current researches in progress. It is divided into sections that are relevant to the subject area under study, such as coatings technology, erosion processes, corrosion processes and erosion-corrosion processes. An additional section on the electrochemical noise acquisition and analysis is also included, explaining current research interests and analysis methods. These sections are intended to provide background information and to gain an initial understanding on the subject areas covered in this research.

The second part of the thesis consists of a single chapter, namely materials characterisation. This chapter explains the type of coatings and substrates used in the research, utilising information obtained from the supplier and open literature. Further characterisation of the coating system is also carried out here, with methodology and experiments such as microscopy and microhardness indentations being explained in detail. The section at the back aims to elucidate the static corrosion properties of the coatings and its substrates, they include results from potentiodynamic polarisation and electrochemical noise measurements. Work carried out in this chapter is used to facilitate the understanding and behaviour of the coating, which was subjected to further experiments in the following part.

Part three of the thesis is divided into four chapters, erosion, flow corrosion, erosion-corrosion and synergy. Chapter 3 presents and discusses results obtained from erosion experiments carried out at a range of kinetic energies (0.02 to 0.8 μJ). The erosion rate in mass loss was analysed with two methods: volume loss-kinetic energy maps and the dimensional analysis. Effects of sand concentration and impingement angle were investigated. The erosion rates of the coatings were compared with other common engineering materials and the erosion mechanisms were proposed. Chapter 4 discusses the results obtained from flow corrosion experiments. The corrosion rates of the coatings were compared with carbon steel substrates and bulk aluminium bronze alloys. The effects of porosity in the coating in affecting the corrosion behaviour was discussed and linked to open circuit potential measurements. The results of erosion-corrosion experiments are presented in Chapter 5. The effects of sand concentration in affecting erosion-corrosion was explained. SEM results were also presented in this section, showing the effects of combined erosion and corrosion on the wear scars. Open circuit potential measurements were used to identify and compare the different corrosion mechanisms under erosion-corrosion and flow corrosion.

Chapter 6 combines the mass loss results and electrochemical current noise results from the previous three chapters and discusses synergy between erosion and corrosion processes. Mass loss results were converted to penetration rate so that comparisons can be made between the experiments. A novel way of predicting synergy by mass loss ratio is presented and discussed here. The link between electrochemical standard deviation values and erosion mass loss was established and discussed. Two relatively new ways of current noise signal processing (DWT and EMD) are presented and compared. A transition from negative to positive synergy was

observed in the DWT and EMD analyses, its significance and relationship to mass loss and standard deviation data was also presented.

The conclusions obtained from all the work is then summarised and presented in Chapter 7. It was arranged in the order of materials characterisation, erosion, flow corrosion, erosion-corrosion and electrochemical techniques. Some concluding remarks are presented, relating the contribution of the current work to the existing knowledge. Suggestions for future work are also presented in this chapter.

Chapter 2 Literature review

This literature review begins with an introduction to the coating types and processes, followed by reviews of the erosion, flow corrosion and erosion-corrosion processes, and finally the electrochemical methods utilised in this investigation.

2.1 Coatings

2.1.1 The requirement for protective coatings in industry

Protective coatings are being used on structural alloys in energy conversion and utilisation systems such as coal plants, marine industry and oils industries to prevent surface degradation by corrosion, erosion and abrasion, or by combinations of these mechanisms. The compositions and structures of the coatings are determined by the roles that they play in the various service environments; their methods of application include both diffusion and deposition processes. The two types of coatings in the deposition process are the organic coatings and metallic coatings.

Metallic coatings usually serve two functions. First, the coating acts as a barrier to the environment, with greater erosion and corrosion resistance than the substrate metal. Second, the coating is usually selected with a more active corrosion potential than the substrate and corrodes galvanically to provide cathodic protection at breaks in the coating. Metal coatings are applied by many different methods, including immersion, plating, cladding, thermal spraying, arc spraying, chemical deposition, and vapour deposition [1]. Due to the nature of the work being carried out, only thermal spraying processes will be discussed in this review.

2.1.2 Thermal spray coatings

Thermal spray and other coatings are used to reduce wear and corrosion on a large number of components in various industries. In some cases the service conditions are very aggressive and therefore the resulting maintenance costs are extraordinary high. Improved coating

materials and appropriate selection and application of coatings are among the most promising way to reduce these problems. The optimum coating composition and process are dependent on the type of wear and the corrosion conditions. The coatings are produced by a process where molten or semi-molten particles with a size range of 40 – 120 μm are impacted onto a substrate surface by using a spray gun. The size of the coating powders depends on the type of application. Larger powders usually have a higher tensile stress during the cooling process, and the coatings are usually thicker [1]. Almost any material that can be melted without decomposition, vaporisation, sublimation or dissociation can be thermally sprayed.

Sprayed coatings have been successfully used in many industrial fields for combating wear and corrosion of structural materials. However, the development for coatings was made essentially following an empirical approach. As coating property requirements become more and more sophisticated, the successful utilisation of thermally sprayed coatings must be based on the better understanding of the coating structure in order to correlate the microstructure to the properties of the coating. Such understanding is of paramount importance when they are applied to wear and corrosion resistance.

2.1.3 Properties of thermal sprayed coatings

Thermal sprayed coatings exhibit a layered structure (Figure 2-1) due to their deposition process: powder particles are randomly sprayed on to the workpiece with a high kinetic energy and in a molten state. A common feature is their lamellar grain structure resulting from the rapid solidification of small splats, flattened from striking a cold surface at high velocities as seen in Figure 2-2.

These splats can range from 100-250 μm in diameter, with a thickness of around 10-30 μm. Porosity (0.025%-50%) is an intrinsic feature of such coatings and, in some cases, unmelted particles are also included due to partial melting or resolidification of some particles of the deposit. When the cross section of the macrostructure is examined, the presence of small and connected pores are generally easy to detect and thus, wear and corrosion are potential threats. A large proportion of thermal spraying is conducted in air or uses air for atomisation. Chemical interactions such as oxidation occur during spraying, metallic particles oxidise over

their surface forming an oxide shell. This is evident in the coating microstructure with oxide inclusions outlining the grain boundaries.

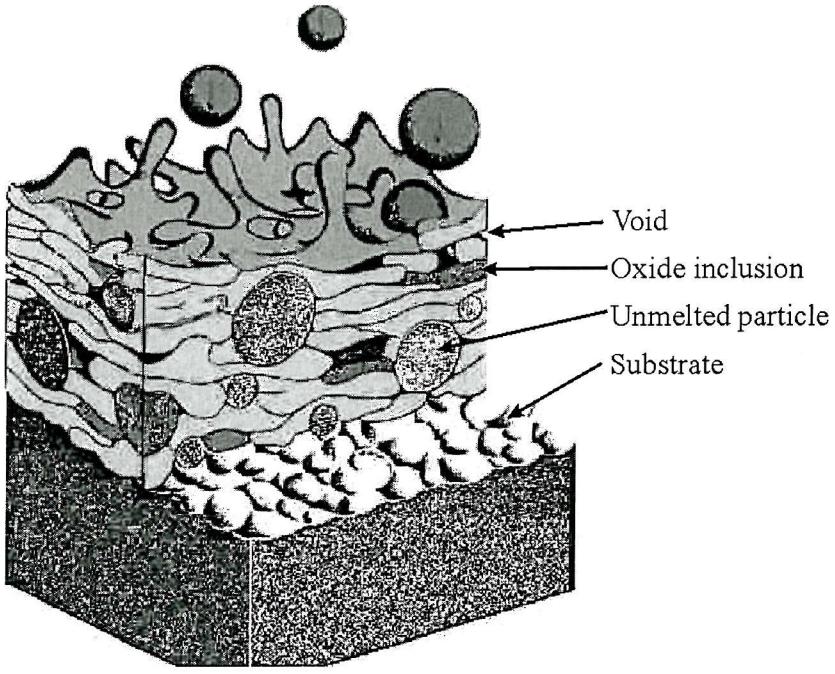

Figure 2-1 *Schematic cross section view of thermally sprayed coatings, showing voids, inclusions, and unmelted particles.*

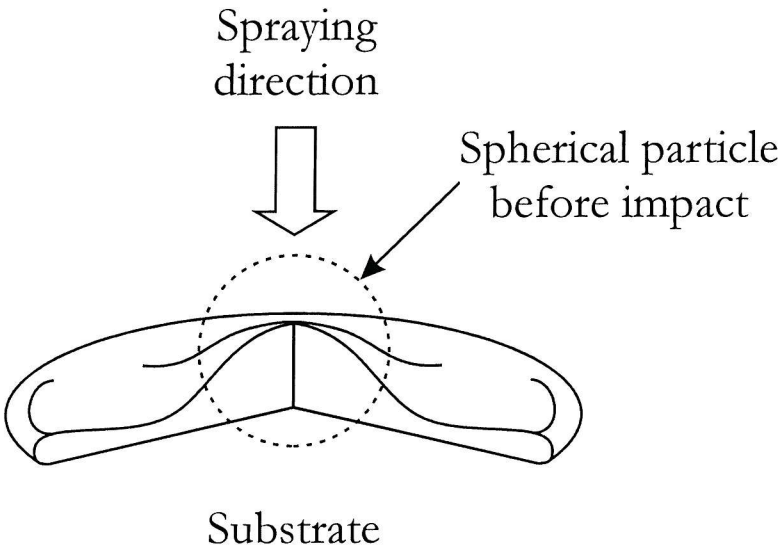

Figure 2-2 *The morphology of a single splat*

2.1.4 HVOF coatings

The HVOF technique is categorised as one of the thermal spraying processes, this process uses a high pressure internal combustion system utilising fuel and oxygen to produce a supersonic gas jet in excess of 2000 ms^{-1} and 2500 °C.

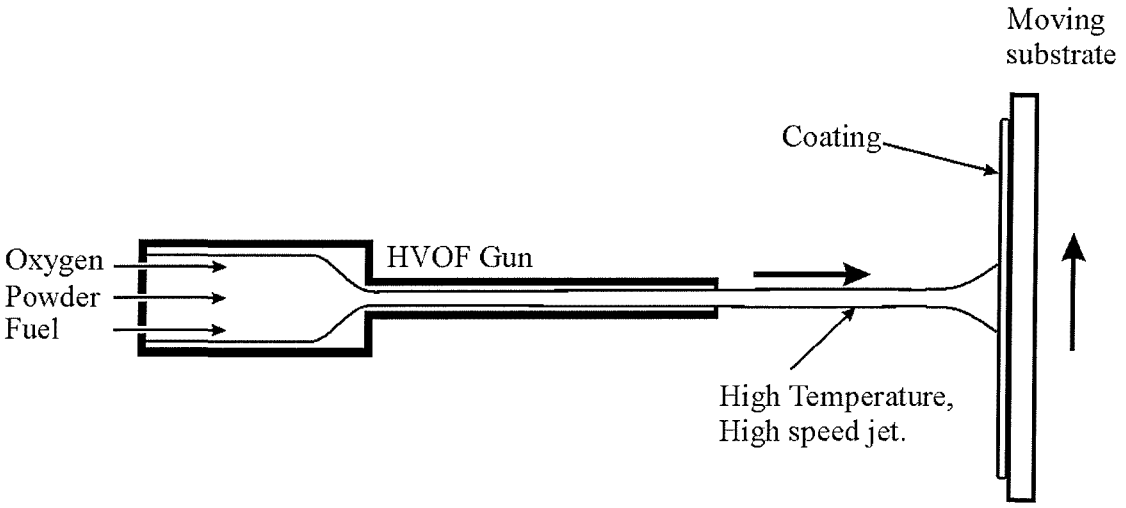

Figure 2-3 Schematic diagram showing the HVOF spraying process.

There are a number of HVOF guns that use different methods to achieve high velocity spraying. One method is basically a high-pressure water-cooled combustion chamber and a long nozzle as shown in Figure 2-3. Fuel (kerosene, acetylene, propylene and hydrogen) and oxygen are fed into the chamber, combustion produces a hot high pressure flame which is forced down a nozzle increasing its velocity to around 1500 ms^{-1} and the pressure to slightly above atmospheric. Powder may be fed axially into the combustion chamber under high pressure or fed through the side of a laval type nozzle where the pressure is lower. Another method uses a simpler system of a high-pressure combustion nozzle and air cap. In this system the fuel gas (propane, propylene or hydrogen) and oxygen are supplied at high pressure, combustion occurs outside the nozzle but within an air cap supplied with compressed air. The compressed air pinches and accelerates the flame and acts as a coolant for the gun. Powder is fed at high pressure axially from the centre of the nozzle.

The inherent advantage of the HVOF process is the ability to spray semi-molten particles at high velocities. This advantage produces coatings characterised by: lower residual stress, higher bond strength, reduced oxide content and very high density compared to those that are produced by conventional thermal spraying. The increase in particle velocity, reduced

particle temperatures and time at temperature during the spraying process can also reduce the oxidation and degradation of the molten particles.

2.1.5 Properties of HVOF

A typical HVOF coatings such as that in Figure 2-4 show lamellar grains appearing to flow parallel to the substrate. The structure is not isotropic, with physical properties being different parallel to the substrate than perpendicular to the coating thickness. Strength in the longitudinal direction can be 5-10 times that of the transverse direction. The coating microstructure is heterogeneous relative to wrought and cast materials. This is due to variations in the condition of the individual particles on impact. It is virtually impossible to ensure that all particles are the exact size and achieve the same temperature and velocity.

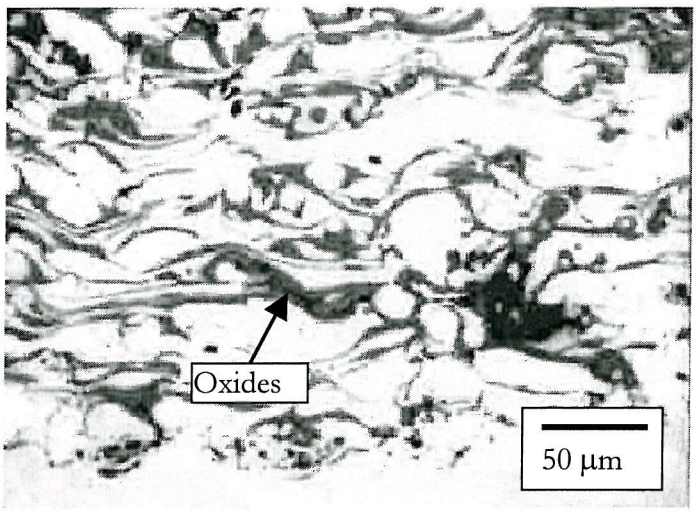

Figure 2-4 Typical cross sectional micrograph of a HVOF sprayed aluminium based coating, showing individual splats and oxides at splat boundaries (dark areas).

Many workers have studied the properties of HVOF coatings under erosion conditions [2,3,4], corrosion conditions [5] and also erosion-corrosion conditions [6]. Stewart et. al. [4] tested HVOF sprayed tungsten carbide (WC) coatings by using the dry sand rubber wheel abrasion technique with fused alumina. It was observed that the wear performance of the sprayed WC coating was inferior compared to the sintered materials due to sub-surface cracking and decomposition of the nanocomposite particles during spraying. Hawthorne *et al.* evaluated WC coatings under erosive conditions in dry air-solid jets [3]. It was concluded that the erosion resistance of the coatings depends on the coating composition and their

microstructural integrity. Neville *et al.* [5] used a.c. and d.c. corrosion experiments to investigate the corrosion behaviour of HVOF sprayed Inconel-625 coatings, corrosion attack was found in the form of pitting and localised attack on discreet splats. It was also mentioned that the vacuum impregnation technique for sealing the coating had no effect on the corrosion resistance. However, these investigations were centred on ceramic coatings based on tungsten, while little or no work was carried out on marine coatings.

2.2 Erosion

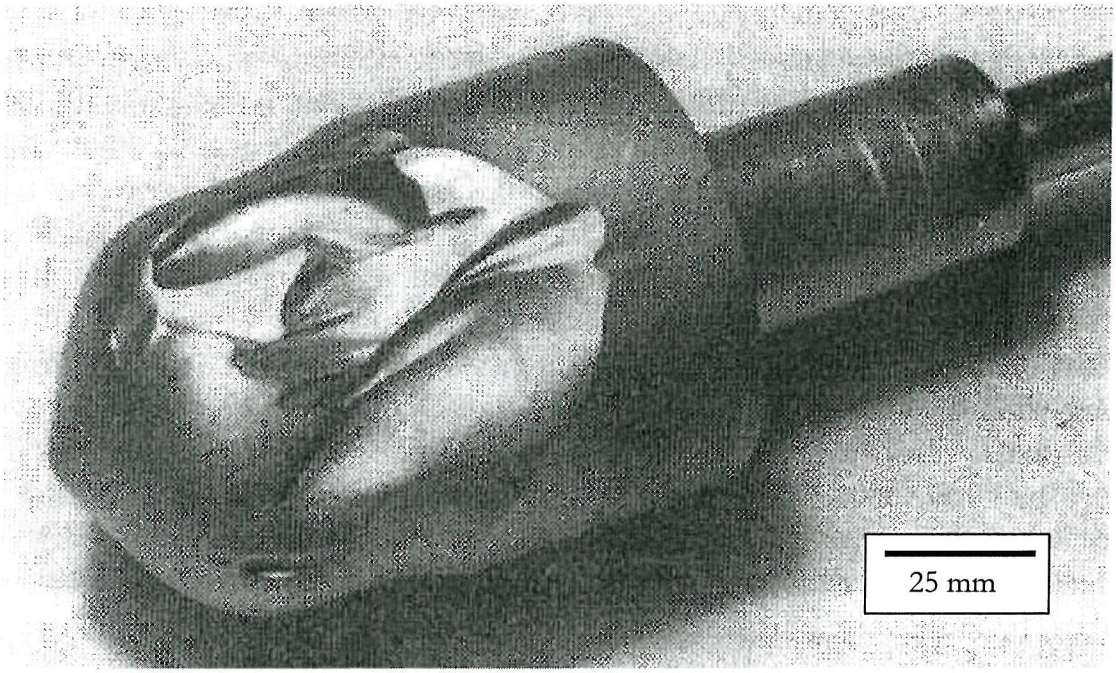

Figure 2-5 Erosion damage of a hardened steel valve plug in slurry flow. [7]

2.2.1 Principles of erosion

Erosion is defined as the wear caused by hard particles striking a surface, carried by a gas stream or entrained in a flowing liquid media [8]. Within the scope of this research project only erosion by solid particle impingement is considered. This type of wear occurs only when the solid particle impacts the surface with sufficient kinetic energy to cause permanent damage [9]. The factors affecting the material loss are the mechanical properties of the solid particle and the substrate material, and the properties of the fluid. A summary of these properties can be seen in Table 2-1.

Various workers have proposed different types of erosion models, in an effort to explain the erosion mechanisms. For ductile materials, the principal erosion mechanisms are cutting and plastic deformation, depending on the angle of impingement [8,10-12]. The erosion rate can then be derived from the material loss due to these mechanisms. Due to the type of work carried out in this thesis, the erosion of brittle materials will not be considered.

Table 2-1 Four major groups of factors influencing the slurry erosion rate of metallic materials.

Liquid:	**Particles**:
Viscosity	Size
Density	Density
Surface activity-lubricity	Shape-angularity
Corrosivity	Hardness-friability
	Concentration
Target/Surface:	**Flow field:**
Ductility-brittleness	Target particle velocity
Melting point	Angle of impact
Microstructure	Boundary layer properties
Toughness and Hardness	Particle-particle interactions
Work hardening	Particle rebound
Surface roughness	Reynolds number
Coating thickness/adhesion	
Coating porosity	

2.2.2 Erosion mechanisms

Until 1958, much of the work carried out was empirical. Finnie developed a model in an attempt to predict slurry erosion rates of ductile and brittle materials [12]. Flow parameters such as velocity and angle of impingement were incorporated into the model for predicting the erosion process. In addition, the erosive particle shape was also incorporated into the model to account for the mechanism of material removal.

By analytically describing the path of the particle and assuming that the volume of the metal removed was the product of the area cut out by the particle tip and the width of the cutting

face, metal removal by the erosion process was accounted for. A detailed review of the model can be found in the work of Speyer [13].

The basic assumptions of the model (cutting of the target metal by the tip of the eroding particle) were criticised for not being able to predict several important aspects of the measured erosion loss. These include the effect of the particle velocity, the occurrence of considerable mass loss at an impingement angle of ~ 90° (the model failed to predict erosion that occurred at 90°), and the impingement angle that maximum erosion occurred (experimental curves had to be moved to make the measured angle and the predicted angle coincide). The slurry erosion work carried out by Bitter [10,11] demonstrated that the cutting action is not the only mechanism by which ductile materials erode. Bitter derived a set of equations to calculate the volume loss due to the actions of cutting wear and plastic deformation wear. The work carried out by Finnie and Bitter formed the foundation for the understanding and modelling of erosion mechanisms by Hutchings [14], Levy [15], Sundararajan [16], Turenne [17] and Meng [18].

Hutchings [19] included a third type of material removal mechanism in the model, based on air erosion experiments. It was suggested that three types of damage might occur during particle impact at low angle. Spherical particles deform the surface by a ploughing action, displacing materials to the sides and front of the erosion crater and creating a heavily strained plastic lip. Further impacts on these features would then detach the lips, causing material removal. For angular particles, Hutchings suggested that two types of cutting could occur. In type I cutting, the particle rolls forwards as it strikes the target surface, causing a strained plastic lip that can be removed by subsequent impacts. In type II cutting the particle rolls backwards and Hutchings suggested that a true machining action can occur where the sharp corner of the particle removes material from the surface. It was stated that type II cutting occurs only over a narrower range of particle geometry and impact conditions.

Another erosion mechanism proposed was the extrusion of thin platelets that can be detached due to further particle impacts [15,16]. Levy [15] proposed that this type of mechanism occurs at both oblique and normal impact angles. Sundararajan [16] proposed that a critical strain must be achieved before the extruded platelets can be detached from the target surface. The concept of critical strain appeared to be similar to the ploughing mechanism, where the target material was removed by multiple impacts on the surface.

2.2.3 Effects of substrate material hardness

A hard material does not necessarily mean that it is more erosion resistant. A hard and brittle material can suffer a significant mass loss when in contact with erosive particles at a normal angle of impact [12]; the mechanism of material removal is through fracturing of the brittle surface. Therefore, the target materials fracture toughness needs to be considered as well [20]. For ductile materials under dry erosion, Levy [15] suggested maximum erosion resistance occurs if the angle of impingement is normal, where plastic deformation wear is the main form of mechanism for material removal. But for low impact angles, the cutting mechanism becomes dominant; hence the material wastage rate will be enhanced, making a ductile material unsuitable in terms of erosion resistance [8].

The erosion resistance of different materials is determined by their service conditions, if it is a low angle impingement, then a brittle material should be used, if it is normal angle, ductile materials can be used. This also depends on the angularity and the shape of the erodent particles.

2.2.4 Effects of carrier liquid viscosity

In general, the erosion rate will decrease with an increase in the carrier liquid viscosity. Levy [21] showed a 16-fold reduction in the rate of erosion of mild steel between slurries of 23 % w/w 250 μm SiC in kerosene and water. Clark [22] suggested two possible explanations for the viscosity changing the flow conditions around the target. The first mechanism suggested that the carrier liquid was increasingly effective in decelerating particles approaching the target surface, thus reducing the kinetic energy of the incoming particle. The second mechanism suggested that a carrier fluid with higher liquid viscosity increases the drag on suspended particles, hence a greater proportion of particles lying on the path of the moving target will be flowing above the specimen surface without impacting it.

2.2.5 Effects of particle concentration

For all particle concentrations, the mass loss due to erosion increases as a function of time, as shown in Figure 2-6. For any given test duration, the wear is proportional to the sand concentration during the experiment, due to a higher amount of erodent particles used to impinge on the surface of the specimen. However, there are many conflicting reports on the literature regarding the effect of particle concentration on the erosion rate. Tsai [23] carried out tests on stainless steels in a slurry pot, with coal particle (24 μm) concentrations between 30 % w/w and 60 % w/w. It was reported that the erosion rate increases linearly with particle concentration.

Turrenne defined the erosion efficiency as the ratio of wear to the sand concentration [24], and stated that the slurry erosion efficiency decreases as the sand concentration increases as seen in Figure 2-7. For concentrations higher than about 13 % w/w, the erosion efficiency becomes constant. The decrease in erosion efficiency is an indication of particle-particle interaction that impedes the erosion of the specimen. The laminar flow of the slurry jet becomes turbulent near the surface of the specimen and the resulting flow conditions lead to the formation of a particle cloud, which leads to a decrease in the erosion efficiency corresponding to a limited protection of the specimen surface.

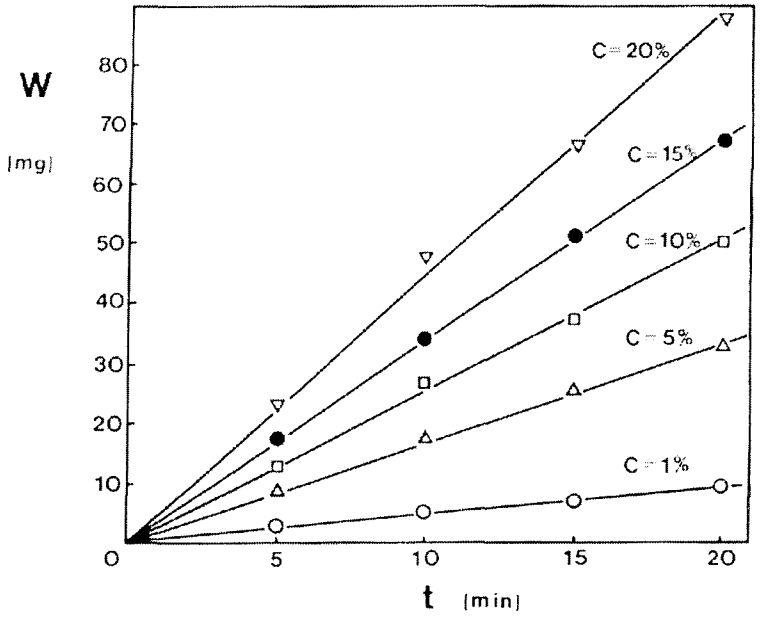

Figure 2-6 Erosive wear (W, mass loss) of aluminium as a function of test duration (t) for different sand mass concentrations [24]

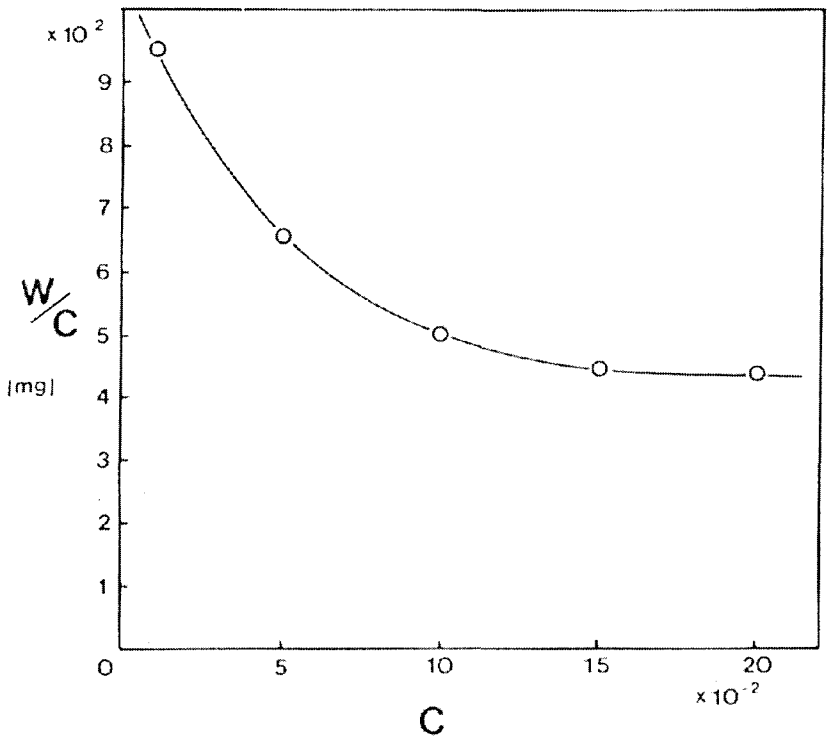

Figure 2-7 Erosion efficiency (W/C) vs. sand mass concentration (C) for aluminium [24].

2.2.6 Effects of particle size and shape

The increment in erosion rate has been shown to be proportional to the erodent particle size [9,25,26]. As the particle size increases, the inertia force of the particle will increase because it is proportional to the cube of the diameter of the particle, provided that the same velocity is used in the experiments. The higher inertial force will prevent the larger particles following the streamline of the slurry jet, hence a higher number of impacts onto the surface of the specimen. Smaller particles have a lower inertial force within the slurry, causing these particles to follow the streamline of the flow without impacting onto the surface of the specimen at all. The effects of particle size in affecting the erosion rate can be seen in Figure 2-8.

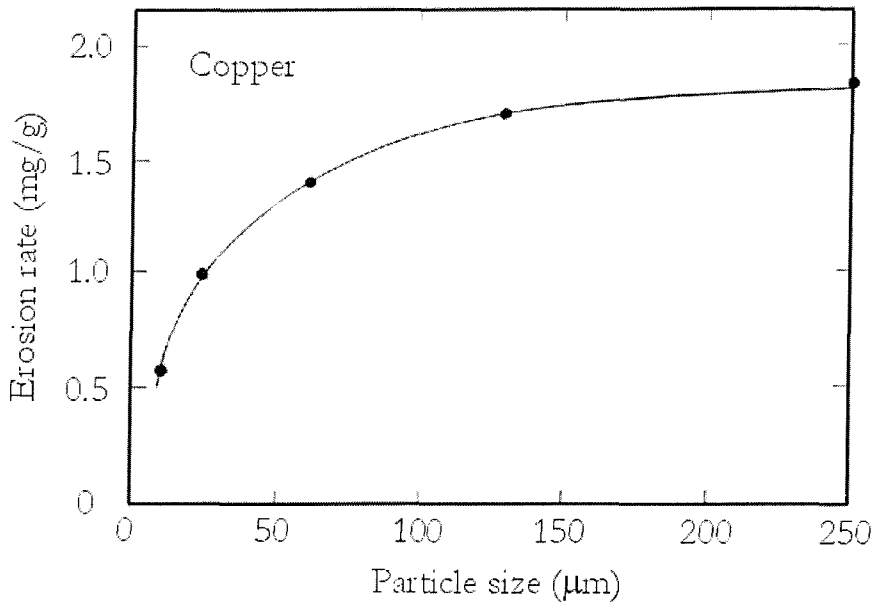

Figure 2-8 Erosion rate as a function of particle size for copper [27].

Lin *et al* [26] carried out slurry erosion experiments on hot rolled AISI 1020 steels with sand-water slurries at 47.1 ms^{-1} velocity. Quartz particles with diameters ranging between 48 μm and 250 μm were used. It was suggested that the erosion rate and particle size showed a linear relationship.

Lynn *et al* [9] used cylindrical specimens in a slurry pot to study the effects of particle sizes between 20 μm and 500 μm. They associated the particle size with the kinetic energy of impacting particles, and found that the erosion rate does not behave linearly with particle size. They also concluded that the decrease in erosion rate with the decreasing particle size reflected the decrease in the proportion of particles impinging on the target surface as well as the decrease in their impact velocities. However, they failed to propose a model showing the relationship between erosion rate and particle size.

The effect of particle shape on the erosion rate of materials is harder to quantify. It is well known that angular particles tend to cut the surface, whereas spherical particles tend to cause plastic deformation [8]. However, Roy *et al.* carried out dry erosion experiments with spherical steel grits and angular SiC particles as erodents. Various copper alloys were eroded at velocities of 38 ms^{-1} and 68 ms^{-1}. They found that the erosion rate is higher when spherical particles (steel shots) rather than angular particles (SiC particles) are used as the erodent, which was related to the integrity (shatter resistance upon impact) of the erodent particles

[28]. It was suggested that plastic deformation on the surface of the target material was the main erosion mechanism.

2.2.7 Effects of erodent recycling

If particles are recycled in erosion testing, their properties may be changed in two ways: by gross fracture or by finer-scale alteration of surface features usually leading to the rounding of angular particles. The degree of fragmentation, assessed optically by Sparks *et al* [29], depended on initial particle size and also on impact intensity: velocity, impact angle and target material hardness. In their paper, Sparks *et al* used silica particles in the size ranges between 125-150 μm and 53-75 μm for the dry erosion work. The scanning electron microscope was used and extensive fracture occurred to the silica particles at impact velocities of 98 ms^{-1}. However, at an impact velocity of 44 ms^{-1}, rounding of the angular silica particles occurred, hence particle recycling at low kinetic energy erosion tests were considered acceptable. In the event that particles undergo fracture during an erosion experiment, the average particle size will be smaller and the erosion efficiency will decrease with a smaller particle size distribution.

2.2.8 Effect of particle impact angle

Impact angle in erosion is defined relative to the target material surface, a normal impact angle occurs at 90° while a glancing angle occurs around 0°. Ductile materials show maximum erosion at angles between 10° and 30°, the erosion rate then falls to a minimum at normal angle. This behaviour is observed in most metals. Brittle materials often show a maximum erosion rate at normal angle and minimum erosion at low angles of impingement [8]. The dependence of erosion rate to impingement angle for ductile and brittle surfaces under air/solid impingement can be seen in Figure 2-9.

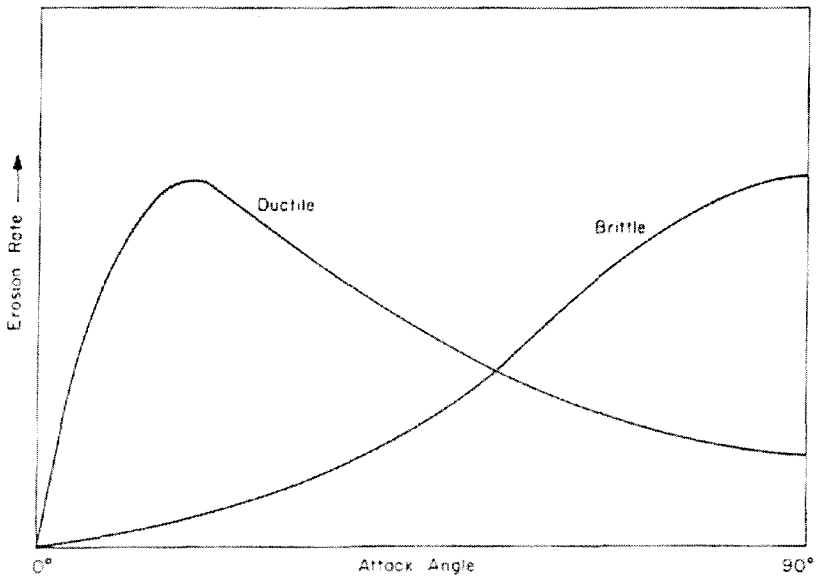

Figure 2-9 Dependence of erosion rate on attack angle for ductile and brittle materials [27].

Benchaita *et al* [30] showed that by eroding a copper plate at a normal incidence angle with a sand-water slurry jet resulted in an eroded crater with a raised centre. This indicated that minimum erosion occurred in the centre of the jet, where the particles strike the surface at a normal angle. The surrounding areas suffered from erosion due to particle deflection, hence a lower angle of impingement. Turrenne *et al* [24] confirmed the findings of Benchaita *et al* [30] in their slurry erosion experiments with aluminium. Clark *et al* [31] used cylindrical specimens in a slurry pot erosion tester to identify the effect of impingement angle. Tests were conducted using silicon carbide particles with diesel oil as the liquid medium. He found that the erosion rates for 1020 steel, Oxygen Free High Conductivity (OFHC) copper, and phosphorous containing steel were highest at around 30° impingement angle.

2.2.9 Types of erosion rigs

Slurry erosion test methods fall basically into two main categories: pipe wear tests and laboratory simulation tests. In wear testing of pipes, pipe specimens are fixed either in operating industrial pipelines or in closed loops. Wear caused by the slurry flow is then recorded by weighing or by monitoring the change in pipe wall thickness. The high cost and the long times needed for detectable wear are major disadvantages, while simulation testing allows relative motion between a test specimen and slurry to be generated more simply. The generally lower cost and flexibility of simulation testing, coupled with better control over the

conditions to which specimens are exposed, make it considerably more reliable for laboratory research into the mechanisms of erosion and the influence of operating variables on wear rates. These test methods are also ideal for candidate material or coatings evaluation before using it in actual service conditions. Different types of simulation testing apparatus have been used in the investigation of slurry erosion, they include immersed jet [32], free jet [24,33,34], slurry pot [25,35], and centrifugal [36].

Figure 2-10 shows a slurry pot tester, the specimens are placed at the end of rotating arms that are immersed in a tank containing slurry. However, because of the unstable inertia flow of the slurry, it is very difficult to measure and control the velocity and impingement angle of the slurry accurately. By using the same test slurry to impact specimens repeatedly, the test is further complicated by blunting and fragmentation of the impacting particles.

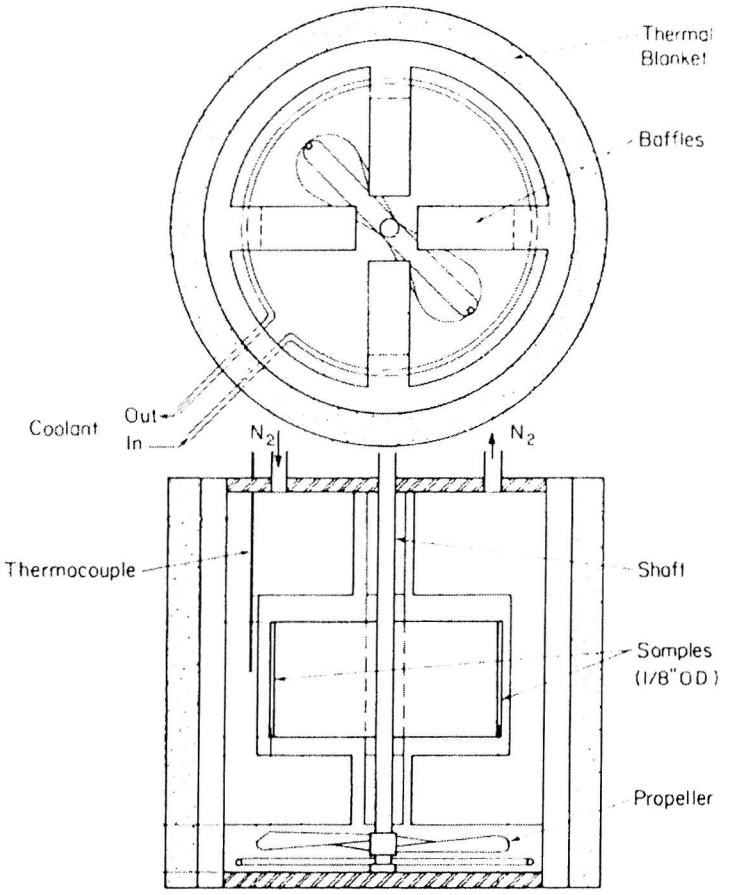

Figure 2-10 A schematic diagram of the slurry pot erosion tester [23].

Another more commonly used technique is the jet impingement as seen in Figure 2-11, which utilises a high pressure water jet containing abrasive particles. The jet impingement angle and velocity can be easily controlled, but if the carrier liquid is of high viscosity, it is difficult to get a high impact velocity. Also, due to the wear of the nozzle, the impact velocity must be measured and calibrated periodically. Levy and Yau [37] mentioned that at solid concentrations of around 5 % v/v, a "blanketing" effect could occur at the point under the jet, which protects the surface from other impinging particles.

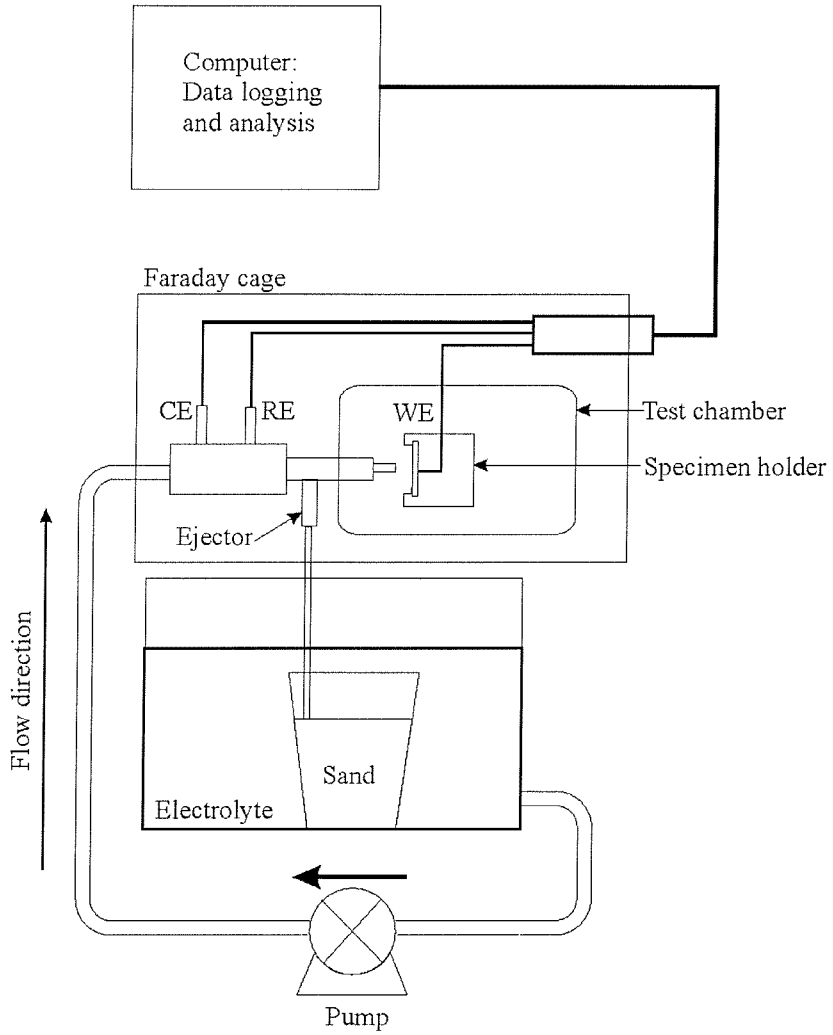

Figure 2-11 A schematic diagram of the jet impingement slurry erosion rig (fitted with a corrosion cell).

2.2.10 Free jet-hydrodynamics

It is important to understand the fluid mechanics of the solid-liquid two-phase flow in a slurry erosion condition, as the particle impact angle and velocity can be altered drastically by different flow conditions. Benchaita *et al.* [30] showed that the flow of the slurry can cause a

W-shaped scar on the surface of a ductile material such as copper when a jet is directed at normal angle to the specimen, as seen in Figure 2-12. The region directly beneath the nozzle is called the stagnation region, and the rest of the surface is the free jet region. It can be seen that the stagnation region did not suffer as much erosion compared to the region adjacent to it, due to the nature of free jet flow, the particle impingement angle at the free jet region is much lower compared to the original normal impact angle.

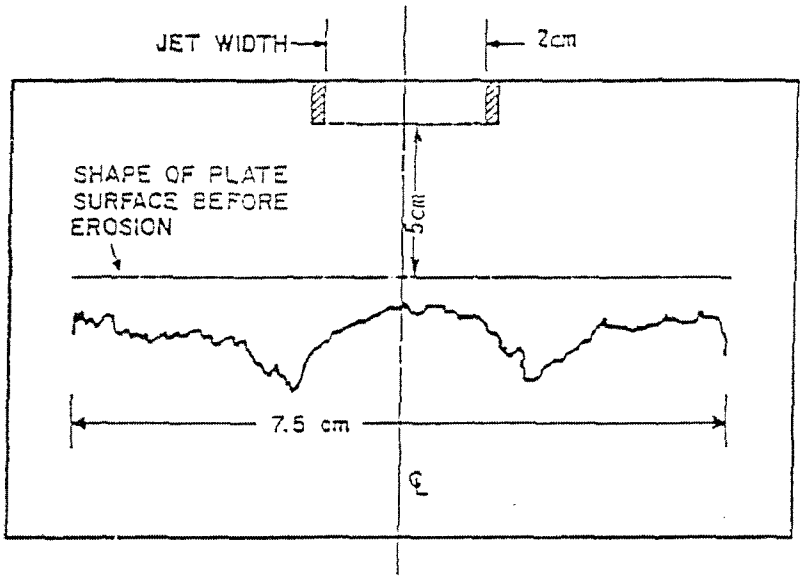

Figure 2-12 Profile of an erosion scar for a copper specimen produced by a slurry jet (particle diameter 700 μm, velocity 8 ms^{-1}) [30].

The model used by Benchaita was based on the following steps: the flow of the liquid media and a single particle trajectory was calculated initially. Subsequently, the erosive action was modelled based on this single particle impact, and then integrated to account for all particles so that the overall erosion rate in the free-jet system can be estimated.

The modelling of the liquid flow, with the determination of particle trajectories were carried out in a 2-D model as seen in Figure 2-13. The principle assumption made by Benchaita was that laminar flow occurred throughout the entire region where the slurry is in contact with the specimen.

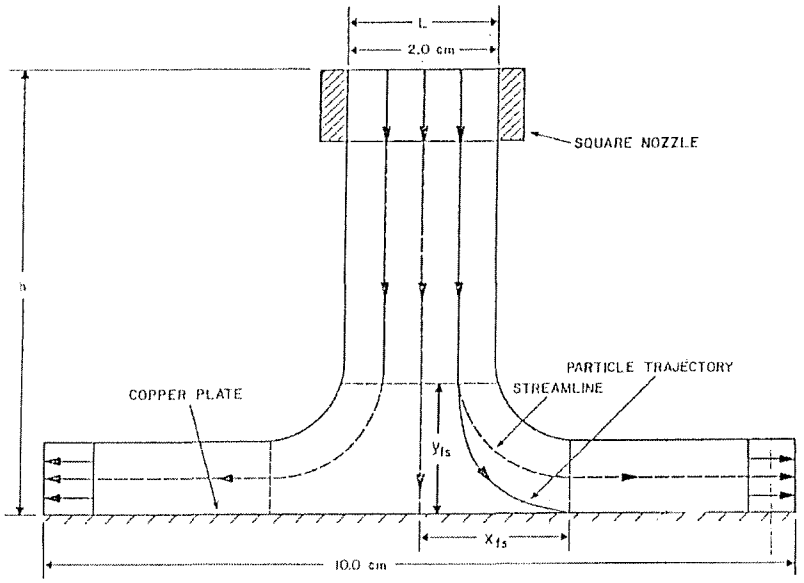

Figure 2-13 Schematic diagram of a two-phase flow (liquid-solid) impinging on a flat plate at normal attack in two dimensional flow [30].

The flow from the exit plane of the nozzle and the outgoing flow from the stagnation point were assumed to be linear. A streamlined transition area exists between these regions, the vertical velocity decreases from a maximum value at the nozzle exit to a zero value at the stagnation point (centre of the specimen surface). This is followed by an increase in the horizontal velocity (at the stagnation point) from a zero value to a maximum value at the exit region. The boundary layer was also calculated to be half the particle diameter, hence the viscous drag on the particles upon impact can be neglected. However, the flow parameter used to calculate the boundary layer was not defined. The flow parameter is related to the geometry of the flow and to the fluid flow rate, small alterations in these parameters can affect the flow conditions and boundary layer in the system. More recently, Turenne *et al* [17] carried out similar methods to model the fluid flow in a normal impingement angle, using numerical methods to solve the differential fluid flow equations. They determined that the flow parameter is inversely related to the stand-off distance between the nozzle exit and specimen surface. This allowed them to define accurately the boundary layer and the fluid flow geometry.

Due to the low concentration of slurries used in Benchaita's model (0.35 % w/w) and Turrene's model (1 % w/w), decelerating effects on the particles in the flow and interaction between particles were neglected. Momentum analysis using the equation of motion was

carried out for single spherical particles, where the buoyancy force (momentum towards the target) with the drag force (liquid viscosity) from the liquid media was compared. Both of the workers agreed that larger particles have a higher inertia, therefore large particles will hit the specimen at approximately the same angle as the jet angle, as seen in Figure 2-14 for particles with a diameter of 1000 μm. Conversely, smaller particles (with smaller inertia) tend to follow the streamline of the flowing liquid, and are consequently swept away by the outgoing flow without impacting the specimen surface as can be seen in Figure 2-14 for particles with a diameter of 200 μm.

In a similar analysis by Lin *et al.* [26], particle trajectories will tend to follow the streamline of the flow during slurry erosion at low impingement angles as seen in Figure 2-15 that smaller particles will tend to be affected by the viscosity of the liquid media. The particle impingement angle will be smaller than the jet angle at direction v_1 and particles moving along direction v_2 will have an impingement angle higher than the jet angle.

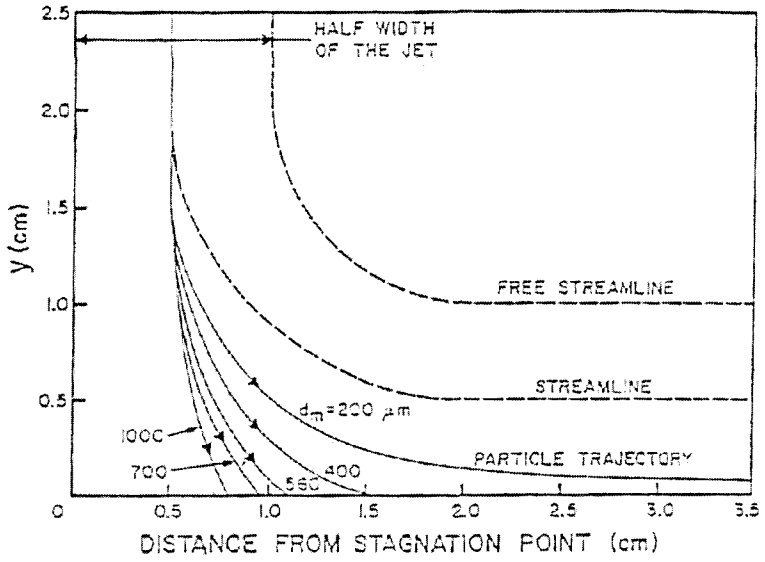

Figure 2-14 Trajectories of abrasive particles of different sizes in the jet (8 ms^{-1} velocity) [30].

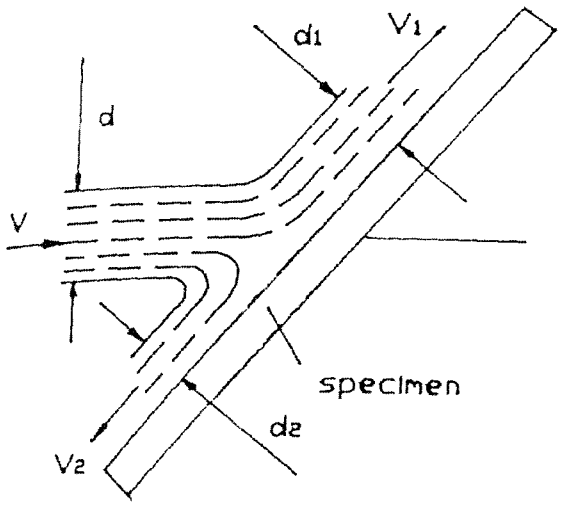

Figure 2-15 Spreading effect of a stream of flow impacting on a flat surface with a low impingement angle (30°) [26]

2.3 Corrosion

2.3.1 Introduction

Corrosion may be defined as the chemical or electrochemical reaction between a metal and its environment that produces a deterioration of the metal and its physical property [38]. It is usually an insidious process which is often difficult to recognise until deterioration is well advanced, types of corrosion include general corrosion (uniform attack on the surface), localised corrosion (pitting, and crevice corrosion) and high temperature oxidation. The scope within this work is restricted to flow corrosion in an aqueous environment.

The literature on theoretical concerns and types of corrosion [38-40] can be obtained easily. Therefore, only specific topics such as flow corrosion, jet impingement corrosion and corrosion of coatings will be reviewed here.

2.3.2 Fundamentals of corrosion

The 'corrosion cell', shown schematically in Figure 2-16 has five essential components: (1) anodic zones; (2) cathodic zones; (3) electrical contact between anodic and cathodic zones; (4) an ionically conductive solution; and (5) a cathodic reactant. The anode and cathode can consist of similar or different metals.

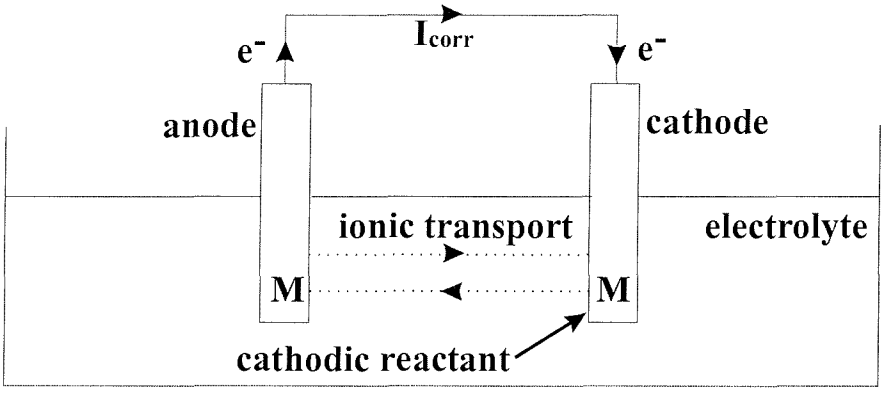

Figure 2-16 A simplified corrosion cell showing various components that are involved in a corrosion process.

The corrosion cell may be viewed as a short circuited electrolysis cell, whose cell voltage provides the driving force for material wastage. In practical situations, the actual anodes and cathodes may be entirely separate and macroscopic or may occur locally on a heterogeneous metal surface - the latter case being more common. Numerous, discrete cells may arise due to differences in the constituent phases of the metal (possibly due to heat treatment or welding), from variations in stress, from natural coatings (e.g. oxides) or protective coating variations.

The overall corrosion process is a chemical reaction representing spontaneous dissolution of the metal (*M*) by reactions with the environment such as:

$$M + \frac{n}{4}O_2 + \frac{n}{2}H_2O \rightarrow M^{n+} + nOH^- \qquad \textit{Equation 2-1}$$

$$M + nH^+ \rightarrow M^{n+} + \frac{n}{2}H_2 \uparrow \qquad \textit{Equation 2-2}$$

where *n* represents the number of electrons involved in the corrosion process.

Each of these cell reactions is the result of an anodic and cathodic reaction occurring simultaneously at identical rates on the corroding surface, i.e.: for copper, an overall reaction for the corrosion in an aqueous environment is:

$$Cu + 2H_2O + O_2 \rightarrow 2Cu^{2+} + 4OH^- \qquad \textit{Equation 2-3}$$

The above reaction can be written in an ionic form:

Anode: $Cu \rightarrow Cu^{2+} + 2e^-$ *Equation 2-4*

Cathode: $O_2 + 2H_2O + 4e^- \rightarrow 4OH^-$ (alkaline or basic conditions) *Equation 2-5*

$2H+ + 2e^- \rightarrow H_2$ (acidic conditions) *Equation 2-6*

2.3.3 Kinetics of corrosion reactions

In an aqueous environment, there are at least two partial electrode reactions involved in the corrosion process, where the exchange of electrons takes place. The anodic partial reaction represents the oxidation of a metal in which free electrons are produced. These are consumed by the reduction of an oxidising agent, represented by the cathodic partial reaction.

It is important to realise that metal corrosion is a non-reversible and non-equilibrium situation. The metal takes on a mixed potential that depends on the thermodynamics and kinetics of both metal dissolution and the balancing cathodic process. Considering the corrosion reaction of copper:

$$Cu + nH^+ \rightarrow Cu^{n+} + \frac{n}{2} H_2 \qquad \textit{Equation 2-7}$$

The reaction continuously leads to the production of Cu^{n+} and H_2 and consumes H^+ in the process. The rate at which electrons are produced in the copper dissolution reaction is balanced by the rate of consumption by the hydrogen evolution reaction.

On open circuit, or if the metal is immersed in the same aqueous electrolyte, the metal must take up the corrosion potential (E_{corr}), the potential where no net current flows, because the anodic and cathodic currents are equal, i.e.:

$$i_{Cu/Cu^{2+}} = i_{H^+/H_2} = i_{corr} \qquad \textit{Equation 2-8}$$

i_{corr} is called the corrosion current.

When a metal is not at equilibrium current with a solution of its own ions, the electrode potential differs from the equilibrium potential by an amount known as the polarisation potential. Polarisation is an extremely important corrosion parameter because it allows useful statements to be made about the rates of corrosion process. In practical situations, polarisation is sometimes defined as the potential change away from some other arbitrary potential, and in mixed potential experiments this is the corrosion potential.

2.3.4 Passivation

The phenomenon where the surface of a metal is covered by a thin layer of protective film is termed as passivation. For metals such as copper, aluminum and stainless steels, this passivating film is inert and forms a barrier, hence protecting the surface of these metals from aggressive species. The transition between active dissolution and a state of passivity is generally marked by a decrease in the anodic current density and hence the corrosion rate. Passive current densities in the order of 10^{-2} Am^{-2} are usually quoted as representing true passivity [41].

Under passivation conditions, there are two components to the overall charge balance involving the film growth and film dissolution respectively [42]:

$$i_{passive} = i_{growth} + i_{dissolution} \qquad \textit{Equation 2-9}$$

In which the $i_{passive}$ is the passive current density and represents the measurable or external current density during film growth. When a constant film thickness is achieved, steady state is

reached hence i_{growth} is equal to $i_{dissolution}$. Consequently, the external current can be equated to the corrosion rate.

The onset of passivation may be designated by the passivation potential, E_p which corresponds to the peak or critical current density, i_{crit} beyond which the current density begins to drop with potential until passivity is complete. The passive region of copper alloys has a potential range between 50 ~ 100 mV Ag/AgCl (SSC) [43,44], where the passive film remains stable and the corrosion rate is low. Beyond this passive region, any further increase in potential will cause passive film breakdown. This was indicated by a sudden increase in current density, indicating an increased corrosion rate.

It is also possible for passive films to breakdown when the surface of the specimen is exposed to a turbulent flow where the shear stress on the surface is sufficient to break or strip the passive film. Bubbles or solid particles that are present in multi-phase flow systems can also break these passive films and cause an increased corrosion rate, as discussed in the next section.

2.3.5 Flow corrosion

Flow corrosion is defined as increased corrosion from increasing turbulence intensity and mass transfer as a result of the flow of a fluid over a surface [45]. Corrosion behaviour of metals under flowing conditions can be very different from those in static conditions. Metals that are usually passive under static conditions can corrode quite rapidly when subjected to a flowing electrolyte. A complete description of flow corrosion for any system requires an accurate definition of heat transfer (thermal), mass transfer (chemical) and momentum transfer (physical) characteristics [45]. Heat transfer in most seawater corrosion systems is generally not sufficient to affect the corrosion process to the same degree as momentum transfer and mass transfer, hence it will not be considered further.

Bengough and May first studied flow corrosion of copper alloys in seawater during the 1920's, by carrying out flow loop tests using a velocity of 3 ms^{-1} [46]. Thickness losses were measured and it was discovered that under flowing conditions, an increase in material loss by 15 % occurred compared to the static experiments. It was suggested that the flowing

turbulent seawater removed the protective oxide layer that was present during the static corrosion experiments. It was also pointed out that the area where the passive film was removed became anodic whereas areas that remained intact became cathodic. Hence a higher material loss was recorded due to the anodic area being polarized by the rest of the surface. Similar experiments were carried out later by May *et al* in 1928 using a jet impingement apparatus [47]. Potential fluctuations of the copper specimen exposed to the impinging jet were recorded by a potentiostat. Potential traces obtained showed an increase in the anodic direction when the protective surface film was broken by the flow, confirming that areas subjected to turbulent flow were anodic due to the loss of the passive protective film. Both the workers agreed that the passive films were removed by the actions of the flowing electrolyte and bubbles entrained within it.

In the case where the mass transfer process is the limiting factor, the boundary layer thickness that exists on the surface of the specimen becomes important. Generally, a thinner boundary layer will allow a higher mass transfer, corresponding to a higher corrosion rate. The mass transfer effects between an impinging turbulent jet of water and a flat brass plate were studied by Rao and Trass [48] and Dawson and Trass [49]. Dawson and Trass defined the following equation for the boundary layer in the wall jet region, where $Sc > 100$:

$$Sh = 0.0294 Re^{0.93} Sc^{0.25} \left(\frac{r_j}{d_j} \right)^{-1}$$ *Equation 2-10*

Here

Sh = Sherwood number = $\frac{kd_j}{D}$

Re = Reynolds number = $\frac{Vd_j}{\nu}$

Sc = Schmidt number = $\frac{\nu}{D}$

d_j = jet diameter (m)

r_j = radius on the plate from the stagnation point (m)

D = diffusion coefficient of the species concerned (m^2s^{-1})

V = mean flow velocity (ms^{-1})

ν = kinematic viscosity (m^2s^{-1})

The wall jet region in their experiments was defined by:

$$\left(\frac{r_j}{d_j}\right)^{-1} \geq 4.5 \qquad \textit{Equation 2-11}$$

According to Rao and Trass [48], when the stand off distance and nozzle diameter ratio is greater than 6.5, the water jet exhibits a fully developed flow until the point of impingement with the specimen surface. The impingement velocity is equal to the nozzle velocity. A stagnation region exists within the wall jet region, and the boundary layer characteristic in this region was equated as:

$$Sh = 0.0107 Re^{1.06}\left(\frac{h_j}{d_j}\right)^{-0.54} \qquad \textit{Equation 2-12}$$

where h_j is the stand-off distance (m) between the jet nozzle and the target surface.

Mass transfer effects from these equations correlated well to their experiments in the wall jet region. However, dissimilarities were observed within the stagnation region, where the actual material loss was much higher than expected. The authors indicated that the increase of mass loss in the stagnation region was due to 'erosion by turbulent eddies'.

Wall shear stress is a direct product of the viscous energy loss within the turbulent boundary layer, and it is related to the intensity of turbulence in the fluid acting on the wall. This is explained by the isothermal pressure loss in turbulent fluid flow within an incremental length due to fluid friction resulting from contact with a stationary wall. Giralt and Trass [50] proposed an equation to describe the wall shear stress (τ_w) within the wall jet region:

$$\tau_w = 0.179 \rho V^2 Re^{-0.182}\left(\frac{r_j}{d_j}\right)^{-2} \qquad \textit{Equation 2-13}$$

And the jet Reynolds number is defined as:

$$Re = \frac{2r_j V}{\nu} \qquad \textit{Equation 2-14}$$

Where r_j is the radial distance (m), ρ is the liquid density (kgm^{-3}), V is the mean jet velocity (ms^{-1}), and ν is the kinematic viscosity (m^2s^{-1}).

Efird [51] stated that in a disturbed flow, a disrupted hydrodynamic boundary layer and a disrupted diffusion boundary layer occurs. The result is a disturbed wall shear stress and mass transfer coefficient that cannot reach steady state due to the above reasons, giving rise to an enhanced corrosion rate.

By using a jet impingement apparatus, Efird *et al* [45] used the above equation to correlate the corrosion rate of AISI 1018 carbon steel with the wall shear stress of the 3 % NaCl solution. They found that the relationship between the wall shear stress and the corrosion rate follows a power function that can be described as:

$$R_{corr} = a\tau_w^{\ b} \qquad \textit{Equation 2-15}$$

Where R_{corr} is the corrosion rate (mmy^{-1}) and τ_w is the calculated wall shear stress (Nm^{-2}). For jet impingement experiments, the coefficient (*a*) was 6.8 and the exponent (*b*) was 0.1.

However, the authors cautioned that the values of the coefficient and the exponent are said to be functions of specific environment and solution chemistry, depending on the ionic strength of the solution, partial pressure of dissolved gasses, and the pH. Thus the relationship cannot be used universally for all types of corroding systems. However, Equation 2-15 showed that the wall shear stress on the specimen surface undergoing flow corrosion increases with the Reynolds number (jet velocity).

Localised or uniform corrosion can occur depending on the conditions where the film breaks down. Ault [52] reported that for copper–nickel alloys, uniform corrosion occurred at flow velocities above 10 ms^{-1}, whereas localised corrosion occurred at flow velocities of 8 ms^{-1}. It was suggested that at high flow velocities, high turbulence on the surface of the specimen

removed substantially all of the passive film on the surface of the copper-nickel alloys, which means that the passive film was only partially removed at low velocities.

More recently, Schmitt *et al* modelled the kinetic energy of the turbulent elements within a flowing liquid media [53]. They correlated the kinetic energy with the wall shear stress when these elements impact a surface, stating that a critical shear stress was required to cause the fracture of passive films and oxides on the surface of the specimen. Depending on the amount of scales removed, uniform or localised corrosion may occur.

2.3.6 Corrosion of nickel aluminium bronze alloys

Nickel-aluminium-bronzes (NAB) are widely used for propulsion and seawater handling systems in naval platforms and, in the UK, were first considered for submarine applications during the late 1950s and early 1960s. The combination offered by nickel aluminium bronzes of high strength, high corrosion resistance and availability in a number of different forms resulted in it being used under a wide variety of conditions and by a wide variety of industries. Nickel aluminium bronze alloy is used for seawater service, water supply, chemical and petrochemical industries, and certain high temperature and corrosive atmosphere conditions. Under seawater service conditions, applications of nickel aluminium bronze include marine propellers, seawater pumps (casings and impellers), valves, heat exchangers and general marine pipework [54-56].

Culpan and Rose [57] and Hasan *et al.* [58] showed that aluminium bronze containing only copper and aluminium have a single phase (α) structure up to about 8% aluminium. Above that level a second phase (β) is formed producing an α-β alloy. If an α-β aluminium bronze is allowed to cool slowly from temperatures above 600 °C the β phase converts to a mixture of α and γ_2 phases at around 565 °C. The γ_2 phase contains higher aluminium content than the β phase, making it susceptible to corrosion when coupled with the more noble α and β phases. If γ_2 is present as a continuous network, a higher rate of penetration of corrosion through the alloy could occur, reducing the overall corrosion resistance.

Nickel aluminium bronzes containing approximately 5% each of iron and nickel additions greatly suppresses the formation of γ_2 phases and also refines the overall grain structure of the

alloy, any γ_2 phases present will be in a discontinuous form [55-57]. The β phase breaks down during cooling through the temperature range 950 to 750 °C to produce α and κ phases. The κ phases are of variable composition containing aluminium, iron, and nickel and its formation effectively increases the amount of aluminium that can be present in the alloy before the danger of γ_2 formation arises. To ensure that the κ phase itself is corrosion resistant the nickel content of the alloy should exceed the iron content.

Dealloying

All of the phases mentioned above adopt different corrosion potentials when immersed in seawater. Specifically, it was found that during the corrosion initiation stage, the copper-rich α phase around the lamellar κ_{iii} (a NIAl-FeAl phase) corrodes, but as the pH within the anodic area drops, propagation commences with preferential attack of the κ_{iii} phase and the subsequent redeposition of copper [59]. Dealloying or dealuminification of nickel aluminium bronze results from the selective dissolution of the anodic Ni-κ and Fe-κ phases, leaving a residue of copper on the surface. This residue has a porous structure and very low mechanical strength but it retains the shape and approximate dimension of the original alloy. Consequently the depth of penetration is very difficult to assess except by destructive methods such as the preparation of metallographic sections. Dealuminification rates lie between 1.8 mm in 9 months [54] and 6 mm in 15 years [60]. Ferrara and Caton [60] reviewed experience in the US Navy with both aluminium-bronze and NAB. Their work also concentrated on selective phase corrosion and they found that NABs with a nominal 5 % iron, 5 % nickel content showed a maximum depth of 6 mm in 15 years. This survey involved the examination of over 400 NAB components. The same workers reported that penetration as deep as 3 mm was recorded after 5 years in service, hence it was postulated that the rate of penetration decreased to virtually zero once a depth of 6.3 mm had been reached.

General corrosion

Nickel aluminium bronzes are generally not affected by general or uniform corrosion under seawater conditions. The long term, steady state corrosion rate is in the order of 1 mpy (0.025 mm/year) [61], 0.0014 in/year or 9 mdd [55]. This good corrosion resistance is attributed to a stable and protective surface film formed on the surface of the alloy when exposed to seawater. This surface film consists of two layers, an inner layer of cuprous oxide (Cu_2O) and

an outer layer of alumina (Al_2O_3) [62]. Under conditions such as biofouling by marine organisms, high water velocity, cavitation and particle impingement, the surface film could be damaged (depassivation occurs). Localised damage of this protective surface film could cause pitting and selective phase corrosion. The strong ability of nickel aluminium bronze to quickly repassivate (heal) results in a low corrosion rate; hence it is used widely under severe conditions.

Galvanic corrosion

Copper and copper based alloys occupy a useful mid-position in the galvanic series: more noble than steel, cast iron, aluminum and zinc; and less noble than stainless steel, titanium and nickel based alloys. The corrosion potential of copper in flowing seawater is ~ -330 mV (SCE); nickel aluminium bronze is - 180 mV (SCE) and aluminium bronze is - 360 mV (SCE) [61]. Tests have been performed at about 25 °C in both natural and chlorinated sea waters on couples of nickel-aluminium bronze (NAB) and Zeron 100 (Z100) superduplex stainless steel. Two NAB/Z100 area ratios (1:1 and 1:10) were used in exposures of 60 days. The results in natural seawater showed severe localised corrosion of NAB both in the crevices and on open surfaces at both area ratios. In chlorinated sea water there was no corrosion at a 1:1 area ratio. The attack is explained in terms of the different cathodic reactions occurring in natural and chlorinated sea waters, and the metallurgical structure of: NAB. Service experiences with couples of NAB and superduplex stainless steel are described and recommendations are given for the avoidance of problems [63].

Biofouling

Nickel aluminium bronzes are more resistant to biofouling than steel and most other common materials used in marine environments. Fouling is generally not a problem in seawater at velocities above 0.5 ms^{-1} [54] since it is difficult for the biofouling organisms to become attached to the alloy surface. Under stagnant or brackish water conditions, crevices can form under marine fouling settlements, leading to the preferential phase corrosion of the κ phase [56,59].

Solid particle erosion-corrosion

Generally, corrosion rates increase with water velocities [52,54,55]. Exposure to high speed flowing corrosive slurries could prevent the protective surface film from forming, it may also be eroded away locally exposing unprotected parent alloy. The continued effect of erosion prevents repassivation and removes the parent alloy via mechanical damage. Accelerated corrosion occurs at depassivated (unprotected) areas, leading to localised perforation. Nickel aluminium bronze is among the most erosion-corrosion resistant of all the copper alloys, performing better than 70/30 cupro-nickel alloys [56].

Cavitation corrosion

At very high speeds, the water pressure behind the trailing surface of an object is reduced to such an extent that the local pressure falls below the vapour pressure of the liquid. Under such conditions, cavities or bubbles can form in these locations, which will subsequently collapse as they are carried to a region of higher pressure. The rapid collapse of bubbles can produce pinpoint pressures of 2000 to 3500 bar. Thus, with repeated blows at such pressures, the material will fail by fatigue and breakdown of crystalline structures [64]. Localised breakdown of protective film could also occur, leading to enhanced corrosion damage to the metal. Nickel aluminium bronze showed consistently good cavitation resistance under both actual operating conditions and accelerated laboratory tests, the high resistance is attributed to their tough homogeneous structure, high corrosion fatigue limit, high tensile strength and good hardness [64]. Under cavitating conditions, the mass loss was 186 times than under quiescent conditions. The α phase was attacked preferentially at the interfaces with the intermetallic κ phases, leading to grain boundary cracking and material loss [65].

2.3.7 Corrosion of metallic coatings

Corrosion of metallic coatings has a huge effect on the corrosion behaviour of the coating substrate system, depending on the following parameters:

1. The chemical composition of the coating and substrate material.
2. The process of applying the metallic coating.
3. The ability of the coating to form insoluble corrosion products when exposed to corrosive media.

Figure 2-17 and Figure 2-18 show different types of coating-substrate corrosion system. In Figure 2-17, the coating applied is anodic to the substrate, i.e. an aluminium coating on carbon steel. For any flaw on the coating system, the coating will corrode preferentially due to galvanic effects when coupled to the carbon steel substrate. Thus the substrate material is protected throughout the exposure in a corrosive environment. This process is similar to the cathodic protection system with a sacrificial anode.

Figure 2-18 shows the coating having a cathodic nature with respect to the substrate, i.e. a copper coating on carbon steel. In the event of coating failure, the substrate will be exposed to the electrolyte and a galvanic couple will cause the substrate to be anodically polarised by the coating. Thus, the coating will be protected by the dissolution of the substrate. This form of coating system is undesirable because the corrosion of the substrate is often visually undetectable, and the failure is often unpredictable. In extreme cases, the bond between the coating and the substrate can be undermined, causing the loss of adhesion between them, leading to the detachment of the coating. This type of corrosion behaviour has been reported by Hodgkiess and Neville [66] and Neville *et al.* [5].

The ability of the coating to form insoluble salts when exposed to corrosive media is also important. Hodgkiess *et al* [66] used HVOF sprayed Inconel, tungsten carbide and nickel chromium coatings for corrosion experiments. They reported that it is common for such coatings to form a thin white deposit comprising of calcium carbonate and magnesium hydroxide on the surface when exposed to the seawater. This was due to a rapid cathodic reaction occurring to prevent further mass transfer reactions to the coating.

The type and deposition process of the coating used is also important. Coatings that are produced by the HVOF processes often contain pores and oxides within the coating. Pores that are interlinked within the coating can act as diffusion paths for aggressive ions to attack the substrate material. However, good HVOF coating processes using hydrogen as the fuel can reduce the amount of pores to prevent such corrosion problem [5].

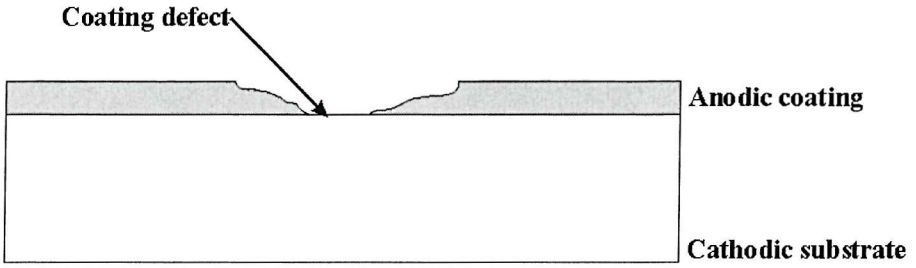

Figure 2-17 A schematic diagram of an anodic coating on a cathodic substrate, showing severe corrosion on the coating due to galvanic effects.

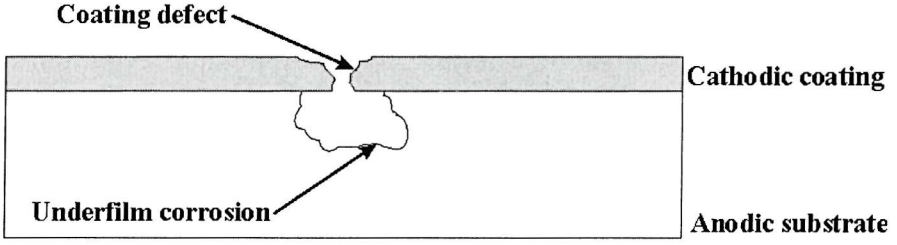

Figure 2-18 A schematic diagram of a cathodic coating on an anodic substrate, showing severe corrosion on the substrate due to galvanic effects.

2.4 Erosion-corrosion

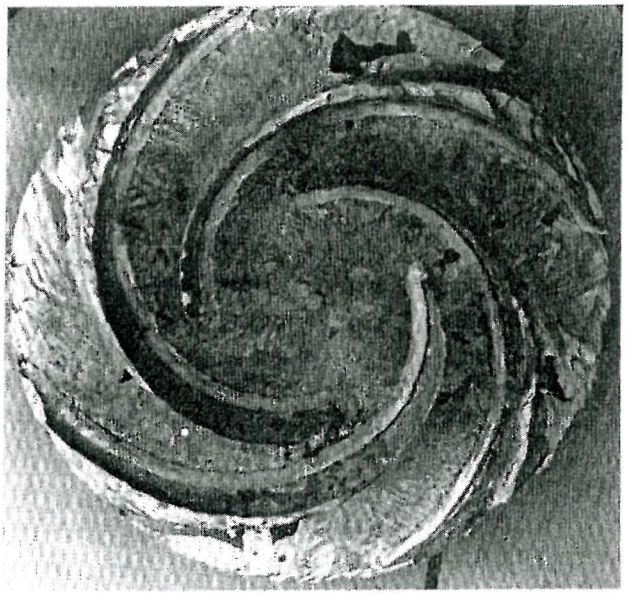

Figure 2-19 Erosion-corrosion of a stainless steel pump impeller, showing grooves formed on the outer region of the impeller due to erosion, and localised corrosion attack (dark regions) throughout the impeller. [38].

2.4.1 Introduction

Erosion-corrosion is defined by the American Society of Testing and Materials [67] as 'a synergistic process involving both erosion and corrosion, in which each of these processes is affected by the simultaneous action of the other, and in many cases is thereby accelerated'. Erosion-corrosion has been previously considered as a process defined by flow corrosion that can occur in single phase or multiple-phase flows. Heitz [68] classified flow induced corrosion into four elements: namely mass and phase transport controlled corrosion, erosion-corrosion and cavitation corrosion as seen in Figure 2-20. However, only erosion-corrosion consisting of a multi-phase flow with sand particles and brine will be considered in this section.

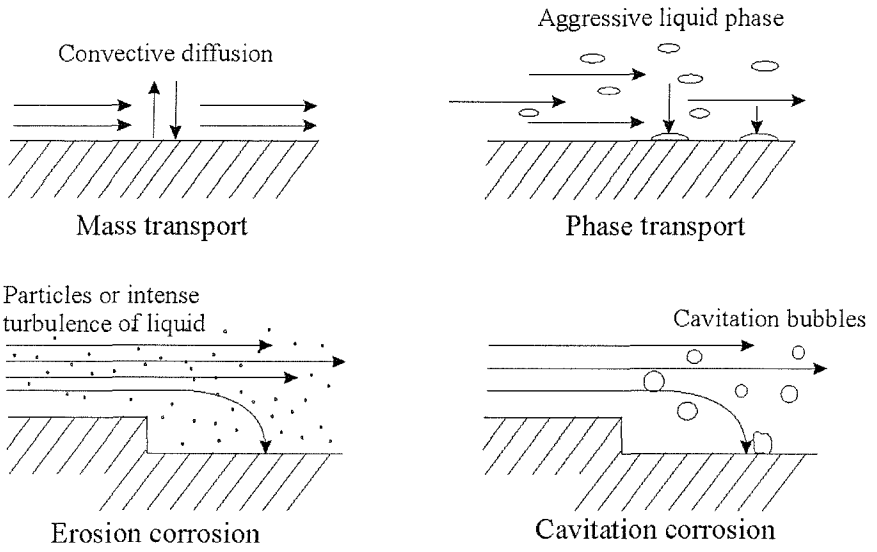

Figure 2-20 Schematic representation of the four main types of flow induced corrosion [68].

It is clear that the mechanisms of erosion and corrosion are very different in nature. Erosion is caused by a mechanical process (erosion section), whereas corrosion is a result of chemical processes (corrosion section). It has been reported that the material loss under erosion-corrosion was higher than simply the separate erosion and corrosion values added together [69-72]. It is, therefore, necessary to understand how the mechanical and chemical processes interact with each other during erosion-corrosion.

Renaud and Chapey [73] studied the erosion-corrosion behaviour of different grades of stainless steels in a slurry that consists of sulphuric acid and SiC particles. The erosion-corrosion data in a sulphuric acid solution was compared to that under pure erosion in (corrosion inhibiting) sodium sulphate solution. It was concluded that the damage resulting from erosion-corrosion of stainless steels was four times more than that observed under pure erosion conditions. The effects of corrosion were only presented in the form of polarisation resistance obtained during the erosion-corrosion experiments, consequently it was impossible to quantify the relationship between erosion and corrosion in their experiments. However, they were able to show that the ability of the stainless steels to form passive films could inhibit material loss under erosion-corrosion conditions by comparing the erosion-corrosion mass losses for stainless steels with different amounts of passivating elements (Cr, Mo, N).

More recently, Li *et al.* [74] studied the erosion-corrosion behaviour of aluminium in a silica sand and brine slurry system. At a 90° impingement angle, it was observed that the erosion-

corrosion rate was nearly 40 % higher than that under pure erosion rate and pure corrosion rate added together. A mechanism of erosion-corrosion was proposed, which considered the mechanical effects of erosion caused by plastic deformation (flakes) on the surface of the aluminium specimens. These highly stressed deformations were then attacked by the corrosive liquid, inducing stress corrosion cracking and hence the detachment of flakes from the surface due to further impacts. It was also proposed that impacts on the surface of the aluminium resulted in disruption and removal of the passive aluminium oxide on the surface, the resulting localised corrosion at these points enhanced material loss due to further impacts.

2.4.2 Synergy between erosion and corrosion

Synergy occurs when the total material loss of a specimen exposed to erosion-corrosion conditions is more than the sum of material loss due to pure erosion and pure corrosion. Table 2-2 lists results obtained by various workers to determine the amount of synergy obtained under wear corrosion conditions.

Table 2-2 The percentage of synergy/ total erosion-corrosion mass loss obtained by various workers studying wear-corrosion interactions.

Author	Experiment	Material	Synergy(%)
Batchelor and Stachowiak [69]	Abrasion corrosion	Mild steel, Zinc and Magnesium	200
Li *et al.* [74]	Erosion-corrosion (slurry jet impingement)	Aluminium	40
Wood and Hutton [72]	Erosion-corrosion (cavitation)	Copper	11-29
Watson *et al.* [71]	Erosion-corrosion (slurry pot)	SS316	36
Neville *et al.* [70]	Erosion-corrosion (slurry jet impingement)	Cast iron	35.4

Batchelor and Stachowiak [69] measured the degradation rates of mild steel, zinc and magnesium under simultaneous abrasion and corrosion, and compared these rates with static corrosion and dry abrasion rates. Synergy predictions in their experiment were based on the ratio of static corrosion rate to the dry abrasion rate (K). If $K < 0.1$, then synergy between wear and corrosion is unlikely. If K is greater than 0.4, synergy is almost certain. However, it was reported that when a value of $K \geq 1$ is observed, the estimation of material life based on dry abrasion or abrasion corrosion was very inaccurate, producing a synergistic value of about 200 %.

It is, therefore, important to define a set of equations to express the overall material removal experienced under erosion-corrosion conditions so that synergy can be quantified. An equation explaining synergy in terms of material loss not accounted for by pure erosion and pure corrosion has been used by Li *et al.* [74] and Wood *et al.* [72]:

$$T = E + C + S \qquad \textit{Equation 2-16}$$

Where T, E and C are the material loss under erosion-corrosion, pure erosion and pure (flow) corrosion conditions respectively. S is the synergy accounting for the higher total material loss under erosion-corrosion conditions. However, this expression of synergy is the sum of increments in erosion and corrosion rates affected by each other, contributions of erosion and corrosion cannot be separated. It is, therefore, difficult to account for the contributions of erosion or corrosion under an erosion-corrosion process. Equation 2-16 shown above assumed that both the erosion rate and corrosion rate is steady and constant throughout the erosion-corrosion conditions. In reality, it is unlikely for both processes to be in steady state as experiments over varying time scales showed different results [75].

Synergy (S) can be further defined in terms of its constituent parts. Matsumura [76] proposed a similar form of the equation for explaining the combined erosion-corrosion damage to a metallic material that incorporates material loss due to the contribution of erosion and corrosion in an erosion-corrosion experiment:

$$T = (E + \Delta E) + (C + \Delta C) \qquad \textit{Equation 2-17}$$

where ΔE was the additional increase in erosion damage due to corrosion and ΔC was the additional increase in corrosion damage due to the effects of erosion. Stack *et al.* [77] and Zhou *et al.* [78] named ΔE as the additive effect and ΔC as the synergistic effect, with the reason that the additive effects can be effectively quantified while the synergistic effect cannot be quantified via direct measurements during an experiment.

Watson *et al.* [71] combined both additive and synergistic effects from the equation above and called it the wear-corrosion synergism, which could explain the synergy expression that was obtained by Li *et al.*[74]:

$$S = \Delta E + \Delta C \qquad \textit{Equation 2-18}$$

The effects of ΔC were quantified by undertaking polarisation resistance measurements during erosion-corrosion experiments, with the determination of the theoretical mass loss from i_{corr} values; this was then compared with the results from a similar experiment without abrasives. ΔE was then obtained by substituting the ΔC value into Equation 2-17.

It is now generally considered that synergy in an erosion-corrosion process constitutes contributions from both erosion and corrosion processes, but the amount of contribution from these two processes requires a more detailed investigation. Whether or not the term additive or synergistic should be given to these processes is irrelevant. However, it is important to determine how much corrosion contributes to erosion and vice versa.

2.4.3 Effects of erosion on corrosion (ΔC)

Generally, it would appear that the majority of mass loss in the event of synergy can be attributed to the erosion processes leading to an overall enhancement of the corrosion rate [71,72,78,79]. It should be noted that many researchers have not rigorously distinguished between the erosion-assisted corrosion and corrosion assisted erosion effects, the usual methodology was principally to consider the overall interaction between erosion and corrosion. Nevertheless, their findings have in general led them to discuss in terms of an erosion enhancement of the corrosion rate.

Zeisel and Durst [79] attempted to model the erosion-corrosion behaviour of materials using data obtained from the literature. They believed that the mechanism of erosion-corrosion was dominated by the removal of the passive film on the surface by impinging hard particles. The removal of passive films from the surface was suggested to increase the amount of corrosion on the exposed surface, leading to an increased material wastage. The predicted erosion-corrosion rate was higher than that obtained by experimental methods, it was suggested that the prediction allowed for a higher rate of corrosion, giving rise to a higher amount of material loss. The effect of corrosion in enhancing erosion wastage was not mentioned in their model.

Wood and Hutton [72] studied the synergistic effects of various materials under slurry erosion-corrosion and cavitation conditions. They obtained the ratio of synergistic wear to corrosive wear (S/C) and the ratio of erosive wear to corrosive wear (E/C). It was subsequently indicated that the synergistic mechanism (S) was due to erosion enhanced corrosion. They suggested that the corrosion films were stripped by the mechanical effects of particle erosion, producing a highly reactive surface that could dissolve further under corrosive conditions, as seen in Figure 2-21. It was also mentioned that synergy can be reduced if the surface was able to repassivate itself quickly, reducing the amount of freshly corroding surfaces and consequently reducing the synergistic effects (ΔC).

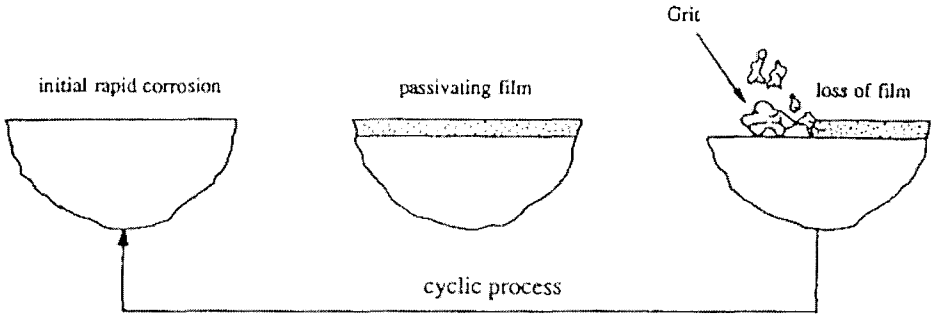

Figure 2-21 Schematic diagram showing the effects of impinging particles in enhancing the corrosion rate. [69]

Using a combination of mass loss measurements and electrochemical techniques, Stack *et al.* [77] and Zhou *et al.* [78] investigated the erosion-corrosion of carbon steels under erosion-corrosion conditions in a rotating cylinder tester. In the active dissolution and passive potential ranges, no evidence was given for the corrosion influence of the erosion rate, it was suggested that the interaction between erosion and corrosion was entirely due to an erosion affected process. Zhou *et al.* suggested that surface roughening of the specimen during particle impact enhanced mass transfer effects increased the corrosion rate at passive-film free surfaces. In the passivation region, it was proposed that the erosion enhancement of corrosion rate was due to the repeated breakdown and subsequent repassivation of the surface as a result of solid particle impacts.

2.4.4 Effects of corrosion on erosion (ΔE)

The effect of corrosion on erosion has been studied less compared to erosion enhanced corrosion, most probably due to the difficulties in actually quantifying a value corresponding to this type of mechanism during an experiment [78].

Matsumura [76] stated that a positive effect of corrosion enhanced erosion could occur. The work hardened layer on the metal surface due to the impact of hard particles could be removed due to corrosion processes. He also suggested that the roughening on the metal surface due to corrosion could increase the erosion wastage.

Li *et al.* [74,80] used electrochemical techniques and mass loss measurements to investigate the erosion-corrosion behaviour of aluminium in 0.5 M NaCl and 0.1 M Na_2CO_3 slurries containing 15 % w/w 600-850 μm silica sand. The slurry velocity was maintained at 3.6 ms^{-1}. They showed that the increase in corrosion rate due to erosion in the NaCl and acidic slurries was much less than the total magnitude of the synergistic effect of erosion and corrosion. It was suggested that the synergistic effect was mainly due to the effects of corrosion on erosion. Microhardness measurements showed that the removal of the surface hardened layer as proposed by Matsumura [76] was not the mechanism of corrosion enhanced erosion in their experiments. It was proposed that the detachment of plastically deformed flakes on the metal surface due to stress corrosion cracking was the mechanism of corrosion enhanced erosion.

It was revealed that a negative synergy resulting from the inhibitive effect of corrosion was observed in the Na_2CO_3 slurry, reducing the total erosion-corrosion rate. Possible suggestions included that the higher solubility of the Al_2O_3 passive film in alkaline environments would lead to blunting of the crack tips by lateral dissolution, thus retarding the speed of crack propagation. Likewise, the silica particles may have undergone some dissolution, reducing their angularity and hence their efficiency at removing material.

Neville *et al.* [70] investigated the slurry erosion-corrosion of cast irons (BS1452) using silica sand as the erodent and 3.5 % NaCl as the corrosive media. They reported that the effect of corrosion in enhancing the weight loss in an erosion-corrosion experiment could exceed 20 % of the total weight loss. They attributed this to the corrosion that occurred at the

graphite/matrix interface of the cast iron, causing a loosening of intermediate grains of metal which are more easily removed by the impacting liquid stream with or without the presence of solids.

2.4.5 Erosion-corrosion of protective coatings

Many investigations cover the erosion-corrosion behaviour of metallic and polymeric based protective coatings [81-85]. In general, coatings on metallic substrates erode either by plastic deformation or cracking and chipping, depending on whether they have primarily ductile or brittle behaviour characteristics. In these cases where the coating consists of both ductile and brittle constituents, the composite will have the erosion behaviour of the dominant material. When a particular coating is exposed to abrasive particles in a corrosive medium, mass transfer effects between the coating/liquid and the substrate/liquid can affect the slurry erosion-corrosion behaviour of the coating due to increased oxide formation. At the same time, porosity introduced during the coating process will allow the liquid to permeate through the coating and cause galvanic corrosion between the coating and its substrate, accelerating the material wastage during erosion.

Bardal *et al.* [2,86] carried out erosion-corrosion tests on a range of metallic and cermet coatings, produced by a range of coating processes (CVD, thermal spray and HVOF). The erosion, flow corrosion and erosion-corrosion experiments were carried out on a rotating disc apparatus, in synthetic seawater. Velocity exponents between 2 and 3 were reported, indicating ductile erosion behaviour. It was also reported that corrosion of the metallic matrix in the cermet coatings undermined the carbide particles, leading to enhanced material loss. Negative synergy values were also found in some of the coatings, attributed to scatter in mass loss measurements. Similar erosion-corrosion behaviours were also found by other workers [84].

HVOF Ni-Cr-Si-B-C coatings have also been subjected to erosion-corrosion experiments in 3.5 % NaCl solution, using a submerged jet impingement rig. The erosion-corrosion mechanism occurs by a surface roughening mechanism due to erosion, followed by corrosion on less noble coating constituents. This resulted in 'unsupported protruding materials' that are consequently removed by further sand particle impingement. Microscopy revealed that

selective corrosion at the splat boundaries resulted in dislodgement of splat particle by erosion [87]. Similar tests were carried out on HVOF WC-Co-Cr coatings by Perry *et al.* [88], it was also reported that preferential corrosion occurred at the metallic matrix under erosion-corrosion conditions. Further sand particle impingement resulted in the removal of the hard carbides.

Other erosion-corrosion literature was also found, but they were centred on polymeric coatings [83-85] and high temperature erosion-corrosion behaviour [6,82,89]. Little information was found on the erosion-corrosion behaviour of HVOF metallic coatings.

2.5 Electrochemical test methods for corrosion

2.5.1 Introduction

Electrochemical test methods are some of the most powerful tools available for the understanding and control of corrosion, and can be applied to a multitude of requirements including:

→ The determination of the controlling parameters and mechanisms of corrosion processes.
→ Monitoring of corrosion rate to allow prediction of component lifetime and optimisation of component replacement, maintenance or repair schedules.
→ Evaluation of different materials for the purpose of materials selection.

Electrochemical tests offer several advantages/benefits for studying corrosion, the test methods are relatively rapid, achieving 'real time' or near instantaneous corrosion rate information. Also, many of the methods can be applied either in the laboratory or in process plants/other service conditions. Another feature of electrochemical tests is the wealth of technical literature. This large technical base provides guidance in the selection of specific electrochemical test methods and also provides assistance in the interpretation of results.

A large collection of literature is available on the subject of electrochemical methods used in corrosion studies [38,40,90,91]. These literature encompass a broad range of methods

available to study corrosion behaviour of metals, only methods that are relevant to the present study will be discussed in this section.

2.5.2 Potentiodynamic polarisation

The polarisation behaviour is related to the corrosion behaviour of the metal. The two primary types of polarisation behaviour are activation and concentration polarisation. Activation polarisation is controlled by the free energy or potential driving force at the electrode interface. Concentration polarisation is a process controlled by the mass transport of reacting species to the electrode surface or reaction products away from the electrode surface (as discussed in Section 2.3).

Polarisation methods to measure corrosion rates have inherent advantages. Usually a few minutes are required to determine corrosion rate by polarisation resistance, whereas conventional weight loss measurements require several days or more. Thus, a rapid, semicontinuous measurement of corrosion may be obtained which is very useful for kinetic studies or for corrosion monitoring. Many workers have used the polarisation curve in their investigation to study the corrosion behaviour of various coatings [92,93].

Bjordal *et al.* [92] carried out potentiodynamic polarisation experiments over a range of ± 50 mV to rank corrosion behaviour of different thermal spray coatings. The corrosion rate was obtained using the Stearn-Geary equation:

$$I_{corr} = \frac{b_a b_c}{2.3(b_a + b_c)R_p} \qquad \textit{Equation 2-19}$$

Where R_p was the linear polarisation resistance, b_a and b_c were anodic and cathodic Tafel constants respectively. The estimated material loss due to corrosion was calculated from the corrosion current density I_{corr}.

Simard *et al.* [93] also used potentiodynamic techniques to explain the corrosion resistance of different types of WC based HVOF coatings in hydrochloric acid. The corrosion resistance of these materials were based on the free corrosion potential and corrosion current densities obtained during polarisation experiments. Higher corrosion current density indicated a low

corrosion resistance. The ability for the coatings to passivate under such conditions was also identified by the potentiodynamic polarisation technique.

Potentiodynamic techniques require that the corrosion potential be stable and unchanging during measurement. Otherwise, the applied overvoltage and current vary by an unknown amount as the background corrosion potential changes during the potentiodynamic measurement. Furthermore, the potentiodynamic scan must be run slowly enough to ensure steady-state behaviour. Finally, the different types of corrosion occurring on the surface cannot be differentiated by this technique.

Thus, the potentiodynamic techniques, which have been standardised for laboratory use, have serious deficiencies for kinetic studies and in service conditions where corrosion potential drift and fluctuation are more typical.

2.5.3 Electrochemical impedance spectroscopy (EIS)

Electrochemical impedance spectroscopy has become a commonly used ac technique for the evaluation of the behaviour of materials in corrosive environments. This technique involves measuring the current response produced when a potential is applied at a certain frequency to an electrode surface, further derivation of electrical circuits' that models the dc corrosion (polarisation resistance) conditions enables electrochemical components such as solution resistance, polarisation resistance and double layer capacitance to be distinguished. Usually such models are obtained on a basis of an intuitive construction in which elements such as capacitors and resistors are associated with physical phenomena. In the case of a coated metal, for example, a resistor and capacitor may be assigned to the exposed metal and another resistor and capacitor may be assigned to the coated metal. This approach has been used successfully for evaluation of impedance data for a number of systems, however, caution is required since models for impedance spectroscopy are not unique, and independent measurements are needed to verify the model used [94]. Another approach is to develop models based on solution of governing equations in the frequency domain. This has been applied in particular to systems in which mass transfer is involved or where a series of reactions is proposed. Usually, such models are integrated with an analogue circuit approach. Electrochemical impedance methods tend to perturbate the system under investigation by

applying potentials at differing frequencies, creating a constant anodic state to the working electrode during experiments. A better method of studying corrosion systems without actually altering the surface chemistry of the electrode is the electrochemical noise method that allows data acquisition for a freely corroding system.

2.5.4 Electrochemical noise method (ENM)

The term "electrochemical noise" was used to describe the spontaneous fluctuations in the potential or current with time of a freely corroding system. This terminology has inevitably led to certain mis-interpretation, since the "noise" is usually measured at relatively low frequencies, and is not an acoustic signal. Enhancement of the measurement techniques, resulted in the simultaneous measurement of current and potential noise signals associated with the evolving corrosion processes. It was discovered that the current or potential transients observed in certain circumstances could be analysed and correlated with other electrochemical techniques such as polarisation resistance, electrochemical impedance and harmonic analysis [95,96]. However, this statement can only be true if the corresponding potential and current transients were measured simultaneously without a phase lag introduced by measuring instruments or the existence of a double layer capacitance on the corroding surface. This can only be achieved in an electrochemical cell consisting of two identical working electrodes and a reference electrode, which is often difficult due to requirements to simulate certain process environments.

Unfortunately classical electrochemical theory does not take into account the dynamic nature of naturally evolving electrochemical processes such as corrosion, and much of the development of the electrochemical noise measurement techniques has been based upon an empirical understanding of the fundamental processes involved.

The theory behind the observations of particular types of corrosion processes and kinetics was particularly lacking. This could mean that observations might fall neatly into some particular pattern, or alternatively do not, which shows a lack of understanding to a particular corroding system. The study of probability, random variables, stochastic processes, fractal dimensions, percolation theory etc., all have some relevance to the overall interpretation of

the observed electrochemical noise signals, and may be used to provide information about the system being studied.

Background

The electrochemical noise technology has been applied over the last 20 years to a wide variety of corrosion related problems in industrial sectors such as, oil and gas, petrochemicals, nuclear power, and aerospace. Specific problems studied include general corrosion [97], pitting corrosion [98], stress corrosion cracking [99], crevice corrosion, coating degradation [100-103] and erosion-corrosion [104-106].

The foundations of electrochemical noise technology lie in the original work undertaken by Iverson [107], who studied transient voltage changes produced in corroding metals and alloys using fairly rudimentary instrumentation. Interest in the use of electrochemical techniques in the late 1970's led to a flurry of activity in the field of electrochemical impedance and harmonic analysis, which were seen as natural extensions to polarisation studies. In part this activity was due to the onset of digital electronic instrumentation and desktop computers. This led to the original electrochemical noise patent application by Hladky [108] in 1981, the principle of non-perturbation of the system is intrinsic to the methodology described. The voltage and current measurement were used to provide an indication of the corrosion of the material under test. In the case of electrochemical noise measurements the voltage or current measured was a function of the corrosion potential and corrosion rate of the test specimen due to naturally occurring reactions; for example, metal dissolution and hydrogen evolution and/or erosion of the electrode under the effects such as slurries in the electrolyte in high velocity fluid systems [109,110]. Methodologies for analysis of the potential signals were detailed including, statistical analysis and frequency domain transforms.

In parallel to the studies of potential noise, work was undertaken to understand the phenomenon of coupling current and associated current noise signals arising from the galvanic coupling of nominally identical materials. This led to a further patent by Eden *et al* [111] in 1986, which described a method and apparatus for the detection of localised corrosion using current noise measurements. Also outlined in the patent is the concept of electrochemical noise resistance that may be derived by comparing the potential and current noise signals.

In recent years, the focus for the application has been towards mitigation of corrosion damage in plant by continuous monitoring and feedback of corrosion related information to plant operators to enable remedial or corrective action to be undertaken to reduce the impact of corrosion related incidents.

Equipment

The system used for measuring the electrochemical noise signals will have several key components, depending on the type of noise measurements undertaken. A typical schematic arrangement for the system is shown in Figure 2-22, where noise data are collected from the sensors and analysed by a computer.

It is common to use a three-electrode arrangement, although the actual electrode configurations used may vary from application to application. Usually, a two-electrode configuration will only allow the acquisition of current or potential noise while a three-electrode system can allow simultaneous acquisition of current and potential noise. The noise signals may need conditioning from the interface and a multiplexer is used to log data from a series of sensors to a data acquisition unit.

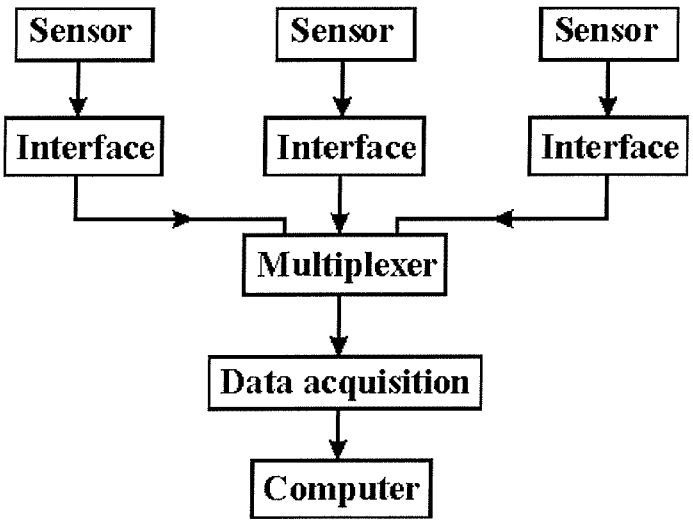

Figure 2-22 A schematic diagram showing the components involved in acquiring electrochemical noise data.

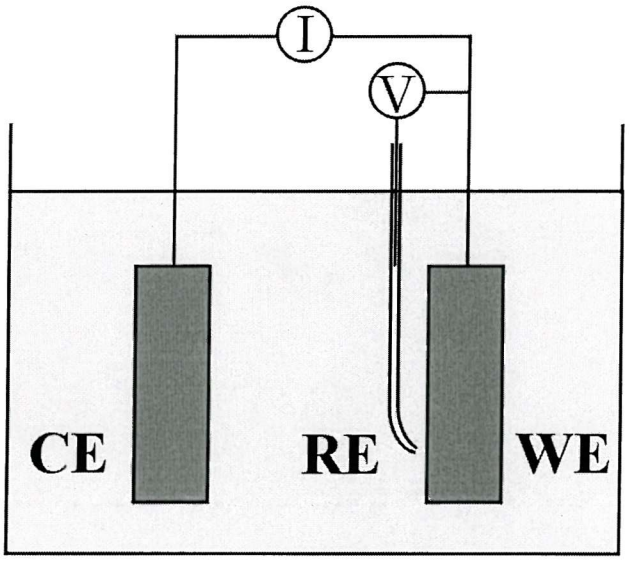

Figure 2-23 A typical three electrode cell configuration, with a working electrode, counter electrode and a reference electrode.

Figure 2-23 illustrates a typical three-electrode cell configuration used for noise measurements at the free corrosion potential, such that the naturally occurring current and potential fluctuations may be monitored simultaneously. A typical configuration consists of a working electrode, a counter electrode (usually graphite or platinum) and a reference electrode (standard calomel or silver/silver chloride). This type of arrangement is useful in the study of the evolution of naturally occurring corrosion processes and is widely used in plant monitoring/surveillance situations [85]. Mabutt *et al.* [112] pointed out that both the working and counter electrodes have to be electrically isolated and this has made the electrochemical noise measurement difficult to use in field applications. Therefore, they proposed an alternative experimental configuration that was easier to use and also to eliminate the drift in current and potential due to the difference in initial potential between the electrodes. Under certain conditions a third working electrode may be substituted for the reference electrode, particularly in plant monitoring situations where reference electrodes are impractical or are difficult to use satisfactorily [113].

For measurement of electrochemical current noise, a zero resistance ammeter (ZRA) needs to be used. The ZRA shown in Figure 2-24 acts to maintain the potentials of the two working electrodes at the same potential (with modern devices the potential difference can be maintained within a microvolt). The current required to maintain the two electrodes at the same potential flows through the feedback resistor R, and the voltage output of the ZRA is related to the current flowing through the system by Ohm's Law (V=IR).

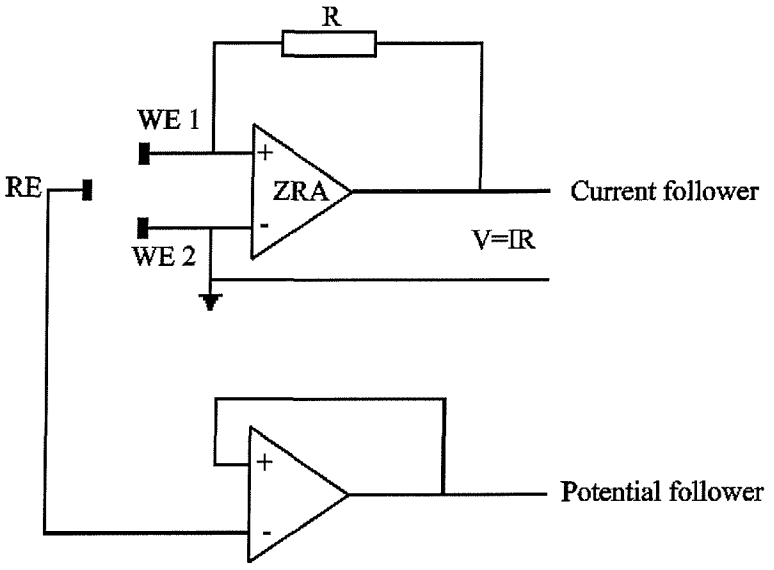

Figure 2-24 Schematic diagram of a zero resistance ammeter

Applications for electrochemical noise measurements

Electrochemical noise has been used to study the corrosion of metal/solution systems [113-115]. There are fundamentally two mechanisms that are of particular importance, these are general corrosion, and processes involving stochastic events such as localised corrosion. Examples of electrochemical noise generated from general and localised corrosion can be found in Cottis and Turgoose [94].

General corrosion processes may be identified by the time record data for these types of processes which exhibit few signs of individual uncorrelated events and showing few, if any, rapid transients. Legat and Dolecek [97] demonstrated that the amplitude of fluctuations depend on the corrosion rate and the electrode area. They concluded that the slopes of the power spectral density (PSD) values could be used as the significant parameter to distinguish between different types of corrosion. The rate and stability of the corrosion process is indicated by statistical treatment of the data. The examination of the types of distribution of both the current and potential data can be used to estimate if the process is indeed Gaussian. General corrosion processes can also be estimated from the moments, skewness, kurtosis, and coefficient of variance and its derivatives [116]. Alternatively, the data may be transformed into the frequency domain. The amplitudes of the signals at specific frequencies, and the slope of the frequency spectrum, can be used to distinguish between general and localised phenomena [117].

Localised corrosion is characterised by transients that may be observed in the time record data. During localised corrosion distinctive potential and current transients can be seen as opposed to uniform corrosion where the electrochemical noise is closer to a white noise process [94]. For example, Hladky *et al.* [115] showed that during a pit initiation process of mild steel in sodium chloride solution, potential fluctuations from a base potential were evident, with the rise time being shorter than the descent time. The general pitting process (time intervals between the rise and fall of potentials/currents) is stochastic, i.e. random in nature, and therefore is essentially a Poisson process. However, the actual event of transients is considered as deterministic. The characteristics of Poisson processes are such that they can easily be distinguished from Gaussian processes by a variety of means, both from an appreciation of the statistics of the data, and from frequency domain information. It should also be possible to differentiate between the different operative mechanisms, such as pitting, stress corrosion cracking and coating delamination, and to provide an indication of the severity of the corrosion problem [113]. This can be achieved by an appreciation of how different processes contribute to the noise signals.

Effects of electrode size

Pistorius [118] conducted electrochemical noise experiments with mild steel and stainless steel electrodes of different sizes in 0.4 M Na_2SO_4; it was shown that increase in electrode area caused an increase in the number of current transients (corrosion rate). However, it was also indicated that by increasing the electrode area, both the electrode capacitance and the area of cathodic reactions increase. Hence, the size of the potential fluctuation in response to a single current transient is inversely proportional to electrode size. Legat and Dolecek [97] used mild steel, stainless steel and aluminium electrodes of different sizes (7 – 50 mm^2) to study the effect of electrode area on the electrochemical noise data. It was demonstrated that the PSD of current was proportional and PSD of potential was inversely proportional to the electrode surface area. However, the linear relationship between the electrochemical noise and the electrode surface area could not be derived due to the lack of data.

Effects of sampling rate

There are two schools of thought on the maximum sampling frequency that is needed [94]. The majority of workers have standardised on a rate of around 2 Hz, which is easy to achieve with voltmeters [97,109,119]. It also provides a good clearance from the power-line frequency

rejection (50 Hz). Another group considers it important to sample at a higher frequency (> 10 Hz) [104,118,120]. This is much more challenging as it allows little clearance for filtering to remove the power-line frequency, and the short time available for each sample makes it more difficult to achieve high resolution and accuracy. The sampling rate must exceed a certain minimum rate to capture the events that constitute the noise in the system measured.

Given a time record consisting of N samples with a sampling frequency of f, the maximum frequency that can be recorded is given by the Nyquist frequency, $f/2$, since a minimum of 2 samples per cycle are necessary to define the sine wave. The lowest frequency that can be resolved is defined by the total duration of the time record (bandwidth), (f/N). If the sampling rate is inappropriately low, aliasing effects occur, and it cannot be removed by post-treatments of the data – an antialiasing filter should be used to prevent this from occurring. The data points obtained from input frequencies above and below the Nyquist frequency are identical due to the nature of the anti-aliasing filter [121].

Interpretation of noise

The simplest approach to the analysis of electrochemical noise, and probably one of the most powerful, is to examine the time records for features that are characteristic of particular types of corrosion. Souto and Burstein demonstrated in Figure 2-25 that the pitting corrosion of titanium alloy was associated with a characteristic rapid rise in current followed by an exponential decay as the pit repassivates [122]. Hladky and Dawson measured the potential noise of mild steel electrodes in chloride containing solutions. They showed that the potential noise signature for crevice corrosion in the time record was characterised by relatively long bursts of very regular peaks occurring at regular time intervals [115] as seen in Figure 2-26. Long term changes in potential may also be associated with the commencement of localised corrosion - the initiation of crevice corrosion will usually cause the potential to fall as the active crevice pulls the potential of the cathode down [94]. This is a time record that would have been interpreted in the past in terms of changes in the corrosion potential with time.

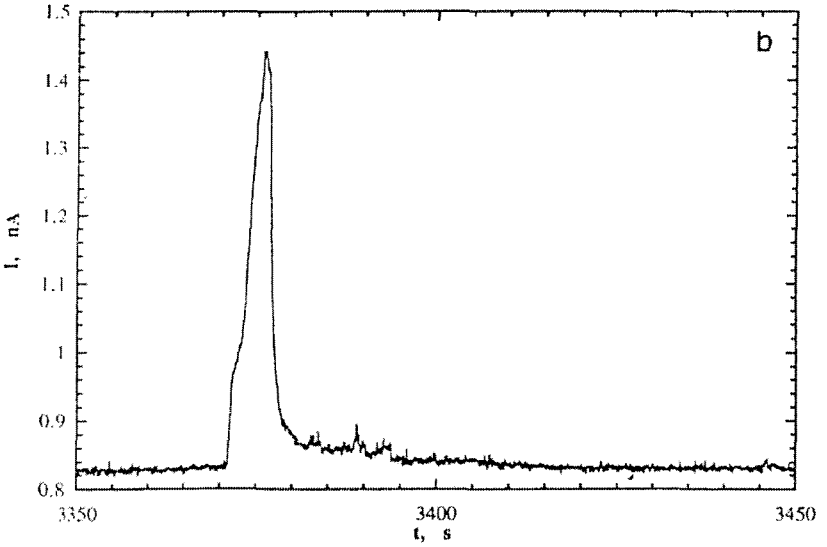

Figure 2-25 Current transient observed for the breakdown process on Ti-6Al-4V in 1.5 M HCl at 0.9 V (SCE), showing a rapid rise and an exponential decay. [122]

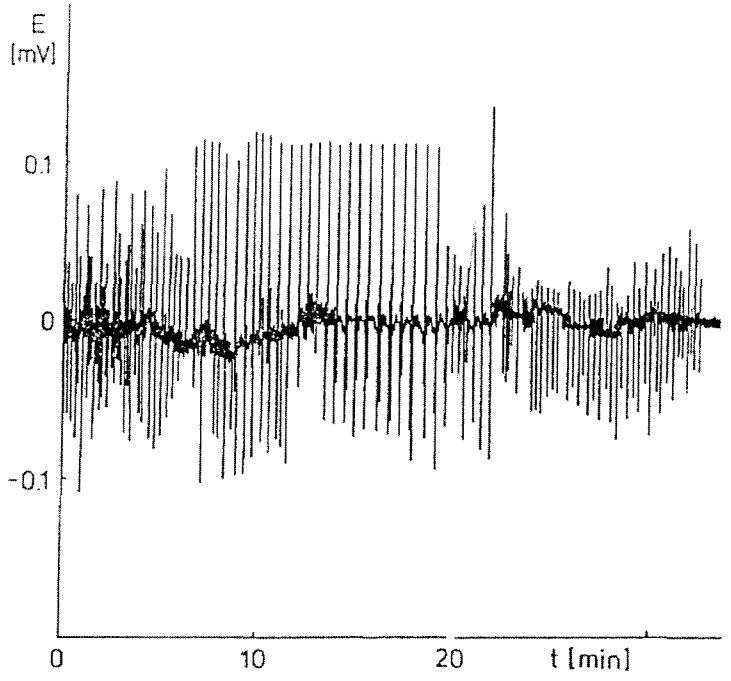

Figure 2-26 Potential noise transients during crevice initiation period for mild steel in 1000 ppm $NaNO_2$ + 1000 ppm NaCl [115]

2.5.5 Analysis of electrochemical noise

Statistical analysis of electrochemical noise

Any observed set of data representing a physical phenomenon and recorded as a function of time can be broadly classified as either deterministic or non-deterministic. Fluctuations in potential or current of a metal-ion electrode are, at present, assumed to represent a stochastic process and therefore classified as non-deterministic and are described in terms of probability and statistics rather than by explicit equations.

Random processes can be subdivided into those which are stationary and those which are non stationary. A process is stationary if its statistical moments, or mean values, are invariable with time; however, in practice, single time records are often said to be stationary if the first moments computed over short time intervals do not vary more than would be expected from normal statistical sampling variations. Non-stationary random processes exhibit first moment variations and are time varying functions that can be determined by performing instantaneous averages over a set of time records forming the process.

A number of statistical parameters may be derived from the time record. The mean (Equation 2-20) is not a part of the noise measurement, especially for the measurements made between nominally identical electrodes, where the expected value of the mean is zero. However, the actual value of the mean has been used to detect localised corrosion. The variance (Equation 2-21, with the mean being substracted) is a measure of the power present in the sampled signal. If the voltage or current is filtered to remove frequencies outside the range that can be measured, for a given sample frequency and time record length, the variance is equivalent to the area under the corresponding power spectrum. The r.m.s (root mean square) shown in Equation 2-22 is a similar measurement to that of the standard deviation, except that the mean is not subtracted from the data before summing the squares of individual values.

Mean: $$\overline{E} = \frac{1}{N}\sum_{k=1}^{N} E[k] \qquad \textit{Equation 2-20}$$

Variance: $$\overline{E_n^2} = \frac{1}{N}\sum_{k=1}^{N}(E_n[k])^2 \qquad \textit{Equation 2-21}$$

Root mean square: $$E_{rms} = \sqrt{\frac{1}{N}\sum_{k=1}^{N} E[k]^2}$$ *Equation 2-22*

Where $E[k]$ is the k^{th} sample in the time record and N is the total number of samples taken.

It has been reported that the statistical parameters of electrochemical noise, such as standard deviation (σ) and the root mean squared (r.m.s.) values of the potential, can represent the corrosion rate of the metal and permit identification of the attack [108,111].

Skewness is a measure of the symmetry of the distribution. It is derived from the third moment by dividing it by the standard deviation cubed, which makes it non-dimensional. A value of zero implies that the distribution is symmetrical about the mean, whereas a positive skew implies that there is a tail in the positive direction, and a negative skew implies that there is a tail in the negative direction.

Kurtosis is a measure of the shape of the distribution compared with the normal distribution. It is derived from the fourth moment, which is divided by the standard deviation in the fourth power, making it non-dimensional. Three is then subtracted to bring the kurtosis for a normal distribution to zero. A kurtosis of zero implies that the distribution has a shape similar to that of the normal distribution. A positive kurtosis implies a more spiky distribution, whereas a negative kurtosis implies a flatter distribution.

Puget *et al.* [85] studied the electrochemical current noise obtained during the erosion-corrosion of polyurethane-coated steel, skewness and kurtosis values were used to explain different corrosion mechanisms. It was proposed that when corrosion occurred, skewness values dropped from a positive value to a value close to zero. This decrease in skewness was followed by a corresponding slight decrease in the kurtosis values. However, the authors cautioned that conclusions should not be drawn from these values without first considering the standard deviation of these parameters. When the coating failed, a negative skewness and an increase in the kurtosis value was obtained, demonstrating a high number of transients in the negative current direction.

The noise resistance, R_n, is obtained by dividing the standard deviation of the potential noise by the standard deviation of the current noise [123]. Gusmano *et al.* correlated the noise

resistance (R_n) with the polarisation resistance (R_p) from electrochemical noise and linear polarisation experiments of carbon steel in Na_3PO_4 [95]. Pistorius [118] measured electrochemical noise of carbon steel in 0.4 M Na_2SO_4 and 0.1 M H_2SO_4. It was shown that the quantitative relationships between the changes of standard deviation of the current/potential noise and corrosion rate depends on factors like electrode size and the nature of the corrosion reactions. Hence, the inability of noise resistance to be used as a substitute to the polarisation resistance under such circumstances.

Frequency domain analysis of electrochemical noise

Spectral analysis in the frequency domain is primarily concerned with estimates of the power present as a function of frequency. The most general form of this analysis produces an estimate of the power present at each frequency; a power spectral density (PSD) graph as a function of frequency is known as a power spectrum. Two power spectrums that are commonly used in the analysis of electrochemical noise data are the Fast Fourier Transform (FFT) and the Maximum Entropy Method (MEM).

Spectral estimation methods require a stationary signal, but corrosion potentials often drift with time. It is therefore common to do trend removal before spectral analysis was carried out. This could be achieved by subtracting a linear regression line from the data. Further literature on the derivation of amplitude spectral density (ASD) and PSD from the FFT method can be found in Proakis [124].

There are currently two different viewpoints in analysing the spectrums obtained from noise experiments - the type of corrosion, whether uniform or localised, were explained by comparing the slopes of the ASD/PSD plot. Searson and Dawson [117] carried out electrochemical noise experiments with mild steel in calcium hydroxide and calcium chloride solutions. Open circuit potential fluctuations were recorded digitally throughout their experiment between two identical electrodes. It was concluded that ASD slopes obtained by the MEM method could be used to identify uniform or localised corrosion. It was pointed out that during localised corrosion such as pitting, ASD plots showed a slope of - 20 $dBdec^{-1}$, uniform corrosion demonstrated an ASD slope of - 40 $dBdec^{-1}$.

Mansfeld and Xiao [113] studied the ASD obtained when iron was exposed to electrolytes of different corrosivity. Potential and current data were transformed into ASD plots using the

MEM method. It was suggested that a high current ASD corresponded to a more severe corrosion, while potential ASD was not directly related to the severity of corrosion. They also showed that the conclusions obtained by Searson and Dawson [117] from their ASD plots were not always correct, because general corrosion can also show a slope of - 20 $dBdec^{-1}$ on the ASD plots.

Legat and Dolecek [97] suggested that the average ASD of the measured current noise at higher frequencies corresponded to the corrosion current density measured using potentiodynamic methods. The ASD slope during uniform corrosion was shown to be around 0 $dBdec^{-1}$ for both potential and current noise.

More recently, Cheng *et al.* [105] attempted to correlate the PSD slope with the transient shape in the time domain. Their theoretical analysis showed that the roll off frequency slope of the PSD at high frequencies corresponded to the behaviour of transient shapes in the collected data during corrosion. It was shown that a transient having a sudden growth and sudden death such as a metastable pitting process would produce a slope of - 20 $dBdec^{-1}$, while transients without a sudden change such as general corrosion will demonstrate a slope of - 40 $dBdec^{-1}$.

Wavelet decomposition

PSD calculations are based on the Fourier Transform and are useful for establishing the presence of periodicities within signals. As mentioned before, drift in the electrochemical signals is inevitable and potential/current transients can be aperiodic [125]. Hence it may be useful to analyse the ENM signals by wavelet decomposition, where regularities within the timescale (duration) can be picked up more easily than the PSD method. Details of the wavelet decomposition method can be obtained from Mallat [126].

A wavelet is a waveform of limited duration that has an average value of zero and an average squared value of unity [126]. A variety of wavelets have been constructed, mostly for image processing applications. Each type of wavelet is characterised by a defining function (ψ) (Equation 2-23), which incorporates a scaling parameter (s) and shifting parameter (u). The scaling parameter resolves the time scale of the data and the shifting parameter moves the wavelet along the data set.

$$\psi_{u,s}(t) = \frac{1}{\sqrt{s}}\psi\left(\frac{t-u}{s}\right)$$ *Equation 2-23*

where t is the location (time) of the wavelet function within the data set.

The wavelet transform (W) is the integral over time of the signal, $f(t)$, by the corresponding wavelet function (ψ^*).

$$Wf(u,s) = \int_{-\infty}^{\infty} f(t)\frac{1}{\sqrt{s}}\psi\left(\frac{t-u}{s}\right)dt$$ *Equation 2-24*

Thus, the wavelet transform measures the correlation between the wavelet function and the corresponding segment of the signal. A typical schematic example of the commonly used Haar wavelet is shown in Figure 2-27.

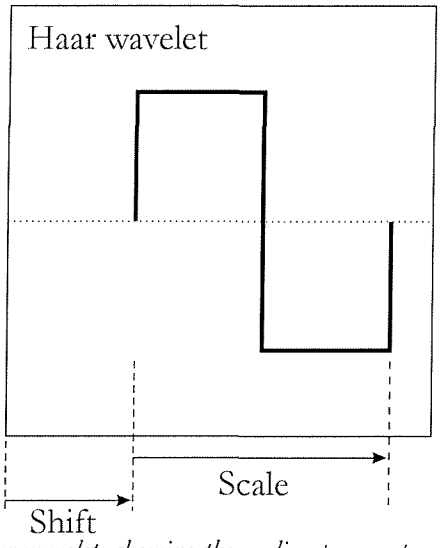

Figure 2-27 Schematic of a Haar wavelet, showing the scaling parameter and shifting parameter.

In principle, integration is required over all possible scales and positions so that a wide bandwidth is obtained from the signal. However, it has been shown [127] that, if repeated application of the wavelet transform at discrete scales based on powers of two (i.e. at scales 2^{-n} s, described as 'dyadic scaling') is used, no accuracy is lost. This procedure is called the discrete wavelet transform (DWT).

Aballe *et al.* [127,128] compared between FFT and the DWT analysis on ECN signals, obtained from static immersion experiments. Al alloys, zinc alloys and stainless steels were immersed in a NaCl and HCl solutions. It was reported that both FFT and DWT methods were useful in differentiating between low and high frequency signals. However, the DWT method was shown to be better than the FFT when signal frequencies are similar. The DWT managed to identify the characteristic time scales that are predominant between the signals. Similar results were also obtained by work carried out by Speyer [125].

Empirical Mode Decomposition (EMD)

The EMD is a novel signal processing technique, proposed by Huang *et al* [129] in 1996. The idea behind the proposition was to overcome the restrictions imposed by both FFT and wavelet decomposition techniques: namely stationarity, linearity and the duration of the signal. Furthermore, leakage generated by the limited length of the basic wavelet function makes the quantitative definition of the energy-frequency-time distribution difficult. Another difficulty of the wavelet analysis is its non-adaptive nature. Once the basic wavelet is selected, one will have to use it to analyse all the data [129].

In the EMD, complicated data sets can be decomposed into a finite and often small number of intrinsic mode functions (IMF), containing frequency information. The technique is based on the direct extraction of the energy associated with various intrinsic time scales, providing similar results to the wavelet transform. The EMD analysis is carried out based on three criteria:

1. The signal must contain at least two extrema points, one being a maximum and the other one being a minimum.
2. The characteristic time scale is defined by the time lapse between the extrema points.
3. If the original signal is totally devoid of extrema points but contained only inflection points, it can be differentiated once or more times to reveal the extrema points.

The EMD method decomposes the signals into intrinsic mode functions, the IMF is a function that satisfies two conditions: (a) The number of extrema and the number of zero crossings must be equal, or differ at most by one. (b) At any point, the mean value of the envelope defined by the local maxima and the local minima is zero.

In the decomposition, the extrema points are identified, with the local maxima points being connected by a cubic spline line (creating an upper envelope). The local minima points are also connected by a cubic spline line (creating a lower envelope). Mean values are calculated based on the upper and lower envelopes, the difference between the original signal and the mean is calculated, resulting in the first 'component'. The process is iterated until the standard deviation between adjacent components lie between 0.2 and 0.3, indicating that they are identical. The final component in the first iteration is defined as the first IMF. The difference between the first IMF and the original signal is recorded as residues. The residues are then subjected to further iterations, resulting in subsequent IMF. The process is repeated until no further IMF can be obtained – usually resulting in a zero value or a trend within the original signal.

2.6 Conclusions from the literature review

A review of selected topics in coatings technology, erosion, corrosion and erosion-corrosion processes and electrochemical methods have been carried out, serving as a background information for the rest of the thesis. Thermal spray coating systems have been discussed with particular emphasis on HVOF coatings. The advantages of the HVOF method over other conventional thermal spraying processes have been presented. Erosion mechanisms for ductile materials were explained, the effects of various experimental parameters that affect the erosion behaviour of materials have also been surveyed. An introduction was made of the major types of erosion test apparatus. The basic theory of corrosion and effects of flow on corrosion was presented with a review of the corrosion behaviour of nickel aluminium bronze alloys. Literature on the erosion-corrosion of bulk materials and coatings were also reviewed, the effects of corrosion and erosion in affecting synergy was presented. Finally, the electrochemical techniques used for monitoring corrosion and erosion-corrosion was introduced, emphasis was made for the relatively novel technique of electrochemical noise acquisition and analysis.

Of all the literature reviewed, little has been found on the following subjects:

- Erosion-corrosion of metallic HVOF coatings.

- A coherent definition of synergy and its estimation in various erosive and corrosive environments.
- Electrochemical noise measurement of metallic coated systems.
- A consistent analysis of electrochemical noise data under dynamic erosion and corrosion conditions.

The current work aims to address the issues listed above.

Chapter 3 Materials Characterisation and Static Corrosion

3.1 Introduction:

The objective of this section is to characterise the physical and mechanical properties of the materials used in the current investigation. They are carbon steel substrates, cast NAB alloy, HVOF AB coating and HVOF NAB coating. The chemical composition, fabrication conditions and some mechanical properties will be discussed. The coatings are further characterised by scanning electron microscopy (SEM), microhardness measurements and porosity estimation.

Corrosion behaviour of both AB and NAB coatings and the NAB substrates was also investigated under static immersion conditions, using 3.5 % NaCl solutions. Results can be used as a reference for the flow corrosion conditions, presented in Chapter 5. Electrochemical noise measurements were used to monitor static corrosion behaviour of the specimens over 5 days. Potentiodynamic polarisation experiments were carried out to determine both E_{corr} and i_{corr}. Results from both techniques were used to rank the corrosion resistant of the materials tested, based on its open circuit potential and current.

3.2 Substrate materials

The substrate materials used in the current work, namely AISI 1020 and BS 4360 steels, have been well characterised elsewhere [130]. Chemical compositions and some mechanical properties are presented here, as they are related to the work carried out in this project.

3.2.1 AISI 1020 steel substrate (1020 steel)

The AISI 1020 steel is designated as UNS G10200 under the unified numbering system (UNS). It is a common engineering material and its initial casting conditions conform to the AISI 1020 grade. The plates are then fabricated by rolling. Further information about the material can be obtained in the ASM metals handbook [130]. Due to its weldability and strength, the AISI 1020 steel is used extensively in construction and piping.

3.2.2 BS4360 steel substrate (4360 steel)

The BS4360 steel conforms to European standard grades BS EN 10025 Fe430A. The nearest American casting standards are ASTM A36 (UNS K02600) and ASTM A529 (UNS K02703). This grade of steel is used within the British construction and piping industry; the fabrication methods are similar to that of AISI 1020 steel. Further information of this steel grade can be found in the ASM metals handbook [130]. Compared to AISI 1020 steel, the BS4360 steel contains added Manganese and Silicon to further increase its weldability and strength.

3.2.3 Nickel aluminium bronze substrate (NAB)

The NAB alloy conforms to those specified by UNS C95800 (as cast) and UNS C63200 (rolled). It is commonly used for fabrication of components for marine applications, such as propeller hubs and plates, nuts, bolts and structural pump parts used in seawater service. The excellent corrosion resistance of the NAB alloy, achieved by formation of a robust protective layer, means that it is a popular material for corrosive marine environments. The ability to form a robust protective layer was attributed to the alloying effects of aluminium [43,131,132].

The standard recommended chemical composition of the three substrate materials are shown in Table 3-1. Some selected mechanical properties of the materials are shown in Table 3-2. The latter shows that the copper based NAB alloys are considerably harder and stronger than the steel alloys.

Table 3-1 Standard recommended chemical compositions for the substrate materials used in the current investigation.

Substrate materials	Standard recommended chemical composition								
	C	Mn	P	S	Si	Fe	Al	Ni	Cu
1020 steel	0.23	0.60	0.04	0.05		Bal			
4360 steel	0.25	1.60	0.05	0.05	0.5	Bal			
NAB alloy						4.5	10	5	Bal

Table 3-2 Some relevant mechanical properties of the substrate materials used in the current investigation.

Substrate materials	Mechanical properties			
	Density (gcm^{-3})	Hardness (*Vickers*, HV_{100g})	Young's Modulus (*GPa*)	Ultimate tensile strength (*MPa*)
1020 steel	7.87	149	200	450
4360 steel	7.87	149	200	450
NAB alloy	7.64	235	115	673

3.3 Coating materials

3.3.1 D1004 Aluminium bronze coating (AB coating)

Similar to the NAB alloy, cast and wrought aluminium bronze are commonly used for fabricating bushings, bearings, nuts and gears that are exposed to a marine environment. Its corrosion resistance properties are also excellent, as it is also able to form a protective film on the surface when immersed. The Diamalloy 1004 AB coating powder was obtained from Sulzer Metco (UK). Its chemical composition is similar to that of aluminium bronze alloys UNS 95300 (cast) and UNS C61800 (wrought). The chemical composition of the AB coating particles is shown in Table 3-3 and the coating properties are shown in Table 3-4. The coating is useful for building up and repairing original cast/wrought materials. The as-received coating particle diameter is about 45 μm ± 15 μm; the gas atomised particle has a spherical morphology. The melting temperature of the particle is 1040° C. The AB coating was deposited using the HVOF method (Diamond Jet spraying system, illustrated in Figure 3-1) by Sulzer Metco. Two types of alloys, 1020 steel and NAB alloy were used as substrates. The as-received coating thickness was 250 μm.

Table 3-3 Standard chemical composition of AB coating power particles:

Element	Al	Fe	Cu
% w/w	9.5	1.0	Bal

Table 3-4 Some material properties of the HVOF AB coating (supplied by Sulzer Metco):

Macrohardness (Brinell)	89
As sprayed surface roughness (R_a, μm)	7 ~ 9
Surface roughness after polishing (R_a, μm)	0.01
Tensile bond strength (MPa)	> 41
Coating weight (kgm^{-2} / 0.1 mm)	0.67
Density (gcm^{-3})	7.64
As sprayed coating thickness (μm)	250

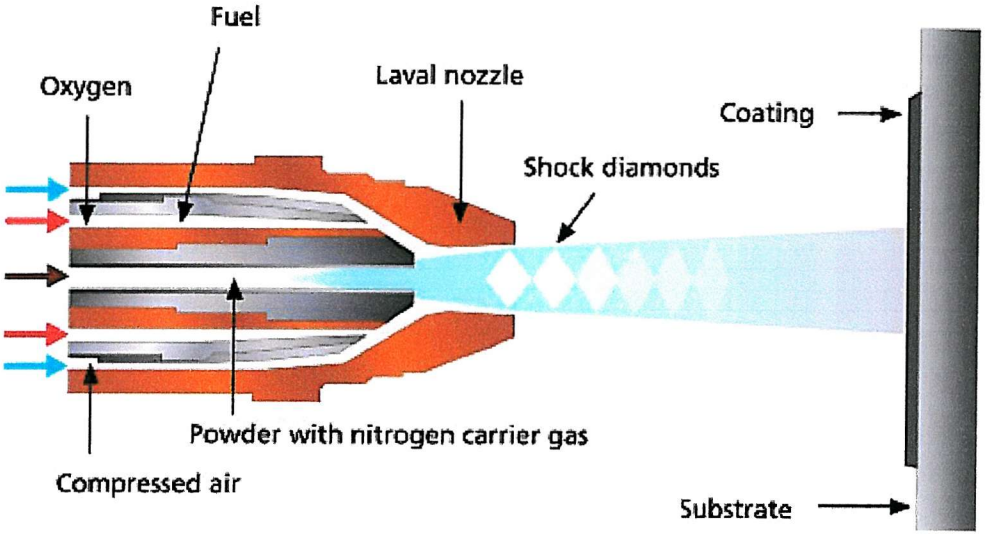

Figure 3-1 An illustration of the 'Diamond Jet' HVOF spray gun system

Oxygen and fuel gas (propylene) was mixed in the flame nozzle just prior to burning. The coating particles are then injected into a stream of carrier gas, along the central axis of the ring of the flame jets. This results in heating of the material and acceleration of the particles into a tight uniform spray pattern. The AB powder was sprayed in a raster pattern at a stand off distance of about 150-230 mm, at normal incidence. Thickness was built up progressively, allowing layered coatings to be built up to the required thicknesses. As the semi-molten particles impinge on the substrate surface, lamellas of semi-molten particles (splats) were formed. The interlocking of the coating splats provided a dense and adherent coating system. The conditions used in HVOF spraying of the AB coating are shown in Table 3-5.

Table 3-5 Coating spray conditions for the HVOF AB coating:

Fuel gas	Propylene
Gas flow rate (Std. Litre per minute)	67
Powder feeder gas	Nitrogen
Stand off distance (mm)	230
Spray rate ($gmin^{-1}$)	60.5
Coverage (m^2hour^{-1} / 0.1 mm)	4.4

The as-sprayed coating has a relatively high surface roughness which is known to affect the sand erosion performance, due to the following reasons: (1) asperities are eroded faster than the bulk material, (2) roughness can alter the impact angle and possibly affect the erosion mechanism, and (3) the characteristics within an erosion scar are most easily identified on a smooth surface. Hence, all the specimens used in the erosion and erosion-corrosion experiments were ground (up to grade 1200 SiC paper) and lapped (up to 3 μm diamond suspension) to a surface finish of $R_a < 1$ μm.

Scanning electron microscopy (SEM)

The JEOL JSM 6400F analytical scanning electron microscope (SEM) was used to investigate the morphology and chemical composition of the AB coating and its substrates. The SEM has a built in digital image enhancement system (secondary electron imaging) for topographical studies of specimen surfaces (resolution ~ 3.5nm). Back scattered electron imaging was used for compositional contrast on plane surfaces (resolution ~ 1 μm), energy dispersive X-ray microanalysis (EDX) with a spatial resolution of ~ 2 μm enables distinction of chemical species present within the coating.

Figure 3-2 shows a transverse section of the aluminium bronze coating. The surface of the coating was kept at the as-received condition, the approximate surface roughness was $R_a = 8$ μm and the coating thickness was between 230-250 μm. Coating splats can be observed in the micrograph as well as partially molten particles with a size range of around 50 μm which are distributed throughout the coating. EDX analysis in Figure 3-3 reveals high amounts of copper in the partially molten and fully molten splat particles, indicating α rich phases. Pores of varying size range (0.1 to 1 μm) are also present throughout the cross section. Inspection of the transverse section did not reveal thermal stress relieve cracks that are associated with cooling after the coating process.

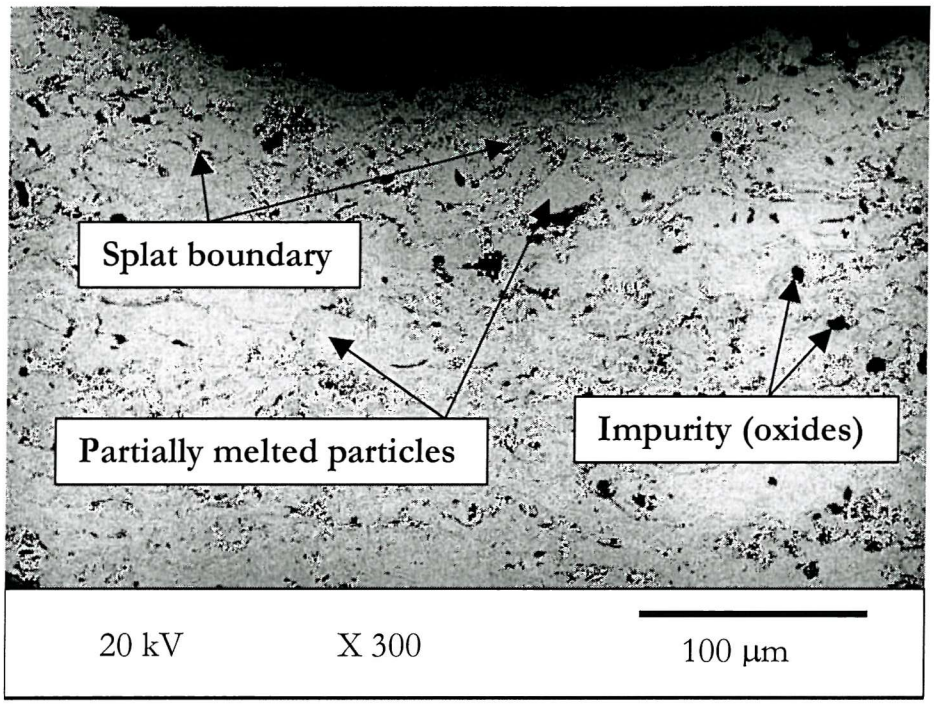

Figure 3-2 *Transverse section micrograph of the HVOF AB coating, showing coating splats, partially melted particles and impurities.*

EDX analysis on the splat boundaries (Figure 3-4) revealed traces of aluminium, copper and oxygen. Molten coating particles can form an outer layer of oxide at high temperatures during the trajectory from the spray gun to the substrate. It is possible for aluminium to be diffused out of the molten particle to form this oxide, since the diffusion coefficient of aluminium is higher than copper [133]. The splat boundaries are more apparent near the coating surface, possibly due to contamination from the fuel gas during a later stage of the spraying process [134]. Grit used for shot peening of the substrate was also found at the coating-substrate interface (not shown in micrograph), with a size range of 20-30 μm. As shown in the EDX analysis in Figure 3-5, the grit was identified as alumina particles.

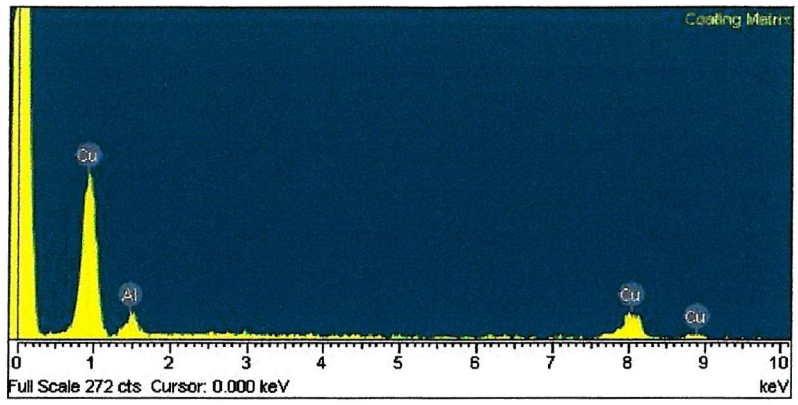

Figure 3-3 *EDX analysis on the AB coating particles, showing the presence of copper and aluminium*

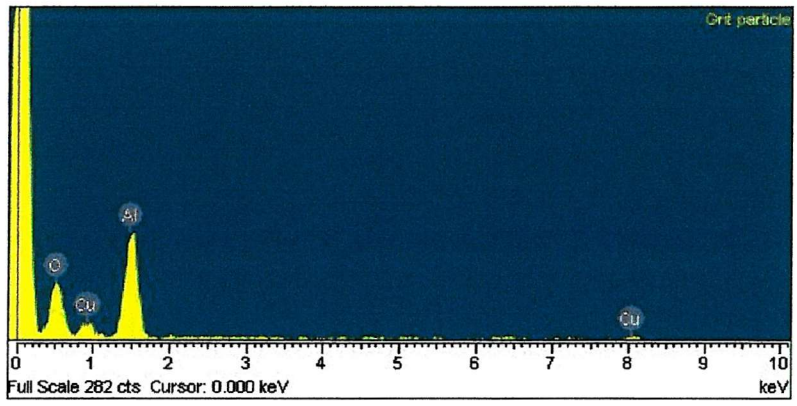

Figure 3-4 *EDX analysis on the coating splat boundary, showing the presence of aluminium oxides*

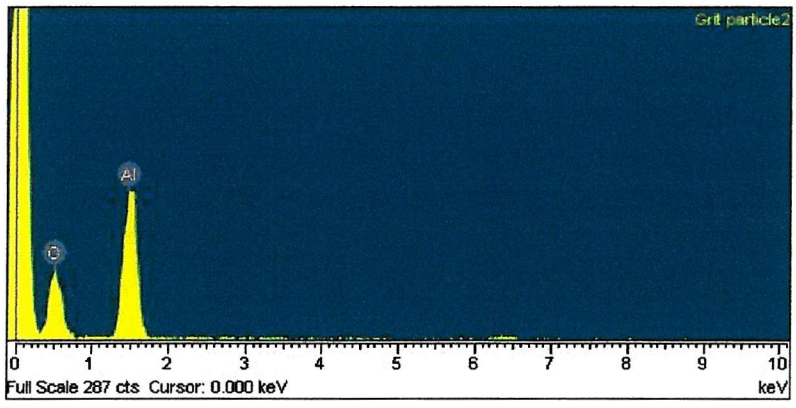

Figure 3-5 *EDX analysis on the alumina grit particles.*

Figure 3-6 shows the coating surface morphology in the as received condition. The figure shows the formation of splats as the semi-molten coating particles impinge on the surface. The surface is highly deformed and it is difficult to distinguish individual splats. Splats were approximated to have size ranges of 10-30 μm. The highly deformed surface contributed to the original surface roughness of 7-9 μm. It is also possible to see the interlocking mechanism

of splats on the surface. Gaps are seen between splats, resulting in pores on the coating surface and within the coating itself.

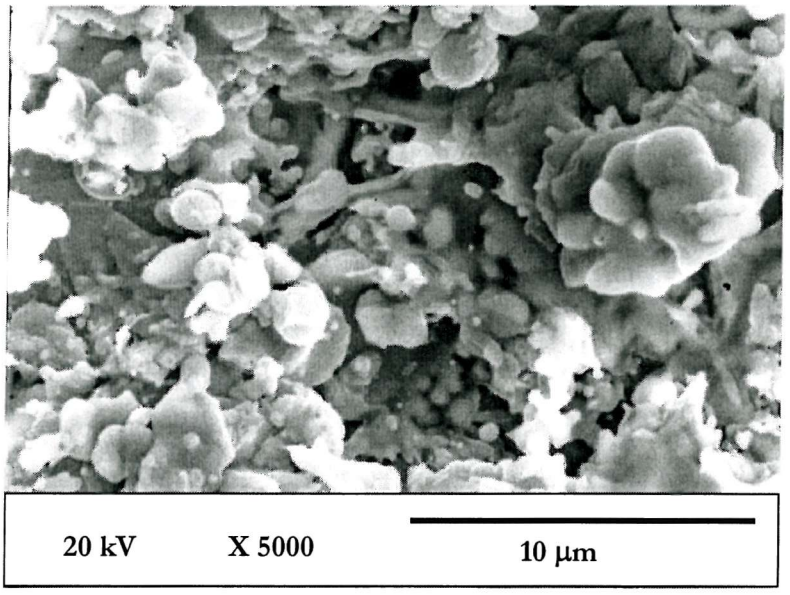

Figure 3-6 SEI of the as-received coating surface, revealing the splat morphology.

Microhardness measurements

The Vickers micro-hardness indenter was utilised to determine the hardness values across the coating thickness. For repeatability, transverse sections of the specimens were mounted in epoxy resins and lapped with 1 μm diamond paste prior to indentations. A load of 100 g was used, the loading time was set at 15 seconds to ensure accurate micro hardness readings. Indentations were carried out from the coating surface into the substrate, with a gap of around 40-50 μm between indentations. The indentations are shown in an optical microscope image in Figure 3-7. Five sets of indentation data were obtained and the values averaged to obtain the micro-hardness value. Key data from the measurements are presented in Table 3-6.

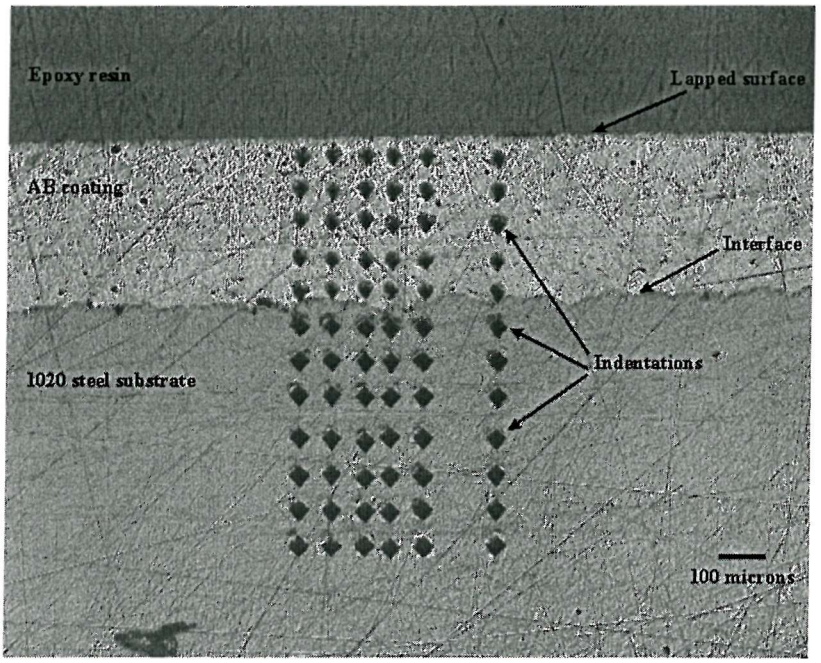

Figure 3-7 *Optical micrograph of the AB coating (transverse section), showing micro-hardness indentation marks from the coating surface to the 1020 steel substrate.*

Table 3-6 *Key micro-hardness data obtained from the AB coating on 1020 carbon steel and NAB substrates.*

AB coating on AISI 1020 steel substrate			AB coating on NAB substrate		
Distance from lapped surface	Mean	Standard deviation	Distance from lapped surface	Mean	Standard deviation
(μm)	*($HV_{0.1kg}$)*	(Error)	*(μm)*	*($HV_{0.1kg}$)*	(Error)
30	259.2	±43.3	20	192.0	±21.6
80	294.8	±20.5	60	329.4	±24.1
120	314.2	±12.4	90	340.0	±10.9
170	317.8	±14.7	140	316.6	±39.6
220	330.2	±33.6	180	331.0	±41.2
260	162.2	±4.4	230	322.8	±29.7
310	150.4	±11.9	280	318.0	±50.1
360	144.2	±10.3	330	242.4	±36.1
410	136.6	±19.8	370	237.6	±5.4
470	130.6	±9.4	410	231.4	±23.9
510	135.8	±8.8	460	238.2	±18.9
560	140.0	±8.3	500	227.0	±28.5

The micro-hardness data from Table 3-6 are subsequently plotted in Figure 3-8 and Figure 3-9, for the AB coating with 1020 steel substrate and NAB substrate respectively. From the figures, micro-hardness of the coating is in the range of 300-330 HV. Low hardness values were obtained near the coating surface, probably caused by edge effects. Some scatter was also observed in the data, this can be attributed to pores and oxides within the coating.

Micro hardness values for the 1020 steel substrate and the nickel aluminium bronze substrate are 150 HV and 240 HV respectively; they are typical for such materials.

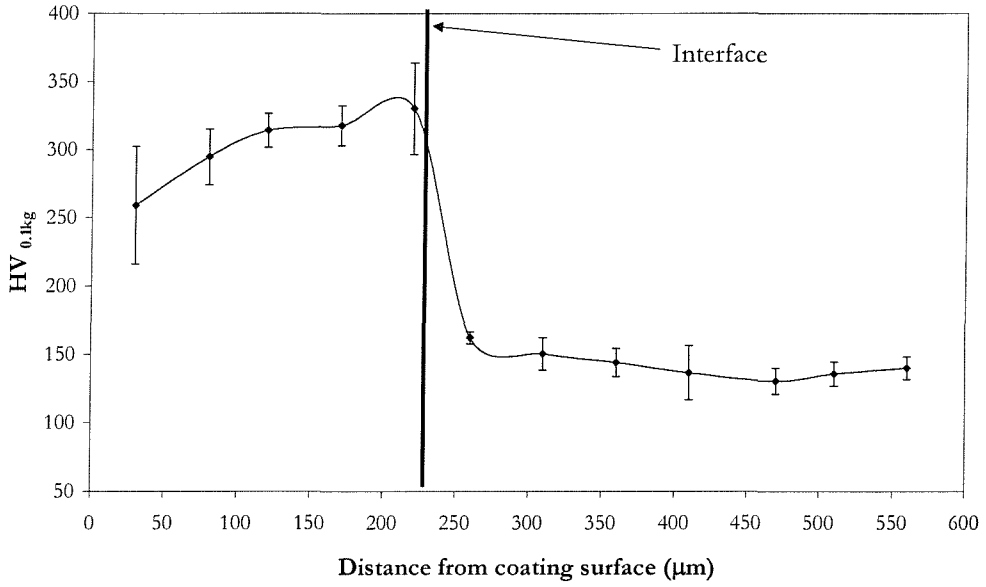

Figure 3-8 Micro-hardness profile across the AB coating to the 1020 steel substrate.

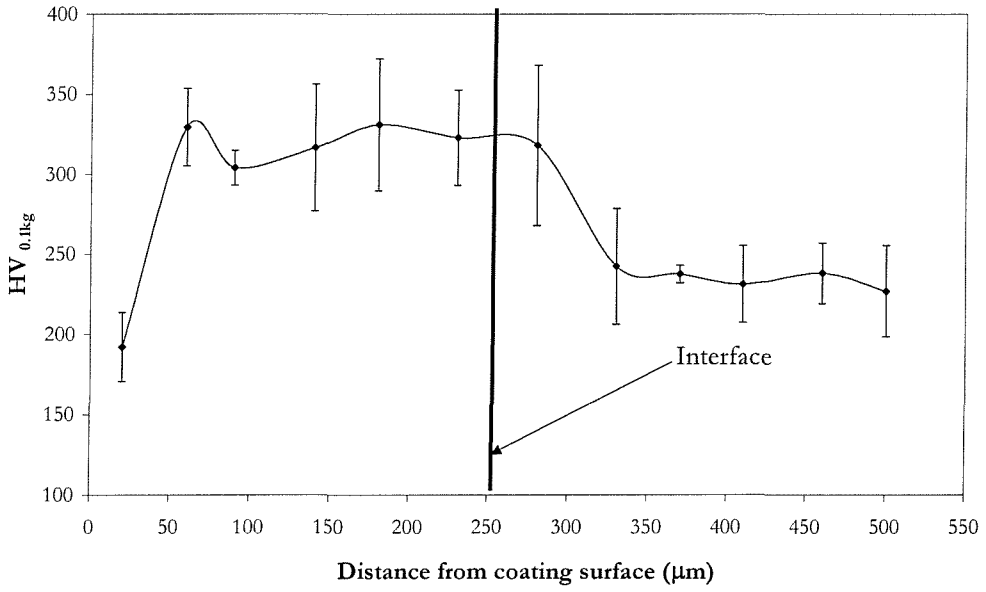

Figure 3-9 Micro-hardness profile across the AB coating to the NAB substrate

Porosity measurements

Optical micrographs of the coating transverse section were taken with a digital camera mounted onto an Olympus B061 optical microscope. A commercial image analysis program (Carl Zeiss KS300) was utilised for calculating the porosity percentage within the coating. Figure 3-10 shows (a) the transverse section image of the coating being transformed into (b) a binary image where a black and white analogy of the features on the surface was obtained. The white areas in the binary image signify the coating matrix while the black areas signify the pores. The binary image was further processed into (c) a reversed image to enhance the pore edges and for porosity estimation.

The software allows calculation of the percentage of white areas from a total predefined area within the coating. The predefined area has to be relatively large to represent the cross section but also narrow enough to exclude the substrate and the mounting resin. Calculations based on an average of four measurements indicated that pores occupy about 1.07% of the total analysed area.

The procedure of transforming an original transverse section coating image into a reversed black and white image involved definitions of cut off points, where 'grey' regions from the image are being separated into either 'black' or 'white' regions. This procedure requires setting the threshold value manually within the image analysis software and visual judgement. Consequently, dissimilar results can be obtained, depending on the original image and individual judgements. Furthermore, specimen surface preparation can introduce impurities onto the surface, further complicating the porosity measurements. To ensure reproducibility and minimise individual judgements, a more rigorous measurement algorithm is desirable.

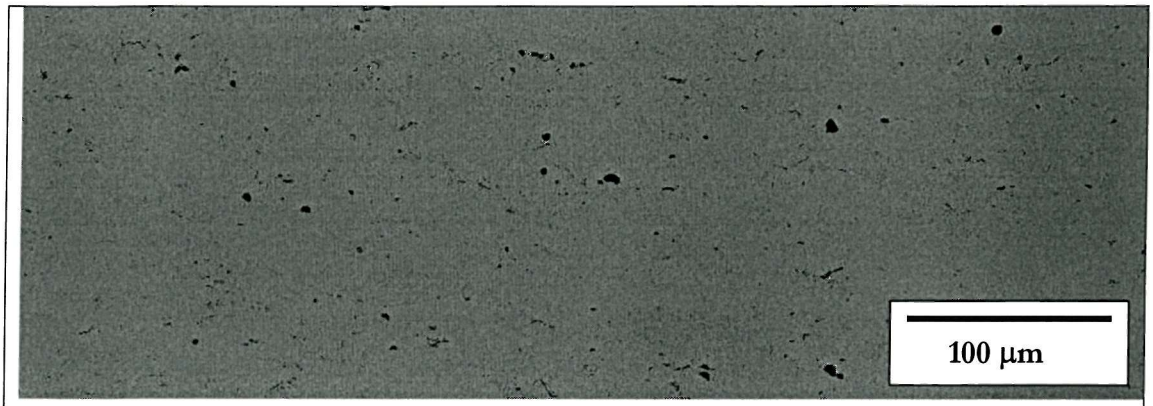

(a) Coating image

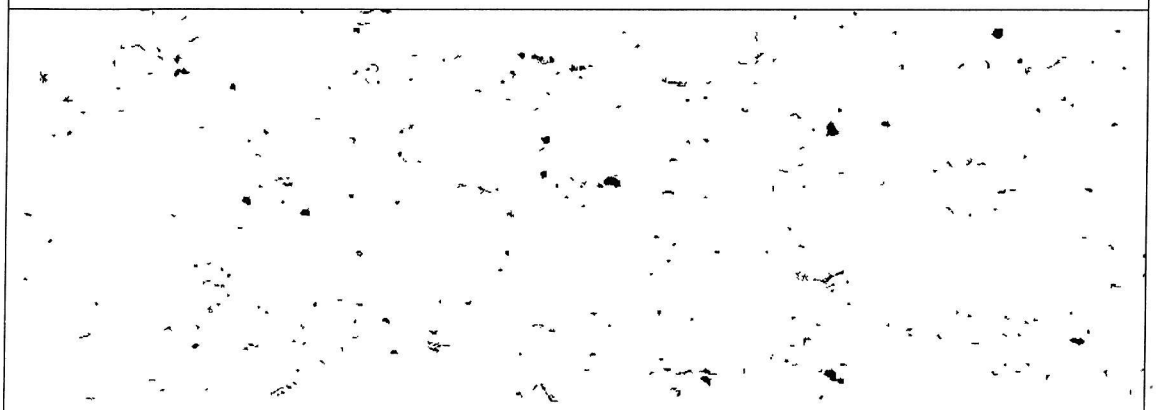

(b) Binary image

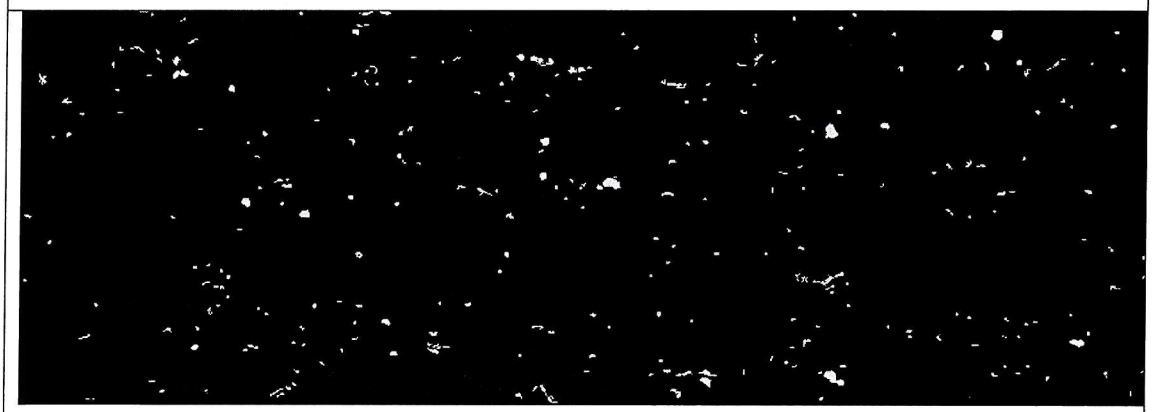

(c) Reversed image

Figure 3-10 Transformation of a microscope image into a reversed image for porosity calculations. In the reversed image (c), white areas indicate the pores within the AB coating. Coating images acquired from 30 µm below the surface (top) to 30 µm above the substrate (bottom).

3.3.2 Nickel aluminium bronze (NAB) coating

A hybrid nickel aluminium bronze (NAB) coating was fabricated and used in the current investigation. The NAB coating is novel as HVOF nickel aluminium bronze powders were not commercially available. The NAB coating was developed primarily for its similarity with the cast NAB alloy; it is intended to reduce the overall galvanic interaction between the HVOF coating and the bulk NAB alloy.

The coating consists of a mixture of three types of commercially available HVOF powders. They are D1004 (aluminium bronze), D1003 (Ni5Al) and D4008NS (AISI Type 316 stainless steel). A mixing ratio of 89 % w/w D1004, 6 % w/w D1003 and 5 % w/w D4008NS gave a chemical composition nominal to that of a cast NAB alloy. Chemical composition of the HVOF powders and the resulting coating is shown in Table 3-7. It was shown that the chemical composition of the NAB coating is almost similar to the bulk NAB alloy, with the exception of 1 %w/w chromium. Some trace elements of molybdenum, silicon and carbon (from D1003 HVOF powders) was also introduced.

Table 3-7 Chemical composition of the commercial HVOF coating powders used for formulating the NAB coating. Bulk NAB alloy compositions are shown (shaded) for comparison.

Element	Al	Ni	Fe	Cr	Mo	Si	C	Cu	Notes (mixing ratio)
	9.5	-	1	-	-	-	-	Bal	D1004 (89 %)
	-	12	Bal	17	2.5	1.0	0.1	-	D1003 (6 %)
% w/w	5	Bal	-	-	-	-	-	-	D4008NS (5 %)
	9	5	4.5	-	-	-	-	Bal	Bulk NAB alloy
	8.71	5.55	4.50	1.02	0.15	0.06	0.01	Bal	NAB coating

HVOF spraying of the NAB coating was carried out by the Centre of Thermal Spray Technology (University of Barcelona), utilising a Diamond jet HVOF gun. As shown in Table 3-8, spray conditions used were similar to that of the previous HVOF AB coating. The NAB coating was applied onto BS4360 steel plates measuring 120 mm by 300 mm. Material properties of the NAB coating are shown in Table 3-9.

Table 3-8 Spray conditions (HVOF) used for fabricating the NAB coating

Fuel gas	Propylene
Gas flow rate (SLPM)	77
Powder feeder gas	Nitrogen
Stand off distance (mm)	300
Spray rate ($gmin^{-1}$)	40
Coverage (m^2hour^{-1} / 0.1 mm)	10.7

Table 3-9 Material properties of the NAB coating

Macrohardness (Brinell)	N/A
As sprayed surface roughness (Ra, μm)	7 ~ 9
Surface roughness after polishing (Ra, μm)	0.01
Tensile bond strength (MPa)	N/A
Coating weight (kgm^{-2} / 0.1 mm)	N/A
Density (gcm^{-3})	7.69
As sprayed coating thickness (μm)	300

Scanning electron microscopy

Figure 3-11 shows a SEM transverse section of the NAB coating, prepared from the as-received condition. The as-sprayed coating thickness was approximately 300 μm, a rough surface was also observed. The coating was built up by semi-molten splats, spreading up to 80 μm in the horizontal direction. Unmelted particles were observed in the transverse section. The coating/substrate interface was well bonded without delaminations, alumina grit used for substrate preparation were also observed at the interface. The NAB coating has a heterogeneous appearance, consisting of the different types of HVOF powders used. EDX analysis was used to determine the composition of individual particles.

EDX spectra obtained from the lighter phases (Figure 3-12) revealed that it consists of aluminium bronze particles. Darker phases were found to be stainless steel particles (Figure 3-13) and Ni5Al alloy particles (Figure 3-14). Traces of gold were also observed in the EDX spectra, due to the specimen surface being sputtered prior to SEM investigations to increase spatial resolution (under secondary electron imaging).

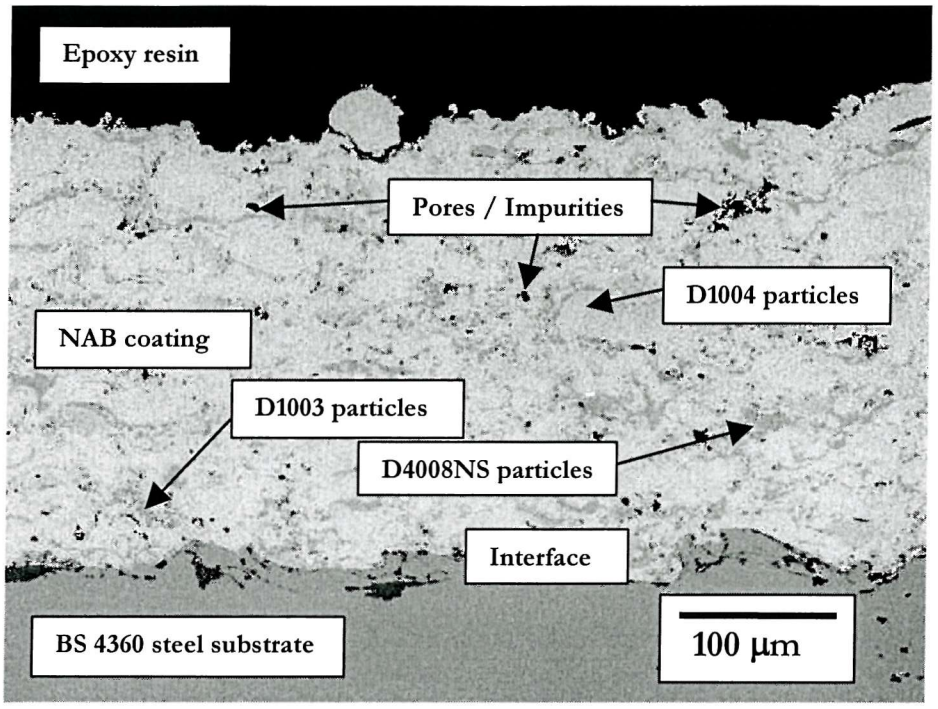

Figure 3-11 Transverse section SEM of the HVOF NAB coating, showing different coating particles/ splats and pores within the coating.

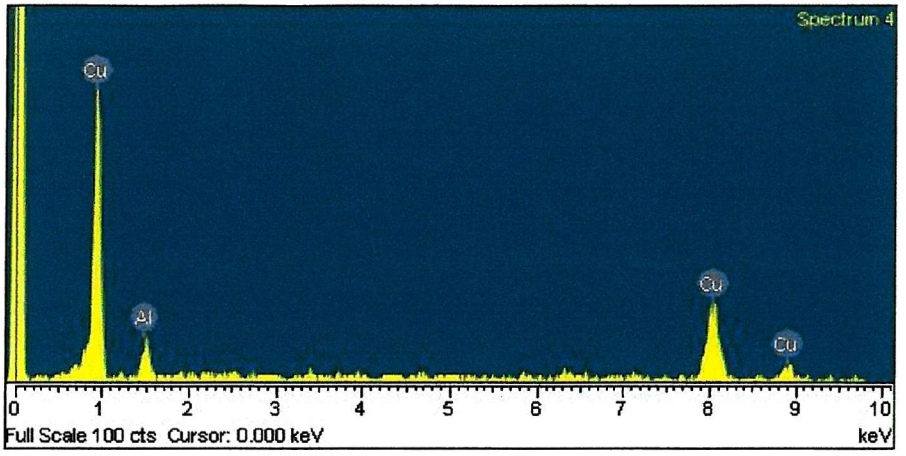

Figure 3-12 EDX spectra of the AB particle

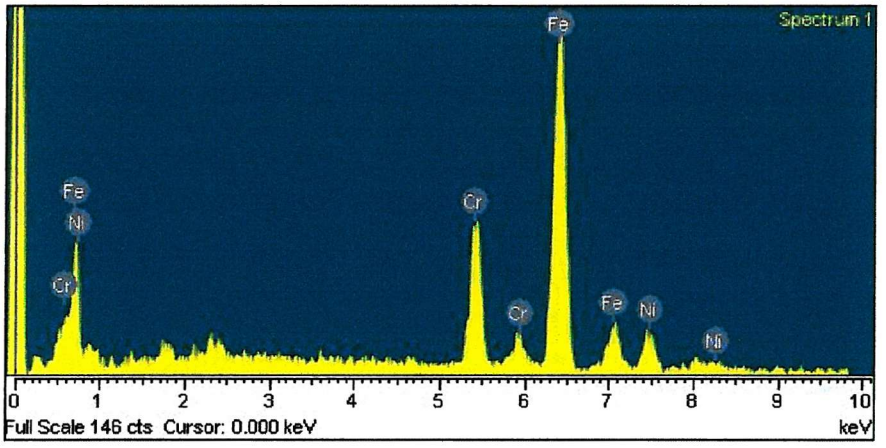

Figure 3-13 EDX spectra of the stainless steel particle

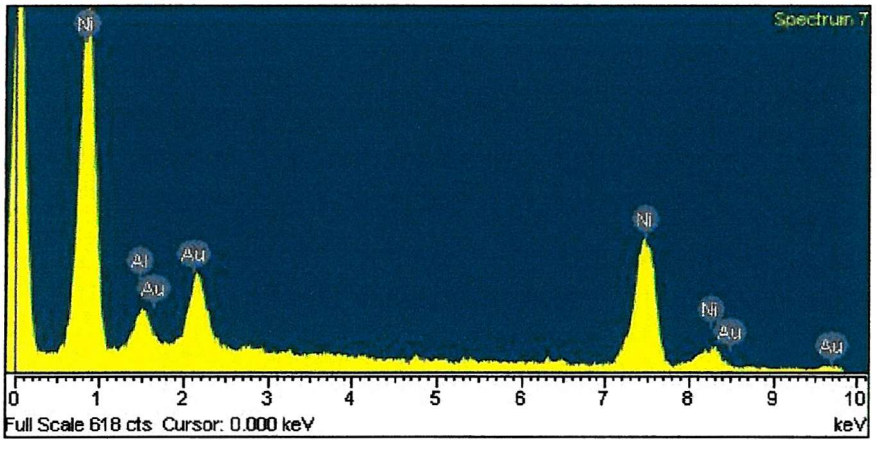

Figure 3-14 EDX spectra of the Ni5Al particle

Micro-hardness measurements

Micro-hardness measurements were also carried out on the NAB coating, using similar procedures to those used to analyse the AB coating. Micro-hardness values were obtained by averaging four sets of indentation data. Standard deviation was calculated so that the amount of data scatter can be determined. A transverse section of the coating revealing the micro-hardness indentation marks is shown in Figure 3-15. The indentation marks on the right side were used to determine the loading conditions. Four rows of indentations on the left side were used for the actual micro hardness calculations.

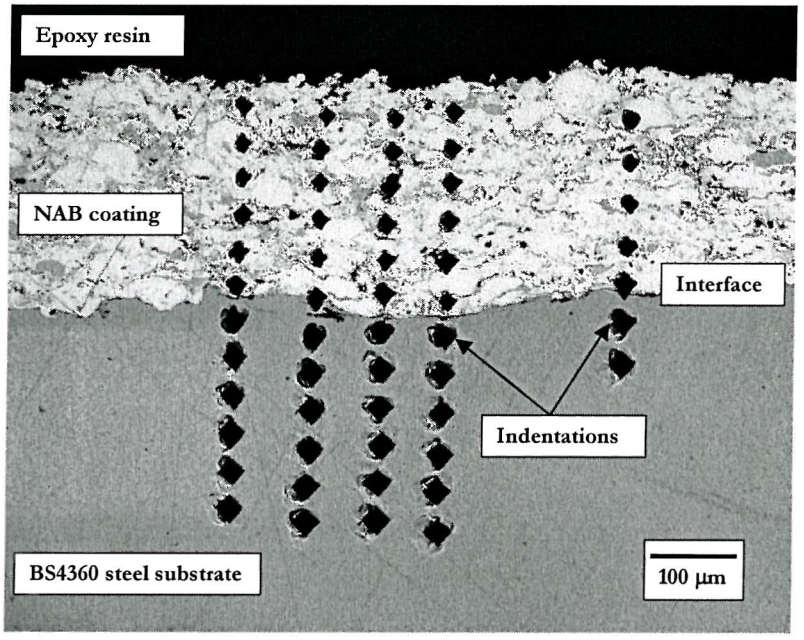

Figure 3-15 Transverse section of the NAB coating, showing micro-hardness indentations.

The averaged micro-hardness values of the NAB coating on 4360 steel substrate are shown in Figure 3-16. The coating hardness decreased with depth, high amounts of scatter (standard deviations) was observed in the data. This phenomenon was mainly caused by the heterogeneous particles with different hardness values. The hardness value of the NAB coating is in the order of 290 $HV_{0.1kg}$. This was found to be similar with that of the AB coating (D1004). The BS4360 steel substrate has a hardness value of approximately 160 $HV_{0.1kg}$, similar to the AISI 1020 steel substrate. Due to the first indentation being carried out further away from the coating surface, edge effects was not observed.

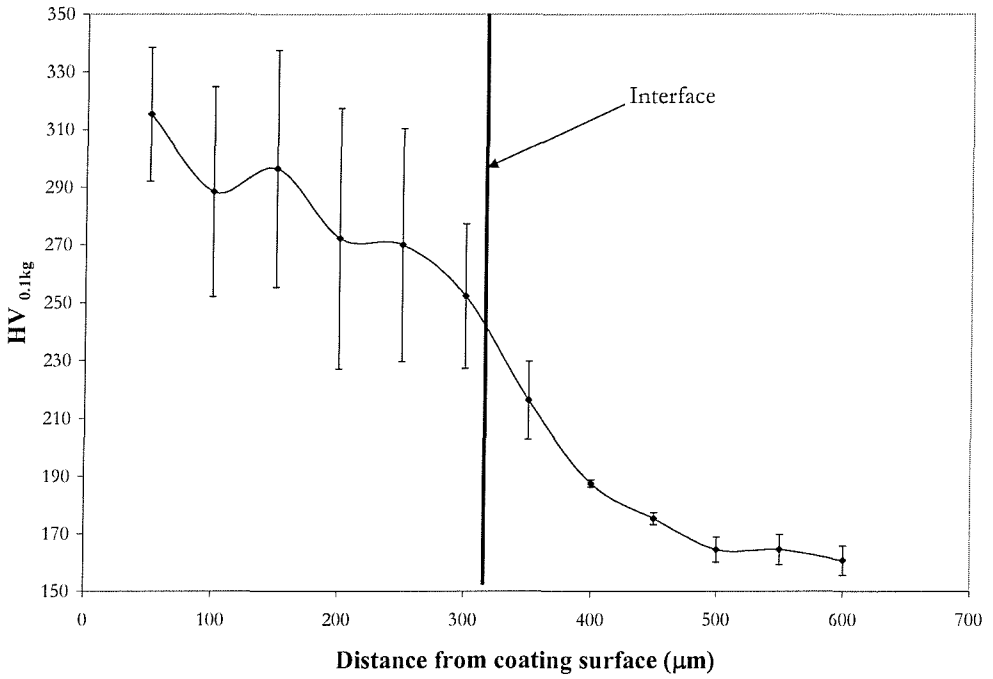

Figure 3-16 Micro-hardness profile of the NAB coating on 4360 steel substrate

Porosity measurements

Porosity of the NAB coating was quantified by using the same procedures utilised for the AB coating. As seen in Figure 3-17, (a) a representative coating cross-sectional image was selected and transformed into (b) a binary image and subsequently into (c) a reversed image. The areas occupied by pores were subsequently quantified and were found to occupy 2 % of the total area investigated. The area percentage was assumed to be proportional to the volume percentage. Porosity of the NAB coating was found to be within the range of typical HVOF coatings, it is also approximately twice that of the AB coating. The difference could be due to variations in spraying conditions (stand off distance) and the in-homogeneity of the coating particles. The different melting points of the particles used in the NAB coating can result in a non-uniform splat formation, with some particles more molten than the rest. Higher levels of porosity would probably affect the corrosion resistance of the NAB coating as aggressive electrolyte can permeate the coating more easily.

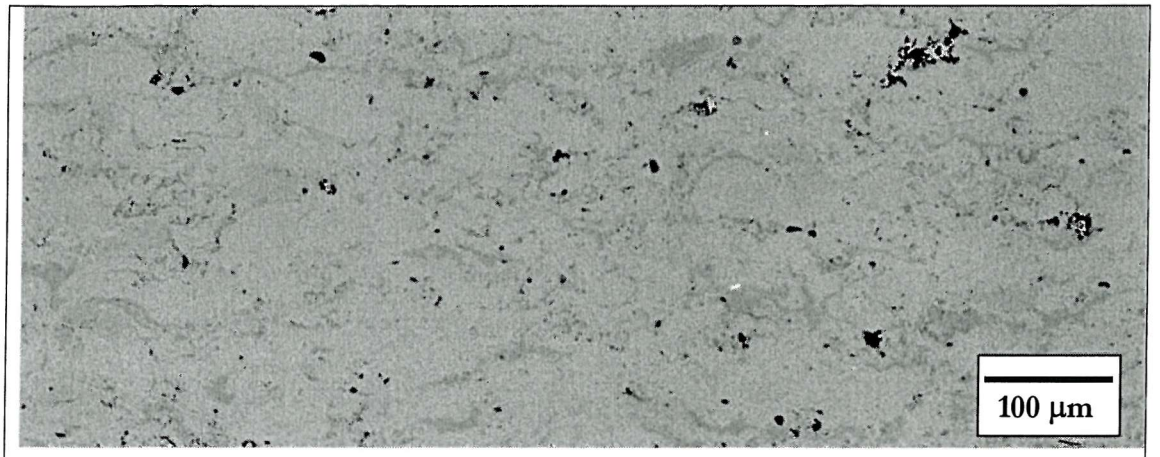

(a) Coating image

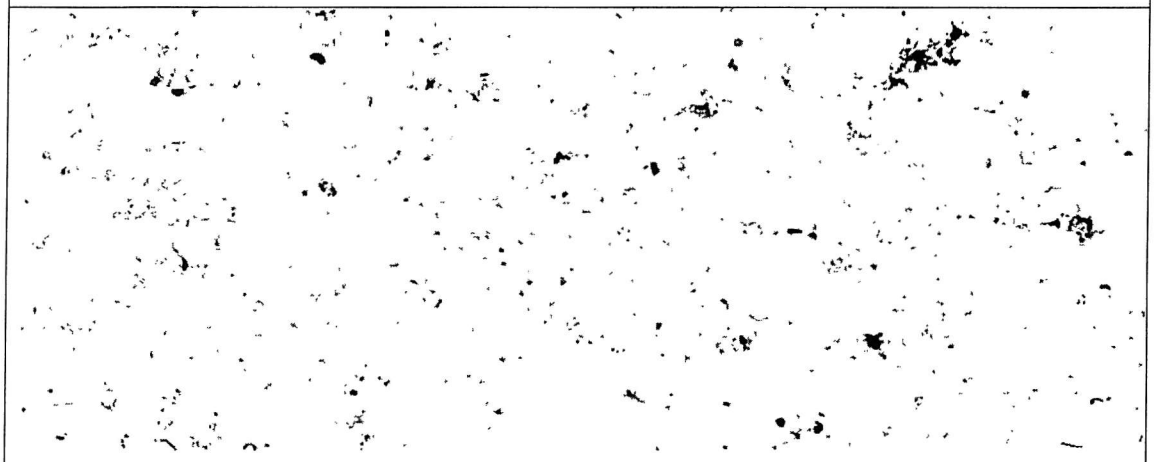

(b) Binary image

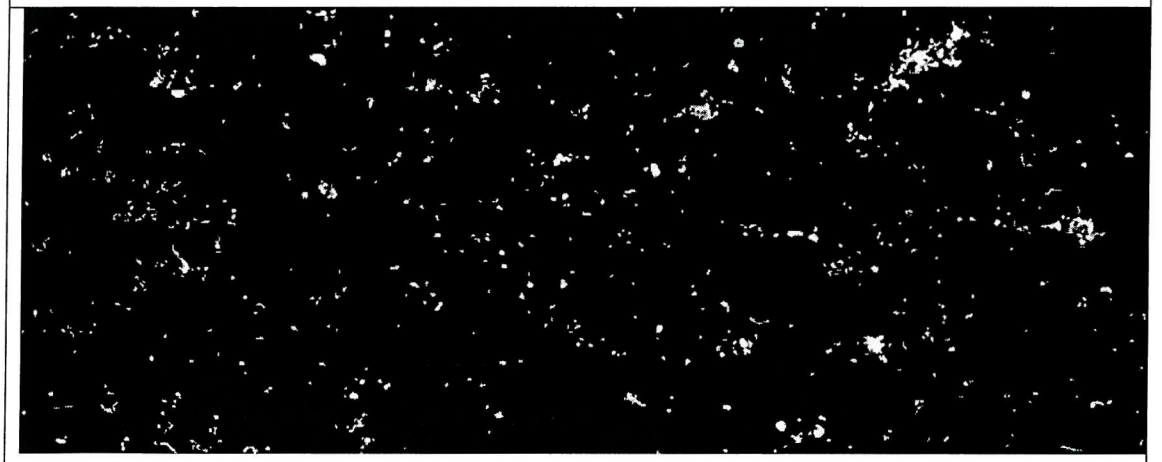

(c) Reversed image

Figure 3-17 Transformation of (a) microscope image into (b) a binary image and (c) a reversed image by the Carl Zeiss KS 300 software. NAB coating images acquired from 30 µm below the surface (top) to 30 µm above the substrate (bottom).

3.4 Static corrosion

3.4.1 Experimental methology

A Gamry PC4/750 potentiostat and associated software have been used to carry out the electrochemical work, particularly for electrochemical noise measurements. The PC4/750 potentiostat consists of a pair of printed circuit boards installed in a computer: a potentiostat card and a controller card.

Communication between the potentiostat and the electrochemical cell was established via five individual leads. Cell cable connections in potentiostatic configuration are shown in Figure 3-18. The working and counter electrodes (WE and CE) are connected to a precision resistor, i.e. 'sense' leads for measurement of potential drop and current carrying leads are kept separate. The 'sense' leads and the reference electrode (RE) are both connected to high impedance inputs (> 10^{12} Ω). For open-circuit conditions, only the WE and RE leads are connected to measure the changing potential.

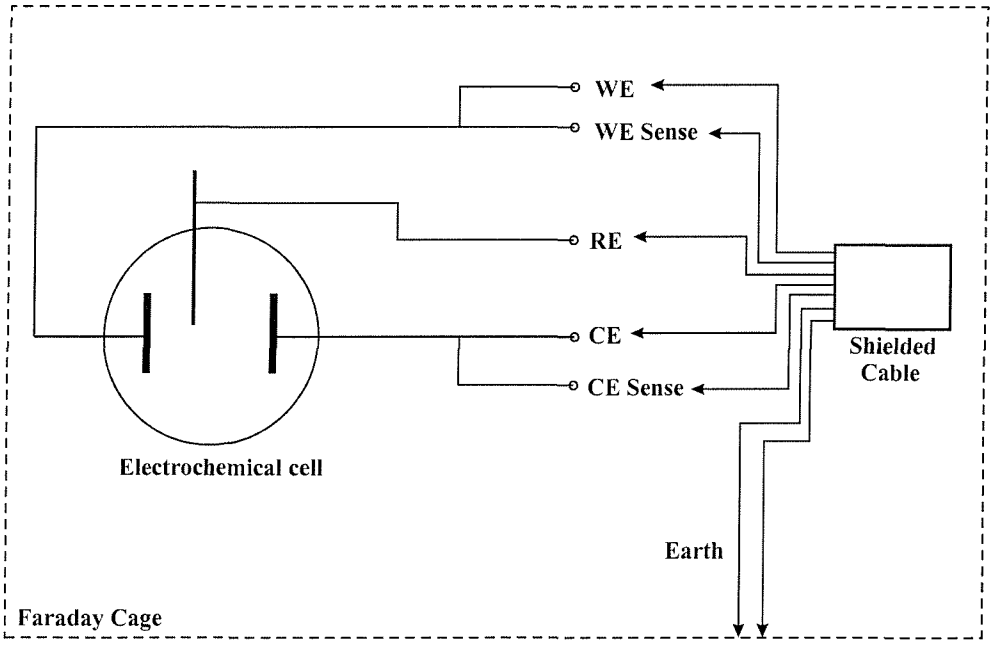

Figure 3-18 Cell cable configurations between the electrochemical cell and the Gamry PC4/750 potentiostat.

Electrochemical potential noise (EPN) acquisition has been carried out by using a 2-electrode cell configuration, consisting of a working electrode and a reference electrode. The cell configuration is shown in Figure 3-19(a). The specimen is encapsulated in a waterproof PTFE electrode holder, with a surface area of approximately 80 mm^2 being exposed to the 3.5 % NaCl solution. A rubber 'O' - ring was used to prevent the solution from entering the specimen holder. The reference electrode is a commercially available single junction Ag/AgCl (SSC) electrode, saturated with 1 M KCl solution. A single junction reference electrode was used to avoid potentiostat instability (noisy signals) that usually occurs on double junction electrodes. All experiments have been carried out in a Faraday cage.

A 3-electrode cell configuration was used for electrochemical current noise (ECN) measurements. A second 'identical' specimen is encased in a PTFE holder and immersed into the solution, to act as a counter electrode. ECN was measured from the current passed between the counter electrode and the working electrode. A schematic representation of the electrochemical cell is shown in Figure 3-19(b).

For potentiodynamic polarisation experiments, a 3-electrode cell configuration was used, similar to that in Figure 3-19(b). The counter electrode was replaced by an inert graphite electrode so that the working electrode can be polarised.

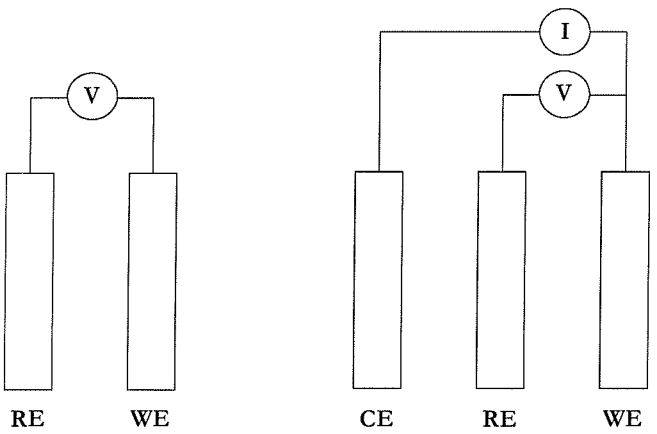

(a) 2 electrode configuration

(b) 3 electrode configuration

Figure 3-19 Schematic diagram of a (a) 2-electrode corrosion cell and (b) a 3-electrode corrosion cell for current measurements.

All specimens were ground and polished to a mirror finish (R_a < 0.01 μm), washed in soap water and degreased in acetone prior to the experiments. 3.5 % NaCl solution was used, under normal atmospheric aeration and ambient room temperatures. After the experiments, the specimens were washed with soapy water and cleaned in acetone. Desiccators were used for drying the specimens prior to further examinations.

For potentiodynamic polarisation experiments, specimens were initially kept in the solution for stabilisation (i.e. 30 minutes). The free corrosion potential of the specimens was monitored and potentiodynamic scanning was started only when variations between E_{corr} measurements were below 2 mV. The scan was initiated at 50 mV below the free corrosion potential, continuing at a rate of 0.2 mVs^{-1} until the specimen was polarised to 400 mV above the free corrosion potential.

For electrochemical noise experiments, specimens were immersed in the solution and data was collected immediately. The sampling rate (F_s) was kept at 2 Hz (2 data points per second). Higher sampling rates are possible but quantisation effects can occur above sampling rates of 200 Hz. Anti-aliasing filtering at 0.5 × F_s was used on the analogue signal before conversion to a digital signal.

3.4.2 Potentiodynamic polarisation results

Figure 3-20 shows the E – *log i* graphs from the potentiodynamic experiments, providing means to rank the materials according to their electrode potentials. The bulk NAB alloy and AB coating are copper-based alloys, hence their corrosion potential is expected to be similar (- 200mV), addition of nickel leads to little improvement in terms of corrosion resistance. The current density for the NAB alloy and AB coating is approximately 3 μAcm^{-2}.

The NAB coating has a more electronegative corrosion potential (- 260 mV). As the coating is heterogeneous and consists of different HVOF powders, the corrosion potential shows an averaged mixed potential between the constituent particles. Current density of the NAB coating was found to be 10 μAcm^{-2}, approximately 3 times higher than that of the AB coating. The NAB alloy, AB and NAB coatings did not exhibit passivation within the scanned potential region.

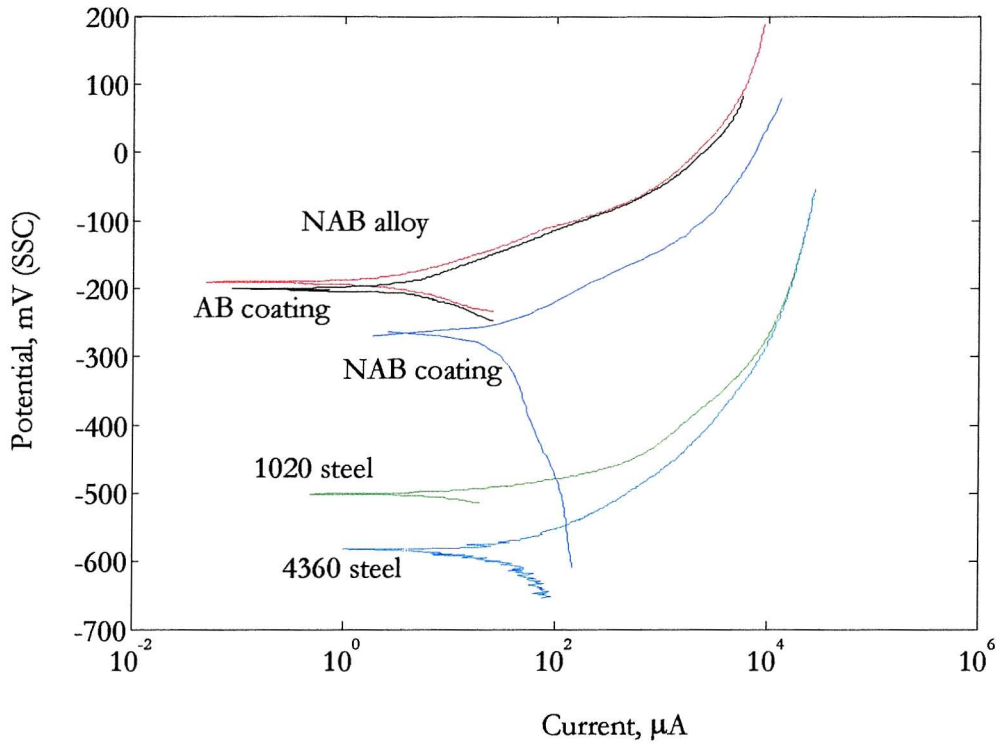

Figure 3-20 Potentiodynamic polarisation (E-logi) graph, showing the free corrosion potential and current of the materials tested. 3.5 % NaCl, 25 °C.

Potentiodymanic polarisation experiments were also carried out on the two carbon steels for comparison with the coatings and the NAB alloy. As expected, passivity was not observed for both materials with uniform dissolution occurring as the potential was stepped towards the electropositive direction. The free corrosion potential for 1020 steel is about - 500 mV and the current density is in the range of 10 μAcm^{-2}. BS 4360 steel is the most active among the materials tested, with the free corrosion potential at - 600 mV and a current density of 15 μAcm^{-2}.

The E_{corr} and i_{corr} values from the graph are tabulated in Table 3-10. It is evident that the copper-based materials have more electropositive potentials (more noble) than the carbon steels. The results indicate that the coatings are cathodic to the carbon steel substrates. Defects in the coating (resulting in the exposure of the substrate) can result in galvanic coupling, causing the substrate to corrode preferentially. Despite being anodic to the coatings, carbon steel substrates were used in this investigation due to their cost effectiveness. In

addition, noise signals resulting from a corroding anodic substrate are more pronounced and easily identifiable.

Table 3-10 E_{corr} *and* i_{corr} *values of the materials under static corrosion conditions, obtained from potentiodynamic polarisation.*

Materials	E_{corr} (mV)	i_{corr} (μAcm^{-2})
Bulk NAB alloy	-200	3
AB coating	-200	3
NAB coating	-260	10
1020 steel	-500	10
BS4360 steel	-600	15

3.4.3 EPN and ECN measurements on 4360 steel

The potential and current noise results are shown in Figure 3-21. Initial instability of the EPN was observed in the first 12 hours. This is probably due to the fresh surface being exposed to the 3.5 % NaCl solution, increasing electrochemical activities resulted in the potential shift towards the electronegative direction, forming corrosion products (iron oxide). Iron oxides are porous and non-adherent to the surface [135], resulting in continuous corrosion of unprotected areas of the surface and potential fluctuations. A potential of about - 740 mV was observed after 3 hours immersion, which is typical for carbon steels [135]. Fluctuations were observed in the first 2 days, between -740 and -760 mV. A stabilised potential was achieved from the fourth day onwards, at about - 760 mV. This potential indicates that both the electrodes have achieved stability/equilibrium in the static 3.5 % NaCl solution. The EPN shows only the corrosion behaviour of the working electrode (i.e. mechanistic information), ECN was measured to determine the corrosion rate of the 4360 steel specimen.

ECN fluctuations were also observed during the first 6 hours, associated with the electrode surfaces acquiring equilibrium in the 3.5 % NaCl solution. The ECN shows the net current oscillating between both electrodes, positive net currents indicate that the working electrode is anodic while a negative net current indicates anodic activity at the counter electrode. During the first 48 hours of experiment, fluctuations in the order of 5 μA was observed, corresponding with those found in EPN measurements. Stabilised corrosion current was achieved after 2 days, the value being approximately - 2 μA.

Current drifts in the positive direction are correlated to electronegative drifts in the EPN. This indicated that when the potential of the working electrode shifts towards the electronegative direction, the surface becomes anodic and current flow increases. This behaviour can be attributed to the non-uniform iron oxide formation, allowing corrosion to occur. It is possible for the surface to have grown a sufficiently uniform layer of iron oxides beyond the second day, stabilising EPN and ECN. The stabilised corrosion current between both the electrodes is about 2 μA.

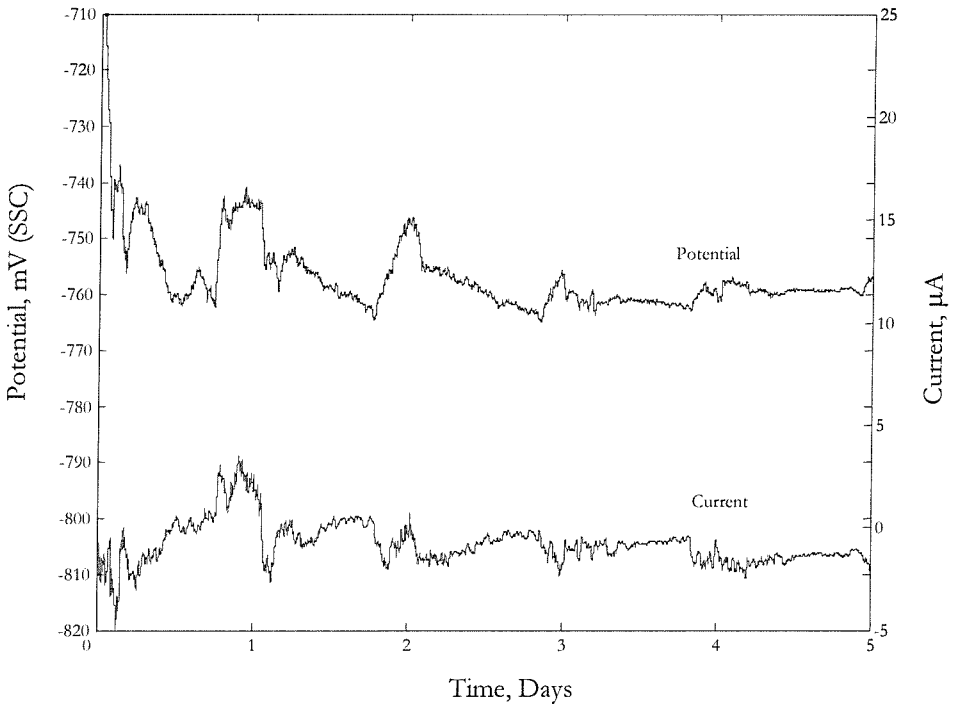

Figure 3-21 EPN and ECN of 4360 steel, static immersion experiment. 3.5% NaCl, 25 °C.

3.4.4 EPN and ECN measurements on NAB alloy substrate

Figure 3-22 shows that the EPN upon immersion was found to be - 260 mV, stabilising to about - 230 mV within the first 12 hours. The drift towards the electropositive direction indicates that a protective film is forming on the electrode surface. Schussler and Exner reported that 800 nm thick protective films are formed on NAB alloys, containing mixed oxides of copper and aluminium [62]. The protective film forms a barrier between the alloys surface and the electrolyte, inhibiting corrosion processes. Potential fluctuations (lasting between 1 and 3 hours) in the electronegative direction are observed, indicating corrosion events such as localised film breakdown or dealloying. Most of the fluctuations are in the

order of 5 mV, a large fluctuation can be observed between day 2 and 3. This type of potential noise is quite typical of materials that undergo localised corrosion, similar noise processes have been reported for metastable pitting of stainless steels [136].

Relatively high levels of fluctuations (0.5 μA) are observed in the first 2 days, possibly due to initial instability when the air formed oxide film is exposed to the electrolyte. The magnitude of the fluctuations became lower (0.2 μA) towards the end of the experiment, due to the formation of a stable protective film on the NAB alloy surface [43,137]. Current fluctuations were nearly 5 times lower than that of BS4360 steel, indicating lower corrosion rates and passivity of the copper based alloy. Correlations were found between the potential fluctuations and the current fluctuations, indicating that localised loss of passivity on the surface corresponds to an increase in the corrosion rate.

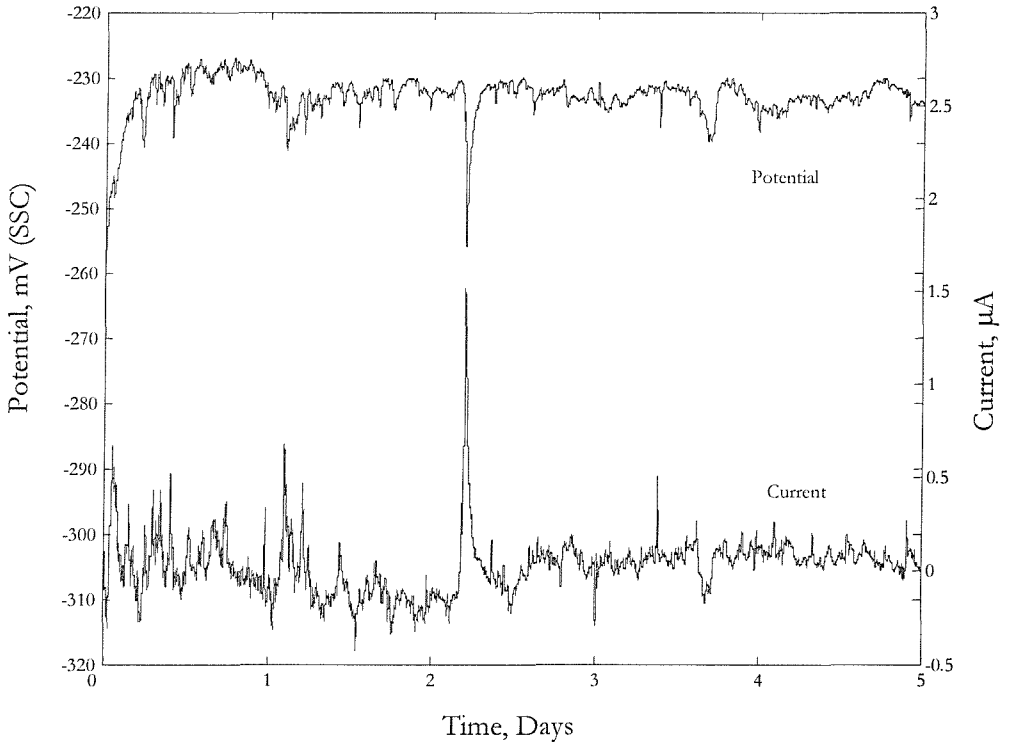

Figure 3-22 EPN and ECN measurements of NAB alloy under static immersion experiment. 3.5% NaCl, 25 °C.

3.4.5 EPN measurement on AB coating

Figure 3-23 shows the EPN measurement for the AB coating, collected over a time period of 5 days in static 3.5% NaCl solution. The open circuit potential immediately upon immersion was around - 215 mV (SSC). The potential of the coating experienced ± 3 mV fluctuations in the first day, with a mean around - 215 mV. A steady drift towards the electronegative direction was observed from the second day onwards, to about - 223 mV. From the third day onwards, sinusoidal potential oscillations superimposed on the electronegative drift were observed. Oscillations were smaller (± 5 mV) between day 2 to day 4, increasing to ± 10 mV on the last day.

Fluctuations in the EPN upon immersion can be associated with the dry coating surface achieving chemical equilibrium in the test solution, involving the formation of corrosion products/films, and ingress of electrolyte into the pores within the coating. Once equilibrium has been achieved, the open circuit potential became more stable (12^{th} hour). Fluctuations in the electronegative direction can be associated with corrosion processes on the coating surface, such as corrosion at the pore openings. The potential of the surface returns to its equilibrium state (- 215 mV) when the insoluble surface film is formed, the film acts as a protective barrier between the coating surface and the electrolyte.

Non-uniform film coverage over the coating surface results from the presence of inclusion and pores within the HVOF AB coating. Localised corrosion can occur at these sites, possibly explaining the potential fluctuations that are observed in the first 24 hours. Visual examination revealed localised corrosion spots on the coating surface. Areas adjacent to the spots showed copper colouration, indicating that dealloying of aluminium has taken place [59,60,138,139].

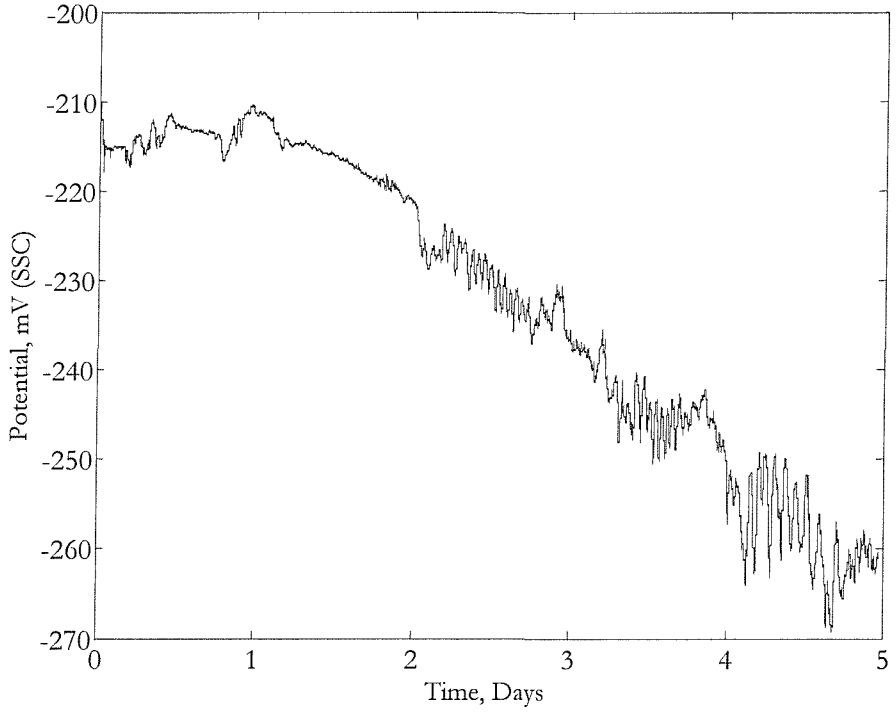

Figure 3-23 EPN measurement of AB coating under static immersion experiment. 3.5% NaCl, 25 °C.

The open circuit potential drifted about 50 mV in the electronegative direction over the 5 day period indicated that the AB coating system became increasingly electrochemically active with time. The permeation of NaCl solution into the coating, through the pore network, can cause an increase in the corrosion rate. Potentiodynamic polarisation (earlier section) showed that carbon steel is anodic to the AB coating. When the electrolyte reaches the coating/substrate interface, galvanic couples are formed between the two materials, resulting in the preferential corrosion of carbon steel.

The E_{corr} of the 1020 steel substrate was - 500 mV while E_{corr} of the AB coating was about - 210 mV, a mixed potential is obtained when both materials are coupled galvanically. Depending on the total area of carbon steel exposed to the 3.5% NaCl solution, mixed potential between carbon steel and the AB coating can vary between - 210 mV to - 500 mV. The potential on the 5th day of the static immersion experiment was shown to be - 260 mV, indicating that galvanic couples are formed between the AB coating and the 1020 steel substrate. The area of carbon steel exposed to the electrolyte is estimated to be relatively small, as the potential shifted only 50 mV in the electronegative direction. This observation

showed that EPN measurements can be used to indicate electrolyte permeation into the coating.

Three distinct regions of potential oscillations are observed from the signals, at the beginning of 48th, 72nd and 96th hours. The amplitude of potential oscillations was shown to increase with time; duration of the oscillations was approximately 90 minutes towards the end of the experiment. Figure 3-24 shows the details of these oscillations, obtained between the 60th and 66th hour in the experiment. Hladky *et al.* [140] suggested that crevice corrosion processes can result in potential oscillations, the severity of corrosion attack was indicated by the amplitudes. Other workers have also shown that crevice corrosion produced potential noise oscillations [115,141].

The corrosion processes occurring at the pores and coating/substrate interface can result the delamination at these areas, providing an environment similar to that of a tight crevice. Coating delamination was confirmed by visual inspection, where localised blisters were found. Due to the electrolyte that is trapped in these areas being stagnant (static immersion), cathodic reactions can result in de-oxygenation and acidification. The more concentrated electrolyte can result in severe localised corrosion at the pores and coating/substrate interface, possibly explaining the potential oscillations.

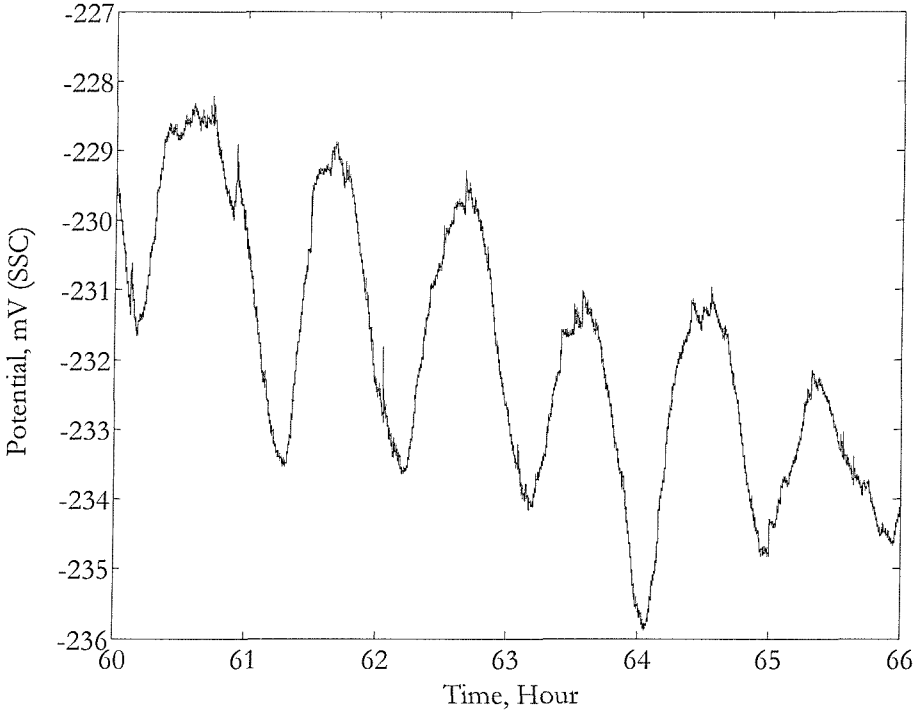

Figure 3-24 Detailed EPN of the AB coating under static immersion, showing potential oscillations between 60th and 66th hours. 3.5% NaCl, 25 °C.

3.4.6 EPN and ECN measurements on NAB coating

The EPN and ECN measurements from the NAB coating, under static immersion, are shown in Figure 3-25. EPN of the NAB coating stabilised very quickly to about - 250 mV within the first 12 hours. Fluctuations in the order of 3 mV were observed in the first 6 hours, this can be associated with the formation of a protective film on the coating surface during immersion [62]. Potential steps towards the electronegative direction were observed, at approximately every 24 hours. This is possibly due to the progression of the electrolyte into the coating pores. A large step was recorded on the 3rd day, with a magnitude of 15 mV. The potential continued to drift towards the electronegative direction until the end of the 5th day, reaching nearly - 310 mV. An overall potential drop of 60 mV was observed in 5 days. The observation indicates that the electrolyte has reached the coating/substrate interface. Corrosion of substrate resulted in a mixed potential between the coating and the substrate.

Within 3 days, small fluctuations in the ECN (up to 0.8 μA) were observed. Short term (metastable) fluctuations in the first 12 hours could be due to initial conditions, where localised flaws on the protective film resulted in spontaneous oxidation. Long term fluctuations (> 1 hour) can be associated with individual corrosion events such as pore corrosion and galvanic corrosion between the heterogeneous coating particles. From the third day onwards, current steps towards the positive direction were observed; these steps corresponded to the potential steps in the electronegative direction. The increase in ECN and decrease in EPN indicates an increase in corrosion rate of the NAB coating. Similar to the AB coating, the EPN showed events such as electrolyte permeation through the pores, into the coating/substrate interface. The potential moved towards a mixed galvanic potential as the amount of steel surface exposed to the electrolyte increases.

High frequency fluctuations were observed on the EPN, up to about 1 μA at the 5th day. The ECN at this stage became similar to that observed previously in the 4360 steel specimens (Section 3.4.3), indicating that steel substrate corrosion occurred. In order to confirm the mechanism of electrolyte permeation through the coating pores, an additional NAB coating specimen was immersed in the 3.5 % NaCl solution for 5 weeks. At the end of the experiment, the coating was sectioned and examined under the scanning electron microscope, shown in Figure 3-26. Severe corrosion at the coating/substrate interface has resulted in delamination in these regions, proving that electrolyte ingress through the pore network has occurred. Corrosion was also found within the coating, causing the disbondment of coating splats. The disbondment of coating splats appears to occur preferentially along unmelted coating particles. Poorly melted particles during the HVOF process can result in an increase of porosity level, due to lack of interlocking between the splats [134]. The porosity will allow the electrolyte to permeate the coating; increasing electrolyte concentration (due to de-aeration) will result in higher corrosion rates [142].

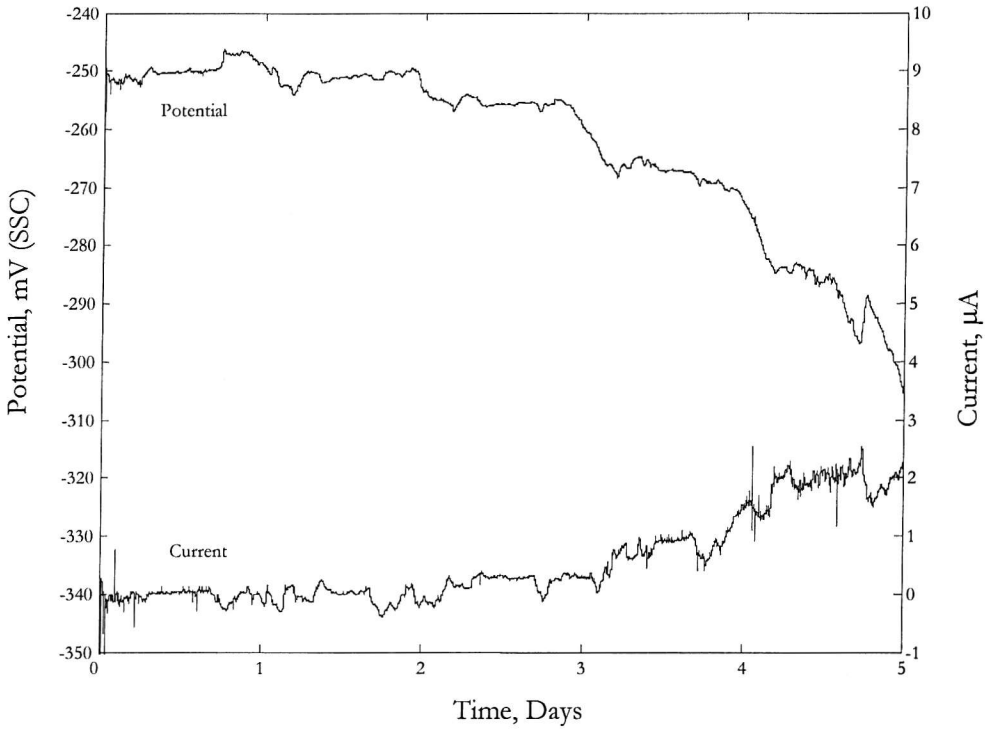

Figure 3-25 *EPN and ECN measurements of NAB coating under static immersion experiment. 3.5% NaCl, 25 °C.*

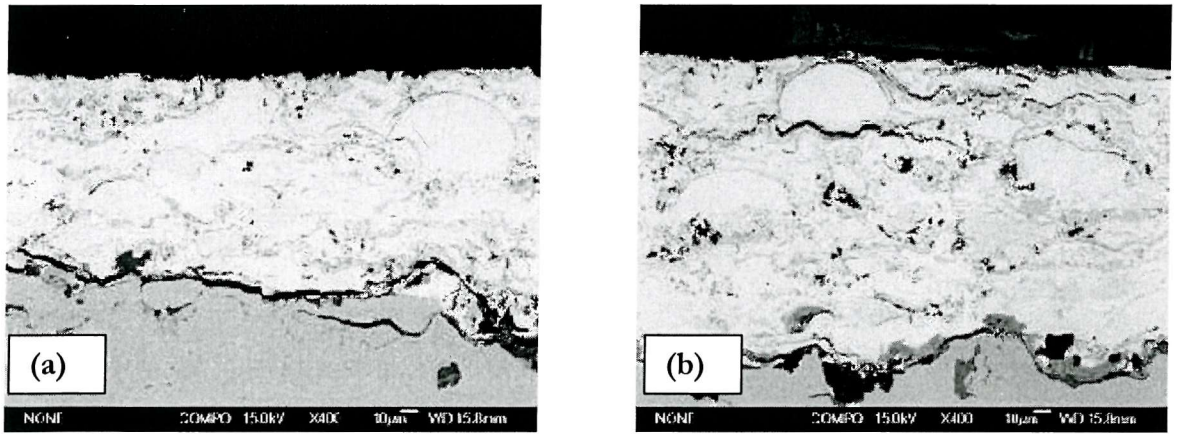

Figure 3-26 *SEM micrographs showing the transverse section of the NAB coating after 5 weeks of static immersion. 3.5% NaCl, 25 °C. The micrograph showed corrosion at (a) the coating / substrate interface and (b) at the pore network.*

3.4.7 Materials behaviour based on ENM

Electrochemical noise measurements showed that the EPN can be used to provide certain mechanistic information on the corrosion behaviour of the specimens. EPN signals for the AB and NAB coatings are different from the NAB substrate, both coatings showed potential drifts towards the electronegative direction. This phenomenon is probably caused by the HVOF coatings being inhomogeneous (consisting of splats) and porous, resulting in electrolyte permeation and corrosion at the coating/substrate substrate. All the copper based materials, including the AB and NAB coatings, revealed EPN noise signals that are different from that of the steel substrate. The EPN of the steel substrate contained higher amounts of high frequency fluctuations. This can be due to the different corrosion processes between the two types of materials: steel corrodes in a uniform manner while the passivating copper alloys undergo localised corrosion.

The AB coating was shown to be more susceptible to electrolyte permeation, the potential drifted in the electronegative direction from the second day onwards. Similar processes occurred to the NAB coating from the 3rd day onwards. The NAB coating consists of AB, stainless steel and NiAl particles, it is possible for the stainless steel particles or NiAl particles to form insoluble corrosion products within the pores, delaying electrolyte permeation. Given time, de-aeration of the electrolyte will cause an increase in acidity and accelerate the corrosion of the pore network, resulting in the substrate being exposed to the electrolyte. Differences in particles chemical composition can also result in galvanic coupling and accelerated corrosion of the more active AB particles in the NAB coating.

In order to compliment the mechanistic information obtained by EPN measurements, the corrosion rate of the materials being tested was determined by using ECN measurements. The 4360 steel was shown to have a higher corrosion current (about 2 μAcm^{-2}) than the bulk NAB alloy (0.1 μAcm^{-2}). This is probably due to the NAB alloy being able to generate a protective film on its surface, reducing the dissolution rate. ECN measurements on the NAB coating revealed low corrosion rates in the first 3 days (0.1 μAcm^{-2}), increasing to 2 μAcm^{-2} from the third day onwards. The increase in corrosion current indicated that electrolyte have permeated the coating and corrosion of the steel substrate occurred.

3.4.8 Comparison between ENM and potentiodynamic polarisation results

Table 3-11 shows the comparison of potential and current values, obtained by means of potential dynamic and ENM techniques. Open circuit potential (OCP) values are shown to be similar between the two methods, confirming that the ENM method is useful for monitoring the corrosion potential. Differences in the potential values are probably caused by the 3-electrode cell configuration in the ENM measurements, it is possible for the 'nominally identical' counter electrode to actually polarise the working electrode. Current density from the potential dynamic polarisation technique was shown to be higher than that obtained from the ENM method. The first method involved current measurements by exciting the electrochemical activities on the electrodes; while the latter was carried out without perturbation to the corroding system. It is possible for the working electrodes to be polarised by the graphite counter electrode during potential dynamic polarisation scans.

The electrochemical noise measurements can be a more useful tool for monitoring the corrosion behaviour of the materials over time, possible events such as electrolyte permeation, pore corrosion and localised loss of passivity can be detected. This is especially useful for monitoring corrosion behaviour of coatings where the mechanisms are usually more complex than those of bulk materials. By combining the results obtained from both techniques, material rankings based on its corrosion resistance can be obtained. Steel is the least corrosion resistant, followed by NAB coating and AB coating, while the bulk NAB alloy is the most corrosion resistant among the materials tested.

Table 3-11 Potentiodynamic Polarisation

Materials	Potentiodynamic polarisation		ENM	
	E_{corr} (mV)	I_{corr} (μAcm^{-2})	E_{corr} (mV)	I_{corr} (μAcm^{-2})
Bulk NAB alloy	-200	3	-230	0.1
AB coating	-200	3	-215	N/A
NAB coating	-260	10	-250	0.1 – 2
1020 steel	-500	10	N/A	N/A
BS4360 steel	-600	15	-760	2

3.5 Corrosion mechanisms of the HVOF AB and NAB coatings

Based on the EPN and ECN measurements, a few corrosion mechanisms of the AB and NAB coatings are suggested and illustrated in Figure 3-27. Immediately upon immersion into the 3.5 % NaCl solution, (a) oxidation of the coating surface occurs, resulting in the growth of a protective film. The formation of the protective film resulted in potential and current fluctuations within the first 3 hours of immersion. Flaws in the protective film surface, such as pore openings and localised impurities in the HVOF coating, can result in localised corrosion and permeation of electrolyte into the pore network.

The electrolyte that is trapped within the pores will be de-aerated, leading to increased acidity and (b) corrosion at the pores. The aggressive electrolyte will also result in corrosion at the pore openings, leading to the dissolution of AB coating matrix and re-deposition of copper on its surface. This type of corrosion will probably cause the EPN fluctuations, lasting between one and three hours. Extensive corrosion at the pore network will can cause the disbondment of coating splats, seen previously in Figure 3-26.

Some of the pore network may be connected between the coating surface and the steel substrate, leading to (c) corrosion at the coating/substrate interface. Corrosion at the interface will result in galvanic coupling between the coating and the steel substrate, causing potential drifts to the electronegative direction and a corresponding increase in current. Severe corrosion at the interface can also cause the delamination and subsequent failure of the coating.

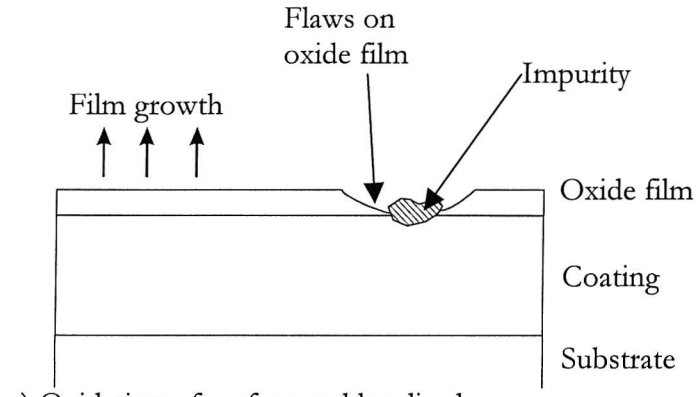

a) Oxidation of surface and localised corrosion at impurity sites

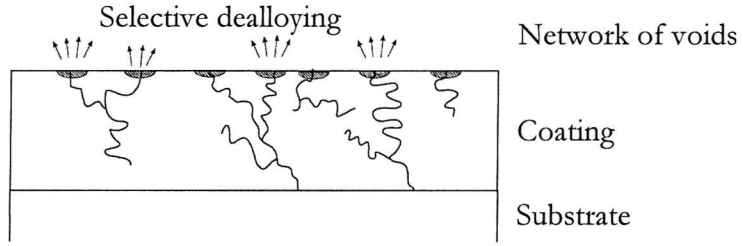

b) Electrolyte ingress into voids and selective dealloying of aluminium

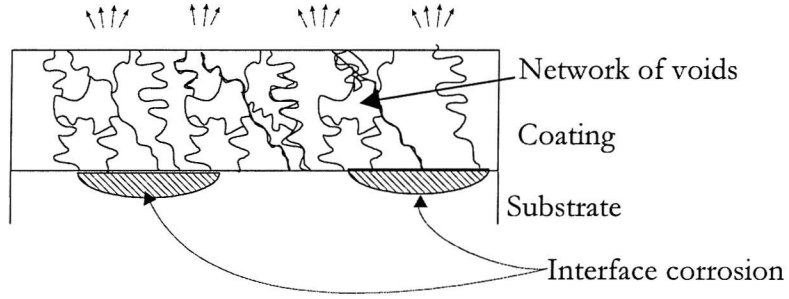

c) Permeation of coating by electrolyte and interface dissolution of substrate material

Figure 3-27 Corrosion mechanisms of the HVOF AB and NAB coatings

3.6 Conclusion

The AB and NAB HVOF coatings have been characterised by microscopy, EDX, microhardness and porosity measurements and finally static immersion tests. This allowed the determination of coating microstructure and its interaction with the corrosion behaviour. The following conclusions can be drawn:

Microscopy revealed that the AB coating consists of homogeneous AB particles in an α-rich phase. Splat boundaries were found to consist of oxides that were formed during spraying. Impurity (oxides and grit) were also observed within the coating microstructure. The NAB coating revealed a heterogeneous microstructure, consisting of different alloy particles. Similarly, impurities that were observed in the AB coating was also found in the NAB coating.

Microhardness indentations showed that the hardness of the AB and NAB coatings are similar. More scatter was observed in the NAB coating hardness profile, due to differences in the individual coating particle (different alloying composition).

Porosity of the AB and NAB coatings were found to be 1 % and 2 % respectively. Higher porosity in the NAB coating is attributed to variations in spraying conditions (stand-off distance) and coating powders of different chemical composition (melting point).

Corrosion resistance ranking of the substrate materials and both HVOF coatings was achieved by potentiodynamic polarisation tests. The steel substrate was found to be most active, followed by the HVOF coatings. The bulk NAB alloy was the most corrosion resistant (noble).

ENM measurements provided means to identify the corrosion behaviour of the materials. Random EPN fluctuations from the steel substrate indicated uniform corrosion processes while transients in the electronegative direction for the bulk NAB alloy indicate localised loss of passivity. Both AB and NAB coatings show gradual EPN drifts in the electronegative direction after 2 days of immersion. The gradual drift indicates that permeation of the

electrolyte into the coating/substrate interface has occurred, resulting in corrosion of the steel substrate.

Current findings confirmed that pores within the HVOF coating are detrimental towards its corrosion resistance. A network of pores between the coating surface and the coating/substrate interface can result in permeation of electrolyte, increased acidity and corrosion at the pore network and coating/substrate interface.

Chapter 4 Erosion

4.1 Introduction

This section explains the work carried out to elucidate the erosion properties of the AB and NAB coatings. The tests were carried out using slurry jet impingement rigs. Erosion properties of the coatings are also compared to that of carbon steel substrates. Results obtained indicate that ductile erosion mechanisms resulted in coatings damage/removal. The AB coating was found to have a lower erosion rate than the NAB coating, while carbon steel substrates show the highest erosion rate.

4.2 Experimental methodology

The current objective is to obtain the erosion rate of the HVOF AB and NAB coatings, at a range of kinetic energy (0.02 to 0.8 μJ). Two types of jet impingement rigs are used to achieve this, the high kinetic energy rig was used for experiments between 0.1 to 0.8 μJ while the low kinetic energy rig provided a range between 0.02 to 0.4 μJ. Specimen surface area was kept at 900 mm^2 and surfaces were lapped to R_a < 1μm prior to the tests.

The high kinetic energy jet impingement apparatus (Figure 4-1) consists essentially of a 10-litre tank in a small pipe loop around which slurry is circulated. The tank acts as a reservoir for the slurry and also locates the test specimen in place in front of the returning flow stream. On re-entering the reservoir, slurry passes through a hardened, stainless steel nozzle and is formed into a jet, seen in Figure 4-7. Circulation is effected by a variable speed Mono Pump controlled by a frequency inverter and flow rate logged by an electromagnetic flowmeter attached to a chart recorder. Pressure in the delivery line is monitored by a pressure gauge while the reservoir is maintained at atmospheric pressure. Jet velocities are determined by the flow rate of the slurry and the diameter of the nozzle:

$$v = \frac{4Q_m}{\pi D^2}$$ *Equation 4-1*

Where v is the jet velocity (ms^{-1}), Q_m the mass flow rate (kgs^{-1}) and D the diameter of the jet nozzle (mm).

Velocities thus determined indicate that the potential energy of slurry in the delivery line is almost completely converted into kinetic energy. Flow rates in the range of 0.3 to 1.0 kgs^{-1}, combined with nozzle diameters of 6, 8 and 10 mm, yield jet velocities of between 4 and 22 ms^{-1} and impact kinetic energies between 0.1 and 0.8 μJ. Specimens were held in front of the jet at a stand off distance of 37 mm, the jet angle can be adjusted to 30°, 60° and 90°. The slurry temperature was monitored and found to be between 20 and 30 °C during the tests. The experiments have been undertaken with Southampton tap water, test duration were kept at 60 minutes to prevent coating perforation. Before and after each test, specimens were washed in water and degreased with acetone, dried in a jet of cold air and then weighed by a precision balance with an accuracy of ± 0.02 mg to obtain mass loss results. Further details of this jet impingement apparatus can be found in previous work by Wood [34].

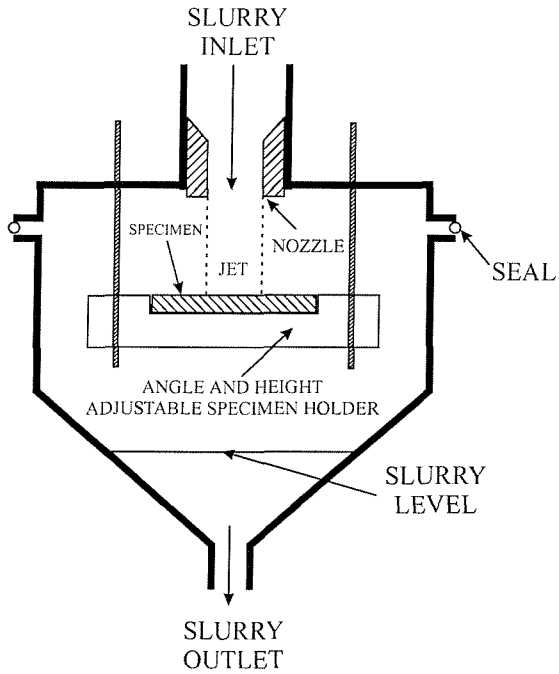

Figure 4-1 The erosion test chamber where the test specimen is located.

A jet impingement apparatus based on that of Zu *et al.* [143] was used to carry out the low kinetic energy experiments. Improvements have been made by Puget [83,85] in that it contains no metallic parts other than the test electrode. A schematic diagram of the rig can be seen in Figure 2-11 of the literature review and information related to its design and

construction can be obtained from Appendix A. For comparison with flow corrosion and erosion-corrosion tests, a 3.5 % NaCl solution was used in all the experiments. As seen in Figure 4-2, the test solution is pumped from a 100 litre reservoir through an assembly consisting of both reference and counter electrodes. The solution then passes through an ejector where sand particles are picked up by a flexible hose, from a bucket situated below. The slurry that formed from this process is then projected onto the specimen surface (working electrode). The counter and reference electrodes are placed upstream so that they are not damaged by the sand particles from the ejector assembly. The different ejector diameters (3 to 3.5 mm) provided flow rates between 6.3 to 9 $kgmin^{-1}$, and nozzle diameters (5 to 5.5 mm) provided velocities between 3.1 and 6.7 ms^{-1}. A valve located at the flexible hose (near the sand bucket) permitted the sand concentration to be varied between 1.5 and 5 % w/w.

The reference electrode is a commercially available single junction Ag/AgCl (SSC) electrode, similar to that used in the static immersion experiments (see Section 3.4.1). The working electrode is enclosed in a hermetically sealed specimen holder to prevent the solution from seeping in. Electrical connection was made possible via a wire soldered to the back of the specimen surface. The stand off distance between jet nozzle and specimen surface was set at 37 mm and the angle of impingement was fixed at 90°. The jet and the specimen holder are enclosed in a perspex container in order that the used slurries could flow back into the sand reservoir. The pure erosion experiment was carried out with the working electrode being cathodically protected at - 200 mV with respect to the E_{corr} (obtained under erosion-corrosion conditions). The erosion rates were subsequently used for evaluation of synergy under erosion-corrosion conditions.

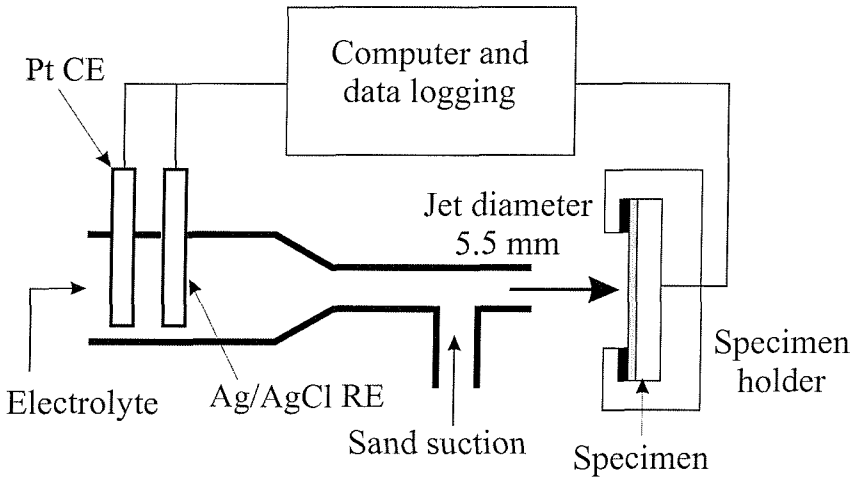

Figure 4-2 The data collection section of the jet impingement rig used for erosion-corrosion experiments.

Full summaries of the experimental conditions and comparison between the jet impingement rigs are listed in Table 4-1.

Table 4-1 Conditions used for the erosion experiments.

		High kinetic energy rig	**Low kinetic energy rig**
Sand:	Type:	Redhill 110	Redhill 110 and 50
	Diameters:	115 μm and 135 μm (sieved)	135 μm and 235 μm (mean diameter)
	Concentration:	2.1 % w/w	1.5, 3.0 and 5.0 % w/w
Liquid medium:	Type:	Southampton tap water	3.5 % NaCl with CP
	Flow rate:	12.5 – 35.0 kg min^{-1}	6.3 – 9.0 kg min^{-1}
	Velocity:	7.6 – 21.3 ms^{-1}	3.1 – 6.7 ms^{-1}
Specimen:	Angle:	30°, 60° and 90°	90°
	Surface Ra:	0.01 μm	0.01 μm
	Size:	50 × 50 × 7 mm	40 × 40 × 5 mm
Impact kinetic energy:		0.1 – 0.8 μJ	0.02 – 0.4 μJ

Gravimetric mass loss measurements were carried out for evaluating the erosion rate. To gain understanding on the erosion mechanism, the erosion scars have been characterised using a Rank Taylor Hobson Form Talysurf model 120L (fitted with a 2 μm radius diamond tip) and the JEOL 6500F SEM.

4.2.1 Relationship between kinetic energy and erosion rate

For the erosion experiments, sand particle kinetic energy (E_k) was calculated using Equation 4-2:

$$E_k = 0.5\, mv^2 \qquad \textit{Equation 4-2}$$

where m and v are the mean particle mass and velocity. The mean particle velocity within the slurry jet is assumed to be similar to the jet velocity.

From Equation 4-2, sand particle kinetic energy (E_k) is dependent on the jet velocity and sand particle diameter.

$$E_k \propto d^3 v^2 \qquad \textit{Equation 4-3}$$

where v is the jet velocity and d is the sand particle diameter.

The erosion rate (V_n) is related to the kinetic energy by:

$$V_n \propto (E_k)^l \qquad \textit{Equation 4-4}$$

Hence by substituting Equation 4-3 into Equation 4-4:

$$V_n \propto d^m v^n \qquad \textit{Equation 4-5}$$

where l is the kinetic energy exponent, m is the diameter exponent ($3 \times l$) and n is the velocity exponent ($2 \times l$).

4.3 Results and discussion

4.3.1 Effects of particle velocity and particle diameter

Table 4-2 shows the mass loss and erosion rate data of the aluminium bronze coating under slurry erosion conditions at different kinetic energies. Measurement of impact scar volume were also being made and compared with the calculated erosion rate. The impact scar volume analysis will be discussed later in Section 4.4.2. Erosion rates of the aluminium bronze are expressed as volume loss per impact (V_u) to allow for sand size variations at a given volume fraction:

$$V_u = \frac{M\pi d^3}{6\rho Q_v t C_v} \qquad \textit{Equation 4-6}$$

where M is the mass loss, d is the mean sand diameter, ρ is the coating density (7.6 gcm^{-3}), Q_v is the slurry volume flow rate, C_v is the volume fraction of sand (0.02) and t is the test duration (3600 s). It was assumed that all particles impact the specimen surface.

Table 4-2 Relationship between kinetic energy and erosion rate for the HVOF aluminium bronze coating.

Kinetic energy, E_k (μJ)	Jet velocity (ms^{-1})	Sieved sand diameter (μm)	Mass loss (g)	Erosion rate, V_u (μm^3/impact)	Impact scar volumes (μm^3)		Volume ratio, V_u/V_{scar}	
					Small scar	Large scar	Small scar	Large scar
0.1	7.6	135	0.004	0.1	-	-	-	-
0.3	16.5	115	0.074	0.6	2.4	15.4	0.3	0.04
0.5	16.5	135	0.079	1.1	2.9	15.7	0.4	0.1
0.8	21.3	135	0.211	2.2	2.5	17.3	0.9	0.1

As shown in Table 4-2 and Figure 4-3, the erosion rate of the AB coating increases with kinetic energy. For comparison, results from 1020 steel were also plotted. From the slopes obtained in Figure 4-3, the kinetic energy exponent (l) for the AB coating is 1.5, indicating that m=4.5 and n=3.0. For the 1020 steel, l = 1.2 indicates m=3.6 and n=2.4. For both materials, the velocity exponents are greater than two, indicating that the erosion rate is not simply a function of kinetic energy dissipation [12]. This phenomenon can be attributed to either one or more of the following factors: sand particle rotation during impact [144], coefficient of friction during contact, and interactions with other particles after rebounding

from an impact [16]. The retardation of particle impact by the squeeze film on the target surface may also affect the velocity exponent [145].

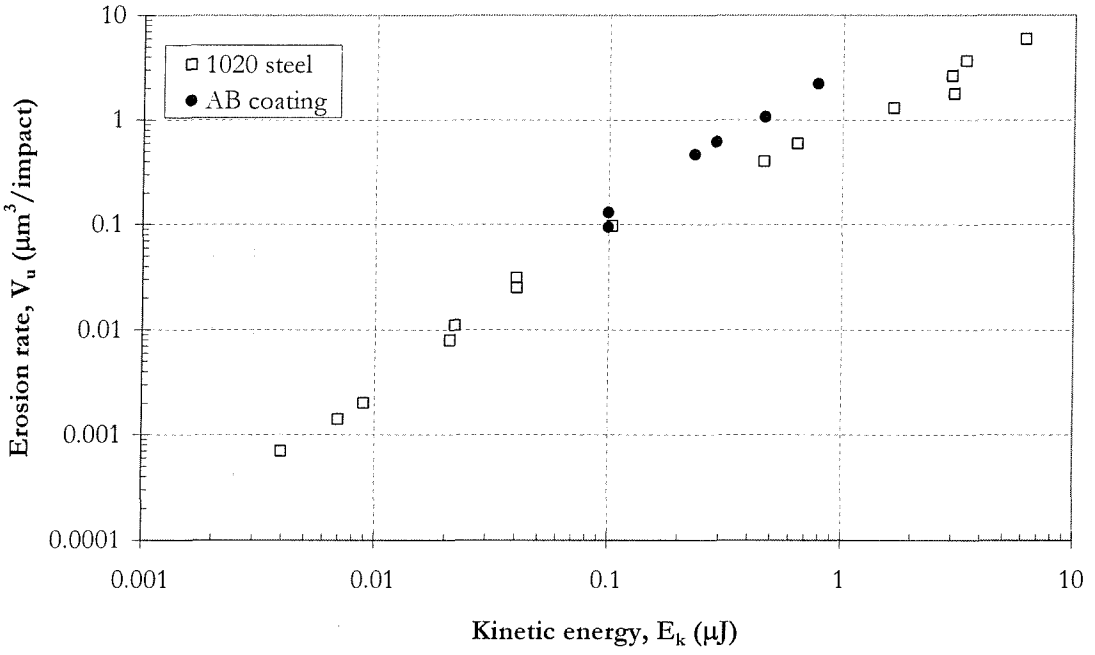

Figure 4-3 *Graph showing the relationship between kinetic energy and the erosion rate for the aluminium bronze coating and AISI 1020 steel (Tap water, 2.1 % w/w silica sand concentration, 90° jet impingement, ambient room temperature ~ 20° C).*

The erosion rates of the NAB coating and 4360 steel substrate, obtained from low kinetic energy jet impingement, have been plotted against kinetic energy in Figure 4-4. Results obtained from AB coating in the high kinetic energy impingement were also plotted to compare erosion performance between the two coating materials. The carbon steel was shown to have the highest erosion rate over the range of kinetic energies (0.01 to 1 μJ), its erosion rate is up to 4 times that of the NAB coating in the low kinetic energy region. This is possibly due to the NAB coating being a harder material. However, the erosion rate between the steel substrate and the NAB coating appears to converge at higher kinetic energies (0.4 μJ), possibly due to the erosion behaviour of the NAB coating being influenced by cracking of splat boundary oxides at these kinetic energies.

The AB coating was shown to have the lowest erosion rate among the materials. The difference in erosion rate between the coatings is possibly due to the AB coating having a

homogeneous microstructure while the heterogeneous NAB coating consists of particles of different alloys with different mechanical properties, as shown in Section 3.3.2 (Chapter 3). However, the similarities in velocity exponent indicate ductile wear mechanisms with respect to velocity for both coatings. The higher percentage of porosity within the NAB coating could also contribute to an increased wear rate. Pores were usually made up of oxides that are formed during spraying and were found to be stress raisers under sand particle impingement [89,146,147].

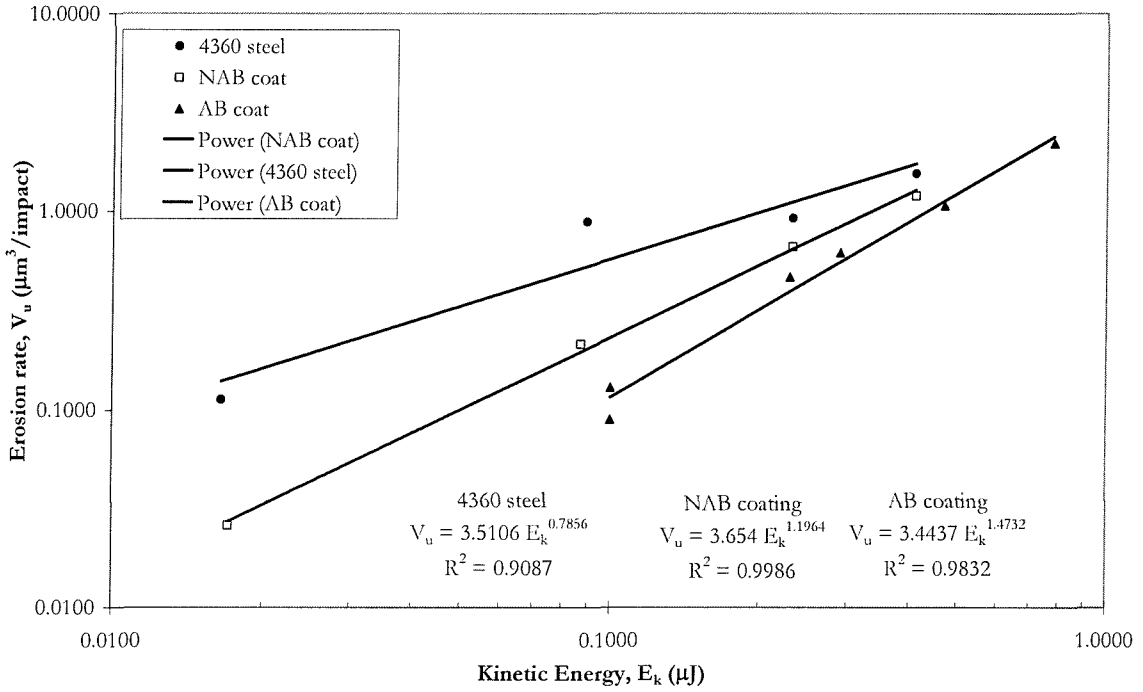

Figure 4-4 Relationship between erosion rate and kinetic energy for 4360 steel, AB coating and NAB coating.

Kinetic energy exponents are obtained graphically from Figure 4-4. They are subsequently converted into velocity exponents (n) by using Equations 4-3 to 4-5. Table 4-3 compares the n values between current test materials and some other bulk materials and HVOF coatings found in the literature. The velocity exponent of the NAB coating is approximately 2.4 and n = 1.6 for the 4360 steel. The n value for the NAB and AB coatings are shown to be within the range obtained by other HVOF coatings, it is also comparable to typically ductile materials like carbon steels and stainless steels [86,146,148].

Table 4-3 Comparison of the velocity exponent between current work and those found in the literature.

Materials	Reference	Velocity exponent, (n)
NAB coating	Current work	2.4
4360 steel		1.6
1020 steel	Current work	2.4
AB coating		3.0
Duplex stainless steel, bulk (UNS S31803)	[86]	2.1
HVOF WC-Co based coating		1.3
HVOF NiAl intermetallic coating	[146]	2.4~2.7

4.3.2 Effects of impingement angle

Results from slurry erosion of the AB coating at different impingement angles are given in Table 4-4. Impingement angles were set at 30°, 60°, and 90°, with the kinetic energy fixed at 0.5 μJ. The data shows that the erosion rate decreases with decreasing impingement angles, contrary to that found in the work carried out by Lin and Shao [26]. However, this trend in erosion rate has been observed by Tilly [149] and Hearley [146] in their air-sand erosion tests. Tilly [149] suggested that abrasive particles can shatter upon impact at 90° impingement, causing the resulting smaller particles to abrade the surface as they move with the slurry streamline (secondary stage erosion mechanism). However, the experiments used a minimum jet velocity of 140 ms^{-1}, thus the sand particle impacts at high kinetic energy (E_k = 270 μJ). The present work utilised a much lower kinetic energy, with a maximum velocity of 21.3 ms^{-1}, it is therefore unlikely that the silica sand particles fracture upon impact.

Table 4-4 Relationship between impingement angle and erosion rate at 0.5 μJ kinetic energy (16.5 ms^{-1} velocity, 135 μm mean diameter silica sand).

Impingement angle	Mass loss (g)	Erosion rate, V_n (μm^3/impact)
90°	0.08	1.1
60°	0.07	0.9
30°	0.05	0.7

An alternative explanation may be given by considering that a brittle erosion mechanism dominates the mass loss [19]. As brittle mechanism is dominated by particle impinging at 90°, it is related to the velocity component that is normal to the specimen surface (v_n). Theoretical and experimental mass loss measurements against v_n are plotted in Figure 4-5. It is clear that

as the impingement angle is decreased, v_n values become smaller and deformation wear becomes less dominant. The higher experimental mass loss at 30° impingement also reveals the dominance of microcutting at low impingement angles.

As shown by EDX analysis in Section 3.3, the splat boundaries consists of Al_2O_3, forming brittle vanes within a ductile matrix. If cracking occurs under particle impingement, it is most likely to occur at the brittle vanes. Cracks parallel to the interface (horizontal) may be formed under high shear stress conditions. The inter-linking of the cracks then leads to individual splats being removed from the coating surface [150], leading to higher material loss at a normal impingement angle. Cracking of splat boundaries will be discussed further in the microscopy section.

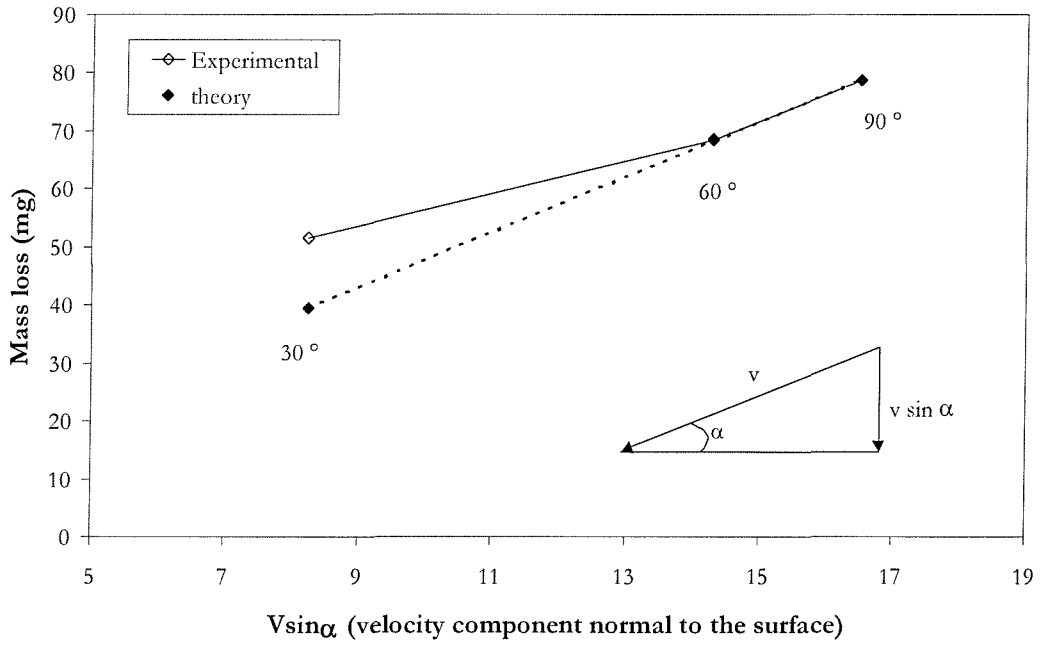

Figure 4-5 *Comparison between theoretical and experimental mass loss measurements against velocity normal to the specimen surface.*

4.3.3 Effects of sand concentration

Mass loss results were also converted into erosion efficiency (η) to investigate the effects of sand concentration on the erosion rate of the NAB coating:

$$\eta = \frac{W}{C} \quad (mg) \qquad \textit{Equation 4-7}$$

where W is the mass loss (mg) and C is the sand concentration (% w/w).

Figure 4-6 shows the relationship between erosion efficiency and sand particle concentration. The results are also compared with that obtained by Turrenne *et al* [24], where erosion experiments have been carried out on aluminium at higher jet velocities (17 ms^{-1}), resulting in higher erosion efficiencies when compared to the NAB coating. The erosion efficiency from the current work was shown to increase as the sand concentration was reduced, showing similar trends obtained by Turenne. It was shown that for sand concentrations greater than 10 % w/w, the erosion efficiency remained constantly low, due to the screening effect of a particle cloud caused by high sand concentrations and increased particle-particle interactions.

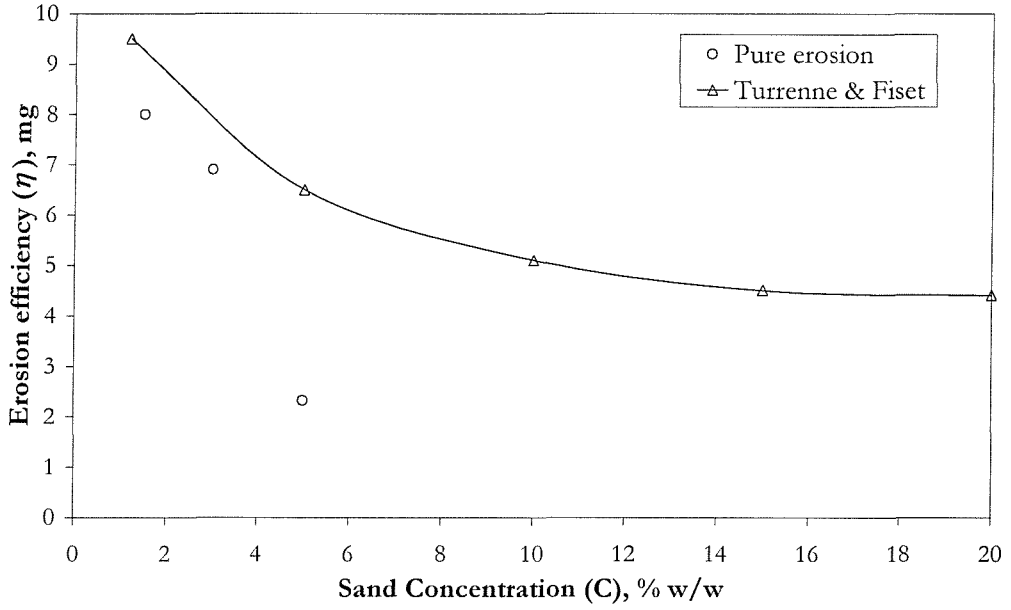

Figure 4-6 Erosion efficiency of the NAB coating versus sand concentration, compared with results obtained by Turenne et al. [24].

4.3.4 Comparison of erosion rate with other materials

Figure 4-7 shows a chart comparing the erosion rates of the AB coating with a number of monolithic materials that are commonly used in the marine industry. The data was acquired from slurry erosion tests, using 0.5 μJ kinetic energy at 90° impingement angle on specimens with similar surface roughness. It can be seen that the erosion rate of the AB coating (1.07 μm^3/impact) is nearly twice that of bulk AISI 316 (0.57 μm^3/impact) and Marinel (0.69 μm^3/impact). However, the 90-10 cupro-nickel alloy (C70600) has a slightly higher erosion rate (1.20 μm^3/impact) when compared to the AB coating. As the error introduced in calculating the mass loss (erosion rate) is large (± 10%); the data should be treated carefully.

The erosion rates were also compared to other HVOF coatings under similar kinetic energy conditions (0.1 μJ), it was 40 times lower than the HVOF AISI 316L coating (4.2 μm^3/impact) [3] and about 5 times higher than that of HVOF tungsten carbide coatings (0.02 μm^3/impact) [150].

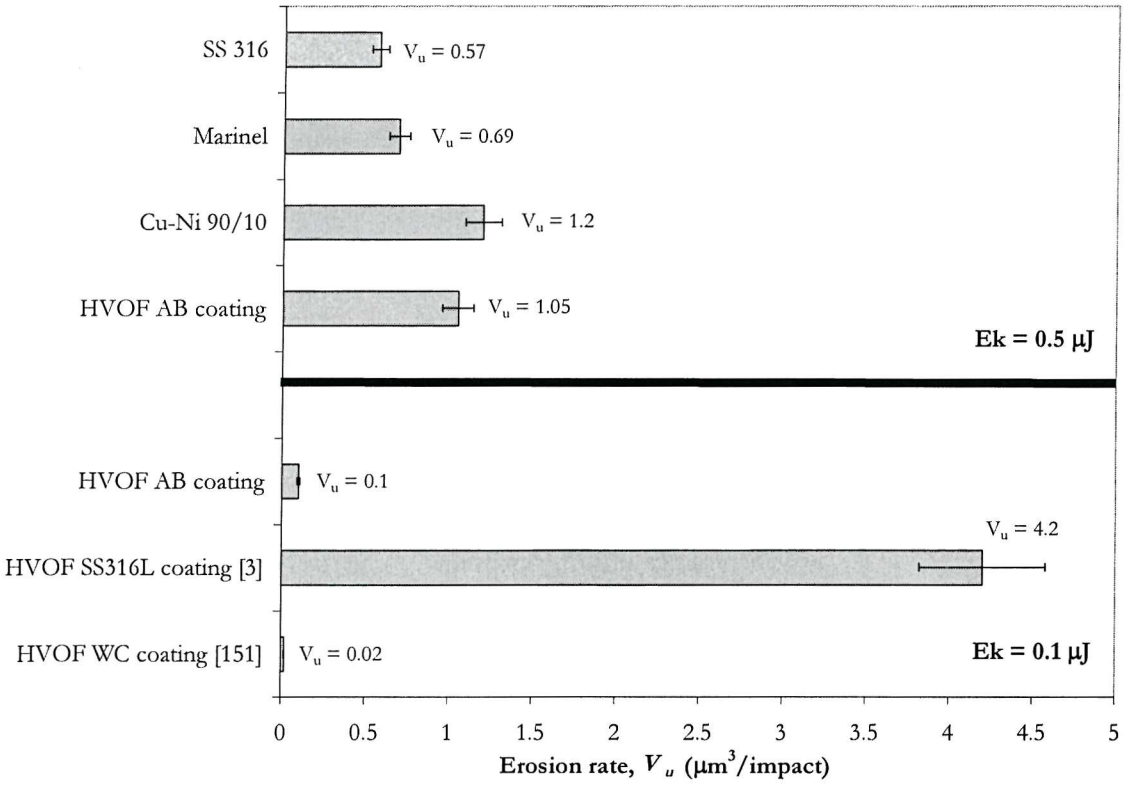

Figure 4-7 Comparison chart between the erosion rate of the aluminium bronze coating and other materials (0.5 μJ and 0.1 μJ kinetic energy at 90° impingement). [3,150]

4.3.5 The dimensional analysis of erosion

Zhang *et al.* [151] analysed the air-solid erosion behaviour of AISI 1015 carbon steel using a dimensional analysis approach. Their erosion rate was expressed as a dimensionless mass loss (mass loss, ξ per unit mass of erodent) and compared it with a dimensionless factor. The dimensionless factor, see Equation 4-8, incorporates parameters such as particle concentration (C_v), particle density ($\rho_{particle}$), mean particle diameter (d), target material hardness (H), jet velocity (v), test duration (t) and impingement angle (α).

$$\frac{\xi}{\rho_{particle}\, d^3} \propto \left(\frac{C_v}{\rho_{particle}}\right)^x \left(\frac{d}{t\sqrt{H/\rho_{particle}}}\right)^y \left(\frac{v}{\sqrt{H/\rho_{particle}}}\right)^z \left(\sum_i^k q_i \alpha^i\right) \qquad \textit{Equation 4-8}$$

where q_i ($i = 1,\ldots,k$) are constants that were determined by a multivariable regression method. The diameter and velocity exponents y and z from the dimensional analysis are analogous to m and n values in Equation 4-5.

Results from the current work including those from tests which varied the impingement angle were analysed using this approach and are shown in Figure 4-8. The dimensionless factors were calculated based on the exponent values obtained from the reference ($x = 1, y = -1, z = 2$) [151]. The graph revealed clear trends with similar slopes, but did not appear to collapse onto a common trend. This can be explained by the following:

1. The difference in the carrying medium (air-solid and liquid-solid) can greatly affect the erosion properties. Actual impact velocities and angles are different between the two systems, due to the viscosity of the fluid, density of eroding particles and the existence of a squeeze film under slurry erosion.
2. The softer ash particles used by Zhang can shatter upon impact, possibly resulting in changes in the erosion mechanisms (particle interactions and abrasion on the surface).

However, Zhang cautioned that the diameter and velocity exponents are sensitive to erosion conditions such as target materials and erodent properties (i.e. it cannot be generally applied to differing erosion systems).

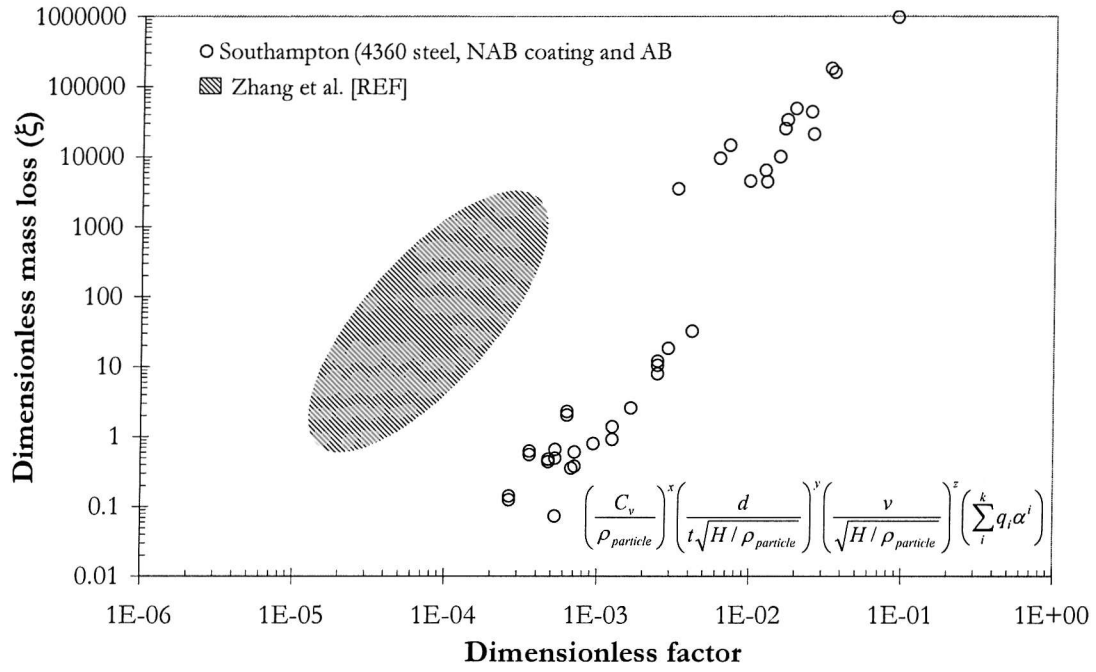

Figure 4-8 *Comparison of dimensionless mass loss against dimensionless factor between the current work and the work carried out by Zhang et al. [151]. The dimensionless factors were calculated based on the coefficients and exponents presented in their paper.* $x = 1, y = -1, z = 2$.

The diameter and velocity exponents were derived from the Zhang approach using graphical methods, averaged values of m = -2.9 and n = 3.4 were obtained for tests carried out in the current work. These can be compared to values obtained by Zhang *et al.* (m = -2.0 and n = 4.0, obtained from ([151] – Figure 10) and noting their slope to be 2). The difference in m and n values can be attributed to the type of erodents used by Zhang and to viscous flow effects [152]. Figure 4-9 shows the dimensional analysis of the current work; plotted against a re-calculated dimensionless factors based on the diameter and velocity exponents obtained graphically (m = -2.9 and n = 3.4). The graph showed better correlation and fewer scatters when compared to those found in Figure 4-8, confirming that the dimensional analysis is indeed sensitive to test parameter alterations in the erosion systems.

Two distinct regions can be found in Figure 4-9. Results from the 1020 steel are obtained from erosion tests using de-ionised water while the rest of the materials are carried out using mains water or NaCl solution with cathodic protection (CP). This indicates the possibility scale formation in the experiments using mains water/NaCl solution with CP. The effects of using mains water as the carrying medium for erosion of the 1020 steel is shown in Figure 4-10. The higher scatter in the dimensional analysis data from mains water experiments indicates that the calculation of the dimensionless factor was affected by variations in the gravimetric mass loss measurements. The variations can be caused by formation of calcite scales to have formed on the specimen surface, as the mains water in Southampton relatively hard (250 ppm Ca^{+} [153]).

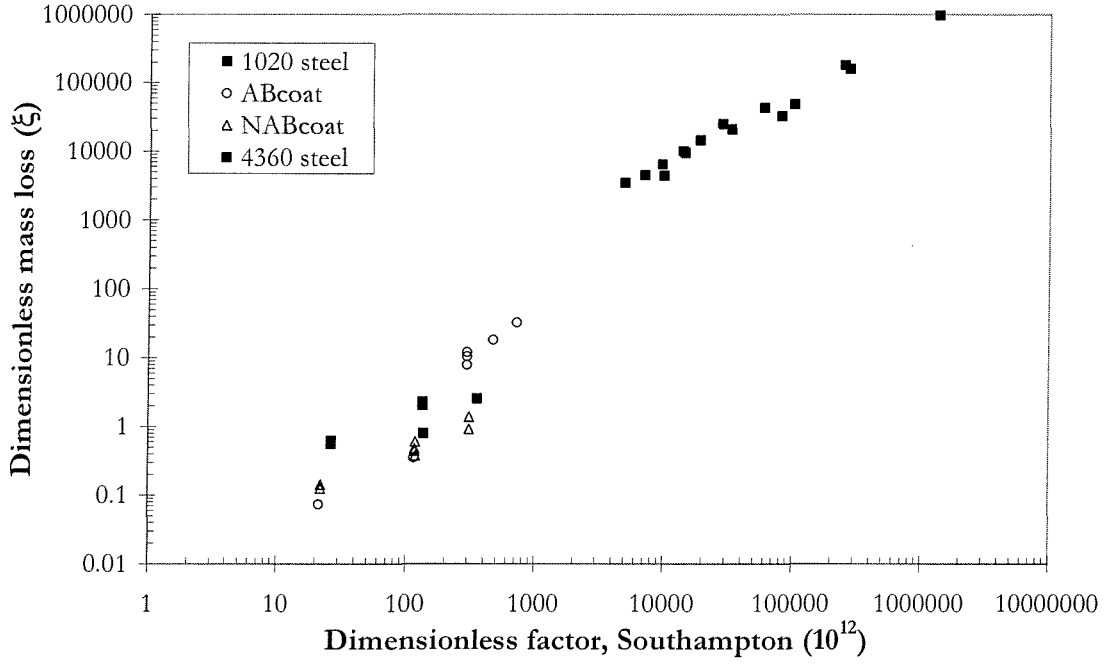

Figure 4-9 *Dimensionless mass loss against dimensionless factor for experiments carried out with DI water and Mains water. Dimensionless factors were calculated based on experimental results obtained in Southampton.* $x = 1, y = -1.5, z = 1.7$.

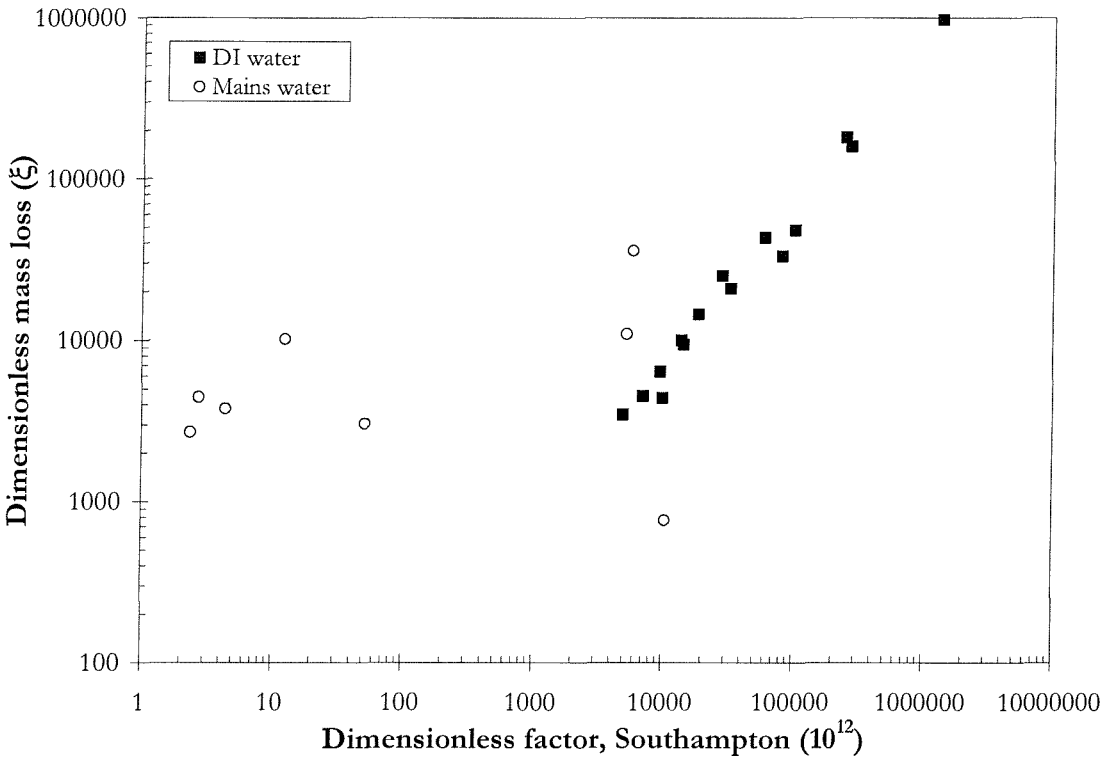

Figure 4-10 Dimensionless mass loss against dimensionless factor for the 1020 steel, erosion results obtained from DI water (black) and 3.5% NaCl solution with CP (white). $x = 1$, $y = -1.5$, $z = 1.7$.

4.3.6 Surface profilometry

Figure 4-11 shows 2D profiles obtained from the mid-section of the AB coating wear scar at different impingement angles. For the 30° impingement specimen (a), the length of the wear scar is approximately 20 mm and is consistent for low angle impingement; the coating was severely eroded at the region where the slurry impacts the surface. The depth of the wear scar is approximately 30 μm. Under 60° impingement (b), the scar is approximately 16 mm. Where the slurry impacts the surface, there is a central un-eroded region (partial conical shaped), probably due to the hydrodynamics of flowing slurries. The profile of the wear scar is generally smoother than that under 30° (a), but it is much deeper at ~ 80 μm. The 90° impingement erosion wear scar (c) appears to be circular when viewed from above, with a diameter of about 14 mm and is approximately 50 to 60 μm deep. The profile revealed a W-shaped scar, typical for ductile materials under slurry erosion at normal impingement angle

[30]. Higher rates of material removal occurred at regions away from the jet centre (1.3 radial distance, 6mm nozzle diameter), leaving a conical shaped un-eroded region in the centre.

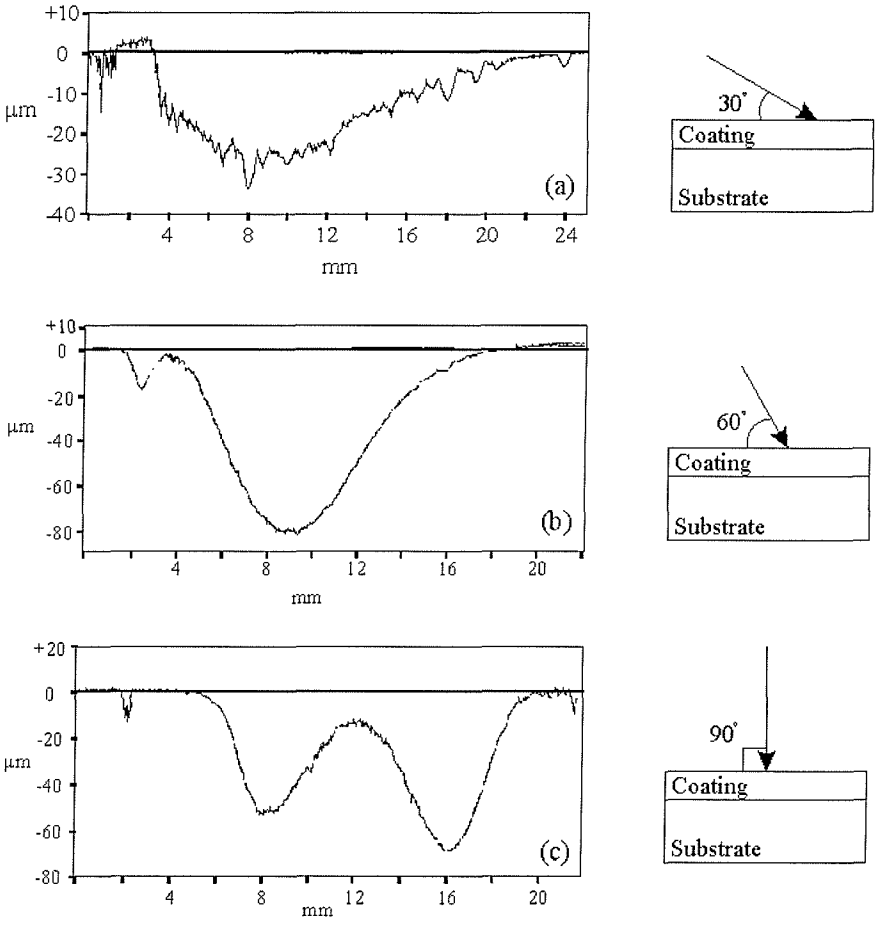

Figure 4-11 2D surface profilometry of the AB coating wear scar produced by slurry erosion at 30°, 60° and 90° impingement angle. Kinetic energy = 0.5 µJ.

A schematic diagram showing the theoretical wear scar length (*H*) at various angles is shown in Figure 4-12. Calculations based on simple trigonometry showed that the length of the wear scar should be 12 mm, 7 mm and 6 mm at 30°, 60° and 90° respectively. The actual measurements revealed much longer scar lengths, indicating that spreading occurred on the slurry jet. Comparison between theoretical and actual values showed that greater amounts of jet spreading occurred at 60° and 90° jet impingement.

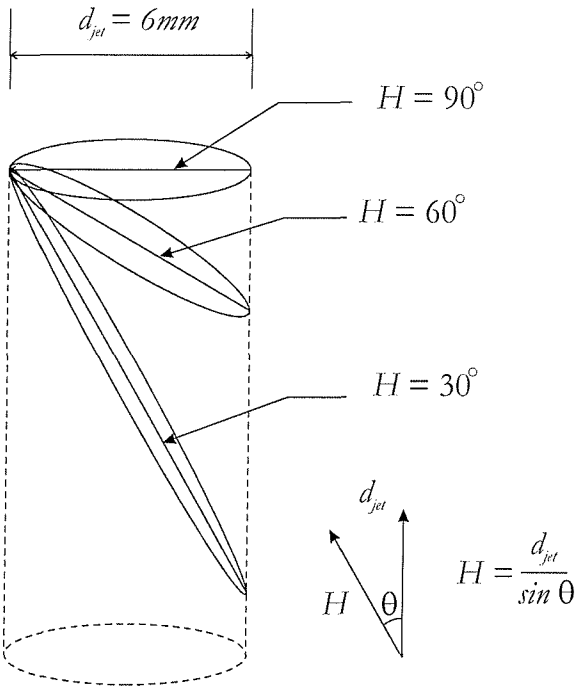

Figure 4-12 Schematic diagram showing the effect of impingement angle on length of wear scars.

It is evident that the erosion volume loss is greatest for the 90° impingement which corresponds well with the mass loss measurements in Table 4-2. The formation of a central cone on the wear scar depends on the hydrodynamics. When the jet approaches the target surface, the normal component of the liquid velocity reduces to zero while the tangential component increases. This momentum change is transferred to the particle but its influence is dependent on the level of momentum already transferred to the particle within the jet. For low momentum particles in the jet, the near-wall fluid momentum change will be significant resulting in the final impingement angle of the particle being much less than the nominal jet impingement angle [154].

Thus, particles impacting a surface in a nominal 90° jet could impinge on the surface at 30°, resulting in high erosion rates at regions away from the stagnation point (cutting type wear), while the stagnation region itself experienced plastic deformation [30]. For a 30° jet, impingement angles can be significantly less than 30°, resulting in lower wear rates.

Investigations on the 2D surface profile of the 30° impingement wear scar showed some depressions that were not observed in experiments with 60° and 90° impingements. The depressions are approximately 800 μm in length and 20 μm deep, which is considerably larger than a typical splat size. It is possible that these depressions are formed by the collective

cutting action of multiple sand particles (due to turbulent) as they contact the coating surface at a very low glancing angle [155].

3D surface profilometry was also carried out on the wear scars of the AB coating. Figure 4-13 illustrates and compares the erosion scars obtained from experiments using different kinetic energy settings at 90° impingement. These profiles were generated by scanning an area of 18 × 18 mm. A fresh surface prior to the erosion experiments was also shown for comparison. As the kinetic energy was increased, the polishing marks are eroded away, the wear scar becomes deeper and the central cone in the middle is more pronounced (sharper and smaller diameter). The size and cone angle depends on the velocity of the impinging jet, reflecting subtle changes in the impact angle distributions at different kinetic energies. Higher velocity slurry jets produce a cutting action nearer to the stagnation point, removing material and then rebound away from the surface of the specimen faster than a lower velocity jet.

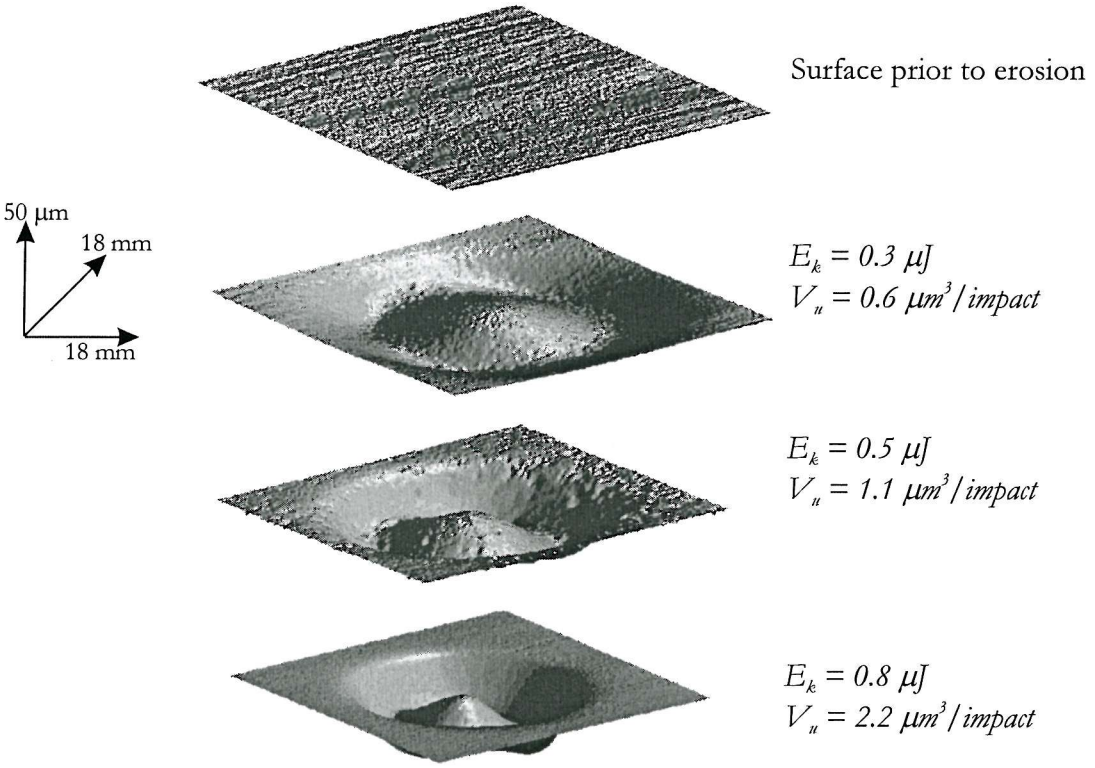

Figure 4-13 3D surface profiling of wear scars of HVOF aluminium bronze coating, obtained from slurry erosion experiments with varying kinetic energy at 90° impingement.

4.3.7 Microscopy

Figure 4-14 shows micrographs of the wear scars identified from the surfaces of the 3D surface profiles. The micrographs on the left hand side show the wear scar directly under the jet (stagnation point/central cone) and the ones on the right side show outer regions of the wear scar. The direction of the slurry flow is from bottom to top.

Individual impact scars within the stagnation point (scar centre) were all similar with no particular orientation, indicating that the flow is non-directional. Plastic deformation wear and cutting wear were observed in these regions for all kinetic energies. It is also difficult to identify individual impact sites due to the high density of plastic deformation on the surface. However, under high kinetic energy conditions (0.8 μJ), a certain amount of scar orientation can be observed. Most of the impact sites show plastic deformation wear, similar to that found by Speyer *et al.* [156] and Levy [15], indicating that sand particle impacts caused material extrusion. Work hardening can occur on the extruded material, subsequent impacts would cause it to fracture, removing it from the coating surface [10].

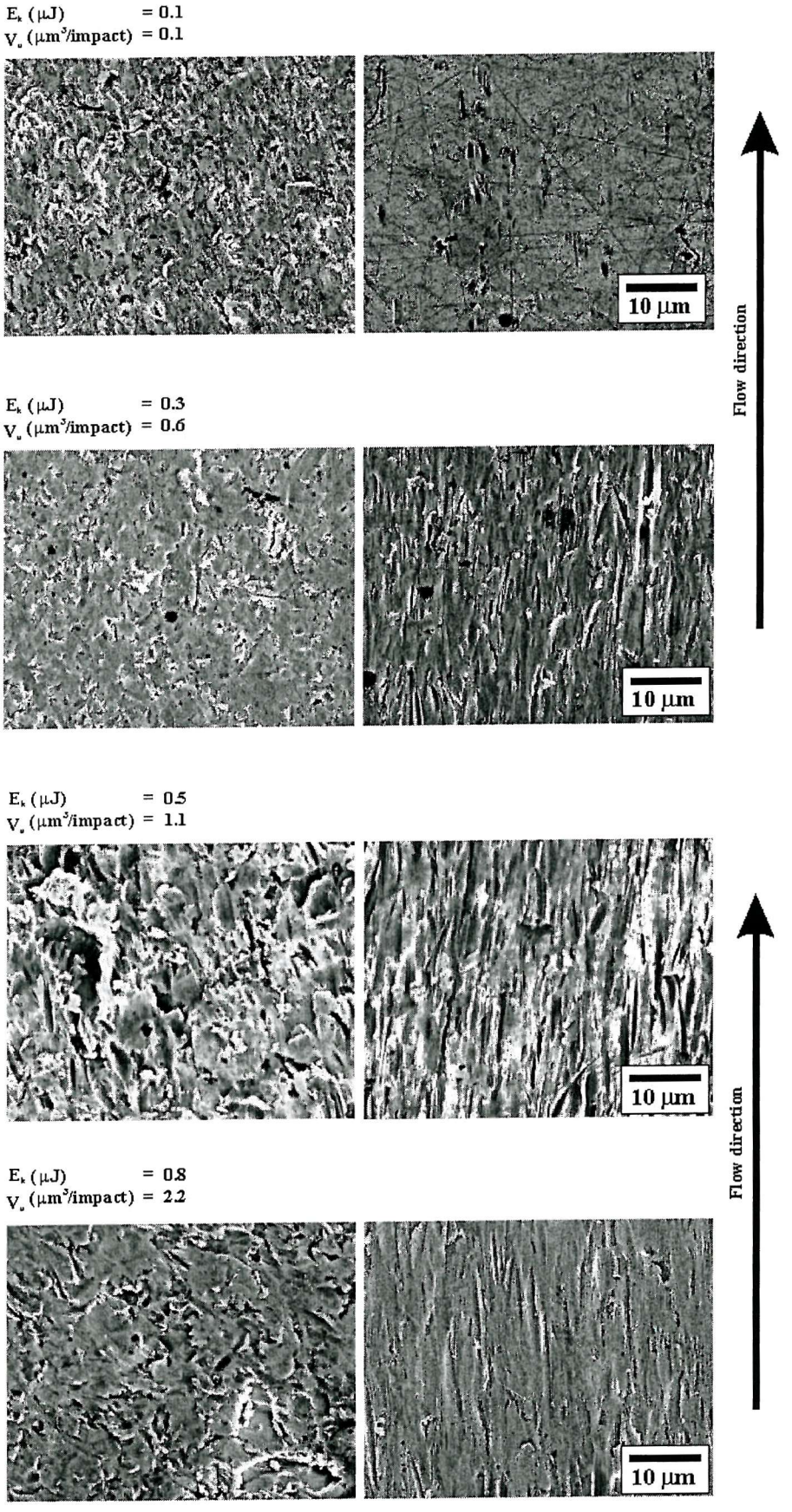

Figure 4-14 SEM examination of the AB coating surface after slurry erosion experiments at different kinetic energies, left side showing the centre of the wear scar and right side showing the outer regions of the wear scar.

The outer region of the erosion scar clearly reveals the slurry flow direction. This region shows a different type of material removal. Plastic deformation lips are not apparent; long scars orientated to the slurry flow direction showed signs of cutting mechanisms (having clean edges on both sides) [8]. Under lower kinetic energy conditions (0.1 μJ), fewer impacts were observed. The cutting marks are shorter and lips were not seen on the sides of the scars, indicating that the momentum normal to the surface was much lower than the higher kinetic energy conditions. At higher kinetic energies, the sand particles cut deeper into the surface due to higher momentum, thereby causing a longer scar. Higher kinetic energy sand particle impact also resulted in the extrusion of work hardened plastic lips on either sides of the cutting marks [8].

The sieved sand particle diameter was 135 μm but the width of the impact sites are in the order of 2 to 3 μm, indicating that only the tip of the sand particles are in contact with the surface during impact. A micrograph of the sand particles used for the experiments is shown in Figure 4-15, revealing sharp tips and blunt areas on the particles. The impact scars were most probably resulted by the angular tips while blunt areas produce plastic deformation wear.

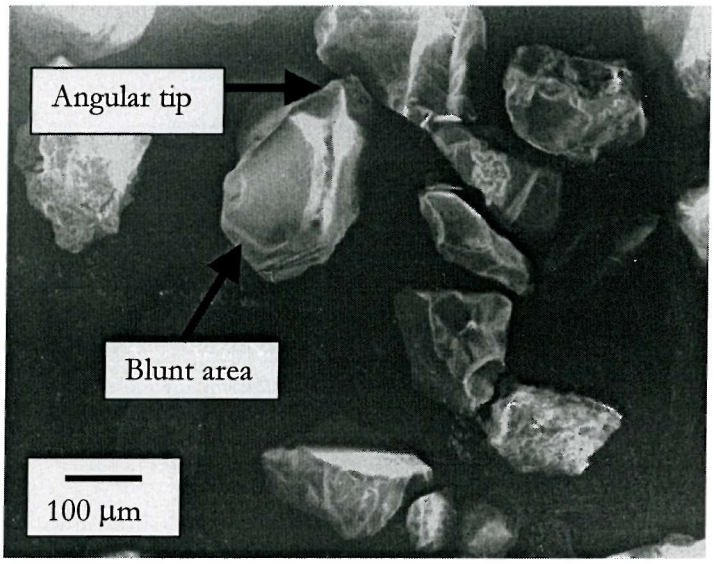

Figure 4-15 SEM micrograph of the Redhill 110 sand used in the erosion tests, showing the angular tips and blunt areas on the sand particles.

A transverse section of the AB coating, taken from an area near the stagnation point is shown in Figure 4-16. Sub-surface cracking is clearly evident. Since the splat boundaries consist of oxides formed during the spraying process, it is possible that these areas are brittle and susceptible to lateral cracking when subjected to constant sand particle impingement. Such behaviour was also observed by Wood *et al.* [150] in their slurry erosion tests on HVOF tungsten carbide coatings. It was proposed that low cycle fatigue imparted by sand impingement caused crack growth at the splat boundaries. When the horizontal cracks intercept with other cracks perpendicular to the interface, individual or multiple coating splats could be removed from the coating matrix, thus enhancing the wear rate. Evidence of brittle cracking at splat boundaries was also observed by Hearley *et al.* [146]. Figure 4-17 showed an area where splat removal probably occurred on the coating surface. The large area (> 100 μm) indicates that multiple splat particle ejection occurred due to failure at the splat boundaries. Cracks perpendicular to the interface was not observed under SEM investigations.

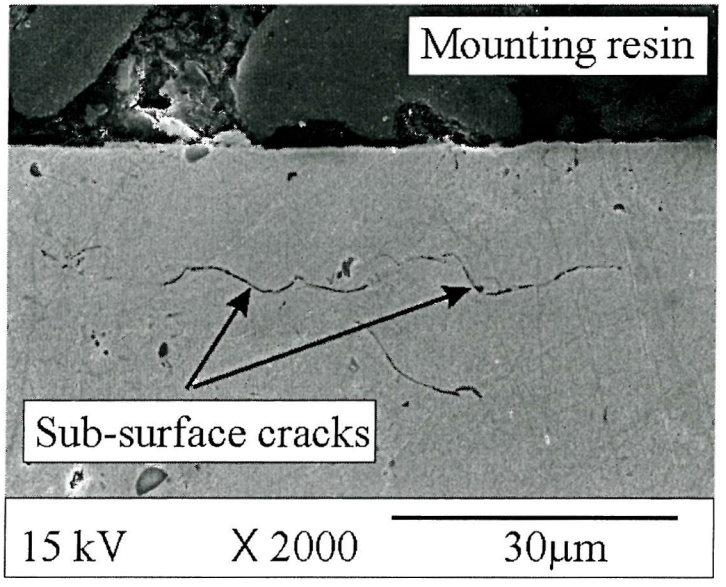

Figure 4-16 SEM image showing the transverse section of the AB coating after slurry erosion experiments. 90° impingement at 0.8 μJ kinetic energy. Section was obtained from the stagnation point region, showing cracks parallel to the coating interface.

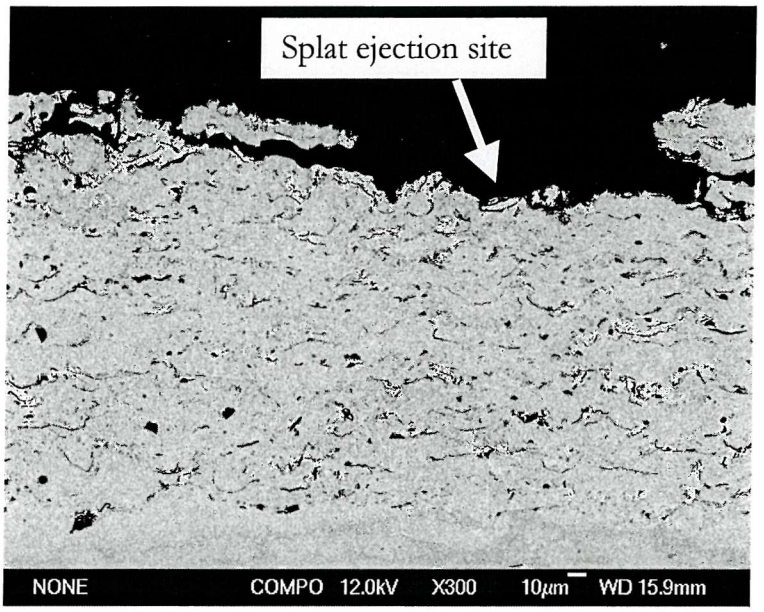

Figure 4-17 SEM image showing the transverse section of the AB coating after slurry erosion experiments. 90° impingement at 0.8 μJ kinetic energy. Section was obtained near the stagnation point region, showing an area where splat ejection occurred.

4.4 Erosion mechanism of the AB and NAB coatings

Examination of the micrographs (Figure 4-14) indicates a generally ductile mechanism for coating removal. However, the erosion rate as a function of impact angle (Table 4-4) showed maximum erosion at a normal impact angle (90°), suggesting a contrasting brittle erosion mechanism. Similar behaviour has been observed by other workers [146,149] and several suggestions were provided:

1. Particle impacts caused [146] intense localised plastic flow, producing lips around the impact craters; the highly stressed lips were cracked and removed by subsequent impacts.
2. Micro-cracking may be initiated at the pore network (splat boundary), leading to detachment of splats and coating removal.
3. The erodent may fragment upon impact, the smaller fragments of the particle are projected radially to produce damage.

From the results obtained, three possible erosion mechanisms can be proposed for the aluminium bronze coating system, they are (i) plastic deformation/extrusion wear, (ii) cutting wear and, (iii) brittle cracking and propagation.

4.4.1 Plastic deformation/extrusion wear

Surface profilometry and SEM showed that plastic deformation wear occurs predominantly at normal impingement angles, usually at the stagnation region. Impinging particles produce work hardened lips that were subsequently broken off by more particle impacts. This type of wear was also observed by Levy [15], it was suggested that material removal resulted from micro-extrusion and forging rather than machining. In order to quantify the contact mechanics of plastic deformation, the dynamic Hertzian theory for single impact has been applied [157]. Calculations were based on 65 – 355 μm particle radius and 7.6 – 21 ms^{-1} jet velocities. The results provided mean contact pressures of 2 to 3 GPa, more than 4 times the yield strength of the materials under investigation, indicating that plastic deformation will occur.

4.4.2 Cutting wear

This mechanism occurs at regions starting from the edge of the slurry jet (0.5 nozzle diameter). Particles entrained in the flow impact the surface at shallow angles (< 90°) [30], removing material by true micro-machining operations and producing plastic lips on the sides of the impact scar [19]. These lips were also work hardened and broken off the surface by subsequent impacts. Impact volumes (V_{scar}) were calculated by measuring the length and width of the scars from SEM micrographs, assuming the scar depth equals the width. The scars fell into two distinct categories, the small scar group having an aspect ratio of about 3 while the large group had a value > 5. V_{scar} values for both small and large groups were subsequently compared with the V_u values in Table 4-2.

As can be seen, V_{scar} values are higher than V_u values, demonstrating that the assumption that all particles impinge and cause damage (which is made in calculating V_u) is an over simplification. The percentage of solids that cause damage are likely to be a function of E_k with fewer particles damaging at lower energies compared to almost 100 % at higher energies. This trend is seen in Figure 4-18, where the ratio of V_u/V_{scar} is plotted against E_k. For relatively high E_k values the V_u/V_{scar} ratio for the small scars approaches unity. Overall, if the small scars dominate then material removal must approach 100 % efficiency [156]. This indicates that the most significant material removal was by cutting wear mechanisms which in

turn is mostly due to the angular particle tips rather than from the relatively blunt areas of the particles.

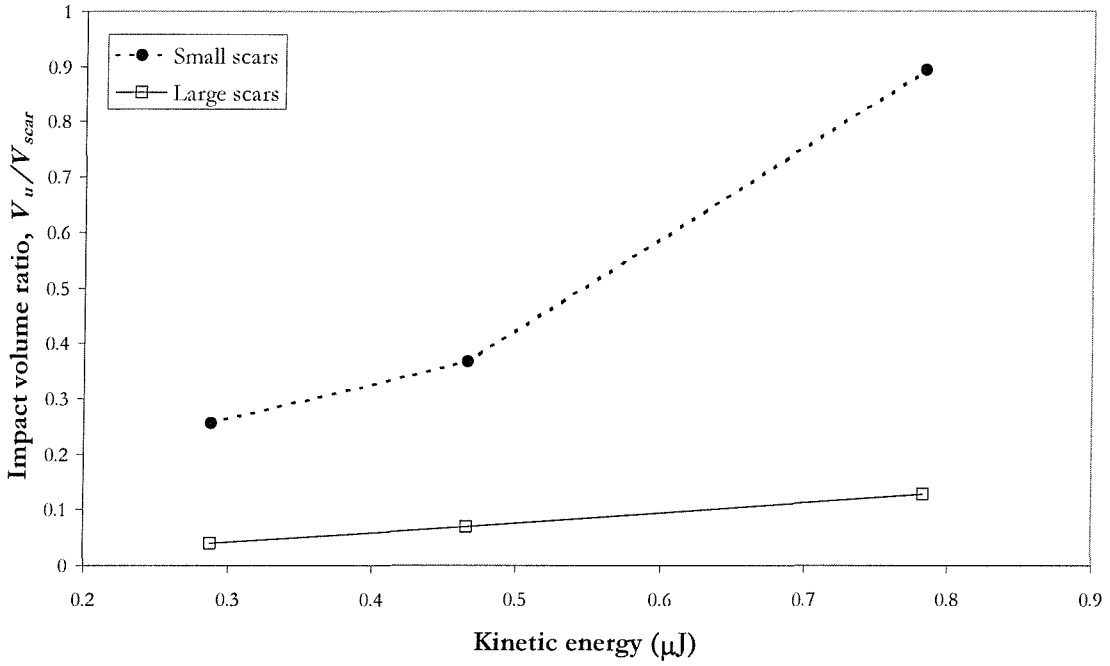

Figure 4-18 Impact volume ratio vs. kinetic energy for both small and large impact scars.

4.4.3 Brittle cracking and propagation

Continuous particle impacts on the coating surface can result in fluctuating stresses, allowing propagation of sub-surface cracks by a fatigue mechanism, leading to a micro-cracked coating [150]. Cracks initiate at defects in the coating and when these cracks interlink large areas of coating could be removed. The splat geometry (horizontal) determines the crack growth path with cracks propagating parallel to the substrate interface along or close to splat boundaries. The splat boundaries are associated with brittle oxides with lower fracture toughness than the coating matrix. Once these cracks interlink with existing coating defects and vertical cracks perpendicular to the substrate interface either partial, mono or multi-splat ejection can occur.

The depth of the fluctuating shear stresses was estimated by dynamic Hertzian contact theory [158], which indicates that maximum shear stresses of about 0.9-1.3 GPa can be produced and occur at 3-30 μm below the coating surface. The micrograph in Figure 4-16 shows that

sub-surface cracking occurred at about 15 μm below the eroded surface, probably at the splat boundaries.

Under slurry erosion conditions, it is possible that more than one mechanism occurs concurrently on the complex AB coating. Interaction between the mechanisms can lead to an accelerated rate of material removal; further work is required to fully understand these interactions.

4.5 Conclusions

Pure erosion experiments have been carried out on AB and NAB coatings, and 4360 steel. A range of kinetic energy (0.02 to 0.8 μJ) was utilised for investigation of the erosion mechanisms and erosion rate. The following conclusions can be drawn:

The erosion rate of the AB coating under 0.5 μJ kinetic energy was found to be twice as high as bulk AISI 316 stainless steel but was comparable to bulk 90/10 cupronickel. At E_k = 0.1 μJ, the erosion rate of the coating was 40 times lower than HVOF 316L and about 5 times higher than the HVOF tungsten carbide coating. Similar erosion rates were obtained from both HVOF AB and NAB coatings.

Under slurry erosion conditions, the velocity exponents (n) for the AB and NAB coatings were found to be between 2.4 ~ 3.0. This indicates that the erosion rate was not purely a function of kinetic energy dissipation. Factors such as sand particle rotation, friction during impact, the presence of a squeeze film, and particle-particle interactions should be considered. The velocity exponents were also found to be higher than bulk materials such as carbon steel and stainless steels. This indicates that although the coating behaves in a ductile manner, its microstructure can greatly affect the erosion properties.

The dimensional analysis has been shown to be sensitive to different erosion systems, results from air-solid erosion and liquid-solid erosion cannot be analysed together. This is due to differences in viscosity, velocity, impingement angle, and squeeze film between the two systems. The velocity and diameter exponents used in the dimensional analysis are sensitive to

experimental parameters such as properties of erosive particle and target material. Changing either of these will result in a similar change in erosion properties.

The mains water used in the experiments can result in scale formation on the specimen surface, affecting the mass loss measurements and producing a more scattered dimensional mass loss. The dimensional analysis has shown sensitivity towards possible scale formation in a pure erosion system.

Surface profilometry in 2D and 3D produced wear scar profiles that are consistent with materials undergoing ductile erosion (W-shaped profiles). The wear profile under 90° jet impingement showed the highest volume loss, due to combined plastic deformation wear, cutting wear and brittle cracking. Reducing the jet impingement angle resulted in cutting wear becoming more dominant than plastic deformation and brittle wear.

SEM investigation of the specimen surfaces showed that combinations of plastic deformation and cutting wear contributed to the material loss. Plastic deformation wear patterns were found mostly in the stagnation region, cutting marks were found in areas away from this region.

SEM examination of transverse sections of eroded coatings showed occasional sub-surface cracking, possibly induced by fluctuating shear stresses. The sub-surface cracks are linked to inter splat regions, its extension and inter linking results in single or multiple splat ejection.

Scar volume analysis was compared to unit volume loss calculations, assuming all particles impinge and damage. At high kinetic energies, it has been shown that the erosion rate is dominated by small particles that generate scars by a micro-cutting process. While at lower energies, it is clear that not all impacting particles do damage but small particle impacts are still dominant. The analysis has shown that the assumption of all particles impinge and cause damage is an oversimplification. The damage efficiency depends on the particle orientation during impact, angular tips are more efficient in material removal by micro-cutting.

Chapter 5 Flow corrosion

5.1 Introduction

This chapter describes the flow corrosion experiments that were carried out on the AB and NAB coatings. Similar experiments were also carried out on 4360 steel specimens for comparison with the coatings. Attempts have been made to quantify the flow corrosion rates of the materials and to understand the flow corrosion mechanisms that occur for the AB and NAB coatings. Flow corrosion rates were quantified by 5 hour jet impingement experiments and mass loss measurements. The mechanisms were elucidated after 5 day jet impingement experiments, the results were analysed by using the SEM/EDX and open circuit potential (OCP) measurements.

5.2 Experimental methodology

5.2.1 Equipment

A fully aerated free-jet impingement rig [83,143] was used to carry out the flow corrosion experiments. The rig configurations are similar to that used under erosion conditions (Chapter 3), except for the absence of solid particles. Solid and flexible polyurethane pipe work was used to prevent galvanic interference with the specimens. The electrolyte was made up of 3.5 % w/w NaCl in tap water. Flow velocities between 3.0 and 6.7 ms^{-1} were used; the Reynolds (*Re*) numbers were calculated [159] and found to be between 19460 and 36100, indicating turbulent flow. The jet impingement angle was fixed at 90°. Rubber gaskets were situated in the specimen holder, exposing a surface area of 900 mm^2 to the jet (Figure 4-2, Chapter 4). Surfaces were lapped to $R_a < 1$ μm prior to the flow corrosion tests. Flow corrosion experiments were carried out for (*i*) 5 hours for quantifying the flow corrosion rate and (*ii*) 5 days for assessing the flow corrosion behaviour when the coating fails.

5.2.2 Gravimetric measurements

Flow corrosion mass losses were measured, using similar methods explained in Chapter 3 (Erosion). The mass loss values (W) were converted to thickness loss per year (mm/year) by Equation 5-1. Flow corrosion rates are expressed as thickness loss per year so that comparisons can be made with results found in the literature. Mass loss results will also be used for synergy calculations, discussed in Chapter 7 (Synergy).

$$mm/year = \frac{8.76W}{\rho A t} \qquad \textit{Equation 5-1}$$

where W is the mass loss (kg), ρ is the material density (kgm^{-3}), A is the exposed area (m^2) and t is the time (hours).

5.2.3 Electrochemical measurements

EPN measurements were taken to monitor the flow corrosion behaviour of the coatings. A silver/silver chloride (SSC) reference electrode was used. Cell arrangements are similar to those in erosion experiments, see Chapter 3. The electrodes were connected to a Gamry PC4-750 potentiostat via a shielded cable, and data logging was carried out with the ESA400 software. Acquisition frequency was fixed at 2 Hz. A Faraday cage was placed around the section of the rig where electrochemical measurements were carried out, so that external sources of interference can be eliminated.

5.3 Results and discussion

5.3.1 Corrosion rate

Figure 5-1 shows the flow corrosion rate of the NAB coatings and the 4360 steel, at different jet velocities. Additional results of the AB coating (at 5.0 ms^{-1}) was plotted for comparison. The differences between the flow corrosion rate of the materials, within the velocity range tested, are small. The averaged rate being 0.9 mm/year (33.5 mpy) for the NAB coating and

3.7 mm/year (146 mpy) for steel. NAB coating was also found to be slightly more corrosion resistant than the AB coating (2.0 mm/year, 78.7 mpy).

Comparison with data from the literature show that the flow corrosion rate of AB and NAB coatings are higher than bulk NAB alloy under static conditions (0.09 mm/year) [132], this might be the result of the flowing electrolyte disrupting the protective film of the surface. It is also possible that the surface films formed on the coatings are different from that found in bulk alloys. For example, static corrosion tests have shown discontinuities (such as pores and impurities) on the protective film on the coatings (Section 3.4). Ault [52] reported that the seawater corrosion rate of typical cast NAB alloys varied as a function of the velocity. The minimum rate was reported to be 0.5 mm/year at 8 ms^{-1}, rising to 0.8 mm/year at 30 ms^{-1}. However, areas of localised corrosion were found, with rates up to 2 mm/year. These findings are similar to that obtained from the NAB coating in the current work.

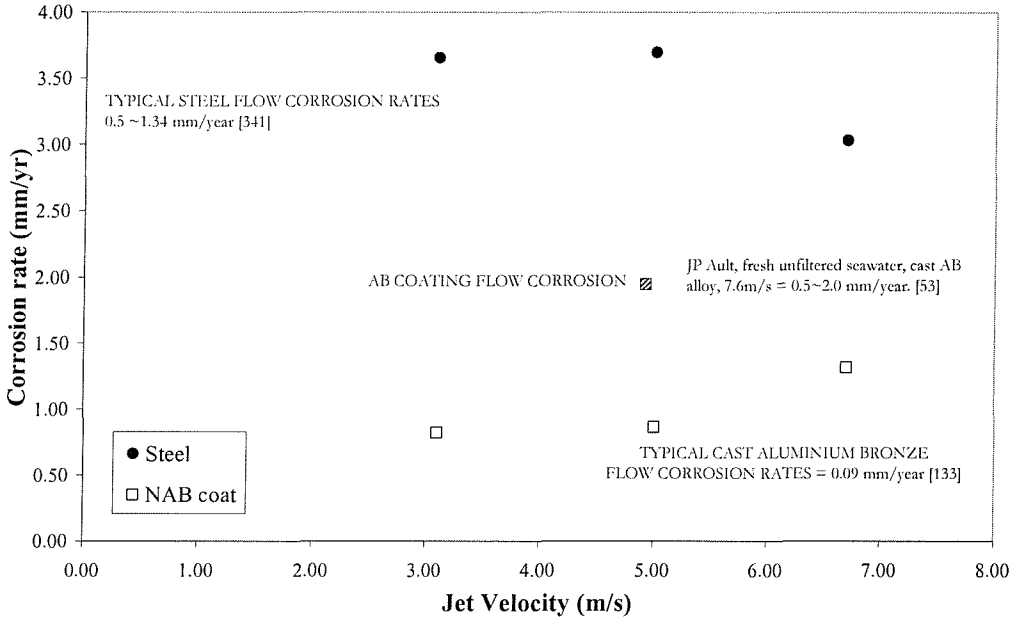

Figure 5-1 Comparison of flow corrosion rates for steel, NAB coating and AB coating at various jet velocities.

The slight increase in the NAB coating corrosion rate at 6.7 ms^{-1} indicates that the surface film might be affected by turbulence intensity in the electrolyte jet. It should also be noted that the operational recommendation for cast bulk NAB alloys in flowing seawater is below 4.3 ms^{-1} [160]. Syrett [161]suggested that increased flow corrosion rates of NAB alloys at high velocity can occur in two steps: (1) increasing the velocity leads to an increased oxygen supply and mass transfer reactions, and (2) when the velocity exceeds the critical range, local

turbulence of the flowing electrolyte can shear off the protective film on the material surface thus increasing the corrosion rate. However, other workers have also reported much higher critical velocity (23 ms^{-1}) for the NAB alloys [61]. This suggests that the critical velocity could be dependent on actual service conditions, such as temperature, oxygen concentration and presence of biological or chemical scale on the alloy surface.

Table 5-1 compares the flow corrosion rate of the AB and NAB coatings with other commonly used marine materials. The coatings were found to be comparable or more superior than the tungsten carbide based HVOF coatings, they are also comparable or slightly less resistant that marine alloys such as cupro nickel and duplex stainless steels.

Table 5-1 Comparison of flow corrosion rates between the AB and NAB coatings and other materials found in the literature.

Material	Flow corrosion rate (mm/year)	Reference
Bulk alloys		
Duplex SS (UNS 31803), 14 ~ 30 ms^{-1}	7 ~ 10	[86]
Duplex SS (2205), 14 ms^{-1}	0.06 ~ 0.2	[2]
Carbon steel, 14.3 ms^{-1}	2.6	[2]
Cupro-nickel alloy, 5 ~ 7 ms^{-1}	0.12 ~ 3.5	[135]
NAB alloy	0.5~0.8	[52]
Coatings		
HVOF WC-Co alloyed, 14 ~ 30 ms^{-1}	7 ~ 10	[86]
HVOF 83WC-17Co, 14.3 ms^{-1}	1.9 ~ 2.5	[2]
HVOF AB, 5 ms^{-1}	2.0	Current work
HVOF NAB, 3 ~ 7 ms^{-1}	0.8 ~ 1.3	

5.3.2 SEM investigations

Visual inspection of the 4360 steel surface revealed a uniform layer of corrosion products on the exposed surface. The corrosion products have a dark grey appearance, possibly mixtures of iron oxides/chlorides and calcareous deposits. Closer investigations under the SEM (Figure 5-2) showed that the corrosion products are spherically shaped, with diameters of approximately 300 nm. They are believed to be by-products of reduction reactions occurring on the surface, possibly carbonates. Identification of these products by EDX was not possible, due to it being smaller that the resolution of X-ray spots (1 μm).

As seen in Figure 5-3 and Figure 5-4, an almost uniform corrosion film has developed on both the AB and NAB coating surfaces. The film appears to contain similar corrosion products to that found on the 4360 steel surface, indicating that similar types of reduction reactions are occurring on the surfaces of the coatings. The spherical corrosion products were smaller than the ones found on the steel surface, reflecting slower reduction rates on the copper based coatings, probably due to the ability of the coatings to form a protective layer on its surface. Monticelli *et al.* [162] have observed similar types of corrosion products on copper alloys in synthetic industrial water of pH 5.5. Fourier-Transform Infra Red (FTIR) spectroscopy was used and the corrosion products were identified as mixtures of $CuCO_3$ and $CaCO_3$.

Some areas of discontinuity were found on the specimen surface, possibly indicating pore openings and dissolution sites. The discontinuities were not found on the monolithic steel specimens. The effects of pore openings on the flow corrosion behaviour of the coatings will be discussed further in the following section.

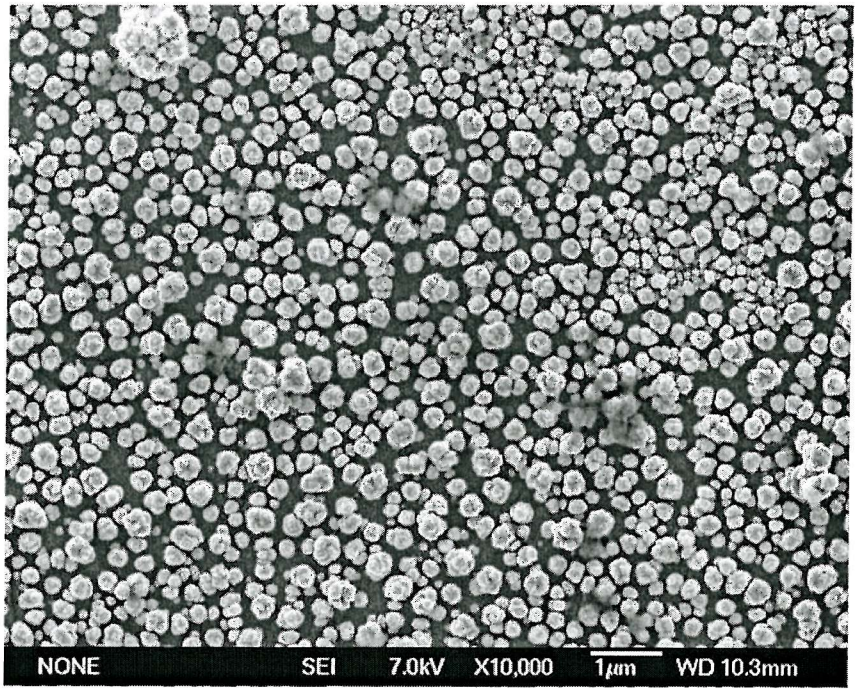

Figure 5-2 Steel flow corrosion surface micrograph. 3.5 % NaCl, 5.0 ms^{-1}, 25 ° C, after 5 hours.

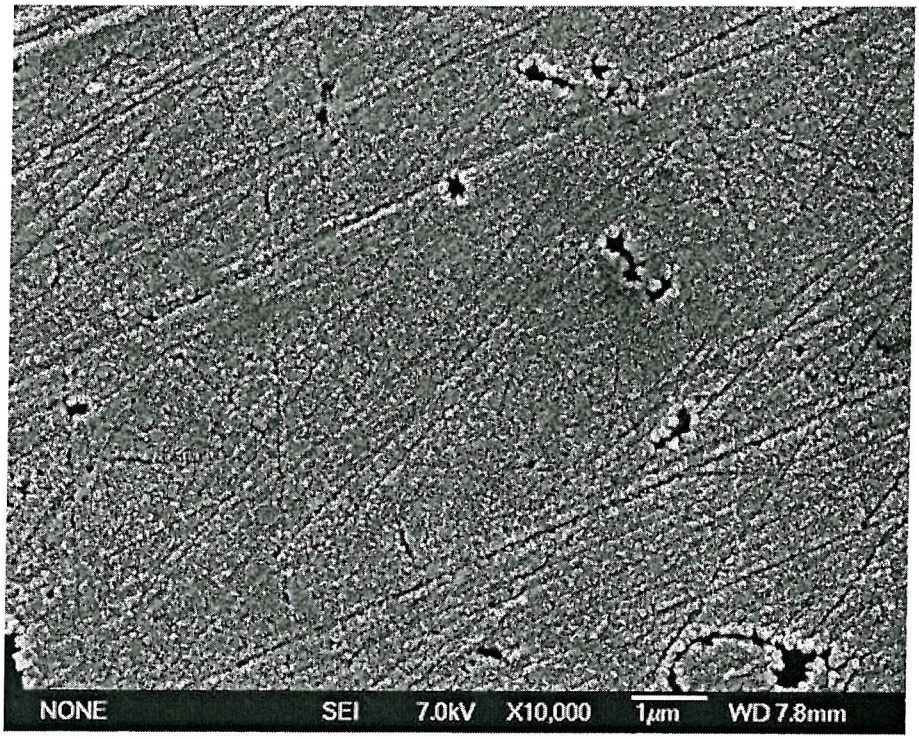

Figure 5-3 AB coating flow corrosion surface. 3.5 % NaCl, 5.0 ms^{-1}, 25 °C, after 5 hours.

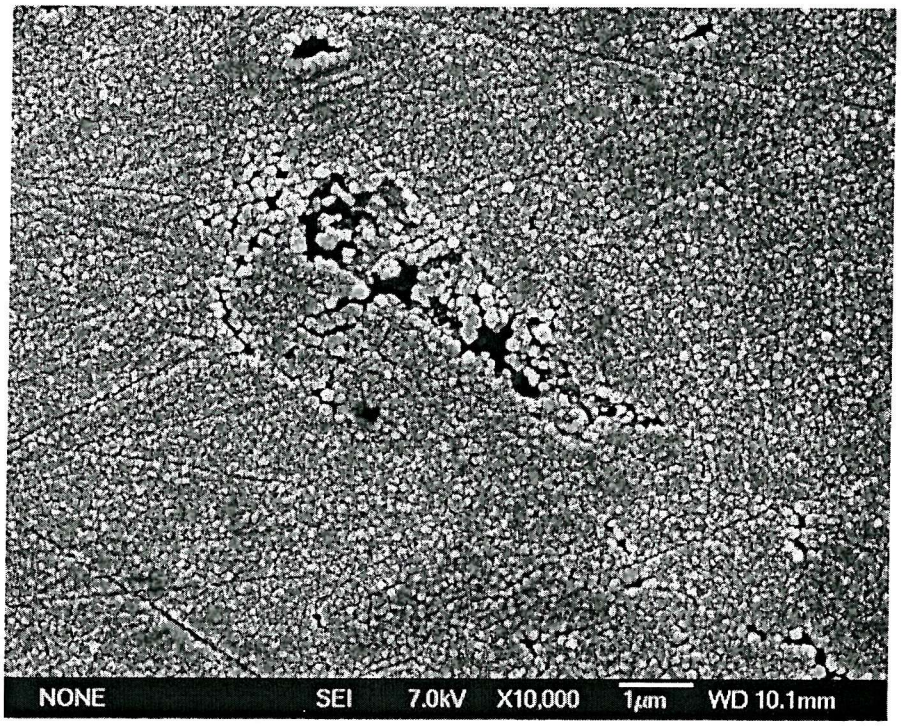

Figure 5-4 NAB coating flow corrosion surface. 3.5 % NaCl, 5.0 ms^{-1}, 25 °C, after 5 hours.

5.3.3 5 day experiments

Figure 5-5 shows the AB coating after 5 days of exposure to flow corrosion. Visual examination revealed evidence of surface filming, scale formation and red rust (which appears to be associated with the scales). The surface film appears to be uniform, whereas the scale features are randomly distributed at localised sites with heights ranging from 10 to 120 μm above the surface film, as seen in Figure 5-6. It is evident that the scale is adherent to the surface, as it is still apparent after 5 days of liquid jet impingement.

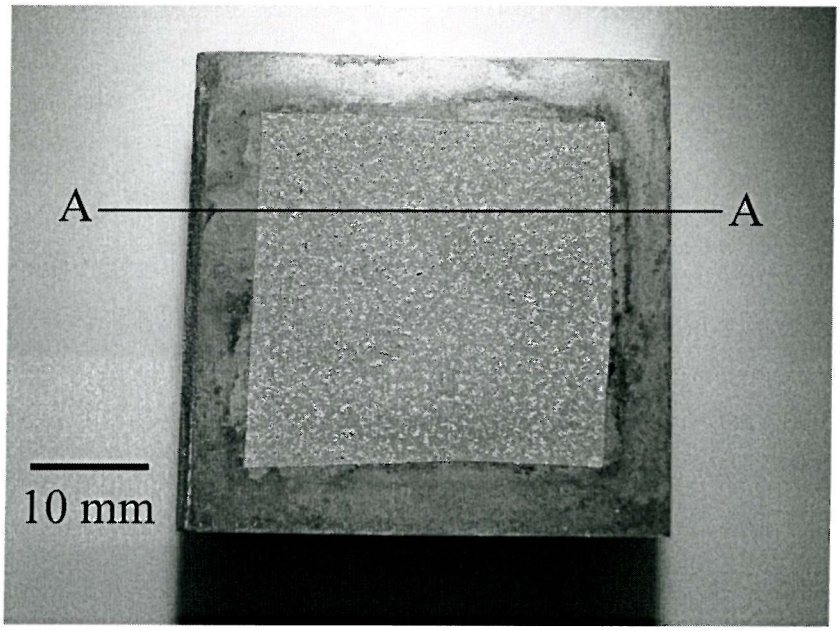

Figure 5-5 AB coating specimen obtained from the flow corrosion experiment, showing the film formation and scaling on the surface exposed to the liquid jet impingement. 3.0 ms^{-1}, 25 °C, 3.5 % NaCl, after 5 days.

Evidence of surface film formation on copper aluminum alloys in static 3.5 % NaCl solution have been provided by Schussler and Exner [62], it was reported that the film consisted of copper oxides and aluminum oxides that could reduce the corrosion rate by reducing the charge transfer and mass transfer kinetics. It was also reported that the film thickness observed was approximately 800 nm. However, on the coatings studied in the current investigation, blisters were formed, as indicated by the profile in Figure 5-6 (taken at section A-A from Figure 5-5). Transverse sections of the coating revealed delamination at the coating/substrate interface. The delamination sites corresponded with the blister location, indicating that electrolyte had permeated the coating, resulting in corrosion of the steel substrate.

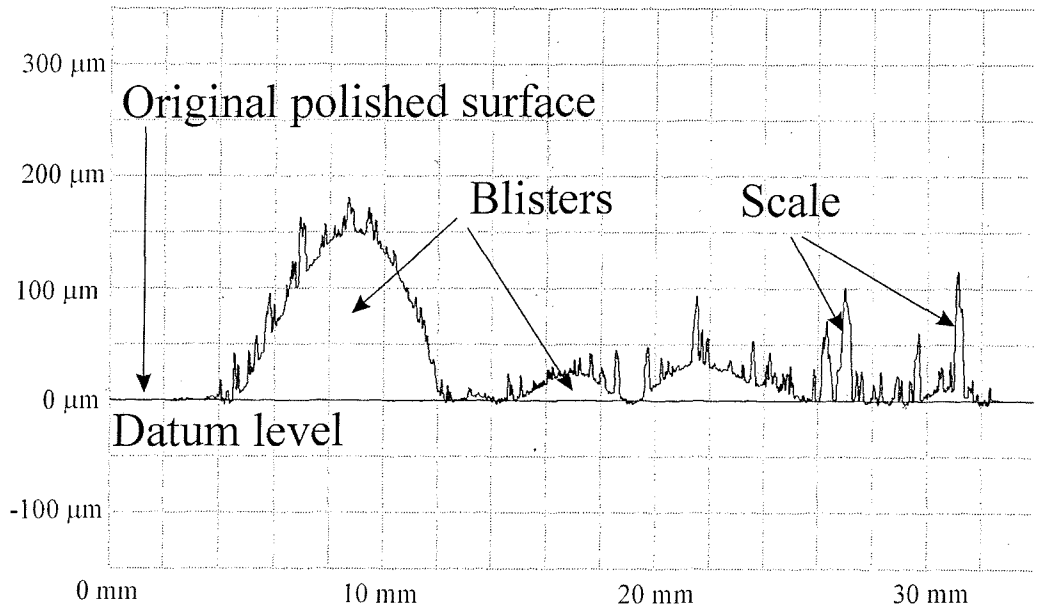

Figure 5-6 *Surface profilometry of the AB coating after 5 days of flow corrosion, taken at A-A (from Figure 5-5), showing the height and distribution of the scale and blister formation. 3.0 ms^{-1}, 25 °C, 3.5 % NaCl.*

SEM examination was carried out on the surface, an example of which is shown in Figure 5-7. A continuous layer of surface film has formed on the surface, ring shaped scale features with central openings were also observed. The micrograph also shows that some of these central openings are sealed.

EDX analysis was carried out to compare the unexposed surface, exposed filmed surface and the localised scale features. Results from Table 5-2 show the presence of contaminants such as Si, P and Ca after the flow corrosion experiment, probably from the mains water. The main constituent of the surface film is thought to be cuprous oxide, mixed with aluminium and iron oxides. These results are consistent with that obtained by Schussler [62]. The localised scale consists mainly of Al and Fe oxides, with higher traces of Fe found in the centre of the scale. This confirmed the visual observation of red rust spots on the surface, indicating that the electrolyte has permeated the coating and corrosion of the steel substrate has occurred.

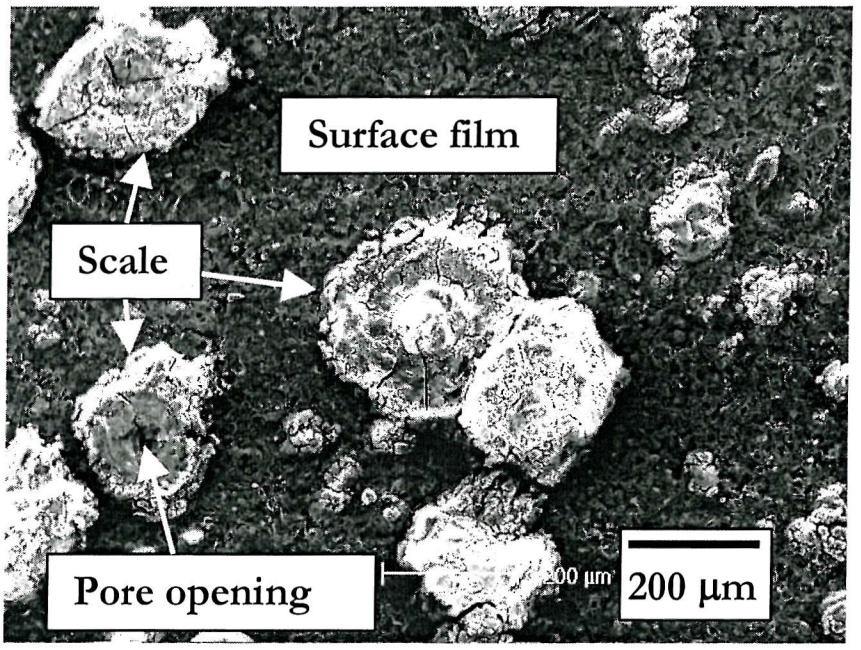

Figure 5-7 *Flow corrosion of the AB coating surface after 5 day jet impingement at 3.5 % NaCl, 3.0 ms^{-1}, 25° C.*

Table 5-2 *EDX analysis of the coating surface after 5-days of flow corrosion.*

Area	Elements							Comments
	Cu	Al	Fe	O	Si	P	Ca	
Unexposed surface	•	•	•					AB alloy.
Exposed film surface	•	•	•	•	•	•	•	Mixed oxides of Cu and Al [62] and impurities.
Localised scale features		•	•	•	•	•	•	Mixed oxides of Al and impurities.

5.3.4 Open circuit potential (OCP) measurements

Of the OCP measured throughout the 5-day experiment, only the first and last days of the measurements are shown as they contain valuable information on the surface film formation and breakdown. Figure 5-8 shows the potential behaviour of the coating during the initial 24 hours. The OCP of a freshly prepared coating when exposed to the flowing electrolyte was –310 mV (SSC). Ennoblement of the potential occurred, up to–250 mV. The increase in OCP reaches a steady state of –230 mV (SSC) from the 3rd day onwards and remained stable until the 5th day.

The increase in the OCP value during the first day indicates anodic dissolution and the formation of a protective layer on the surface during flow corrosion experiments [62]. The process is similar to that found under static immersion tests (Section 3.4). This observation is consistent with work carried out by Wojcik [163] where a freshly prepared copper surface was subjected to flowing synthetic seawater, resulting in a potential rise of 90 mV during the first 3 days. Similarly, Williams carried out jet impingement flow corrosion experiments in seawater at 4 ms^{-1} for various grades of copper bronzes [54]. It was reported that the steady-state corrosion potential for aluminum bronze alloys under such conditions was –230 mV (SCE), this potential corresponds well with the steady-state potential in the current work.

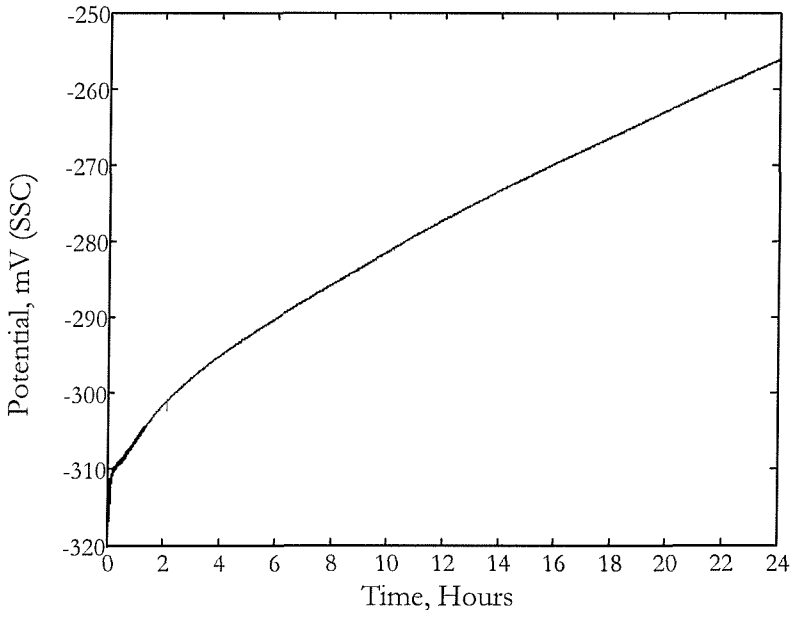

Figure 5-8 *E_{corr} measurement during the first day of flow corrosion of the AB coating, showing a gradual increase over the 24 hours, indicating the formation of a protective layer. 3.0 ms^{-1}, 25 °C, 3.5 % NaCl.*

The OCP behaviour of the AB coating on the 5th day is shown in Figure 5-9, revealing potential transients in the electronegative direction. These transients are characterised by a sudden decrease followed by a gradual recovery to steady state. The magnitudes of these transients are between 2 to 5 mV, with the recovery time lasting between 1 to 5 hours. The transients are similar to those observed in the work carried out by Vreijling *et al.* [164]. They were produced when a HVOF sprayed metallic Ni-Cr alloy was exposed to slow flowing natural seawater. The potential transients produced by the Ni-Cr coating system showed a larger magnitude (100 mV) and lasted for 5 hours.

The occurrence of transients was attributed to the breakdown of the protective film and its subsequent repassivation. It is possible that the transients observed on the AB coating involved similar mechanisms of film breakdown and subsequent repair. Other possibilities that could contribute towards such transients include corrosion at the 1020 steel substrate at the coating/substrate interface or the pore networks, possibly explaining the blisters observed in the surface profile. Further work needs to be carried out to determine the source of these transients in order to confirm this.

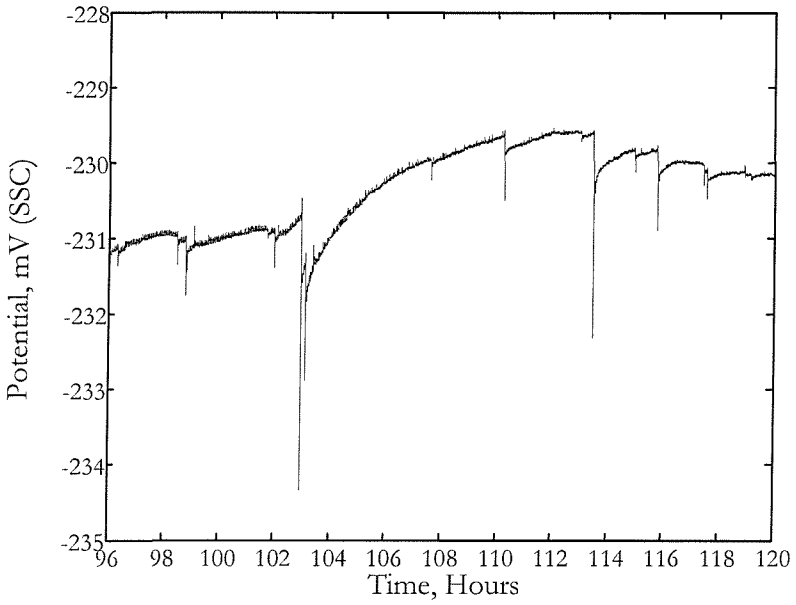

Figure 5-9 *E_{corr} measurement during the fifth day of flow corrosion of the AB coating, showing potential transients. 3.0 ms^{-1}, 25 °C, 3.5 % NaCl.*

5.4 Corrosion mechanisms of the AB and NAB coatings

Surface SEM, EDX and profilometry results indicated that the interconnected pores within the coating are responsible for electrolyte permeation and corrosion at both the coating and coating/substrate interface. Corrosion processes occurred in three steps (1) initial corrosion on the coating surface and electrolyte ingress into the pores, (2) corrosion of the coating – in the pore network and finally (3) galvanic coupling between the steel substrate and the coating. The three corrosion processes will be discussed below.

5.4.1 Coating surface corrosion and dealloying

As a result of the HVOF coating process, the final morphology and composition of the splats are different from the original coating powders. Unmelted particles, splats with different chemical composition and phases, oxides and impurities are present within the coating. For cast aluminum bronzes, the decomposition of β-phase into $\alpha + \gamma_2$ phase at 565 °C could prove detrimental to their corrosion resistance [57]. Similar behaviour could occur on the HVOF aluminum bronze coating as the HVOF process involves temperatures between 2000 and 3000 °C. Air cooling after the spraying process can cause the formation of aluminium rich γ_2-phase within the coating splats. When exposed to electrolyte, the more active γ_2-phase within the splats will corrode anodically while the copper rich α-phase would act as cathodes.

$$2Cu + H_2O \rightarrow Cu_2O + 2H^+ + 2e^- \qquad \textit{Equation 5-2}$$

$$2Al + 3H_2O \rightarrow Al_2O_3 + 6H^+ + 6e^- \qquad \textit{Equation 5-3}$$

The cathodic reactions are:

$$2H_2O + O_2 + 4e^- \rightarrow 4OH^- \qquad \textit{Equation 5-4}$$

$$Cu^{2+} + 4e^- \rightarrow Cu \qquad \textit{Equation 5-5}$$

The reduction of copper ions and enhanced dissolution of aluminium are responsible for the dealloying process in aluminium bronze alloys [60,139]. The dissolution of copper and aluminium in Equations 5-2 and 5-3 will form an insoluble protective layer on the coating surface. This protective layer consists of two sub-layers, Cu_2O is enriched at the top while Al_2O_3 is predominant at the bottom [62,137]. These reactions can be associated with the ennoblement of the OCP as seen in Figure 5-8.

5.4.2 Pore network corrosion

Impurities and pore openings on the coating surface can result in discontinuities on the protective layer. The pores can allow the electrolyte to permeate the coating, resulting in similar reactions observed in Equations 5-2 and 5-3. For the NAB coatings, the AB coating

particles can be further anodically polarised by the stainless steel particles [160]. The stainless steel particles can also form an insoluble passive layer, the thickness of the passive layer (~5 nm) implies that not all the pores can be blocked, especially the larger ones (> 1μm).

As corrosion proceeds, the pore network may eventually be de-aerated, the oxygen reduction reaction in Equation 5-4 will cease to occur. Also, the chloride ions can react with the H^+ produced by anodic reactions to form hydrochloric acid:

$$H^+ + Cl \rightarrow HCl \qquad \textit{Equation 5-6}$$

This will result in a low pH (acidic) environment within the pore network, increasing the dissolution rate of the coatings. Under acidic conditions, formation of a non-adherent and soluble $CuCl$ can occur [137]:

$$Cu + Cl \rightarrow CuCl + e^- \qquad \textit{Equation 5-7}$$

It is possible for the $CuCl$ to be transported to the coating surface and be re-deposited as Cu_2O or CuO. Similar reactions can also occur on the aluminium rich phases within the coating:

$$Al^+ + Cl \rightarrow AlCl \qquad \textit{Equation 5-8}$$

$$Al^{3+} + 2OH^- + Cl \rightarrow Al(OH)_2Cl \qquad \textit{Equation 5-9}$$

These products can also be transported to the coating surface and re-deposited as Al_2O_3.

5.4.3 Coating/substrate interface corrosion

Interconnected pore networks within the coating permit the electrolyte to reach the coating/substrate interface. The 4360 steel substrate will be polarised anodically by the noble AB coating resulting in severe corrosion of the substrate. This can result in the delamination of the coating interface, forming blisters that were observed previously in Figure 5-6. The transportation of ferrous ions to the coating surface can result in the formation of iron oxides, indicated by rust spots observed visually and by EDX (Table 5-2).

The corrosion at the pores and coating/substrate interface occurs under acidic conditions, similar to those found in pitting and crevice corrosion. It is possible for the oxidation and subsequent protective film regeneration to cause the potential transients observed in Figure 5-9.

5.4.4 Scale formation on the coating surface

The tap water used for the experiments contained about 250 ppm of calcium ions [153], making it possible for the formation of carbonate scale. Carbon dioxide dissolved in the water forms carbonic acid, H_2CO_3, and reduces the pH by dissociation to H^+ and the bicarbonate ion, HCO_3^-:

$$CO_2 + H_2O \rightarrow H_2CO_3 \rightarrow H^+ + HCO_3^- \qquad \textit{Equation 5-10}$$

The bicarbonate ion forms insoluble calcium carbonate, $CaCO_3$, surface films by:

$$Ca^+ + 2HCO_3^- \rightarrow Ca(HCO_3)_2 \rightarrow CaCO_3 + CO_2 + H_2O \qquad \textit{Equation 5-11}$$

Similar metallic carbonates can also be formed by the dissolution of copper and aluminium within the coating. These reactions are probably responsible for the formation of scale features that are observed in Figure 5-7.

5.5 Conclusions

Flow corrosion experiments have been carried out on the AB and NAB coatings, as well as the steel substrate, at two different conditions (5 hours and 5 days). The following conclusions can be drawn:

1. The flow corrosion rate of the NAB coating was between 0.8 ~ 1.3 mm/year and was slightly lower than the AB coating which had a rate of 2.0 mm/year.

2. Both coatings showed lower corrosion rates when compared to the 4360 steel substrate (3.0 mm/year). Comparison with results from the literature showed that the flow corrosion rates of the coatings are higher than typical alloys used in the marine industry.
3. Surface filming occurred on both the coating surface, indicating that they behave similarly to bulk AB/NAB alloys. However, the films are not uniform, reflecting the presence of open pores on the coating surface. EDX analysis on the film revealed combinations of Al and Cu oxides.
4. Scale features were formed on the coating surfaces, EDX analysis revealed Al and Fe oxides, indicating the corrosion of the coating and steel substrate. The pore openings are believed to be areas where corrosion products from within the coating are transported to the coating surface.
5. The corrosion mechanism of the AB coatings are determined. Combinations of pore network corrosion and coating/substrate interface corrosion resulted in the formation of blisters and coating delamination.
6. The evaluation of the OCP was found to be a useful technique in monitoring film formation during exposure to the electrolyte jet. The technique shows promise in detection of localised corrosion occurring within the pores and coating/substrate interface, possibly explaining the transients observed on the 5th day of the experiment.

Chapter 6 Erosion-corrosion

6.1 Introduction

This chapter describes the erosion-corrosion experiments, carried out on the AB and NAB coatings. Similar experiments were carried out on 4360 steel specimens for comparison with the coatings. This chapter attempts to quantify the erosion-corrosion rate and mechanisms for both the coatings by using a jet impingement apparatus. 5 hour tests were used for evaluating the erosion-corrosion rates, from which mass loss measurements were quantified. Erosion-corrosion mechanisms were established from 5 day jet impingement experiments, the results were analysed using the SEM and open circuit potential measurements.

6.2 Experimental methodology

Erosion-corrosion experiments have been carried out on jet impingement rigs, previously described for the pure erosion (Chapter 4) and flow corrosion (Chapter 5) conditions. The electrolyte was made up of 3.5 % w/w NaCl in tap water and silica sand particles (135 μm and 235 μm) were utilised. Specimens were allowed to corrode freely under slurry jet impingement. The impingement angle of the jet on the specimen surface was 90°. A range of velocities (3.1 ~ 6.7 ms^{-1}) and sand concentrations (1.5 ~ 5.0 % w/w) were utilised to investigate the effects of kinetic energy and sand concentration. Procedures were similar to that explained in the pure erosion and flow corrosion chapters (Chapter 4 and Chapter 5 respectively). A surface area of 900 mm^2 was exposed to the slurry jet and all surfaces were lapped to R_a < 1 μm before the tests were carried out. 4360 steel was used as a reference material and as a substrate for the NAB coating.

Gravimetric measurements were carried out by using a precision balance with a range of 200 g and an accuracy of ± 0.02 mg. The procedures are similar to that described in earlier sections. The results have been separated into two sections, the effect of kinetic energy and the effect of sand concentration. As with the pure erosion experiments, mass loss under

erosion-corrosion was expressed as volume loss per unit impact, V_n. Also, the open circuit potential (OCP) was collected throughout the experiment under free corrosion conditions.

6.3 Results and discussion

6.3.1 Erosion-corrosion rate

Figure 6-1 shows the relationship between V_n and kinetic energy under erosion-corrosion condition. The figure presents results obtained from the 4360 steel, AB coating and NAB coatings. It clearly demonstrates that material loss increased with kinetic energy. This is associated with higher energy sand particles generating more severe plastic deformation wear and cutting wear (refer pure erosion mechanisms, Chapter 4). Furthermore, higher kinetic energy impacts can cause rupture of the protective surface film, increasing the charge transfer reactions on the coating surface [165]. It has been previously reported that the highly stressed plastic deformation lips can be susceptible to stress corrosion cracking and therefore can be easily removed from the surface by subsequent impacts, further increasing the wear rate [72,74]. Both effects of protective film removal and stress corrosion cracking of the plastic deformation lips can result in synergy between erosion and corrosion, this phenomenon will be discussed in the following chapters.

Trend lines were fitted to the points and good correlations were found. The kinetic energy exponents are translated to velocity exponents (refer Equation 4-5, Chapter 4). The velocity exponents (n) for the NAB coating and 4360 steel were found to be 2.4 and 1.8 respectively. A separate experiment was also carried out on the AB coating at E_k = 0.23 μJ. The erosion-corrosion rate of the AB coating was found to be slightly lower than that of the NAB coating, possibly due to AB coating having a homogeneous microstructure while the heterogeneous NAB coating consists of heterogeneous particles of different alloys and different mechanical properties. The higher porosity within the NAB coating could also contribute to an increased wear rate [89,146,147].

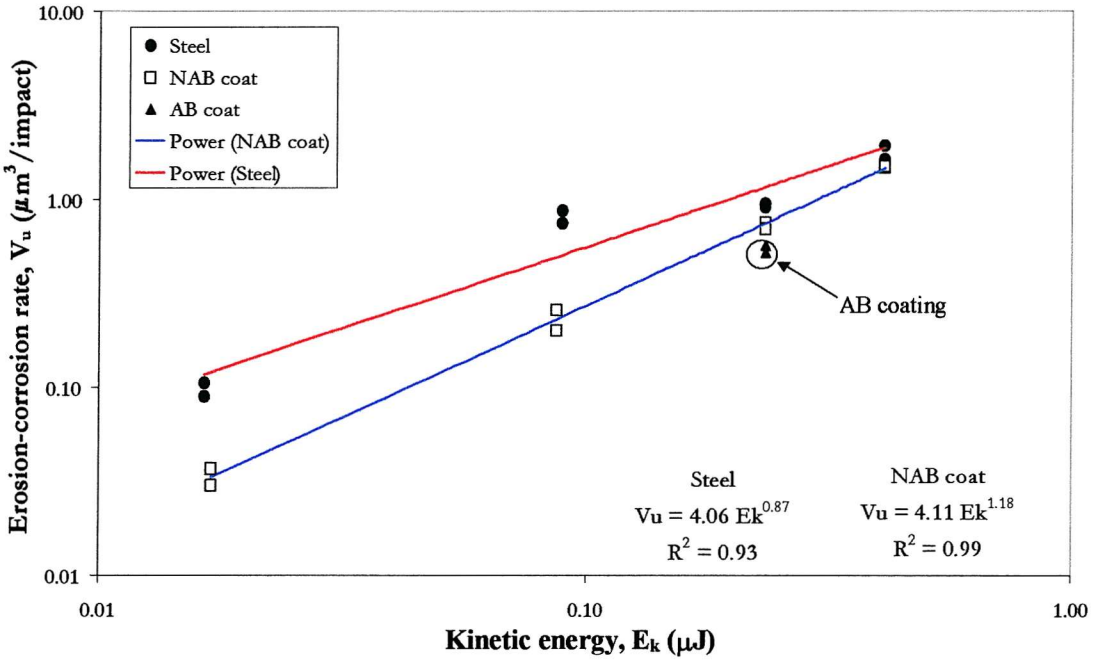

Figure 6-1 *Relationship between erosion-corrosion rate and kinetic energy. 25 °C, 3.5 % NaCl, 3 %w/w sand concentration.*

For the NAB coating, the velocity exponents under erosion-corrosion conditions (n = 2.36) are slightly lower than pure erosion conditions (n = 2.40). This is consistent with HVOF coating erosion results obtained by Bardal *et al* [2]. The lower velocity exponent is associated with the ability for the coatings to form an adherent oxide film on its surface under corrosive conditions. This can possibly reduce the coating wear rate, especially when the oxide layer remains intact under particle impingement. This is further confirmed by the 4360 steel which is a non-passivating material. The velocity exponent under erosion-corrosion (n = 1.74) is higher than pure erosion conditions (n = 1.58). Uniform corrosion, coupled with stress corrosion cracking of the work hardened plastic deformation lips contributed to an increased wear rate under erosion-corrosion conditions.

The velocity exponents have also been compared with results obtained from the literature and are shown in Table 6-1. The n value for the NAB coating is shown to be consistent with exponents obtained by other HVOF coatings, it is also comparable to typically ductile materials like duplex stainless steels [2,86]. The observation indicates that ductile mechanisms are responsible for material removal (refer Chapter 4).

Table 6-1 Comparison of the velocity exponents under erosion-corrosion condition, found in the current work and those from the literature.

Materials	**Reference**	**Velocity exponent (*n*)**
NAB coating (EC) 4360 steel (EC)	Current work	2.4 1.8
Duplex stainless steel, bulk (2205) (EC) HVOF WC-Co based coating (EC)	[2]	2.7 2.7
Duplex stainless steel, bulk (UNS S31803) (EC) HVOF WC-Co based coating (EC)	[86]	2.2 0.6

The higher wear rate of the BS4360 steel can be explained by considering the hardness values and standard electrode potentials. Hardness and yield strength values for carbon steels are 30% lower than the NAB coating (refer Chapter 3), resulting in more severe plastic deformation and cutting wear. Carbon steels are also more anodic than the copper alloys [135]; the increased corrosion rate and its inability to form a protective layer can result in higher dissolution rates under erosion-corrosion conditions. At the lowest kinetic energy condition (~0.02 μJ), the material loss for steel is nearly an order of magnitude higher than that of the NAB coating. At higher kinetic energy (~0.4 μJ), the wear rates for both materials became similar. The increase in NAB coating wear rate at high kinetic energy can possibly be linked to cracking of brittle alumina at the splat boundaries (previously discussed in Chapter 4).

The erosion-corrosion rate for the 4360 steel and the NAB coating was also compared to that of pure erosion, shown in Figure 6-2. The data was plotted on a linear scale to accentuate the higher volume loss due to erosion-corrosion. It is evident that the erosion and erosion-corrosion rates for both materials are very similar up to 0.23 μJ. Beyond that kinetic energy, the effects of corrosion resulted in higher volume loss as a result of synergy.

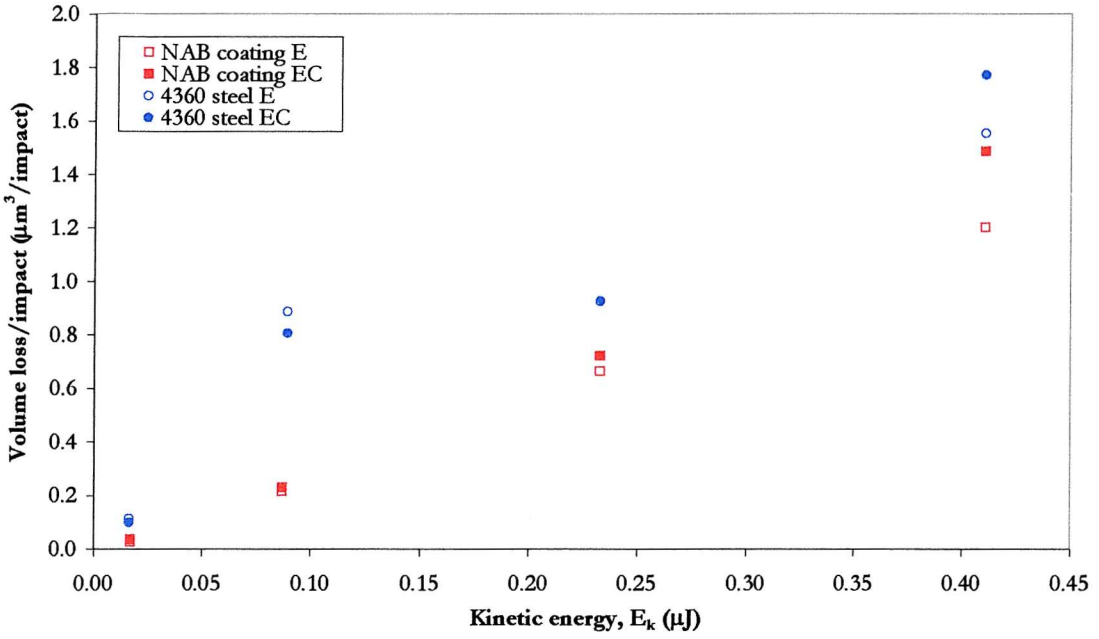

Figure 6-2 *Comparison between erosion and erosion-corrosion rates for both 4360 steel and NAB coating.65*

6.3.2 Effects of sand concentration

Figure 6-3 shows the relationship between material removal efficiency and sand particle concentration under erosion and erosion-corrosion conditions. The results are compared with pure erosion and those obtained by Turrenne *et al* [24]. Similar trends in material removal efficiency were found for pure erosion and erosion-corrosion conditions. Erosion-corrosion showed higher material removal efficiencies at 5 %w/w, probably due to the added effects of corrosion in the system. This is due to increased surface film removal by the particles, resulting in enhanced corrosion.

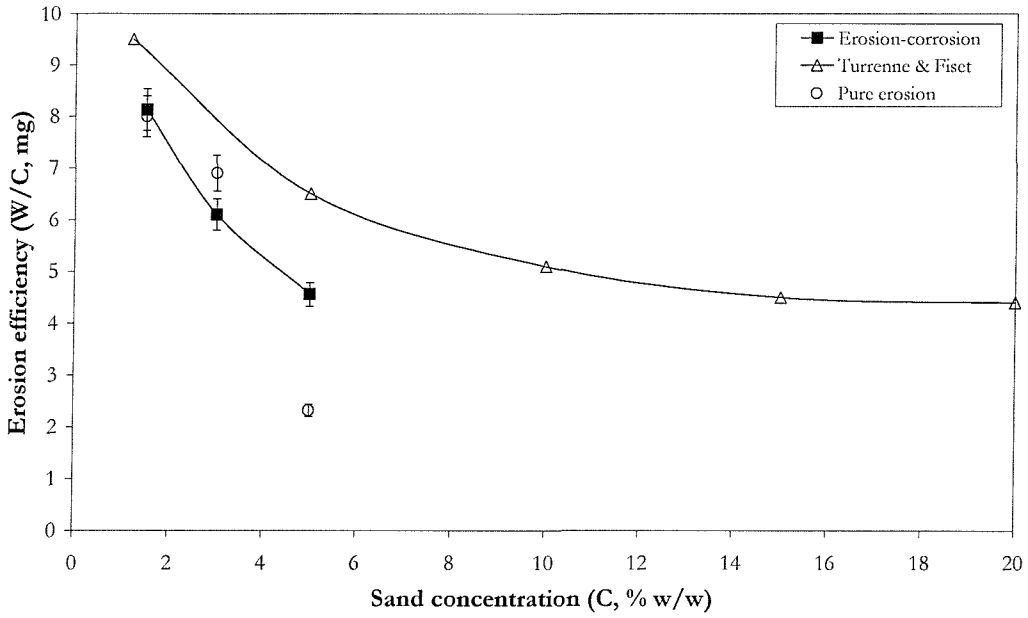

Figure 6-3 *Material removal efficiency versus sand concentration for NAB coating and data from Turenne and Fiset [24]. 5.0 ms^{-1}, 25 °C, 3.5 % NaCl, 235 μm sand particle diameter.*

6.3.3 SEM investigations

Micrographs were taken from the 4360 steel surface after erosion-corrosion tests, shown in Figure 6-4. A micrograph at low magnification, obtained from the centre region is shown in Figure 6-4a. Randomly distributed wear scars, due to a ductile wear mechanism can be seen. Sand particles impact the surface at normal incidence, resulting in multiple plastic deformation sites in this region. A higher magnification micrograph in Figure 6-4b shows the plastic deformation in detail. It is apparent that plastic lips from the wear scar have superimposed over each other. This observation is in agreement with those observed for ductile materials [3,28] and are associated with extrusion and plastic lip formation wear [148].

Figure 6-4c shows the outer region of the erosion-corrosion specimen at low magnification, it reveals cutting wear scars on the surface. The cutting/ploughing action also caused the formation of plastic lips on either side of the cutting mark. These types of wear scars at the outer region have also been observed by other workers [3,87]. The cutting marks are associated with particles contacting the surface at oblique angle, due to the hydrodynamic streamlines of the slurry jet [87].

The micrographs are also similar to those found for the AB coating under pure erosion conditions (see Chapter 4). However, darkened areas and white spots were found on the surface (Figure 6-4a and Figure 6-4c). Darkened areas were also observed in recent work by Neville and Xu [166], on the erosion-corrosion of stainless steels in 3.5 % NaCl. It was reported that the dark regions are associated with corrosion products. The white spots are similar to those observed under flow corrosion conditions (refer Chapter 5), associated with calcite scales. More corrosion products were found on the outer regions of the surface, possibly indicating that reduction reactions occur here more easily. The results are consistent with those of Neville *et al.* [167], they suggested that anodic reactions occur predominantly at the centre region while cathodic reactions occur at the outer regions. This is associated with increased numbers of impacts and cutting wear occurring near the centre region, producing fresh surfaces and increasing the dissolution rate.

Fractured plastic deformation lips were also observed, shown in Figure 6-4d. This is possibly due the work hardened (highly stressed) lips undergoing stress corrosion cracking, causing it to be easily fractured by subsequent particle impacts.

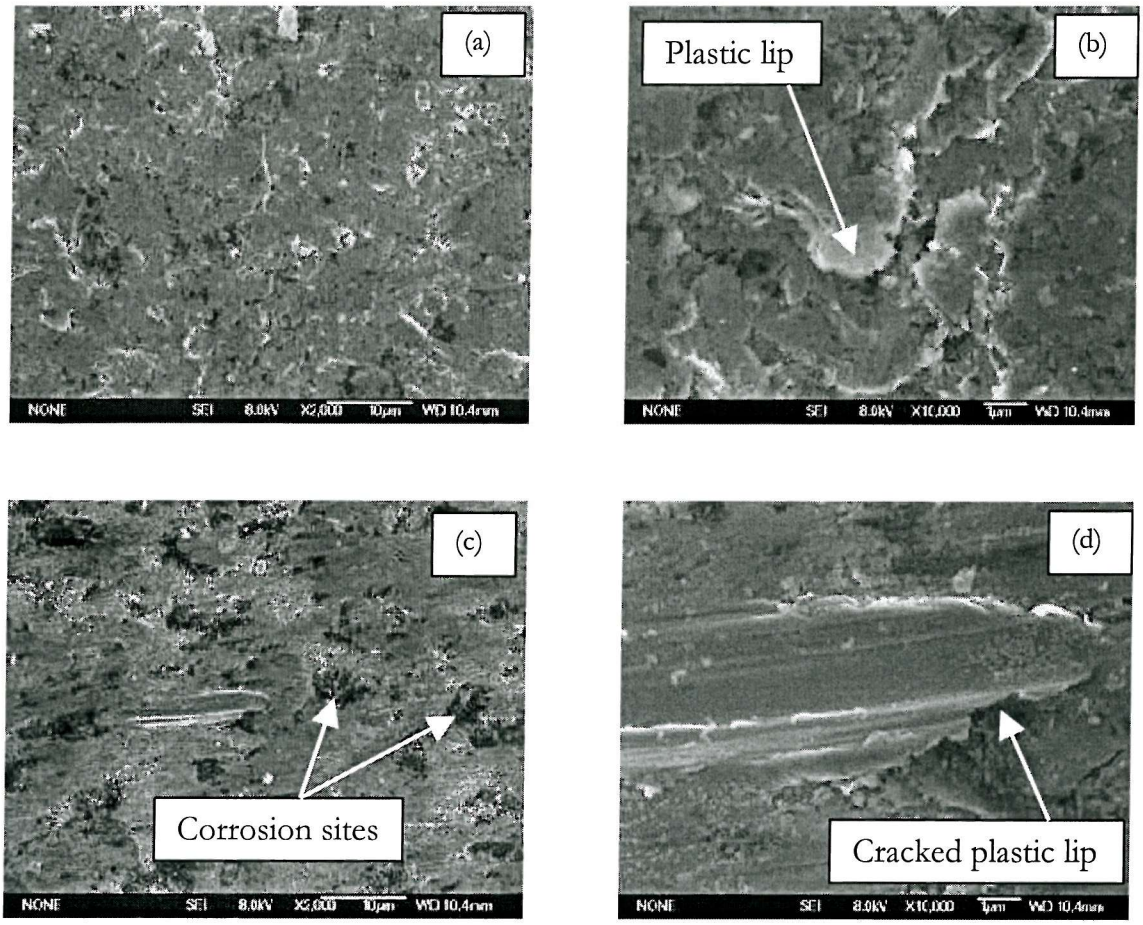

Figure 6-4 *Micrographs showing the 4360 steel surface after 5 hours erosion-corrosion. 5.0 ms^{-1}, 25 °C, 3.5 % NaCl, 3 % w/w sand concentration.*

SEM investigation on both the AB and NAB coating surface revealed a similar ductile wear mechanism to that of the 4360 steel. A representative NAB coating surface micrograph after erosion-corrosion is shown in Figure 6-5, similar erosion-corrosion features were found for both coatings. Figure 6-5a and Figure 6-5b shows the centre region of the wear scar at low and high magnifications respectively. Similar micrographs are obtained for the outer regions, shown in Figure 6-5c and Figure 6-5d.

Corrosion sites, indicated by darker areas, were also observed throughout the entire coating surface. Noel *et al.* [168] suggested that the cutting/ploughing process removed the protective film on the surface, resulting in anodically polarised cutting marks and adjacent cathodic areas. These findings demonstrated the effects of erosion enhanced corrosion, whereby protective layers are removed under solid particle impingement.

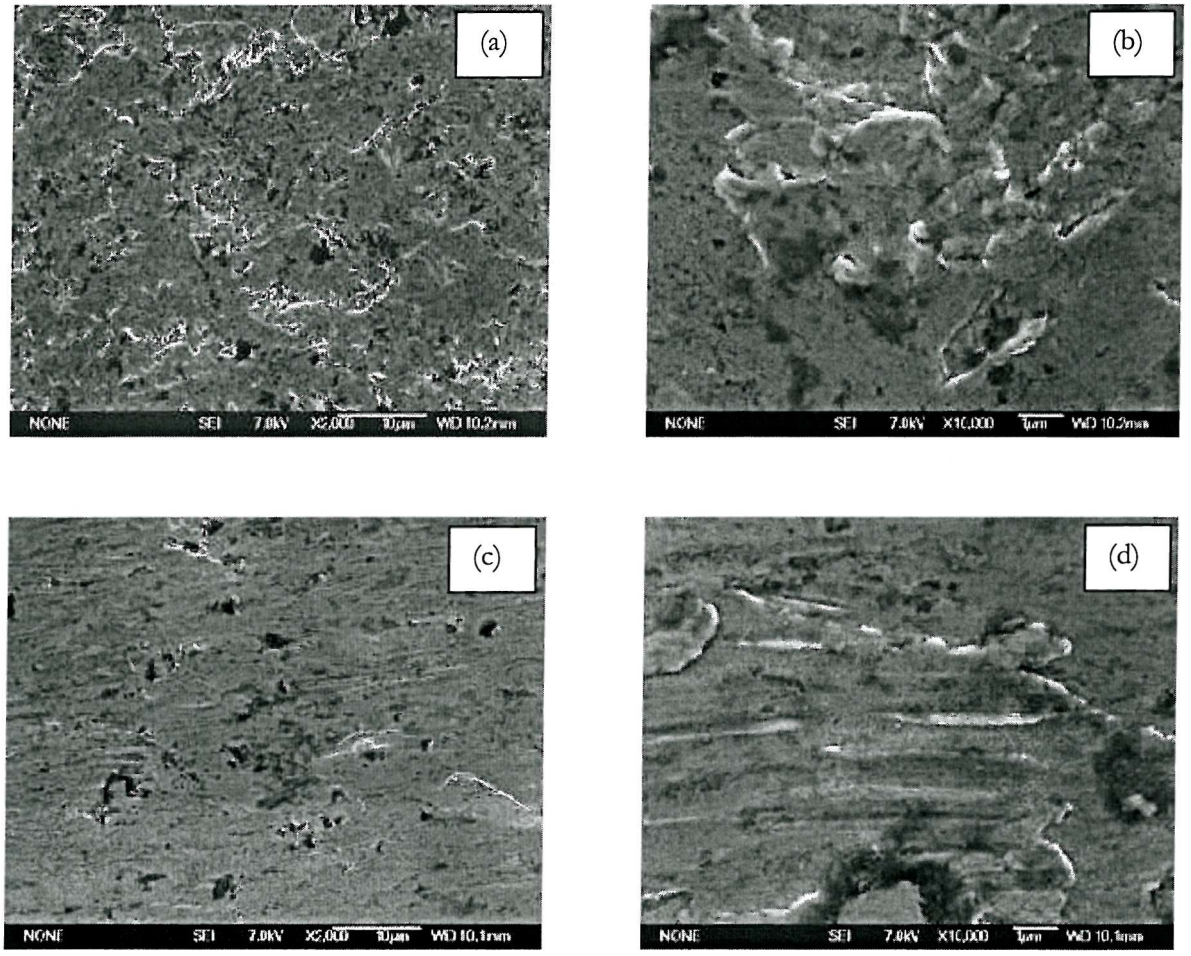

Figure 6-5 *Micrographs showing the NAB coating surface after 5 hours erosion-corrosion. 5.0 ms^{-1}, 25 °C, 3.5 % NaCl, 3 % w/w sand concentration.*

6.3.4 5 day experiments

Visual examination carried out on the AB coating surface, after 5 days of erosion-corrosion, did not reveal signs of the extensive scaling previously seen in the flow corrosion specimens (Chapter 5). This is probably due to the sand particle impingement deforming the surface and removing the calcite scales. The area directly under the slurry jet revealed a fresh surface free from surface films, while filming was observed at the outer areas.

A schematic representation of the surface is shown in Figure 6-6. A W-shaped erosion feature was observed on the specimen surface exposed to slurry jet impingement. Red rust was also observed at the region of maximum erosion, indicating the evidence of coating failure (perforation) and subsequent corrosion of the steel substrate. As seen in Chapter 4, W-shaped

scars demonstrate ductile erosion mechanisms, involving plastic deformation and cutting wear. These mechanisms are commonly found in copper and its alloys [30]. These outer regions showed a copper coloured (red tinted) surface, suggesting signs of dealloying of aluminum from the coating [60,139]. This observation confirmed that the outer regions are mainly cathodic and reduction reactions such as copper re-deposition occurred here. The wear feature shows greater penetration on the right side, probably due to the vertical orientation of the specimen (with the right side at the bottom). The effect of gravity on the slurry jet resulted in higher sand concentrations, consequently causing most material damage in this area.

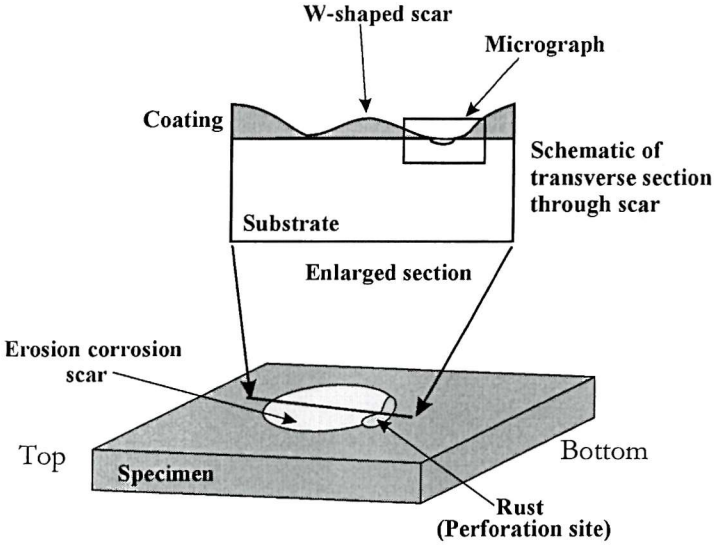

Figure 6-6 Schematic diagram of a post erosion-corrosion test sample, showing the transverse section of the wear feature where coating perforation occurred.

Figure 6-7 shows an optical microscope image obtained from a transverse section of the erosion-corrosion scar. It is evident that the coating has perforated after 5 days of slurry jet impingement, exposing the carbon steel substrate to the 3.5 % NaCl solution. The thickness of the coating was reduced from an initial 200 μm to less than 50 μm adjacent to the area of perforation; the coating thickness at the centre of the W-shaped scar was approximately 120 μm. The coating has also suffered from delamination adjacent to the site where the substrate was exposed. The delamination was possibly due to corrosion of the anodic carbon steel substrate when coupled galvanically to the noble aluminum bronze coating.

The coating/substrate interface remained intact at other areas, no signs of blisters were observed. The observations indicate that the rate of electrolyte permeation through the AB

coating might be slower when compared to flow corrosion conditions (Chapter 5). The plastic deformation on the surface could seal the pore openings on the surface, hindering electrolyte permeation into the coating.

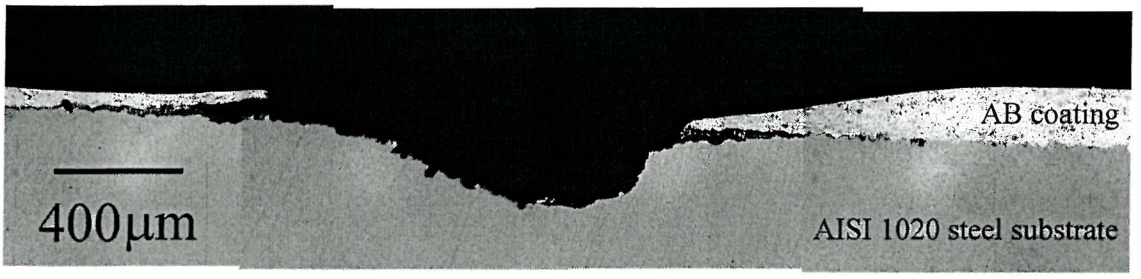

Figure 6-7 *Optical micrograph showing an area of the transverse section where the coating was penetrated after 5 days of erosion-corrosion. 3.0 ms^{-1}, 20 °C, 3.5 % NaCl, 5 % w/w sand concentration.*

6.3.5 Open circuit potential (OCP) measurements

The OCP of the AB coating, under erosion-corrosion conditions, on the first day is shown in Figure 6-8. The general behaviour is similar to that under flow corrosion conditions, a slight increase in OCP values from - 340 mV to - 320 mV (SSC) was observed. Such an increase can be associated with ennoblement processes: when the clean surface was exposed to flowing slurry charge transfer processes occur which transforms the air formed film into a protective layer. The ennoblement lasted only an hour, as opposed to 24 hours under flow corrosion condition (Figure 5-8, Chapter 5). This is probably caused by the sand particle impingement, removing and preventing the growth of a stable protective layer. The OCP then increased slowly for the next few days, finally settling down at - 300 mV (SSC) after 3 days. The steady-state potential of the coating under erosion-corrosion conditions is 70 mV more electronegative when compared to flow corrosion conditions, this can be attributed to increased corrosion rates. A more active surface is found under erosion-corrosion as impinging sand particles continuously remove/damage the surface film.

Figure 6-9 shows the OCP of the coating, obtained on the 5th day of the erosion-corrosion experiment. The OCP value was at its steady state of - 300 mV (SSC) in the first 10 hours, a potential drift occurred from the 110th hour onwards, with the OCP value drifting to - 430 mV (SSC) in the final 10 hours. The potential drift was attributed to coating perforation as

seen in Figure 6-7. The mixed potential of - 430 mV suggests a galvanic couple has developed between the carbon steel and the AB coating, similar to those found in static immersion experiments (Section 3.4). Around the 107th hour, a potential step of 2 mV occurred, possibly an indication of the early stages of coating failure.

Comparisons with flow corrosion data (Figure 5-8 and Figure 5-9, Chapter 5) show higher amplitude OCP fluctuations under erosion-corrosion conditions. Standard deviation values were calculated when the OCP achieved steady state, the values are found to be 0.06 mV and 0.29 mV for flow corrosion and erosion-corrosion respectively. This five times difference in standard deviation indicates a more reactive surface, possibly due to increased corrosion rate by sand particle impingement [125]. The results indicate that OCP measurements can be used for differentiating flow corrosion and erosion-corrosion conditions.

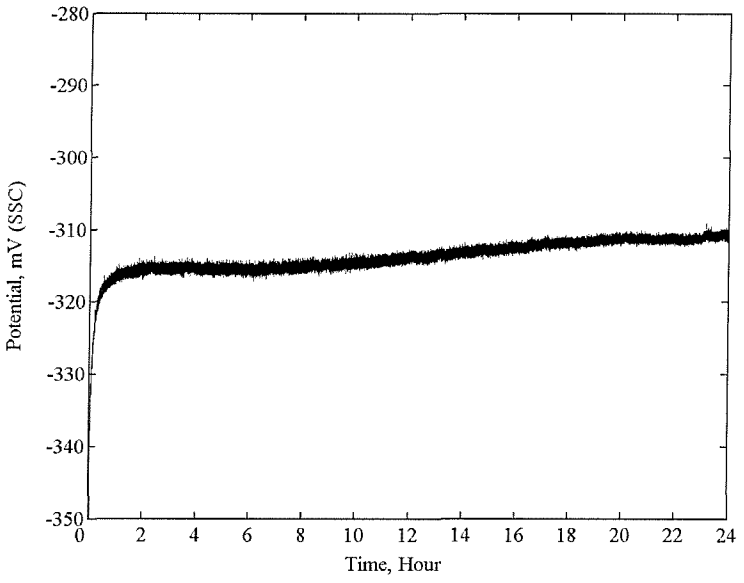

Figure 6-8 *OCP measurements during the first day of the AB coating erosion-corrosion experiment, showing higher oscillating potential levels. The initial increase indicated surface film formation. 3.0 ms^{-1}, 20 °C, 3.5 % NaCl, 5 % w/w sand concentration.*

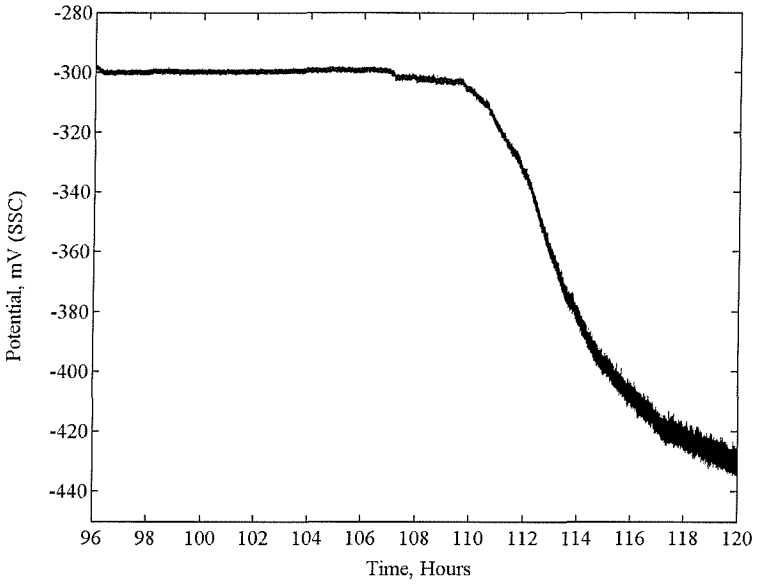

Figure 6-9 *OCP measurements during the 5th day of the AB coating erosion-corrosion experiment, showing a potential step of 2 mV (at the 107th hour). Early stages of coating failure were shown, followed by a potential drift of 130 mV towards the electronegative direction indicating corrosion of the carbon steel substrate. 3.0 ms^{-1}, 20 °C, 3.5 % NaCl, 5 % w/w sand concentration.*

6.4 Conclusion

Erosion-corrosion experiments have been carried out on the AB and NAB coatings and the 4360 carbon steel substrate. Experiments with two durations (5 hours and 5 days) have been designed to quantify and investigate the erosion-corrosion rate and mechanisms of the coatings and carbon steel. The following conclusions can be drawn:

1. Lower velocity exponents are obtained for the NAB coating under erosion-corrosion conditions. This can be explained by the ability of the coatings to form a protective layer on the surface under erosion-corrosion conditions. Carbon steels showed increased velocity exponents due to the added effects of corrosion (inability to form a protective film and uniform corrosion).
2. The velocity exponent values obtained under erosion-corrosion are found to be within the range of other passivating materials found in the literature, such as HVOF WC-based coatings and duplex stainless steels.
3. The physical aspects of material removal under erosion-corrosion, for both coatings and the carbon steel substrate, are similar to that under pure erosion conditions – involving ductile mechanisms. Additional material loss was attributed to the effects of corrosion, involving charge and mass transfer processes and the stress corrosion cracking of the work hardened plastic lips.
4. Plastic deformation on the coating surface have a pore sealing mechanism, preventing electrolyte from permeating the coating to cause coating/substrate interface corrosion (seen in flow corrosion conditions, Chapter 5).
5. A galvanic couple between the noble coating and the active substrate is formed when the coating perforates. This leads to enhanced corrosion at the coating/substrate interface, adjacent to the perforation site.
6. Standard deviation of the OCP measurements can be used to distinguish between flow corrosion and erosion-corrosion condition. Erosion-corrosion produced standard deviations that are 5 times higher than under flow corrosion, associated with increased corrosion sites. These sites are formed by solid particles impinging on the surface and removing the protective layer.
7. The OCP can also be used to detect the onset of coating perforation. This is shown by a drift in the electronegative direction. The drift is due to mixed potentials between the

coating and the exposed substrate, similar to those found under static immersion tests (Section 3.4).

Chapter 7 Synergy

7.1 Introduction

Synergy is defined as the extra material loss resulting from the interaction of erosion and corrosion processes [169], its relation to erosion (E), corrosion (C) and erosion-corrosion (T) processes is shown in Equation 7-1. In the current investigation, corrosion (C) rates were obtained from flow corrosion experiments described in Chapter 5. As previously observed in erosion-corrosion (Chapter 6), synergy can result from 'erosion enhanced corrosion' (ΔC) and 'corrosion enhanced erosion' (ΔE). In this section, mass loss and profilometry measurements will be used for evaluating the synergistic effects (S) under erosion-corrosion.

$$T = E + C + S \qquad \textit{Equation 7-1}$$

Results of the NAB coating noise measurements were also analysed by using both statistical and frequency domain methods. The electrochemical current noise (ECN) was obtained from flow corrosion and erosion-corrosion experiments. The results are presented in the order of mass loss, surface profilometry, standard deviation, wavelets and empirical mode decomposition.

7.2 Gravimetric mass loss measurement

Figure 7-1 shows S percentages obtained from T, E and C experiments at three different velocities. Only the experiment utilising a 6.7 ms^{-1} velocity demonstrated a positive synergy (11 % for NAB coating and ~ 3 % for steel), experiments at lower velocities show negative synergy. For erosion-corrosion experiments at ambient room temperature, the majority of material loss usually results from mechanical damage as a result of erosion. Hence, negative S percentages are obtained when the rates of T and E are similar, shown in Table 7-1. This implies that the contributions of C towards the total material loss under erosion-corrosion conditions are minimal.

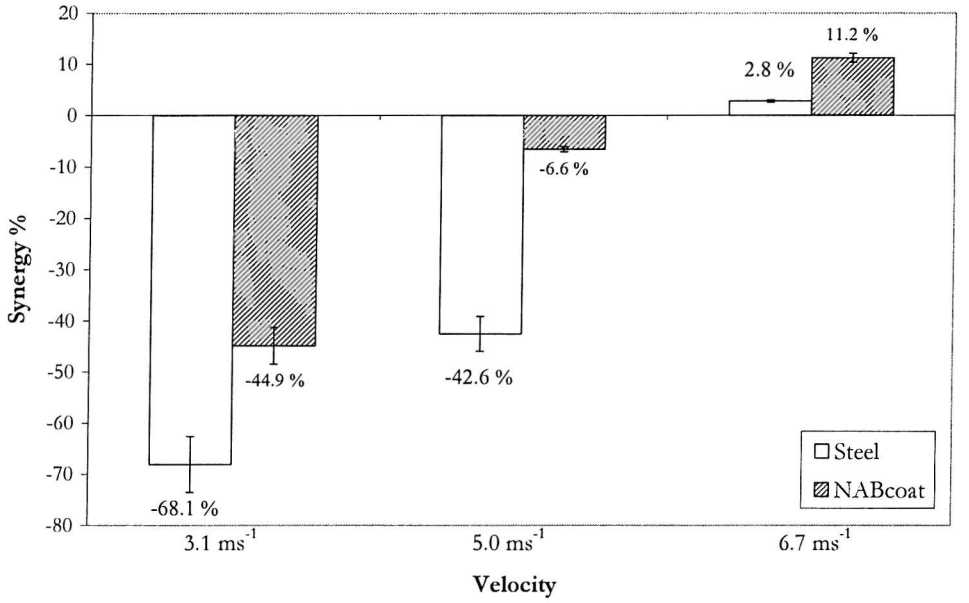

Figure 7-1 Comparison of synergy percentage, expressed as percentage of mass loss.

As seen in Table 7-1, flow corrosion can also increase the difference between T and E+C values, resulting in negative synergy. This is especially true when substantially thick oxide films or corrosion products are formed on the flow corrosion and erosion-corrosion surfaces, affecting the mass loss measurements.

Table 7-1 Synergy results obtained from mass loss measurements, for 4360 steel and NAB coating.

Material/velocity	Mass loss (mg)					Percentages	
Steel	T	E	C	E+C	S	E/T %	S/T %
3.1 ms^{-1}	18.5	20.3	10.8	31.1	-12.6	109.7	-68.1
5.0 ms^{-1}	27.5	27.5	11.7	39.2	-11.7	100.0	-42.6
6.7 ms^{-1}	100.5	88.1	9.6	97.7	2.8	87.7	2.8
NAB coating	T	E	C	E+C	S	E/T %	S/T %
3.1 ms^{-1}	4.9	4.6	2.5	7.1	-2.2	93.9	-44.9
5.0 ms^{-1}	18.3	16.9	2.6	19.5	-1.2	92.3	-6.6
6.7 ms^{-1}	49.1	39.7	3.9	43.6	5.5	80.9	11.2

In order to reveal the effects of C in determining positive/negative synergy effects, ratios of S/T and E/T are plotted in Figure 7-2. The figure consists of data points obtained from current results and those found in the literature [2,71,75,86,92,166,167,170-173]. The results were mostly obtained from mass loss measurements from synergistic based experiments (i.e. where T, E and C mass loss measurements were made). As seen in Table 7-2, the data points were obtained from the slurry jet, slurry pot, two-body abrasion rig and cavitation tunnels. A wide range of experimental condition was used: velocity ranges between 3.0 and 29.3 ms^{-1},

sand sizes between 63 and 230 μm, 0.03 ~ 5.0 % w/w sand concentration and three types of electrolytes (tap water, NaCl and Na_2SO_4). Corrosion rates from the table were obtained under dynamic conditions.

Figure 7-2 demonstrates that irrespective of the experimental conditions, target materials and apparatuses used, the transition between positive and negative synergy occurs at the same position. This observation allows for the determination of a synergy constant (SC) defined by a zero synergy and the E/T ratio being 0.83. The effect of E/T ratio on the extent of synergy implies the extent corrosion affects the total material loss under erosion-corrosion (T).

When the ratio is greater than 0.83, corrosion has a negative effect on the overall system (i.e. negative synergy or antagonism). This can be a result of passive film formation or thick oxide formation (e.g. high temperature erosion-corrosion), protecting the surface from further oxidation and subsequent materials loss. E/T ratios lower than 0.83 indicates high levels of erosion and corrosion interactions and is associated with an actively corroding surface. Under such conditions, both erosion enhanced corrosion and corrosion enhanced erosion contributes toward a positive synergy value.

Table 7-2 Review of experimental conditions and rigs used for evaluating synergy.

Material	Experiment	Rig	Velocity (ms^{-1})	Sand type	Electrolyte	Angle	Notes	Reference
Bulk A 514 steel, SS 316 and low alloy steel	Abrasion-corrosion	Slurry pot/ Cylinder anvil	5.8 – 15.6	Silica sand (50-70 mesh)	Tap water	N/A	Corrosion rates obtained from current density (dynamic)	[71]
HVOF WC based coatings and steel	Erosion-corrosion	Slurry pot	14.3	Silica sand (230 μm)	Synthetic seawater	N/A	Corrosion rates from mass loss (dynamic).	[2]
Duplex stainless steel and HVOF WC coatings	Erosion-corrosion	Slurry pot	14.3	Silica sand (200 μm)	Synthetic seawater	M/A	Corrosion rate obtained from current density (dynamic).	[92]
Stainless steels and HVOF WC coating	Erosion-corrosion	Slurry pot	14.3 – 29.3	Silica sand (200 μm)	Synthetic seawater	N/A	Corrosion rate obtained from current density (dynamic).	[86]
Bulk A 514 steel, SS 316 and low alloy steel	Abrasion-corrosion	Slurry pot	5.8	Silica sand (50-70 mesh)	Tap water	N/A	Corrosion rates obtained from current density (dynamic)	[171]
Co-based alloy and austenitic cast iron	Erosion-corrosion	Jet impingement (immersed)	17	SiC particles (variable size)	3.5 % NaCl	90°	Corrosion rate obtained from current density (dynamic). Temperature 18 – 50 °C	[167]
Bulk copper, brass, bronze, mild steel, and stainless steel	Cavitation-corrosion	Ultrasonic cavitation	N/A	N/A	3.5 % NaCl	N/A	Corrosion rates obtained from current density (dynamic)	[170]
Copper	Cavitation-corrosion	Cavitation tunnel	14.7	N/A	Sea water	N/A	Corrosion rates obtained from current density (dynamic)	[172]
Carbon steel, cupro-nickel and duplex stainless steel	Erosion-corrosion	Jet impingement (free jet)	4 – 16	Silica sand (63 μm)	3 % NaCl	90°	Corrosion rates obtained from mass loss measurements (dynamic)	[75]
Carbon steel and stainless steels	Erosion-corrosion	In-service	0.5	Pea gravel (6.4 mm)	Synthetic mine water	N/A	Corrosion rates obtained from mass loss measurements (dynamic)	[173]
Stainless steels	Erosion-corrosion	Jet impingement (immersed)	17	SiC particles (variable size)	3.5 % NaCl	90°	Corrosion rate obtained from current density (dynamic).	[166]
Carbon steel, AB and NAB HVOF coatings	Erosion-corrosion	Jet impingement (free jet)	3.1 – 6.7	Silica sand (135 and 235 μm)	3.5 % NaCl	90°	Current work. Corrosion rates obtained from mass loss measurements (dynamic)	N/A

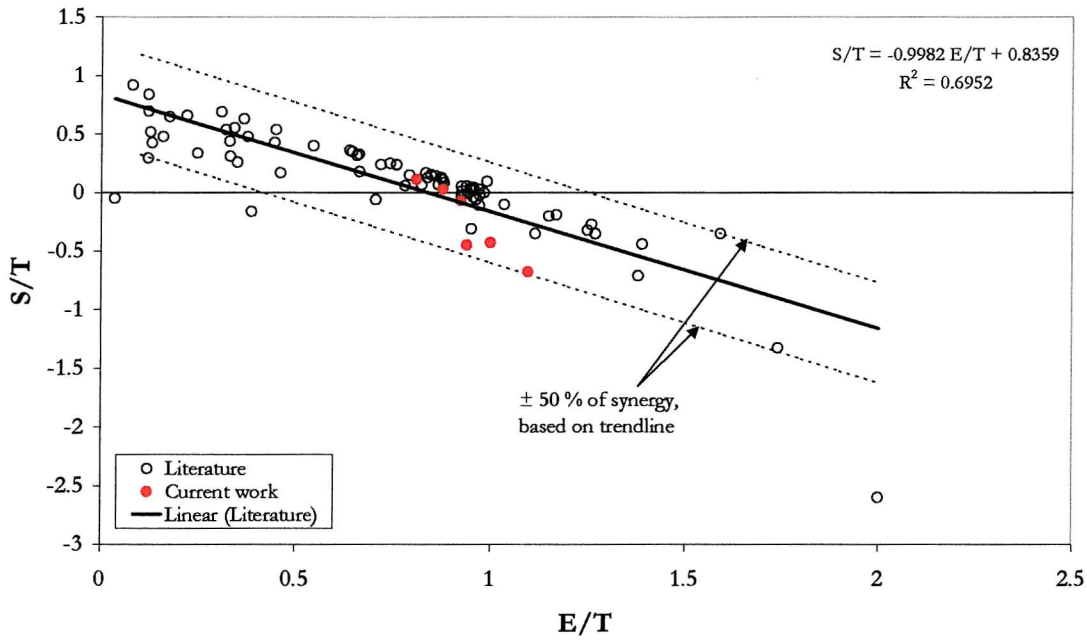

Figure 7-2 *Comparison between S/T ratio and E/T ratio for abrasion-corrosion, erosion-corrosion and cavitation-corrosion conditions.*

The SC can be used to determine the extent of synergy (whether positive or negative) for materials under various operating conditions, provided that the pure erosion and erosion-corrosion rates are known. This estimation technique is also applicable for various types of systems that undergo combined mechanical and chemical degradation (i.e. abrasion-corrosion, erosion-corrosion and cavitation-corrosion).

As seen in Figure 7-2 and Table 7-1, transitions from positive to negative synergy can occur for both carbon steels and NAB coating. This shows that the synergy can be affected by operating conditions such as erodent type, target materials, impact kinetic energy, and solids concentration. These variables can affect the overall corrosion behaviour such as passive film rupture/removal [165,174] and mass transfer [175]. Higher kinetic energy conditions (by increasing the particle size or velocity) can also increase synergistic effects by overcoming the sub-viscous layer or oxide film that exists on the specimen surface [31,77,176].

Calculations of synergy based on gravimetric measurements can be affected by inaccuracies caused by incorporating the mass of corrosion products. The gravimetric measurement errors from the current work can add up to nearly 50 % of the synergy, inevitably producing scatter in the data. Upper and lower limits of scatter (± 50 %) were calculated based on the trendline

and plotted as dotted lines, it was shown that most of the results fall within these limits. Data scatter could also be a result of the following:

1. Estimation of corrosion rates from Faradaic mass loss calculations or static corrosion experiments. Faradaic mass loss estimation may not be accurate because of the surfaces being polarised anodically at the stagnation point while the free jet region remains cathodic [167]. This can result in an internal circuit, resulting in lower current flow into the counter electrode [177]. Static corrosion rates cannot be used for synergy calculations because mass transfer reactions are higher under flowing conditions [175].
2. Use of cathodic protection for pure erosion experiments. As seen in Chapter 4, pure erosion experiments under cathodic polarisation can be affected by the deposition of calcareous deposits, affecting the mass loss measurements and synergy calculations. Furthermore, hydrogen bubble evolution and embrittlement could occur during cathodic polarisation, increasing the wear rate and complicating the synergy calculation.
3. The existence of surface films/scale on the specimen surface before weighing, due to interests in investigating the corrosion products from flow corrosion and erosion-corrosion. These products can also affect the mass loss measurements.
4. In coated systems, permeation of electrolyte into the coating/substrate interface during flow corrosion experiments can also affect the mass loss results. Experimental time should be kept short enough to prevent electrolyte permeation into the interface but sufficiently long to record a mass loss value.

In order to determine the exact transition point between positive and negative synergy, such errors have to be minimised so that a more accurate trendline can be obtained.

To further understand the contributions of erosion and flow corrosion towards synergy in the current work, their individual contributions to total material loss are plotted in Figure 7-3 for the 4360 steel and Figure 7-4 for the NAB coating. Material loss was expressed as mass loss per hour (mg/hour) so that comparisons can be made between flow corrosion (C), pure erosion (E), erosion-corrosion (T). The summation of pure erosion and flow corrosion (E+C) was also plotted, the difference between T and E+C being synergy (S). The graphs were plotted based on the assumption that C, E, and T occur uniformly over the target surface area.

The figures show that flow corrosion rates for both steel and NAB coating remained almost constant throughout the velocity range tested. The erosion and erosion-corrosion rate appears to increase with jet velocity, increasing rapidly at the highest velocity 6.7 ms^{-1}. The increasing material loss under solid particle impingement can be associated with the higher kinetic energy sand particles, resulting in more plastic deformation/cutting and higher corrosion rates.

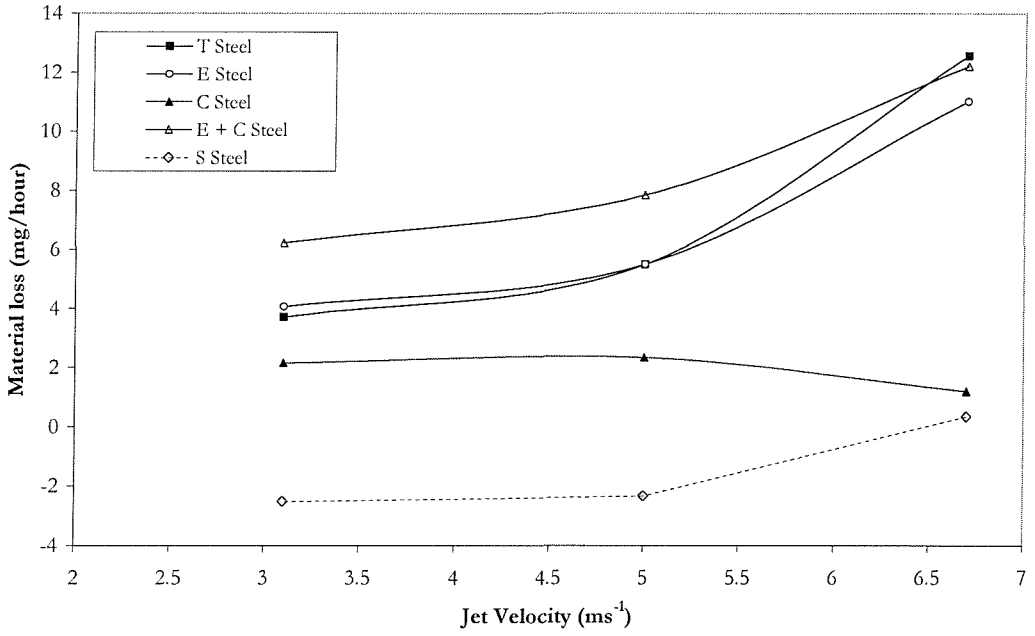

Figure 7-3 *Synergy trends for 4360 steel at different velocities. 3 % w/w sand concentration, 3.5 % NaCl solution, 20 °C.*

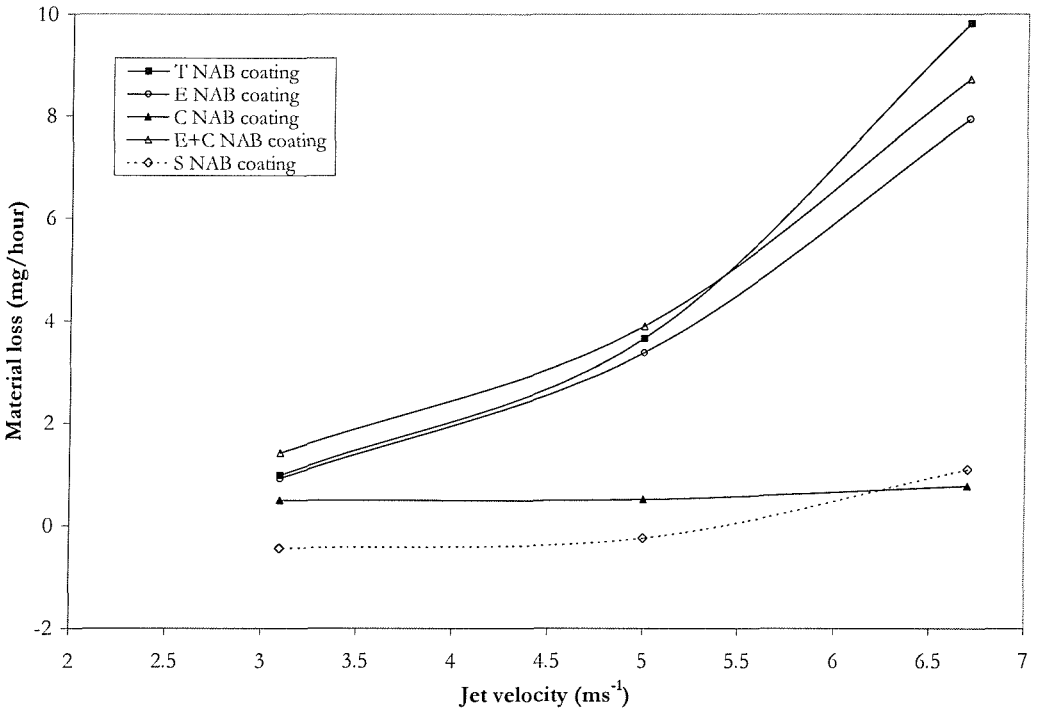

Figure 7-4 *Synergy trends for NAB coating at different velocities. 3 % w/w sand concentration, 3.5 % NaCl solution, 20 °C.*

At 6.7 ms^{-1}, the difference between erosion and erosion-corrosion appears to be larger (smaller E/T ratio) for both materials, resulting in positive synergy at that kinetic energy. This could be linked to the critical flow velocity being exceeded [160] at 6.7 ms^{-1} and thereby accelerating the mass transport reactions [161] (also refer Section 2.3.6 – critical velocity for NAB alloys). At the same time, particle impingement on the surface can alter the repassivation kinetics on the NAB coating, affecting the formation of stable oxide films. Cutting or plastic deformation could also remove the oxide layer exposing a fresh surface and increasing the anodic dissolution.

Similar graphs to Figure 6-3 and Figure 6-4 were presented by Bardal *et al* [86]. Synergy experiments were carried out on WC-Co based HVOF coatings and duplex stainless steels, using a rotating slurry pot tester and at higher velocity ranges. It was shown that between 14 and 30 ms^{-1}, positive synergy existed for the HVOF coating while negative synergy was observed for the duplex stainless steel. It was demonstrated that the duplex stainless steel has a much higher critical flow velocity under flow corrosion conditions [160], hence contribution of corrosion was not significant (i.e. E/T ratio is closer to 1).

Critical velocity based arguments can only be used to explain the increased synergy of the NAB coating at 6.7 ms^{-1}. This explanation cannot be applied to the 4360 steel, as it corrodes uniformly and does not form an adherent protective layer. Observation of the synergy plot in Figure 7-2 revealed that $E/T \geq 1$, indicating that corrosion plays a minor role in material removal under erosion-corrosion. The observation cannot be accurate, as the 4360 steel is known to be a relatively active material under flow corrosion and erosion-corrosion [135], the value for E/T should be less than one. The negative synergy observed in 4360 steel could possibly be influenced by errors introduced by mass loss measurements, it will be discussed further in the profilometry section.

7.3 Surface profilometry

Surface profilometry has been utilised for identifying the erosion mechanisms (ductile/brittle) and for estimating the amount of material loss under E, C and T conditions. The measurements were carried out by a Taylor Hobson 120L Form Talysurf apparatus. As seen in Figure 7-5, 2D profiles were measured across the centre of the specimen surface, moving across the erosion scar. Procedures for analysing the 2D profiles can be found in Appendix B. All profiles were plotted with the same vertical scale to facilitate comparisons between the E, C and T experiments.

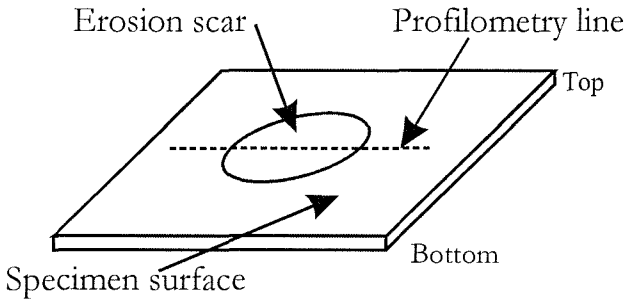

Figure 7-5 Diagram showing the location of 2D surface profile measurements.

7.3.1 NAB coating

Figure 7-6 shows the 2D profiles for the NAB coating. The profiles were obtained from T, E, and C experiments using 5.0 ms^{-1} jet velocity and 3.0 % w/w sand concentration. W-shaped scars are observed for both E and T conditions. The erosion-corrosion wear scar diameter is 11.0 mm, with the cone-shaped undamaged area at the centre. The nominal wear depth is approximately 45 μm. Slight differences in wear depth were probably caused by an asymmetrical slurry jet stream.

Under pure erosion conditions, the nominal wear depth was 33 μm. No scars were observed under the flow corrosion condition. The surface profile was similar to an as-polished specimen where edges are worn off more than those in the centre (from the grinding process). Visual inspection revealed evidence of surface filming, similar to those observed by other workers [62,132,160]. However, contacting surface profilometry was not able to determine the presence of a surface film.

The erosion-corrosion wear scar was approximately 12 μm deeper and nominally 1 mm wider than the pure erosion wear scar. This wear depth can be used as an indication of corrosion enhanced erosion and could be due to (i) the removal of work hardened surfaces by corrosion, (ii) enhanced mass transfer reactions and (iii) preferential corrosion at splat boundaries resulting in loosened splats [75,76]. An important aspect of profilometry is its ability to identify a localised region of maximum penetration under erosion-corrosion as seen in Figure 7-6a, indicating highly synergistic areas.

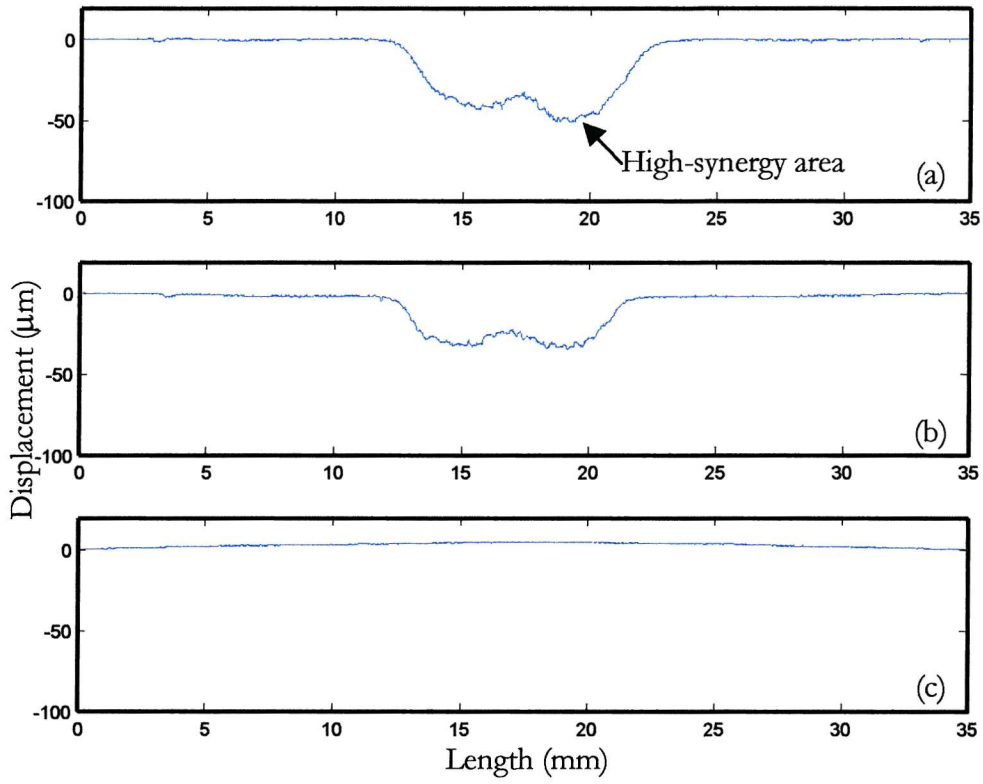

Figure 7-6 *2D profile of NAB coating under (a) erosion-corrosion, (b) pure erosion, and (c) flow corrosion. 5.0 ms^{-1}, 235 μm sand diameter, 3.0 %w/w sand concentration, 25 °C.*

7.3.2 AB coating

2D profiles for the AB coating are shown in Figure 7-7, the wear scars are similar to those of the NAB coating. Under erosion-corrosion, the scar diameter was found to be 11 mm, with approximately 28 μm wear depth. Pure erosion showed a scar diameter of 10 mm with an averaged wear depth of 27 μm. The slight increase in wear depth indicates the effects of corrosion in enhancing material removal under erosion-corrosion conditions. The maximum depths obtained from erosion and erosion-corrosion are lower than those of NAB coating, conforming with the results obtained by gravimetric mass loss (see Table 7-3) and indicating that it is slightly more erosion-corrosion resistant.

Wear depth ratios of E and T were obtained from the NAB coating and the AB coating. $E/T_{(NAB)} = 0.73$ and $E/T_{(AB)} = 0.96$. The values were compared with that obtained from mass loss measurements ($E/T_{(NAB)} = 0.92$ and $E/T_{(AB)} = 0.86$). Large differences in the comparison

indicate that surface profilometry cannot be used as a quantitative method for measuring the material wear rate. Differences between the mass loss and profilometry methods can stem from the position where the profiles are taken for each specimen. Furthermore, wear rate by mass loss measurements were based on average material loss over the whole surface; while 2D profilometry methods are carried out on specific positions.

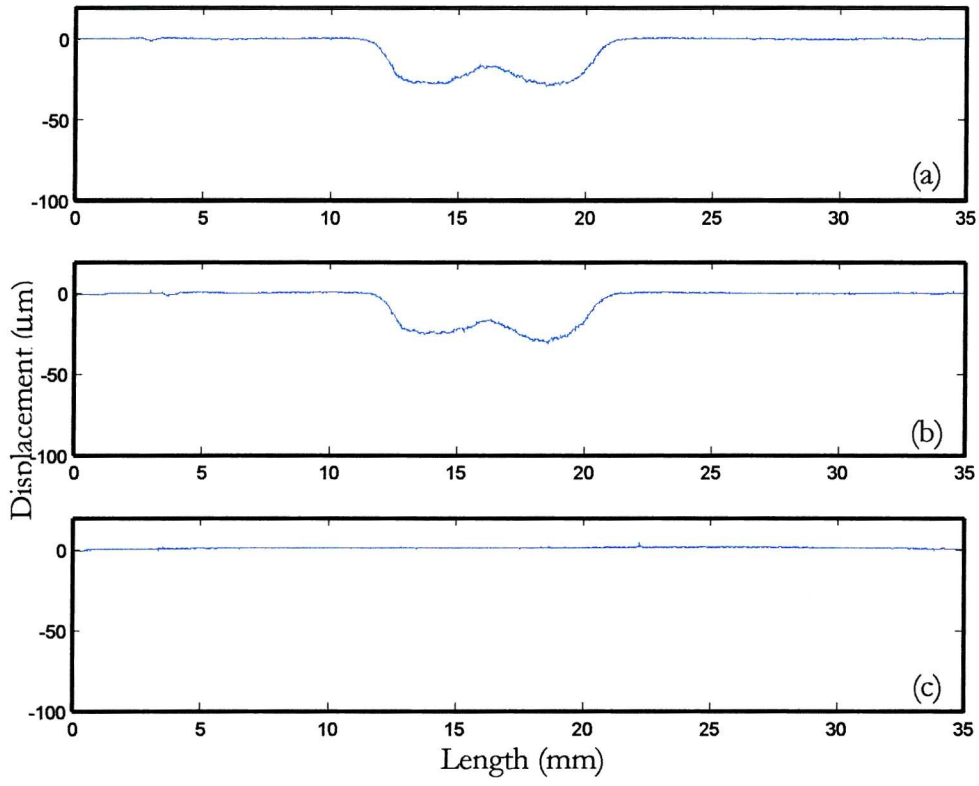

Figure 7-7 *2D profiles of the AB coat under (a) erosion-corrosion, (b) pure erosion, and (c) flow corrosion. 5.0 ms^{-1}, 235 μm sand diameter, 3.0 % w/w sand concentration, 25 °C.*

7.3.3 4360 steel

Figure 7-8 shows the 2D profiles of the 4360 steel. For erosion-corrosion, the W-shaped feature was not observed. The scar diameter was only 9 mm while the wear depth was 36 μm. Cavities with depths up to 57 μm were also observed at the edge of the central wear scar, near the wall jet region. The cavities were observed in this region because cutting wear is predominant, leading to pitting processes. The combined effects of cutting and pitting corrosion resulted in more severe material loss. Pitting under flow corrosion was previously

observed by Hodgkiess *et al* [87], on HVOF cermet coatings. It was reported that pitting occurred at areas that experience high shear forces, such as the wall jet region.

Carbon steels are known to undergo uniform corrosion, corroding actively without the formation of an adherent oxide film. It is possible for enhanced corrosion at the highly stressed plastic deformation region (stagnation point) to result in severe stress corrosion cracking of work hardened plastic lips at the centre of the wear scar (see Chapter 6). Such processes can increase material removal, possibly explaining the absence of a W-shaped feature under erosion-corrosion condition.

A W-shaped feature was observed under the pure erosion condition. The scar diameter and wear depth was found to be 10 mm and 43 μm respectively. The profiles indicated that the pure erosion scar is about 7 μm deeper than the erosion-corrosion scar. However, it is possible for the wear volume to be larger under erosion-corrosion, due to the absence of a central uneroded cone. Mass loss measurements in Table 7-3 indicate that the volume loss between pure erosion and erosion-corrosion are similar. For the current observation, 3D surface profilometry with volume loss estimation could be a better method for comparison with the gravimetric mass loss measurements.

Visual examination of the specimens revealed signs of crevice corrosion near the rubber gasket (used for masking the specimen surface). Crevice corrosion was confirmed by profilometry, shown here as downward spikes at the edges of the profile. The depth of crevice corrosion was in the order of 70 μm. The presence of crevice corrosion under pure erosion condition indicated that cathodic protection was not sufficient to fully suppress corrosion for the carbon steel. Subsequently, the mass loss analysis for the steel specimens will be affected by the effects of corrosion. This observation can possibly be used for explaining the scatter that was observed for the dimensional analysis under pure erosion conditions (Figure 4-10, Chapter 4) and synergy calculations (Figure 7-2).

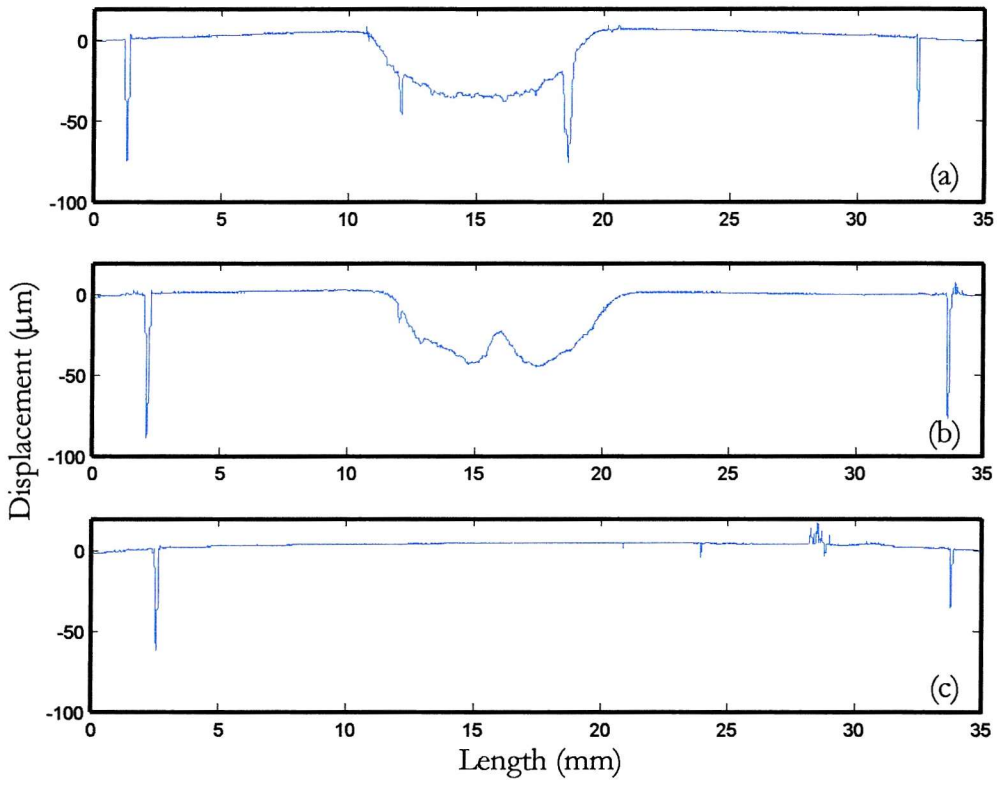

Figure 7-8 *2D profiles for 4360 steel under (a) erosion-corrosion, (b) pure erosion, and (c) flow corrosion. 5.0 ms^{-1}, 235 μm sand diameter, 3.0 %w/w sand concentration, 25 °C.*

Table 7-3 *Comparison between results obtained from profilometry and gravimetric mass loss measurements. 5.0 ms^{-1}, 235 μm sand diameter, 3.0 %w/w sand concentration, 25 °C.*

Materials	Experiment	Profilometry		Gravimetric	
		Nominal wear depth (μm)	E/T ratio	Mass loss (mg)	E/T ratio
NAB coating	T	45	0.73	18.3	0.92
	E	33		16.9	
	C	0		2.6	
AB coating	T	28	0.96	14.1	0.86
	E	27		12.1	
	C	0		5.9	
BS 4360 steel	T	36	1.19	27.5	1.00
	E	43		27.5	
	C	0		11.7	

7.4 Standard deviation analysis

ECN results have been initially analysed by calculating their statistical standard deviation (refer Section 2.5.4, Chapter 2). They were calculated from electrochemical noise sequences after the specimens had reached steady state flow corrosion and erosion conditions (i.e. between the 3rd and 4th hours of a 5 hour experiment). It should be noted that the standard deviation is being used for indicating the ECN perturbations due to multiple particle impacts (not single impacts). The results are presented to show the effects of velocity on synergy.

Figure 7-9 compares the mass loss and standard deviation under flow corrosion (C) conditions, for the NAB coating and 4360 steel, using flow velocities between 3.0 and 6.7 ms^{-1}. ECN data was not plotted for flow corrosion of 4360 steel at 6.7 ms^{-1} because noise measurements were not being carried out. It is evident that the standard deviation for the NAB coating increased linearly with flow velocity. The increase in the ECN standard deviation indicates greater current fluctuations, most likely due to increasing mass transport reactions, as more oxygen becomes available on the specimen surface [178-181].

Standard deviation values for the NAB coating were found to be between 0 and 0.05 μA, the values are approximately six times smaller when compared to that of the 4360 carbon steel (about 0.3 μA). The higher standard deviation values of the 4360 indicate a higher flow corrosion rate. This is probably caused by the inability of the steel surface to form a uniform and stable protective film, as seen in the SEM micrographs in Chapter 5.

It has been reported that current noise standard deviation can be associated with the corrosion rate of the materials (mass loss) [118,119,182]. However, mass loss measurements can be affected by the existence of a surface film/corrosion products on the specimen surface. In the current work, the surface film/corrosion products were not removed before mass loss measurements, in order that SEM investigation could be carried out on the specimens (Chapter 5).

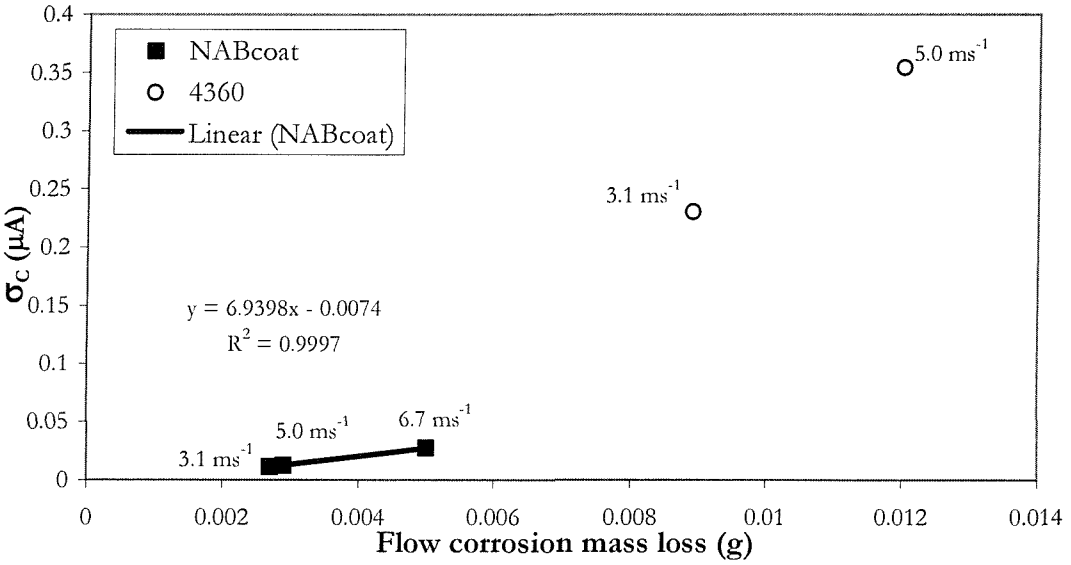

Figure 7-9 *Standard deviation of flow corrosion ECN and mass loss at various jet velocities for the NAB coating and 4360 steel. 3 % w/w sand concentration, 3.5 % NaCl solution, 25 °C.*

Figure 7-10 compares the mass loss and standard deviation under erosion-corrosion (T) conditions. The results are based on experiments using different sand particle kinetic energies (0.02 to 0.41 μJ), the variation in kinetic energy was achieved by changing the flow velocity and particle size.

Under erosion-corrosion conditions, the standard deviation for the NAB coating (0.05 ~ 0.3 μA) is nearly 6 times higher than that found in flow corrosion conditions. Standard deviation values also increased in a linear manner, with respect to sand particle kinetic energy. This indicated that higher kinetic energy sand particles resulted in more cutting and plastic deformation wear, breaking off the surface film and exposing fresh coating surface in the process [110,183]. The removal of surface film by higher kinetic energy particles corresponds to increased electrochemical activity [110,174].

The standard deviation for the 4360 steel appears to be uncorrelated under erosion-corrosion conditions. The values are similar at around 0.25 μA (also similar to flow corrosion conditions). The inability of the 4360 steel to form a protective film means that the amount of fresh surface exposed under slurry impingement does not differ much with respect to the kinetic energy used. This can result in similar standard deviation values at all kinetic energies.

Their similarity with those found under flow corrosion conditions indicates that the corrosion rate under both conditions can be similar. It is possible for the erosion processes to result in increased surface roughness (higher surface area) [49,184], subsequently increasing the standard deviation [185]. However, this was not reflected in the current noise standard deviation values for the 4360 steel.

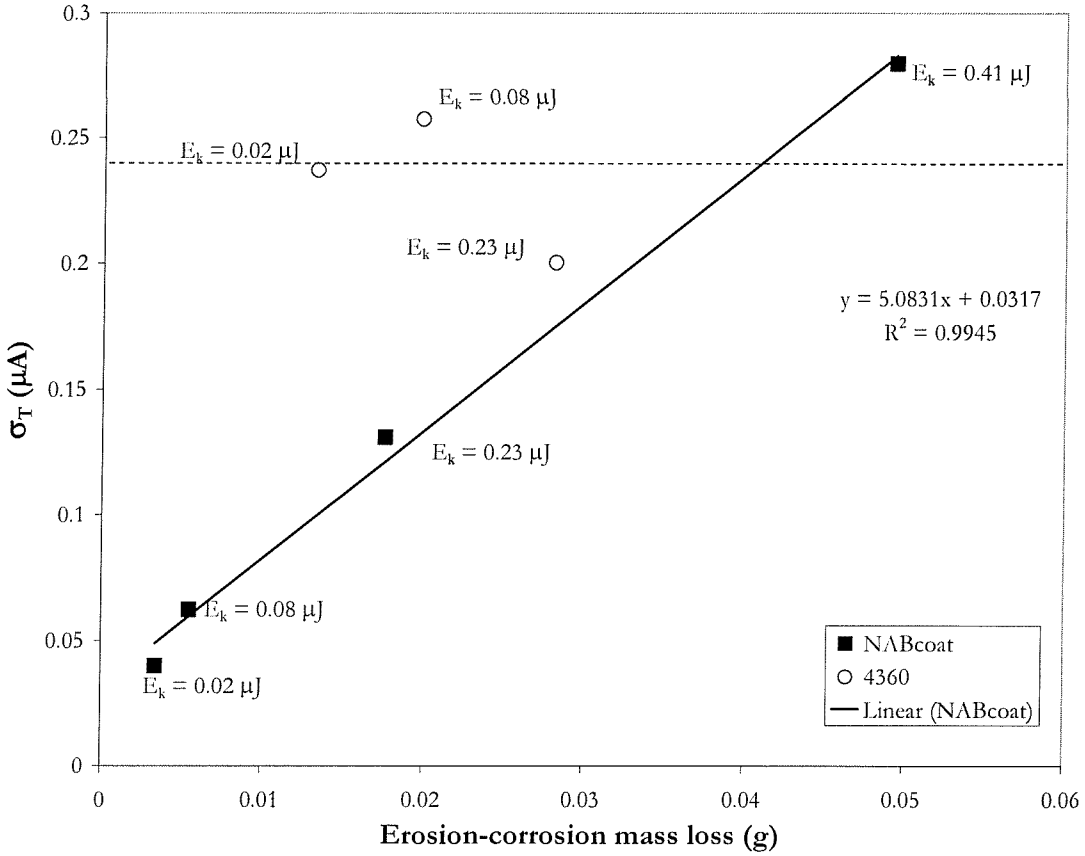

Figure 7-10 Standard deviation of erosion-corrosion ECN and mass loss at various jet velocities for the NAB coating and 4360 steel. Results obtained from 2 different sand sizes (235 μm and 135 μm), 3 % w/w sand concentration, 3.5 % NaCl solution, 25 °C.

Comparisons between the NAB coating and the 4360 steel revealed that the standard deviation values are related to the area of fresh surface exposed to the aggressive electrolyte/slurry (i.e. corrosion rate). This effect is more pronounced for the NAB coating surface, as it is able to form a protective film. The standard deviation was shown to increase when flow corrosion conditions (Figure 7-9) are changed to erosion-corrosion conditions (Figure 7-10). This phenomenon shows the erosion enhanced corrosion (ΔC) effects, possibly due to the removal of surface film or cracking at the splat boundaries. It is therefore possible to associate the flow corrosion and erosion-corrosion standard deviations values to mass loss

under pure erosion conditions. The objective is to estimate the pure erosion rate by electrochemical current noise measurements.

Figure 7-11 shows the relationship between the current noise standard deviation ratio and the pure erosion mass loss at various kinetic energies, for the NAB coating and the 4360 steel substrate. The standard deviation ratio was obtained by dividing the erosion-corrosion standard deviation (σ_T) with flow corrosion standard deviation (σ_C), indicating the enhanced corrosion under solid particle impingement.

For the NAB coating, the enhanced corrosion rate has a logarithmic relationship with the erosion rate, the increased electrochemical activity has a power law coefficient of about 0.5. The 4360 steel does not produce a protective film on it surface, so the effects of enhanced corrosion will be minimal. This is demonstrated by the standard deviation ratio, the values are close to unity at all kinetic energies.

The figure indicates that pure erosion rates can be estimated from a system undergoing erosion-corrosion, based on the standard deviations obtained from the electrochemical current noise. This method of estimating the erosion rate should be used with care as different engineering materials behave differently under slurry impingement.

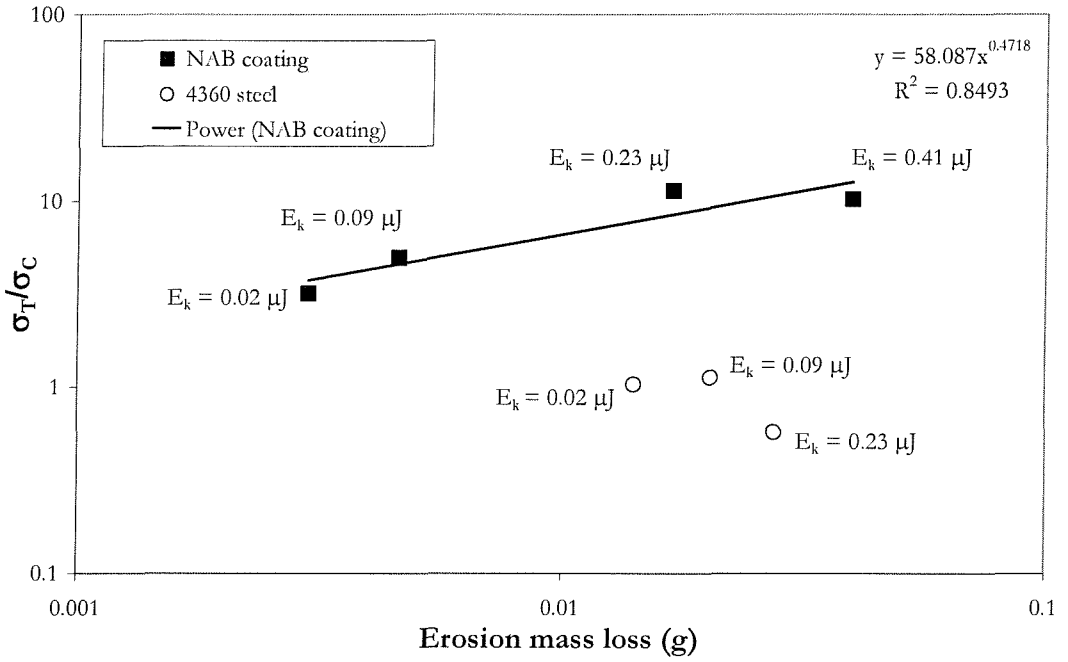

Figure 7-11 The relationship between ECN standard deviation ratio for erosion-corrosion (T) and flow corrosion (C) versus mass loss for pure erosion (E). Mean sand particle sizes 235 µm and 135 µm, 25 °C. 3.5% NaCl solution for flow corrosion and erosion-corrosion.

For the NAB coating, the flow corrosion noise and the erosion-corrosion noise can be measured under actual service conditions. The noise standard deviation ratio can be obtained and the pure erosion rate can be estimated. This type of measurement shows promise for materials that passivate or systems utilising corrosion inhibitors, under sand particle impingement conditions.

As seen previously (in Figure 6-7, Chapter 6), the AB coating thickness is reduced as erosion-corrosion proceeds, resulting in greater potential noise fluctuations and higher standard deviation values. Coating perforation can lead to large current noise fluctuations that are similar to that of 4360 steel, possibly consequences include a sudden increase in the standard deviation ratio. This indicates that the standard deviation ratio could be used to monitor coating perforation. No sudden changes in the standard deviation ratio was observed for the NAB coating at the velocity range tested indicating that coating perforation did not occur during the tests, this was confirmed by inspection of the transverse section.

In order to gain a further understanding of the effects of erosion enhanced corrosion, the standard deviation ratios were also plotted against synergy ratio (S/T), seen in Figure 7-12.

As the standard deviation ratios indicate the addition of electrochemical activity (corrosion rate) on the surface under solid particle impingement, its increase will result in a similar increase in the levels of synergy. At lower kinetic energy conditions, sand particles might not have sufficient energy to cause surface film rupture. Sasaki *et al.* reported that the threshold kinetic energy required to cause passive film rupture for stainless steels is in the order of 0.03 μJ [165]. The protective layer on NAB alloys is approximately 800 nm [62] (as opposed to 10 nm for stainless steels), indicating that a higher kinetic energy is required to cause film damage. If protective films are sustained on the specimen surface under erosion-corrosion, standard deviation values will be similar to that under flow corrosion conditions. This can result in a negative synergy and both erosion and corrosion processes are then considered as antagonistic.

The sand particles will have higher damage efficiencies as their kinetic energy increases. This will result in unsustainable protective films, leading to higher standard deviation ratios and mass losses. A possible transition region is shown at the vicinity where the electrochemical standard deviation ratio values are close to 10; synergy levels were shown to shift from negative to positive. This transition can be caused by the following processes:

- Increased surface film removal by higher energy particles, leading to more exposed surfaces and an increase in corrosion rate. This is a result of erosion enhanced corrosion (ΔC) processes.
- Higher kinetic energy sand particles can remove the work hardened and corroded plastic deformation lips at a higher efficiency, leading to corrosion enhanced erosion (ΔE) processes.

The erosion enhanced corrosion (ΔC) process can be resolved electrochemically by obtaining the differences between erosion-corrosion standard deviation and flow corrosion standard deviation. Figure 7-13 shows the effects of ΔC on the percentage of synergy for the NAB coating within the range of kinetic energy tested. It is clear that ΔC increases with kinetic energy, subsequently leading to enhanced synergy. The enhanced synergy will lead to greater erosion-corrosion mass loss and smaller E/T ratio as seen previously in Figure 7-2.

The calculation of standard deviation ratio can therefore be used as a monitoring procedure to estimate the critical level of synergy at predetermined operating conditions. This has a similar function to the synergistic constant that was previously obtained from gravimetric mass loss measurements (Figure 7-2). More information on the effects of kinetic energy on the current noise standard deviation can be found in Appendix C. The current work utilised only four different kinetic energy settings, resulting in only four data points. Further work at other kinetic energy or materials can be carried out to confirm the validity of using electrochemical standard deviation ratio in identifying the transition region between positive and negative synergy.

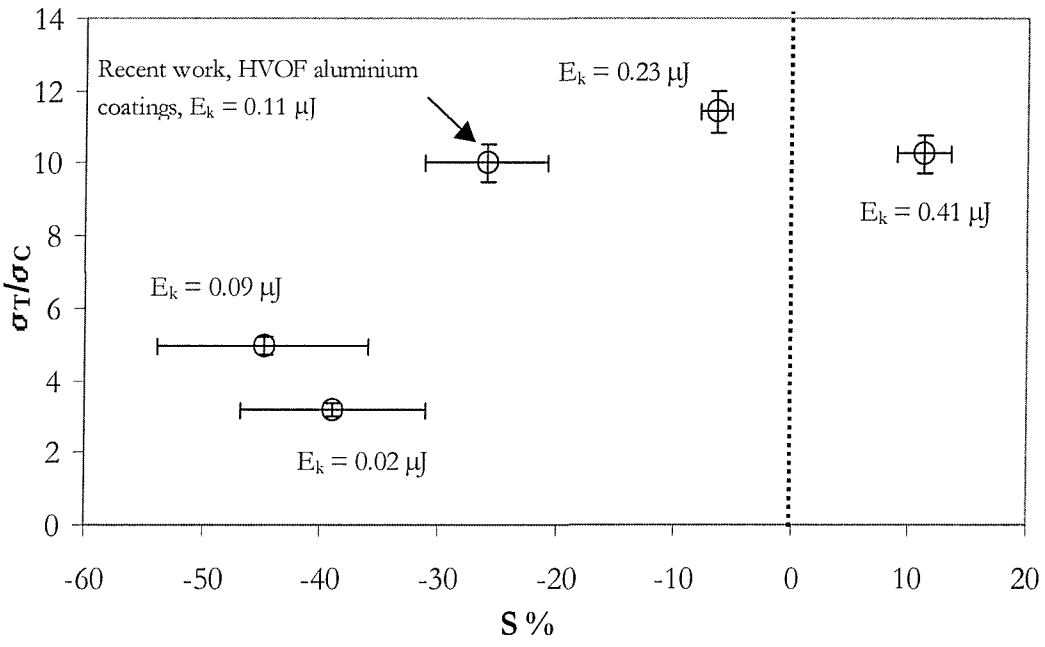

Figure 7-12 Relationship between the standard deviation ratio and synergy (S) percentage for the NAB coating and that of recent work carried out by Speyer [125].

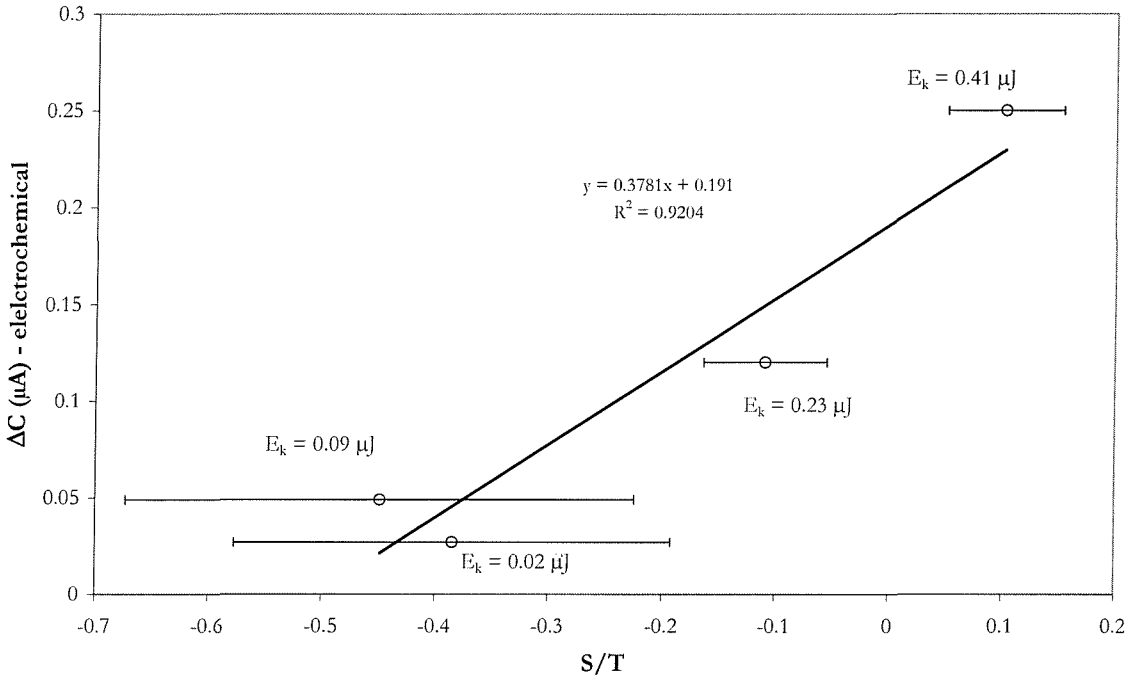

Figure 7-13 The effects of erosion enhanced corrosion (ΔC) in affecting the percentage of synergy for the NAB coating.

7.5 Time frequency analysis of electrochemical current noise

Due to the stochastic nature of the electrochemical systems that undergo flow corrosion and erosion-corrosion, the time frequency signal analysis method may be useful as a tool for analysisng the electrochemical current noise (ECN) signals. The ECN fluctuations can be associated with the corrosion activities occurring on the surface, thus the variance/power of the ECN at predetermined times throughout the flow corrosion and erosion-corrosion experiments can be quantified by this method. Preliminary analysis was carried out on the ECN signals by using the discrete wavelets transform and the empirical mode decomposition method, both relatively novel and powerful signal processing techniques. The results and discussions are presented in Appendix D, where few definite conclusions can be drawn. Nevertheless, the present work can be used as a foundation for future ECN analysis under flow corrosion and erosion-corrosion conditions.

7.6 Conclusions

In this chapter, the synergistic effects between erosion and corrosion have been estimated on NAB coating, AB coating and the 4360 steel specimens. The following conclusions can be drawn:

1. Positive synergy was found for the materials only at the highest kinetic energy condition (6.7 ms^{-1}). This was probably due to interactions between (i) corrosion enhanced erosion (ΔE) enhanced plastic deformation/cutting wear due to corrosion at the plastic lips and (ii) erosion enhanced corrosion (ΔC) such as increased mass transport processes. In the case of the NAB coating, ΔC can also be a result of protective film removal since a flow velocity of 6.7 ms^{-1} is higher than the critical flow velocity.
2. For a system undergoing erosion-corrosion processes, the extent of synergy can now be determined by obtaining the ratio between pure erosion mass loss and erosion-corrosion mass loss. A constant that defines the transition between positive and negative synergy was attained, the value being $E/T = 0.83$. This constant can be used for estimating the magnitude of synergy for any materials subjected to erosion-corrosion in actual service conditions.
3. In terms of metallic materials selection for components in service, corrosion properties such as the ability to form/regenerate a sufficiently thick and adherent protective layer are crucial. This will ensure that E/T ratios will be larger than 0.83 and will result in negative synergy. Nevertheless, excellent corrosion properties alone will not necessarily guarantee prolonged material life, the protective layers will inevitably fail under extremely aggressive conditions such as increased electrolyte corrosivity or particle kinetic energy.
4. Surface profilometry was found useful for showing the erosion mechanisms. The W-shaped wear scars indicate ductile wear mechanisms for the materials tested. Due to the profiles showing only specific locations within the wear scars, the differences between T, E and C wear rates cannot be accurately quantified. However, the profiles provide a useful indication of maximum material penetration under erosion and erosion-corrosion conditions.
5. For the 4360 steel specimens, the absence of a W-shaped scar under erosion-corrosion was probably caused by corrosion enhanced erosion at the stagnation point. Evidence of crevice corrosion was also found within the profiles, resulting in data scatter for mass loss calculations and synergy estimation.

6. Current standard deviation for the NAB coating was found to increase with jet velocity under FC condition. The increase in current fluctuations can possibly be associated with increased mass transport, corrosion at the pore network and dealloying processes.
7. Under flow corrosion conditions, standard deviation of the 4360 steel was six times larger than the NAB coating, indicating the uniform corrosion behaviour due to the lack of a protective layer.
8. For the NAB coating, the current standard deviation under T is six times larger than FC. The higher corrosion rates can be linked to the removal of the protective layer by sand particle impingement and cracking/corrosion at the splat boundary.
9. The standard deviation ratio (σ_T/σ_C) can be used for estimating the pure erosion rate for the NAB coating. The ratio indicates the effects of corrosion on total material loss. The transition between negative and positive synergy was also determined by equating the ratio with synergy. This transition appears to occur at the vicinity of $\sigma_T/\sigma_C = 10$, more work should be carried out to confirm the exact transition region.

Chapter 8 Conclusions and further work

8.1 Conclusions

This work has been carried out to evaluate the erosion-corrosion behaviour of HVOF aluminium bronze and nickel aluminium bronze coatings. Particular emphasis was given to the analysis of the electrochemical current noise response and its correlation to synergy under erosion-corrosion. Detailed conclusions have been provided at the end of each chapter, this chapter intends to provide a general summary of those conclusions and some suggestions for future work.

Materials characterisation

Both the HVOF aluminium bronze and nickel aluminium bronze coatings and their steel substrates have been characterised. Microscopy revealed that the microstructures of both coatings are different, the AB coatings consists of homogeneous AB particles while the NAB coating is made of heterogeneous particles with different alloying elements. The difference in microstructure can result in the NAB coating being more noble but less erosion resistant than the AB coating. The hardness of the materials provided an approximate indication of their erosion and erosion-corrosion properties, higher scatter in the NAB coating hardness profile revealed the different hardness values of its constituent particles. Potentiodynamic polarisation was used to confirm the corrosion resistance of the materials, the copper-based coatings were more noble than their steel substrates. Both coatings were also found to be more anodic than the cast NAB alloy. The static corrosion behaviour of the coatings are highly dependent on the amount of porosity as they allow the permeation of electrolyte into the coating/substrate interface. Localised acidification of electrolyte within the pore network resulted in enhanced corrosion attack and detachment at the splat boundaries.

Erosion

The AB and NAB coatings showed similar erosion rates within the kinetic range tested. Comparison with other bulk materials and HVOF coatings showed that the AB and NAB coatings are comparable with engineering materials used in the marine environment. Contact

surface profilometry and microscopy revealed that ductile mechanisms are responsible for erosion of the coatings. Highest mass loss was recorded at normal impingement, indicating the dominance of brittle erosion mechanisms. The erosion mechanisms of HVOF coatings are different from bulk materials as it contains a porous microstructure. It was demonstrated that under normal impingement, cracking at the brittle splat boundary could result in the removal of single/multiple splats and enhancing the wear rate. Wear maps based on volume loss and kinetic energy and dimensional analysis were investigated. The dimensional analysis appears to be more comprehensive as it incorporates materials hardness into the wear map. Refinement of this technique is required because large amounts of scatter were found in the data, indicating that changes in the erosion may occur during the tests (the erosion resistance of work hardened materials has a non-linear dependence on hardness). However, the dimensional analysis was found suitable for evaluating of mass loss discrepancies that are linked to scale formation on the specimen surface.

Flow corrosion

Flow corrosion rates of the HVOF coatings have been quantified. The penetration rate for the AB coating and NAB coating was found to be is 2 mm/year and 1.3 mm/year respectively. The flow corrosion rates for the coatings were found to be within the range obtained by cast NAB alloys (0.5 ~ 2.0 mm/year). Lower corrosion rates for the NAB coating can be associated with galvanic coupling between the coating particles, corrosion of the more anodic stainless steel particles could result in oxides that can cause partial pore sealing. As with bulk NAB alloys, surface filming occurred on the AB and NAB coatings under flowing conditions. However, the surface films contain imperfections particularly at open pores on the coating surface that could reduce its corrosion resistance. The most important flow corrosion mechanism of the coatings involved permeation of electrolyte into the coating/substrate interface after 5 days, resulting in its delamination. Open circuit potential measurements detected localised corrosion events occurring within the pore network and coating/substrate interface. The critical velocity for the NAB coating was found between 4 and 6 ms^{-1}, increased corrosion rates were observed beyond 6 ms^{-1}.

Erosion-corrosion

Erosion-corrosion mechanisms for the AB and NAB coatings are a combination of erosion and corrosion. Similar velocity exponents and surface profiles between erosion and erosion-corrosion showed that wear occurs by ductile mechanisms. The addition of corrosion resulted in increased charge transfer (associated with protective layer removal) and corrosion at the work hardened plastic deformation lips, further enhancing the material loss. Little or no signs of corrosion were found at the coating/substrate interface, indicating that the pores were possibly sealed by the plastic deformation lips and electrolyte permeation was minimised. Open circuit potential measurements revealed a mixed potential (galvanic coupling) between the noble coating and active substrate when the coating perforates, resulting in coating delamination at the vicinity of the perforation site. Potential standard deviation under erosion-corrosion was 5 times larger than those of flow corrosion, thus providing a method to detect the presence of solid particle impingement.

Synergy

Synergy values were quantified from E, C and T experiments on the 4360 steel and the NAB coating. Within the range of kinetic energy used, negative synergy was found below 5.0 ms^{-1} while positive synergy was found at 6.7 ms^{-1}. Under low kinetic energy conditions, the erodents have a lower propensity in causing mechanical damage as a protective layer exists between the target material and the erodent, leading to low ΔC and ΔE values and resulting in negative synergy. Increasing the kinetic energy beyond the critical flow velocity resulted in higher mass transfer while turbulence effects and mechanical damage can result in the removal of the protective layer, leading to enhanced ΔC and ΔE and more material removal.

A novel method of estimating the extent of synergy based on mass loss measurement was proposed, it involves determining the ratio between erosion mass loss and erosion-corrosion mass loss. As the amount of synergy depends on the erosion-corrosion mass loss (due to effects of ΔC and ΔE), ratios lower than 0.83 indicates enhanced T and positive synergy. Similarly, E/T ratios higher than 0.83 will result in negative synergy. 2D contact surface profilometry was inconclusive in quantifying the extent of synergy under erosion-corrosion. However, it was useful for the quantification of maximum penetration under both erosion and erosion-corrosion conditions.

Electrochemical current noise standard deviation was useful for estimating the kinetics of corrosion under flow corrosion and erosion-corrosion conditions, its values are proportional to the jet velocity and sand particle kinetic energy. The current noise standard deviation ratio between erosion-corrosion and flow corrosion indicated the effects of erosion enhanced corrosion (ΔC). The ratio can be correlated with the erosion mass loss, indicating that erosion rates of engineering materials can be estimated by electrochemical measurements. Preliminary results also indicate that the ratio can also be used for estimating the extent of synergy in a system undergoing erosion-corrosion. However, insufficient evidence was found to conclude this relationship in a precise manner.

Concluding remarks

The present work, based on the HVOF AB and NAB coatings, have further strengthened the existing ideas in the literature in a number of selected ways:

→ Pores are detrimental towards the erosion and corrosion resistance of HVOF coatings.In order to minimise corrosion failure, the coating process needs to be optimised or sealants should be utilised after spraying to reduce the amount of pores within the coating.

→ Potential measurements can be utilised for identifying coating perforation and the presence of solid particle impingement. A further contribution has been made in terms of using open circuit potential measurement for monitoring corrosion under dynamic conditions.

→ Controversial results were found in the literature regarding the critical velocity of NAB alloys in seawater (between 4 and 22 ms^{-1}). Current results showed that the critical velocity for HVOF NAB coating is in the region of 5 ms^{-1}. Negative synergy was found on the NAB coatings below this critical velocity.

→ Sand particle kinetic energy was detrimental towards the erosion-corrosion resistance of engineering materials, especially for those that can generate a protective layer under corrosive conditions. The removal of these protective layers by high kinetic energy particles can contribute to large synergistic values under erosion-corrosion, resulting in enhanced material loss.

The present work has also contributed towards the determination of a synergy constant by mass loss measurements and defining the transition between positive and negative synergy. Pioneering work has been carried out by using the electrochemical noise standard deviation to estimate the extent of synergy and erosion rate for the NAB coating. A novel and powerful signal processing technique (EMD) has also been contributed for the analysis of electrochemical current noise under dynamic conditions. The use of electrochemical noise measurements as a non-perturbing corrosion monitoring tool is recommended for systems undergoing flow corrosion and erosion-corrosion. The detection of sand particle impingement, localised corrosion within the pore network, and coating perforation is possible with this technique. Furthermore, correlation of electrochemical noise analysis with mass loss results at various kinetic energies was useful for quantifying synergy under erosion-corrosion, indicating that future predictions of synergy could be carried out in-situ.

8.2 Further work

Erosion experiments have indicated that cracking at the splat boundaries can induce extra material loss under normal impingement angle. More work can be carried out by fabrication of HVOF coatings with different oxidation rates at the splat boundaries and subjecting them to erosion tests. The erosion rates and mechanisms can then be correlated with the amount of oxides at the splat boundary so that the best HVOF spraying conditions can be determined.

As pore networks within the coating can affect the corrosion behaviour, future work can also be carried out on the effects of pore sealing. Comparisons can be made between pore sealing by sealant and heat treatment processes. In addition, heat treatment processes could also alter the chemical composition of the coating particles by reducing the anodic phases and improving the corrosion resistance of the AB and NAB coatings.

As mentioned earlier, pores and oxides within the HVOF coatings can complicate the analysis and determination of erosion, flow corrosion and erosion-corrosion mechanisms. Fundamental investigations could be carried out on bulk alloys where the corrosion and erosion behaviours can be more easily characterised, so that the correlation of electrochemical responses to the type of corrosion can be determined.

Preliminary results of using heterogeneous particles in the NAB coating showed an improved corrosion resistance when compared to the homogeneous AB coating. The selection of alloying particles in metallic HVOF coatings could prove to be an interesting pursuit. An optimised system will produce closely packed insoluble oxides at the pore network and hinder electrolyte permeation. Further more, the different hardness of the constituent particles can also be used for improving the erosion resistance of HVOF coatings.

Electrochemical potential and current noise was useful in identifying the occurrence of corrosion on the HVOF coatings. More work can be carried out to link individual corrosion processes/mechanisms with the noise fluctuations. Under erosion-corrosion conditions, the use of standard deviation ratio for estimating synergy can be confirmed by designing experiments with different kinetic energy settings and target materials.

The EMD technique shows promise as a tool for analysis the electrochemical noise of systems undergoing erosion-corrosion. More work could be carried out to identify the instantaneous frequencies of the individual IMFs, so that the time scales of individual corrosion processes on the surface can be elucidated.

References

1. Chapman, B. N. and Anderson, J. C., 'Science and technology of surface coating', (1974), London, Academic Press

2. Bardal, E., Eggen, T. G., Rogne, T., and Solem, T., 'The erosion and corrosion properties of thermal spray and other coatings', *Int.Thermal Spraying Conf.*, (1995), Kobe, JAPAN

3. Hawthorne, H. M., Arsenault, B., Immarigeon, J. P., Legoux, J. G., and Parameswaran, V. R., 'Comparison of slurry and dry erosion behaviour of some HVOF thermal sprayed coatings', *Wear*, **229**, (1999), pp. 825-834

4. Stewart, D. A., Shipway, P. H., and McCartney, D. G., 'Abrasive wear behaviour of conventional and nanocomposite HVOF- sprayed WC-Co coatings', *Wear*, **229**, (1999), pp. 789-798

5. Neville, A., Perry, J. M., Hodgkiess, T., and Chua, H. P., 'Wrought and high-velocity oxy fuel sprayed Inconel 625 - examination of corrosion aspects', *Proceedings of the Institution of Mechanical Engineers Part L- Journal of Materials-Design and Applications*, **214**, (2000), No. L1, pp. 41-48

6. Wang, B. Q., 'Erosion-corrosion of thermal sprayed coatings in FBC boilers', *Wear*, **199**, (1996), No. 1, pp. 24-32

7. Glaeser, W and Wright, I. G., 'Metals Handbook 9th Ed., Corrosion', Vol. 13, (1986), Ohio, ASTM Int'l. Metals Park

8. Hutchings, I. M., 'Tribology-Friction and wear of engineering materials', (1992), Edward-Arnold

9. Lynn, R. S., Wong, K. K., and Clark, H. M., 'On the particle size effect in slurry erosion', *Wear*, **149**, (1991), No. 1-2, pp. 55-71

10. Bitter, J. G. A., 'A study of erosion phenomena - Part 1', *Wear*, **6**, (1963), pp. 5-21

11. Bitter, J. G. A., 'A study of erosion phenomena - Part 2', *Wear*, **6**, (1963), pp. 169-190

12. Finnie, I., 'Erosion of surface by solid particles', *Wear*, **3**, (1960), pp. 87-103

13. Speyer, A. J., 'Wear corrosion sensing in flowing seawater', Mphil/PhD transfer thesis, (2001), University of Southampton

14. Hutchings, I. M. and Winter, R. E., 'Particle erosion of ductile metals: a mechanism of material removal', *Wear*, **27**, (1974), pp. 121-128

15. Levy, A. V., 'The platelet mechanism of erosion of ductile materials', *Wear*, **108**, (1986), pp. 1-21

16. Sundararajan, G, 'A comprehensive model for the solid particle erosion of ductile materials', *Wear*, **149**, (1991), No. 1-2, pp. 111-127

17. Turenne, S. and Fiset, M., 'Modelling of abrasive particle trajectories during erosion by a slurry jet', *Wear*, **162-164**, (1993), pp. 679-687

18. Meng, H. C. and Ludema, K. C., 'Wear models and predictive equations - their form and content', *Wear*, **181**, (1995), pp. 443-457

19. Hutchings, I. M., 'Mechanisms of the erosion of metals by solid particles', Erosion: Prevention and Useful Applications, ASTM STP 664, (1979), pp. 59-76, ASTM

20. Fang, Q., Xu, H., Sidky, P. S., and Hocking, M. G., 'Erosion of ceramic materials by sand/water slurry jet', *Wear*, **224**, (1999), pp. 183-193

21. Levy, A. V., 'Erosion-corrosion of metals in coal liquefication environments', *Materials Performance*, **19**, (1980), pp. 45-51

22. Clark, H. M., 'The effect of carrier liquid viscosity on the erosion rate of steel by solid/liquid suspensions and the nature of the wear debris produced', *Proc.5th Int'l Congress on Tribology, Euro Trib.'87*, (1989), pp. 354-359, Helsinki, Finland, Finnish Soc. of Tribology

23. Tsai, W., Humphrey, J. A. C., Cornet, I., and Levy, A. V., 'Experimental-measurement of accelerated erosion in a slurry pot tester', *Wear*, **68**, (1981), No. 3, pp. 289-303

24. Turenne, S., Fiset, M., and Masounave, J., 'The effect of sand concentration on the erosion of materials by a slurry jet', *Wear*, **133**, (1989), No. 1, pp. 95-106

25. Clark, H. M., 'On the impact rate and impact energy of particles in a slurry pot erosion tester', *Wear*, **147**, (1991), No. 1, pp. 165-183

26. Lin, F. Y. and Shao, H. S., 'The effect of impingement angle on slurry erosion', *Wear*, **141**, (1991), No. 2, pp. 279-289

27. Finnie, I., 'Some reflections on the past and future of erosion', *Wear*, **186**, (1995), No. 1, pp. 1-10

28. Roy, M., Tirupataiah, Y, and Sundararajan, G, 'Effect of particle shape on the erosion of Cu and its alloys', *Materials Sc.and Engineering - A*, **165**, (1993), pp. 51-63

29. Sparks, A. J. and Hutchings, I. M., 'Effects of erodent recycling in solid particle erosion testing', *Wear*, **162**, (1993), pp. 139-147

30. Benchaita, M. T., Griffith, P., and Rabinowicz, E., 'Erosion of a metallic plate by solid particles entrained in a liquid jet', *J.Eng.Ind.*, **105**, (1983), pp. 215-227

31. Clark, H. M. and Wong, K. K., 'Impact angle, particle energy and mass loss in erosion by dilute slurries', *Wear*, **186-187**, (1995), pp. 454-464

32. Oka, Y and Matsumura, M, 'Erosive wear testing apparatus – Simulation of erosion caused by slurry of low impingement velocity', *Proc.Int.Conf.Wear of Materials*, (1983), pp. 360-366, ASME

33. Elkholy, A., 'Predictions of abrasive wear for slurry pump materials', *Wear*, **84**, (1983), No. 1, pp. 39-49

34. Wood, R. J. K., 'The sand erosion performance of coatings', *Materials and Design*, **20**, (1999), pp. 179-191

35. Levy, A. V. and Hickey, G., 'Liquid solid particle slurry erosion of steels', *Wear*, **117**, (1987), No. 2, pp. 129-146

36. Tuzson, J. J., 'Laboratory slurry erosion tests and pump wear rate calculations', *Journal of Fluids Engineering-Transactions of the Asme*, **106**, (1984), No. 2, pp. 135-140

37. Levy, A. V. and Yau, P., 'Erosion of steels in liquid slurries', *Wear*, **98**, (1984), No. 1-3, pp. 163-182

38. Jones, D. A, 'Principles and prevention of corrosion', **2**, (1996), Prentice Hall

39. Fontana, M. G., 'Corrosion Engineering', **3rd Ed.**, (1987), McGraw Hill

40. Tretheway, K. R. and Chamberlain, J., 'Corrosion for science and engineering', **2nd Ed.**, (1995), Longman

41. Macdougall, B. and Graham, M. J., 'Corrosion mechanisms in Theory and practice', **First edition**, (1995), New York, Marcel Dekker, Inc

42. Corlett, N., 'Theoretical erosion-corrosion mapping for dilute aqueous slurries', PhD. Thesis, (1998), Corrosion and Protection Centre, UMIST

43. Chun, Y., Pyun, S., and Kim, C., 'Effect of aluminium content on the anodic behaviour of copper aluminium alloys in 3.5% NaCl solution', *Materials Letters*, **20**, (1994), pp. 265-270

44. Wood, R. J. K., Hutton, S. P., and Schriffrin, D. J., 'Mass transfer effects of non-cavitating seawater on the corrosion of Cu and 70Cu-30Ni', *Corrosion*, **30**, (1990), No. 12, pp. 1177-1201

45. Efird, K. D., Wright, E. J., Boros, J. A., and Hailey, T. G., 'Correlation of steel corrosion in pipe flow with jet impingement and rotating cylinder tests', *Corrosion*, **49**, (1993), No. 12, pp. 992-1003

46. Bengough, G. and May, R., 'Seventh report to the corrosion research committee of the institute of materials', *The J.of the Inst.of Metals*, **32**, (1924), pp. 81-269

47. May, R. and Stacpoole, R. W. D., 'The jet impingement apparatus for the assesment of corrosion by moving seawater', *The J.of the Inst.of Metals*, **77**, (1950), pp. 331-344

48. Rao, V. V. and Trass, O., 'Mass transfer from a flat surface to an impinging turbulent jet', *The Canadian J.of Chem.Eng.*, **1964**, (1964), No. June, pp. 95-99

49. Dawson, D. A. and Trass, O., 'Mass transfer in a turbulent radial wall jet', *The Canadian J.of Chem.Eng.*, (1966), No. 6, pp. 121-129

50. Giralt, F. and Trass, O., 'Mass transfer from crystalline surfaces in turbulent impinging jet, Part I: Transfer by erosion', *The Canadian J.of Chem.Eng.*, **53**, (1975), pp. 505-511

51. Efird, K. D., 'Jet impingement testing for flow accelerated corrosion', *NACE Corrosion 2000*, (2000), Paper no. 52, NACE

52. Ault, J. P., 'Erosion-corrosion of nickel aluminium bronze in flowing seawater', *NACE Corrosion 1995*, (1995), Paper no. 281, NACE

53. Schmitt, G., Bosch, C., Mueller, M., and Siegmund, G., 'A probabilistic model for flow induced localised corrosion', *NACE Corrosion 2000*, (2000), Paper no. 49, NACE

54. Williams, W. L., 'Aluminium bronzes for marine applications', *Journal of the American Society of Naval Engineers*, **69**, (1957), pp. 453-461

55. Macken, P. J. and Smith, A. A., 'The aluminium bronzes - Properties and production processes - Corrosion and oxidation resistance', **2nd Ed.**, (1966), pp. 107-137, London, Copper Developement Association

56. CDA Publication no.80, 'Aluminium bronze alloys - Corrosion resistance guide', (1981), Copper Developement Association, UK

57. Culpan, E. A. and Rose, G., 'Microstructural characterization of cast nickel aluminium bronze', *Journal of Materials Science*, **13**, (1978), pp. 1647-1657

58. Hasan, F., Jahanafrooz, A., Lorimer, G. W., and Ridley, N., 'The morphology, crystallography, and chemistry of phases in as-cast nickel aluminium bronze', *Metallurgical Transactions A-Physical Metallurgy and Materials Science*, **13**, (1982), No. 8, pp. 1337-1345

59. Rowlands, J. C., 'Studies on the preferential phase corrosion of cast nickel aluminium bronze in seawater', **Vol. 2**, (1981), pp. 1346-1351, Proceedings of the 8th international congress on metallic corrosion, Mainz, West Germany

60. Ferrara, R. J., 'Dealloying of aluminium bronze and nickel aluminium bronze castings in seawater', (1980), pp. 166-192, Tri-Service Conference on Corrosion, US Airforce Academy, Colorado

61. Tuthill, A. H., 'Guidelines for the use of copper alloys in seawater', *Materials Performance*, **26**, (1987), No. 9, pp. 12-22

62. Schussler, A. and Exner, H. E., 'The corrosion of nickel-aluminium bronzes in seawater - I. Protective layer formation and the passivation mechanism', *Corrosion Science*, **34**, (1993), No. 11, pp. 1793-1802

63. Francis, R., 'Coupling of superduplex stainless steel and cast nickel-aluminium bronze in seawater', *British Corrosion Journal*, **34**, (1999), No. 2, pp. 139-144

64. Rheingans, W. J., 'Selecting materials to avoid cavitation damage', *Materials in Design Engineering*, **48**, (1958), pp. 102-106

65. Al Hashem, A., Caceres, P. G., Riad, W. T., and Shalaby, H. M., 'Cavitation corrosion behaviour of cast nickel-aluminium bronze in seawater', *Corrosion*, **51**, (1995), No. 5, pp. 331-342

66. Hodgkiess, T. and Neville, A., 'An assesment of galvanic effects in thermally sprayed coating systems', *Thermal spray: A united forum for scientific and technological advances*, (1997), ASM International

67. Annual book of ASTM standards, 'ASTM G40, Metals corrosion - Wear and Erosion', (1996), No. 03.02, ASTM

68. Heitz, E., 'Chemomechanical effects of flow on corrosion', *Corrosion*, **47**, (1991), No. 2, pp. 135-145

69. Batchelor, A. W. and Stachowiak, G. W., 'Predicting synergism between corrosion and abrasive wear', *Wear*, **123**, (1988), No. 3, pp. 281-291

70. Neville, A., Hodgkiess, T., and Xu, H., 'An electrochemical and microstructural assessment of erosion- corrosion of cast iron', *Wear*, **235**, (1999), pp. 523-534

71. Watson, S. W., Friedersdorf, F. J., Madsen, B. W., and Cramer, S. D., 'Methods of measuring wear corrosion synergism', *Wear*, **181**, (1995), pp. 476-484

72. Wood, R. J. K. and Hutton, S. P., 'The synergistic effect of erosion and corrosion - trends in published results', *Wear*, **140**, (1990), No. 2, pp. 387-394

73. Renaud, L., Chapey, B., Bosson, J. C., Oltra, R., and Charles, J., 'Erosion-corrosion properties of austenitic and duplex stainless steels', *Proc.Duplex Stainless Steels Conference*, **Vol. 2**, (1991)

74. LI, Y., Burstein, G. T., and Hutchings, I. M., 'The influence of corrosion on the erosion of aluminium by aqueous silica slurries', *Wear*, **186**, (1995), No. 2, pp. 515-522

75. Wood, R. J. K., 'Erosion-corrosion synergism for multi-phase flowline materials', *Extraits de la Houille Blanche*, **7-8**, (1992), pp. 605-610

76. Matsumura, M, 'Erosion-corrosion of metallic materials in slurries', *Corrosion Reviews*, **12**, (1994), No. 3-4, pp. 321-340

77. Stack, M. M., Zhou, S., and Newman, R. C., 'Identifications of transitions in erosion-corrosion regimes in aqueous environments', *Wear*, **186**, (1995), No. 2, pp. 523-532

78. Zhou, S., Stack, M. M., and Newman, R. C., 'Characterization of synergistic effects between erosion and corrosion in an aqueous environment using electrochemical techniques', *Corrosion*, **52**, (1996), No. 12, pp. 934-946

79. Zeisel, H. and Durst, F., 'Computations of erosion-corrosion processes in separated two-phase flows', *NACE Corrosion 1990*, (1990), Paper no. 29, NACE

80. LI, Y., Burstein, G. T., and Hutchings, I. M., 'Influence of environmental composition and electrochemical potential on the slurry erosion-corrosion of aluminium', *Wear*, **181**, (1995), pp. 70-79

81. Levy, A. V., 'The erosion-corrosion behaviour of protective coatings', *Surface & Coatings Technology*, **36**, (1988), No. 1-2, pp. 387-406

82. Wang, B. Q., Geng, G. Q., and Levy, A. V., 'Erosion-corrosion of thermal spray coatings', *Surface & Coatings Technology*, **43-4**, (1990), No. 1-3, pp. 859-874

83. Puget, Y., Tretheway, K. R., and Wood, R. J. K., 'The performance of cost-effective coatings in aggressive saline environments', *NACE Corrosion 1998*, (1998), Paper no. 688, NACE

84. Rogne, T., Solem, T., and Berget, J., 'Effect of composition and corrosion properties of the metallic matrix on the erosion-corrosion behaviour of HVOF sprayed WC-coatings', *NACE Corrosion 1998*, (1998), Paper no. 495, NACE

85. Puget, Y., Trethewey, K., and Wood, R. J. K., 'Electrochemical noise analysis of polyurethane-coated steel subjected to erosion-corrosion', *Wear*, **233-235**, (1999), pp. 552-567

86. Bjordal, M., Bardal, E., Rogne, T., and Eggen, T. G., 'Erosion and corrosion properties of WC coatings and duplex stainless steel in sand-containing synthetic sea water', *Wear*, **186-187**, (1995), No. 2, pp. 508-514

87. Hodgkiess, T., Neville, A., and Shrestha, S., 'Electrochemical and mechanical interactions during erosion-corrosion of a high-velocity oxy-fuel coating and a stainless steel', *Wear*, **233-235**, (1999), pp. 623-634

88. Perry, J. M., Neville, A., Wilson, V. A., and Hodgkiess, T., 'Assessment of the corrosion rates and mechanisms of a WC-Co-Cr HVOF coating in static and liquid-solid impingement saline environments', *Surface & Coatings Technology*, **137**, (2001), pp. 43-51

89. Wang, B. Q. and Lee, S. W., 'Erosion-corrosion behaviour of HVOF NiAl-Al2O3 intermetallic-ceramic coating', *Wear*, **239**, (2000), pp. 83-90

90. Shreier, L. L., 'Corrosion Vol. 2 – Corrosion control', **3rd Ed.**, (1976), Newnes-Butterworths

91. Thompson, N. G. and Payer, J. H., 'DC Electrochemical test methods', Corrosion testing made easy, (1998), No. 6, Houston, Texas, NACE

92. Bjordal, M., Bardal, E., Rogne, T., and Eggen, T. G., 'Combined erosion and corrosion of thermal sprayed WC and CRC coatings', *Surface & Coatings Technology*, **70**, (1995), No. 2-3, pp. 215-220

93. Simard, S., Arsenault, B., Laul, K., and Dorfman, M., 'Performance of HVOF-sprayed coatings in aqueous environments', *Thermal Spray: Surface Engineering via Applied Research*, **May 2000**, (1999), pp. 983-990, ITSC 2000: 1st International Thermal Spray Conference, Montreal, Quebec, Canada, 8-11 May 2000

94. Cottis, R. A. and Turgoose, S., 'Electrochemical impedance and noise', (1999), Houston, Texas, NACE

95. Gusmano, G., Montesperelli, G., Pacetti, S., Petitti, A., and D'Amico, A., 'Electrochemical noise resistance as a tool for corrosion rate prediction', *Corrosion*, **53**, (1997), No. 11, pp. 860-868

96. Mansfeld, F., Han, L. T., Lee, C. C., and Zhang, G., 'Evaluation of corrosion protection by polymer coatings using electrochemical impedance spectroscopy and noise analysis', *Electrochimica Acta*, **43**, (1998), No. 19-20, pp. 2933-2945

97. Legat, A. and Dolecek, V., 'Corrosion monitoring-system based on measurement and analysis of electrochemical noise', *Corrosion*, **51**, (1995), No. 4, pp. 295-300

98. Miramontes, G., Farden, D. C., and Tallman, D., 'Transient analysis and simulation of pitting corrosion for the estimation of noise resistance', *Corrosion*, **56**, (2000), No. 9, pp. 928-934

99. Leban, M., Dolecek, V., and Legat, A., 'Comparative analysis of electrochemical noise generated during stress corrosion cracking of AISI 304 stainless steel', *Corrosion*, **56**, (2000), No. 9, pp. 921-927

100. Garcia, E., Mojica, J., Rodriguez, F. J., Enesca, J., and Arpio, J. J., 'Assessing of three industrial paint coatings by electrochemical noise', *NACE Corrosion 1998*, (1998), Paper no. 379, NACE

101. Mills, D. J., Bierwagen, G. P., Skerry, B. S., and Tallman, D., 'Investigation of anticorrosive coatings by the electrochemical noise method', *Materials Performance*, **34**, (1995), No. 5, pp. 33-38

102. Moon, M. and Skerry, B. S., 'Interpretation of corrosion-resistance properties of organic paint films from fractal analysis of electrochemical noise data', *Journal of Coatings Technology*, **67**, (1995), No. 843, pp. 35-44

103. Skerry, B. S. and Eden, D. A., 'Characterization of coatings performance using electrochemical noise analysis', *Progress in Organic Coatings*, **19**, (1991), No. 4, pp. 379-396

104. Bastos, I. N., Huet, F., Nogueira, R. P., and Rousseau, P., 'Influence of aliasing in time and frequency electrochemical noise measurements', *Journal of the Electrochemical Society*, **147**, (2000), No. 2, pp. 671-677

105. Cheng, Y. F., Luo, J. L., and Wilmott, M., 'Spectral analysis of electrochemical noise with different transient shapes', *Electrochimica Acta*, **45**, (2000), No. 11, pp. 1763-1771

106. Mattin, S. P. and Burstein, G. T., 'Detailed resolution of microscopic depassivation events on stainless steel in chloride solution leading to pitting', *Philosophical Magazine Letters*, **76**, (1997), No. 5, pp. 341-347

107. Iverson, W. P., 'Transient voltage changes produced in corrosing metals and alloys', *Journal of the Electrochemical Society*, **115**, (1968), pp. 617-618

108. Hladky, K, 'Corrosion monitoring', US Patent, (1986), No. 4,575,678, United States

109. Legat, A., 'Influence of electrolyte movement on measured electrochemical noise', *Corrosion*, **56**, (2000), No. 11, pp. 1086-1092

110. Burstein, G. T. and Sasaki, K., 'The birth of corrosion pits as stimulated by slurry erosion', *Corrosion Science*, **42**, (2000), pp. 841-860

111. Eden, D. A., John, D. G., and Dawson, D. A., 'Corrosion monitoring', US Patent, (1992), No. 5,139,627, United States

112. Mabutt, S. J. and Mills, D. J., 'Novel configurations for electrochemical noise measurements', *British Corrosion Journal*, **33**, (1998), No. 2, pp. 158-160

113. Mansfeld, F. and Xiao, H., 'Electrochemical noise analysis of iron exposed to NaCl solutions of different corrosivity', *Journal of the Electrochemical Society*, **140**, (1993), No. 8, pp. 2205-2209

114. Bertocci, U., 'Applications of a low noise potentiostat in electrochemical measurements', *Journal of the Electrochemical Society*, **127**, (1980), No. 9, pp. 1931-1934

115. Hladky, K and Dawson, J. L., 'The measurement of localised corrosion using electrochemical noise', *Corrosion Science*, **21**, (1981), No. 4, pp. 317-322

116. Eden, D. A., 'Electrochemical noise – The first two octaves', *NACE Corrosion 1998*, (1998), Paper no. 386, NACE

117. Searson, P. C. and Dawson, J. L., 'Analysis of electrochemical noise generated by corroding electrodesunder open circuit conditions', *Journal of the Electrochemical Society*, **135**, (1988), No. 8, pp. 1908-1915

118. Pistorius, P. C., 'Design aspects of electrochemical noise measurements for uncoated metals: Electrode size and sampling rate', *Corrosion*, **53**, (1997), No. 4, pp. 273-283

119. Tan, Y. J., Bailey, S., and Kinsella, B., 'The monitoring of the formation and destruction of corrosion inhibitor films using electrochemical noise analysis (ENA)', *Corrosion Science*, **38**, (1996), No. 10, pp. 1681-1695

120. Huet, F., Kunzt, C., and Takenouti, H., 'Measurement of electrolyte resistance fluctuations in corrosion applications', *NACE Corrosion 1998*, (1998), Paper no. 378, NACE

121. Cottis, R. A., Al Ansari, M. A., Bagley, G., and Pettiti, A., 'Electrochemical noise measurements for corrosion studies', *Electrochemical Methods in Corrosion Research Vi, Pts 1 and 2*, **289-292**, (1998), pp. 741-754

122. Souto, R. M. and Burstein, G. T., 'Study of corrosion processes with electrochemical noise measurements', *Electrochemical Methods in Corrosion Research Vi, Pts 1 and 2*, **289-2** , (1998), pp. 799-806

123. Chen, J. F. and Bogaerts, W. F., 'The physical meaning of noise resistance', *Corrosion Science*, **37**, (1995), No. 11, pp. 1839-1842

124. Proakis, J. G. and Manolakis, D. G., 'Digital signal processing', (1996), Prentice Hall

125. Speyer, A. J., 'Wear/corrosion sensing in flowing seawater', PhD thesis, (2002), University of Southampton

126. Mallat, S., 'A wavelet tour of signal processing', **2**, (1999), San Diego, Academic press

127. Aballe, A., Bethencourt, M., Botana, F. J., and Marcos, M., 'Using wavelets transform in the analysis of electrochemical noise data', *Electrochimica Acta*, **44**, (1999), pp. 4805-4816

128. Aballe, A., Bethencourt, M., Botana, F. J., and Marcos, M., 'Wavelet transform-based analysis for electrochemical noise', *Electrochemistry Communications*, **1**, (1999), No. 7, pp. 266-270

129. Huang, N. E., Shen, Z., Long, S. R., Wu, M. C., Shih, H. H., Zheng, Q., Yen, N. C., Tung, C. C., and Liu, H. H., 'The empirical mode decomposition and the Hilbert spectrum for nonlinear and non-stationary time series analysis', *Proc.R.Soc.Lond.A*, **454**, (1998), No. 1971, pp. 903-995

130. , 'ASM Metals Handbook Vol. 1 - Properties and selection: Iron, steels and high performance alloys', **10th Ed.**, (1990), No. 1, Ohio, ASM International

131. Ashour, E. A. and Ateya, B. G., 'Electrochemical behaviour of a copper-aluminium alloy in concentrated alkaline solutions', *Electrochimica Acta*, **42**, (1997), No. 2, pp. 243-250, Elsevier Science

132. Meigh, H. J., 'Cast and wrought aluminium bronzes - Properties, processes and structure', (2000), London, IOM Communications Ltd

133. Kofstad, P., 'High temperature oxidation of metals', (1966), Wiley

134. Herman, H., Sampath, S., and McCune, R, 'Thermal spray: current status and future trends', *MRS Bulletin*, **25**, (2000), No. 7, pp. 17-25

135. , 'ASM Metals Handbook Vol. 13 - Corrosion', **10th Ed.**, (1990), No. 13, Ohio, ASM International

136. Wharton, J. A., Wood, R. J. K., and Mellor, B. G., 'Wavelet analysis of electrochemical noise measurements during corrosion of austenitic and superduplex stainless steels in chloride media', *Corrosion Science*, **45**, (2003), No. 1, pp. 97-122

137. Ateya, B. G., Ashour, E. A., and Sayed, S. M., 'Corrosion of alpha-Aluminium bronze in saline water', *Journal of the Electrochemical Society*, **141**, (1994), No. 1, pp. 71-78

138. Culpan, E. A. and Foley, A. G., 'The detection of selective phase corrosion in cast nickel aluminium bronze by accoustic emission techniques', *Journal of Materials Science*, **17**, (1982), pp. 953-964

139. Ferrara, R. J. and Caton, T. E., 'Review of dealloying of cast aluminium bronze and nickel aluminium bronze alloys in seawater service', *NACE Corrosion 1981*, (1981), Paper no. 198, NACE

140. Hladky, K and Dawson, J. L., 'The measurement of corrosion using electrochemical 1/f noise', *Corrosion Science*, **22**, (1982), No. 3, pp. 231-237

141. Yang, M. Z., Luo, J. L., and Wilmott, M., 'Oscillation of potential and current during the initiation of crevice corrosion on carbon steel', *J.Material Sci.Letters*, **17**, (1998), pp. 1071-1075

142. Normand, B, Herbin, W., Landemarre, O., Coddet, C, and Pagetti, J., 'Electrochemical methods to the evaluation of thermal spray coatings corrosion resistance', *Materials Science Forum*, **289-292**, (1998), pp. 607-612

143. Zu, J. B., Hutchings, I. M., and Burstein, G. T., 'Design of a slurry erosion test rig', *Wear*, **140**, (1990), pp. 331-344

144. Finnie, I. and McFadden, D. H, 'On the velocity dependence of the erosion of ductile metals by solid particles at low angles of incidence', *Wear*, **48**, (1978), pp. 181-190

145. Clark, H. M. and Burmeister, L. C., 'The influence of squeeze film on particle impact velocities in erosion', *International Journal of Impact Engineering*, **12**, (1992), No. 3, pp. 415-426

146. Hearley, J. A., Little, J. A., and Sturgeon, A. J., 'The erosion behaviour of NiAl intermetallic coatings produced by high velocity oxy-fuel thermal spraying', *Wear*, **233-235**, (1999), pp. 328-333

147. Mann, B. S. and Arya, Vivek, 'Abrasive and erosive wear characteristics of plasma nitriding and HVOF coatings: their application in hydro turbines', *Wear*, **249**, (2001), No. 5-6, pp. 354-360

148. Tan, K. S., Wood, R. J. K., and Stokes, K. R., 'The slurry erosion behaviour of High Velocity Oxy-Fuel (HVOF) sprayed aluminium bronze coatings', *Wear*, **To be published**, (2004)

149. Tilly, G. P., 'A two stage mechanism of ductile erosion', *Wear*, **23**, (1973), No. 1, pp. 87-96, Elsevier

150. Wood, R. J. K., Mellor, B. G., and Binfield, M. L., 'Sand erosion performance of detonation gun applied tungsten carbide/cobalt chromium coatings', *Wear*, **211**, (1997), pp. 70-83

151. Zhang, L., Sazonov, V., Kent, J., Dixon, T., and Novozhilov, V., 'Analysis of boiler-tube erosion by the technique of accoustic emission. Part I - Mechanical erosion.', *Wear*, **250**, (2001), pp. 762-769

152. Lin, F. Y. and Shao, H. S., 'Effect of impact velocity on slurry erosion and a new design of a slurry erosion tester', *Wear*, **143**, (1991), pp. 231-240

153. , 'Drinking water quality report 2001', (2001), Southern Water, Worthing, West Sussex, UK

154. Wood, R. J. K. and Speyer, A. J., 'Erosion-corrosion of candidate HVOF aluminium based marine coatings', *Wear*, (2003), No. Special issue on tribo-corrosion, pp. In press-

155. Karimi, A and Schmid, R. K., 'Ripple formation in solid-liquid erosion', *Wear*, **156**, (1992), pp. 33-47

156. Speyer, A. J., Wood, R. J. K., and Stokes, K. R., 'Erosion of aluminium-based claddings on steel by sand in water', *Wear*, **250**, (2001), pp. 802-808

157. Timoshenko, S. P. and Goodier, J. N., 'Theory of Elasticity', **3**, (1970), New York, McGraw-Hill

158. Wheeler, D. W. and Wood, R. J. K., 'Solid particle erosion of CVD diamond coatings', *Wear*, **233-235**, (1999), pp. 306-318

159. Douglas, J. F., Gasiorek, J. M., and Swaffield, J. A., 'Fluid mechanics', **3**, (1995), London, Longman

160. Oldfield, J. W. and Masters, G. L., 'Collation of data comparing properties of aluminium bronze with cast stainless steels and Ni-resist in offshore seawater environments', (1996), London, CDA publication no. 115, Copper Developement Association

161. Syrett, B. C., 'Erosion-corrosion of copper-nickel alloys in seawater and other aqueous environments - A literature review', *Corrosion*, **32**, (1976), No. 6, pp. 242-252

162. Monticelli, C., Fonsati, M, Meszaros, G., and Trabanelli, G., 'Copper corrosion in industrial waters - a multi method analysis', *Journal of the Electrochemical Society*, **146**, (1999), No. 4, pp. 1386-1391

163. Wojcik, P. T., Charriere, E., and Orazem, M. E., 'Experimental study of the erosion-corrosion of copper and copper-nickel alloys at the corrosion potential and anodic potentials.', **Tri-service conference on corrosion**, (1997), North Carolina, Naval surface warfare centre

164. Vreijling, M. P. W., Westing, E. P. M., Ferrari, G. M., Svaldi, P., Westendorp, F. P. E., Bullock, E., and de Wit, J. H. W., 'The effect of thermal spray process on the protective behaviour of NiCr alloys in seawater', **Intercorr/96 online corrosion conference**, (1996), http://www.corrosioncource.com/events/intercorr

165. Sasaki, K. and Burstein, G. T., 'Observation of a threshold impact energy required to cause passive film rupture during slurry erosion of stainless steel', *Philosophical Magazine Letters*, **80**, (2000), No. 7, pp. 489-493

166. Neville, A. and Hu, X., 'Mechanical and electrochemical interactions during liquid-solid impingement on high-alloy stainless steels', *Wear*, **251**, (2001), No. 1-12, pp. 1284-1294

167. Neville, A., Reyes, M., and Xu, H., 'Examining corrosion effects and corrosion/erosion interactions on metallic materials in aqueous slurries', *Tribology International*, **35**, (2002), No. 10, pp. 643-650

168. Noel, R. E. J. and Ball, A., 'On the synergistic effects of abrasion and corrosion during wear', *Wear*, **87**, (1983), pp. 351-361

169. Annual book of ASTM standards, 'ASTM G119, Metals corrosion - Wear and Erosion', (1996), No. 03.02, ASTM

170. Kwok, C. T., Cheng, F. T., and Man, H. C., 'Synergistic effect of cavitation erosion and corrosion of various engineering alloys in 3.5% NaCl solution', *Materials Science and Engineering A*, **290**, (15-10-2000), No. 1-2, pp. 145-154

171. Madsen, B. W., 'Measurement of erosion-corrosion synergism with a slurry wear test apparatus', *Wear*, (1988), No. 127, pp. 142-

172. Wood, R. J. K., 'Use of profilometric measurements in cavitation erosion and corrosion studies', *Proc.Inst.Mech.Engineers*, **204**, (1990), No. Part C: Journal of Mechanical Engineering Science, pp. 63-65

173. Schumacher, W, 'Service validation of corrosive wear synergy', *Wear*, **251**, (2001), No. 1-12, pp. 1279-1283

174. Burstein, G. T. and Sasaki, K., 'Effect of impact angle on the slurry erosion-corrosion of 304L stainless steel', *Wear*, **240**, (2000), pp. 80-94

175. Dawson, J. L., Shih, C. C., John, D. G., and Eden, D. A., 'Electrochemical testing of differential flow induced corrosion using jet impingement rigs', *NACE Corrosion 1987*, (1987), Paper no. 453, NACE

176. Clark, H. McI, 'Particle velocity and size effects in laboratory slurry erosion measurements OR... do you know what your particles are doing?', *Tribology International*, **35**, (2002), No. 10, pp. 617-624

177. Oltra, R., Chapey, B., Huet, F., and Renaud, L., 'Coupling of accoustic emission and electrochemical noise measurement techniques in slurry erosion-corrosion studies.', (1996), pp. 361-374, American Society for Testing and Materials

178. Roberge, P. R. and Beaudoin, R., 'Behaviour of the corrosion potential and corrosion current of Cu-Ni alloys under erosion-corrosion conditions. Effect of oxygen.', *Journal of Applied Electrochemistry*, **18**, (1988), pp. 601-607

179. Mahato, B. K., Voora, S. K., and Shemilt, L. W., 'Steel pipe corrosion under flow conditions - 1. An isothermal correlation for a mass transfer model', *Corrosion Science*, **8**, (1968), pp. 173-193

180. Matsumura, M, Noishiki, K., and Sakamoto, A., 'Jet-in-slit test for reproducing flow-induced localized corrosion on copper alloys', *Corrosion*, **54**, (1998), No. 1, pp. 79-88

181. Sekine, I, Yuasa, M, Niwa, S., Goino, T., Iino, H., Kakinuma, H., Higashiguchi, M., and Tanaki, T., 'Erosion-corrosion behaviuor of copper alloys under flowing water conditions', *Corrosion Engineering*, **40**, (1991), pp. 621-629

182. Cheng, Y. F. and Luo, J. L., 'Metastable pitting of carbon steel under potentiostatic control', *Journal of the Electrochemical Society*, **146**, (1999), No. 3, pp. 970-976

183. Oltra, R., Gabrielli, C., Huet, F., and Keddam, M., 'Electrochemical investigation of locally depassivated iron. A comparison of various techniques', *Electrochimica Acta*, **31**, (1986), No. 12, pp. 1505-1511

184. Sasaki, K. and Burstein, G. T., 'The generation of surface roughness during slurry erosion-corrosion and its effects on the pitting potential', *Corrosion Science*, **38**, (1996), No. 12, pp. 2111-2120

185. Cottis, R. A., 'Interpretation of electrochemical noise data', *Corrosion*, **57**, (2001), No. 3, pp. 265-285

186. Motard, R. L., Joseph, B., and Dai, X. D., 'Interpretation of Electrochemical Voltage Noise in Corrosion of Mild and Stainless Steels', **Intercorr/96 online corrosion conference**, (1996), http://www.corrosionsource.com/events/intercorr

187. Aballe, A., Bethencourt, M., Botana, F. J., Marcos, M., and Sanchez-Amaya, J. M., 'Use of wavelets to study electrochemical noise transients', *Electrochimica Acta*, **46**, (30-4-2001), No. 15, pp. 2353-2361

188. Benzaid, A., Huet, F., Jerome, M., Wenger, F., Gabrielli, C., and Galland, J., 'Electrochemical noise analysis of cathodically polarised AISI 4140 steel. III. Influence of hydrogen absorption for stressed electrodes', *Electrochimica Acta*, **47**, (15-10-2002), No. 27, pp. 4333-4338

189. de Sanchez, S. R. and Schriffrin, D. J., 'The use of high speed rotating disc electrodes for the study of erosion-corrosion of copper base alloys in sea water', *Corrosion Science*, **28**, (1988), No. 2, pp. 141-151

190. Lush, P. A. and Carr, M. J., 'Copper dissolution in sea water under mixed activation and diffusion control', *Corrosion Science*, **19**, (1979), pp. 1079-1088

Appendix A – Design and construction of the jet impingement rig

The current investigation involves the design and construction of a jet impingement rig that was used in the erosion, corrosion and erosion-corrosion experiments. The purpose of this experimental rig is to provide a nominally constant set of conditions/parameters for the three types of experiments. The rig was based on the original design proposed by Zu *et al.* [143], consisting of a top electrochemical section, a middle section containing the electrolyte reservoir and sand particles and finally an impeller pump situated in the bottom section. Similar features were found on the rig used in the current work, shown in Figure A-1.

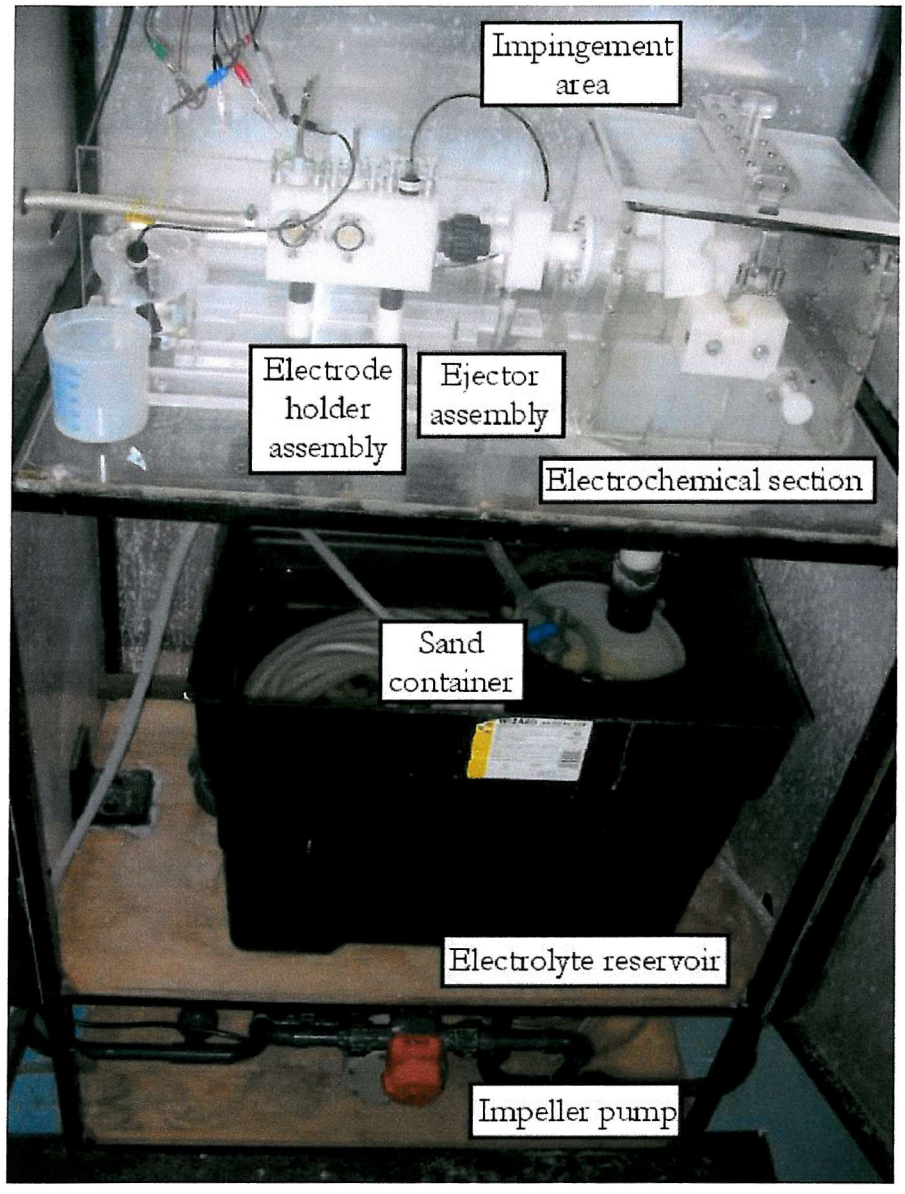

Figure A-1: The jet impingement rig used in the current work.

As seen in the flow diagram in Figure A-2, the electrolytes were circulated from the reservoir through a filter and an impeller pump, passing through the counter and reference electrodes before reaching the ejector assembly. A pressure drop occurs when the electrolyte exits the ejector nozzle, creating a vacuum that lifts the sand particles from the sand container. A ball valve on the sand lift tube was used to control the amount of sand lift into the ejector assembly. The mixture of electrolyte and sand particles (slurry) is projected onto the target material surface via the jet nozzle. A funnel was used for channelling the slurry back into the sand container where sand particles were separated from the electrolyte by sedimentation.

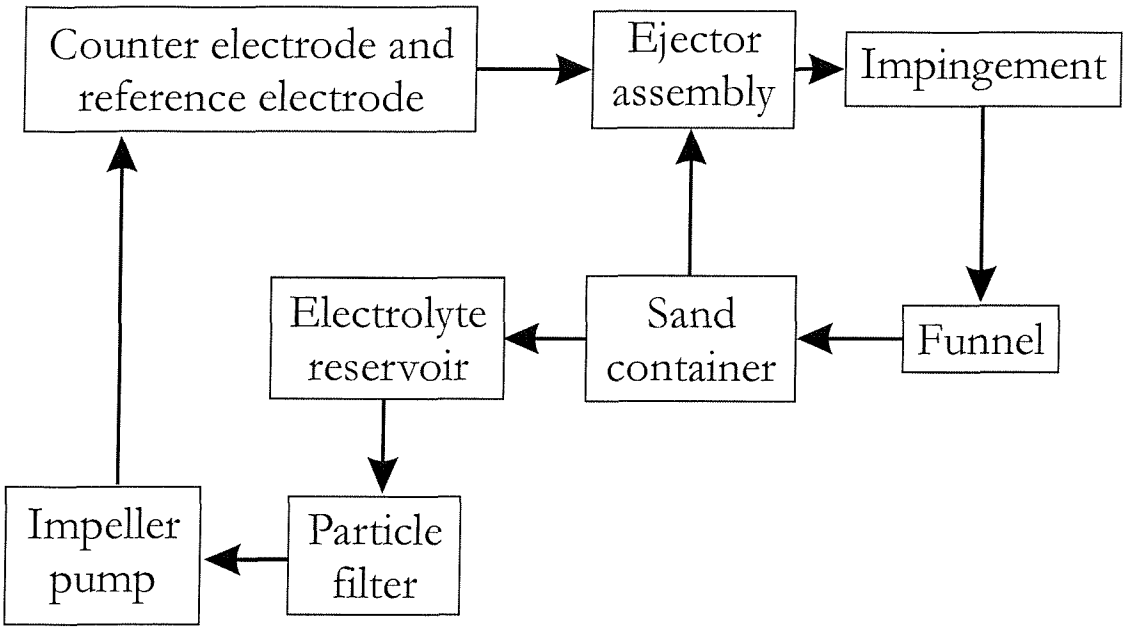

Figure A-2: Flow diagram of the jet impingement rig.

Several modifications were being made to accommodate the types of experiments carried out in the current investigation:

1. A new impeller pump was fitted, providing a maximum flow rate of 32 l/min. When compared to the previous jet impingement rig (6 l/min) [83,125], the higher flow rate permitted the jet velocity to be increased up to 6.7 ms^{-1}.
2. The previous jet impingement rig utilised graphite counter electrodes that are brittle and prone to fracture when inserted into the electrode holder. Platinum electrodes are used in the current work, they were encapsulated into a cartridge and welded to a platinum wire for cell connections. The cartridge is then inserted into the electrode holder assembly, shown in Figure A-3.
3. A chlorodised silver reference electrode was used for potential measurements and potentiostatic control. The reference electrode was also situated in the electrode holder assembly seen in Figure A-3.
4. Two types of ejector nozzles (3.0 and 3.5 mm) and outer nozzles (5.5 and 6.5 mm) were used, a combination of the two provides flow rates between 7.4 and 9.8 l/min and jet velocities between 3.1 and 6.7 ms^{-1}.
5. Hand adjustment on the ball valve at the bottom of the slurry tube allows the slurry concentration to be controlled, the slurry concentration was fixed at 1.5, 3.0 and 5.0 % w/w.

6. The specimen holder in the slurry impingement section was redesigned. Previous work requires a wire to be soldered onto the back face of the specimen, which will inevitable affect mass loss measurements. In order to minimise these discrepancies, a connector assembly was fabricated, providing a secure contact to the specimen and allows connection to a wire that runs to the electrode holder assembly. A rubber washer was used to prevent electrolyte from entering the specimen holder. An exploded view of the specimen holder assembly is shown in Figure A-4 while the assembly procedure is shown in Figure A-5.

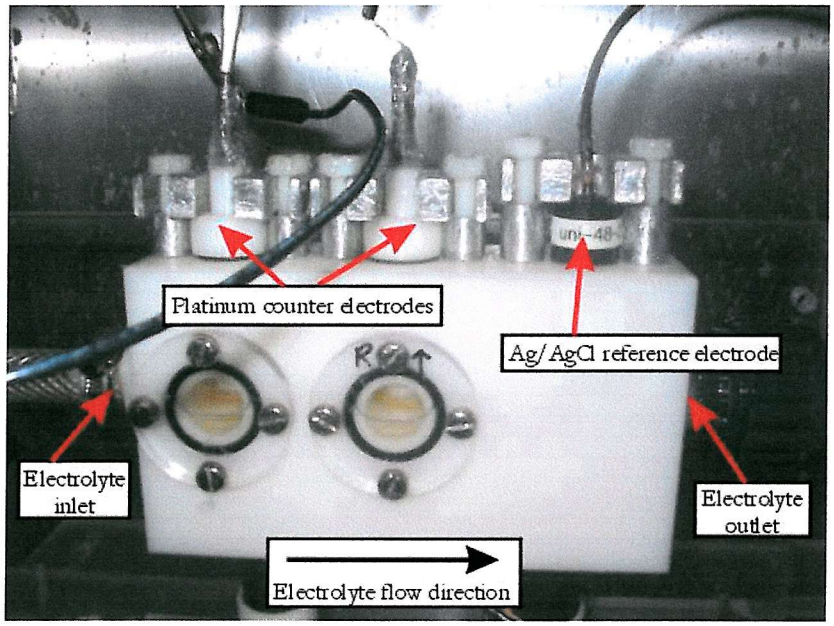

Figure A-3: The electrode holder assembly.

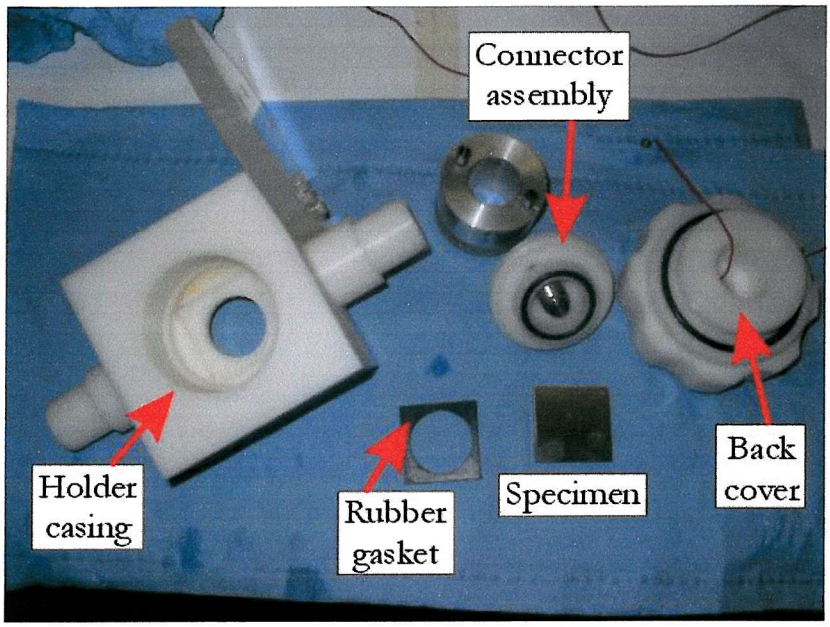

Figure A-4: An exploded view of the specimen holder assembly.

The following procedures (shown in Figure A-5) are used for securing the specimen into the specimen holder:

(a) Place rubber gasket and specimen into the holder casing.
(b) Assemble the connector assembly to the back face of the specimen, ensure that the connector is in contact with the specimen.
(c) Secure the connector assembly and attach a conducting wire to the connector.
(d) Insert the other end of the conducting wire through the back cover.
(e) Move the back cover towards the holder casing, pull any extra lengths of conducting cable through the back cover.
(f) Secure the back cover to the holder assembly.

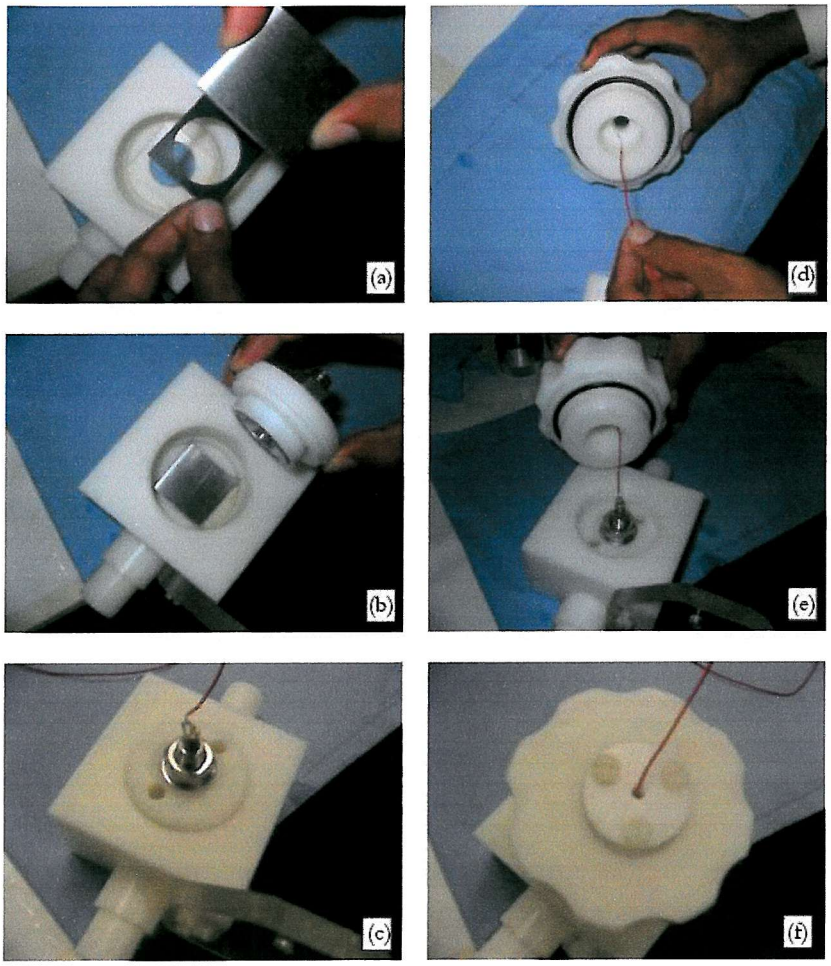

Figure A-5: Procedures for encapsulating the specimen into the specimen holder.

Appendix B – Procedures for obtaining the 2D surface profiles

Original 2D surface profiles from the Taylor Hobson 120L Talysurf are obtained in the binary data file format. In order to process the data in MATLAB, the binary files were converted to ACSII format. The file conversion was carried out with the following MATLAB code:

```
%       Open the graphical user interface to interactively retrieve a filename and save
%       it in the variables n = name and p = path. These two variables will be required
%       to call 'readdat.m'. The pause command is required to get the message window
%       disappear before the DOS commands are carried out.

 [n, p] = uigetfile('*.prf', 'Select Data-Set to be Fitted')
 pause(0.5)


%       If a file was chosen by the operator convert it into an ASCII-file by running the
%       standalone program BIN2ASC.EXE in DOS mode.
%       The file name and path are fixed in
%       bin2asc.exe as c:\convert.map. The file chosen by the operator is copied to C root
%       and renamed to the default name (convert.map), then translated into an ASCII-file
%       (convert.dat) and finally copied back to the original place with the original
%       name (however, with extension *.dat). The routine deletes afterwards all the files
%       which are no longer required.

 if (n~=0)

   dos(['copy ', p, n, ' C:\convert.prf']);                    %get hold of a copy of the file
   dos('C:\conv_dep C:\convert.prf -A  C:\output.dat');        %convert from binary to ascii

   n(size(n,2)-2) = 'd';                                       %change the filename to *.dat
   n(size(n,2)-1) = 'a';                                       %which is the extension of the
   n(size(n,2)-0) = 't';                                       %converted file

   dos(['copy C:\output.dat ' 'C:\2Dprof\' n])

   dos('del C:\convert.prf');
   dos('del C:\output.dat');


 end
```

Once the binary files are converted to ASCII format, the headers and footers were removed in MS Excel. The data file is then imported into MATLAB and plotted as a raw profile. Due to the non-level specimen surfaces, a linear least squares fitting is required to generate a level profile. Points were selected from the periphery of the specimen (the un-eroded area) as they show the original surface. The profiles were subsequently modified with the curve fitting line

and presented as a truly level surface profile. The MATLAB code used for curve fitting is provided below:

```
%       KS Tan - 20th SEPTEMBER 2002 - Version 1.00

%       This routine prompts the user to select relevant points that would be
%       subsequently used for a linear least squares fit. The slope and intersection
%       was then extracted from the linear least squares fit, so that another set
%       of datas could be produced. The new set of data is then substracted from the
%       original data set so that the whole profile could be corrected.

%       STEP 1:- Prompting the user to select a set of data to be used

%       Message display
disp('USE THE MOUSE TO SELECT THE REQUIRED POINTS,')
disp('FINISH BY PRESSING (RETURN)')

%       User is prompted to select points with their mouse
[x,y]=ginput;

%       Extra commands to plot the selected points
%figure;
%plot(x,y);

%xlabel('linearfit line - X');
%ylabel('linearfit line - Y');

%       STEP 2:- Linear curve fitting
p=polyfit(x,y,1);   % Linear least squares fit, 1 degree.

slope=p(:,1);               % Identify slope
const=p(:,2);               % Identify intersection constant

f=polyval(p,x);             % Producing a new set of Y-data based on the linear fit equation

figure                      % Plotting and comparing selected data and fitting results
plot(x,y,'o',x,f,'-')
title('Comparison of selected data and curve fitting result');


% STEP 3:- Generating a new string of data based on the linear curve fitting

curvefitY=(slope*Distance)+const;   % Y=mX + C

newY=Height-curvefitY';   % Correcting the 2D profile by fitting the least squares line.

figure                          % Plotting the corrected profile

plot(Distance,newY);

title('Corrected 2D profile of');
xlabel('Distance (mm)');
ylabel('Displacement (Microns)');

clear slope;
clear const;
clear f;
clear p;
clear x;
```

```
clear y;
clear curvefitY;

end;
```

The flow diagram in Figure B-1 shows the procedures explained above.

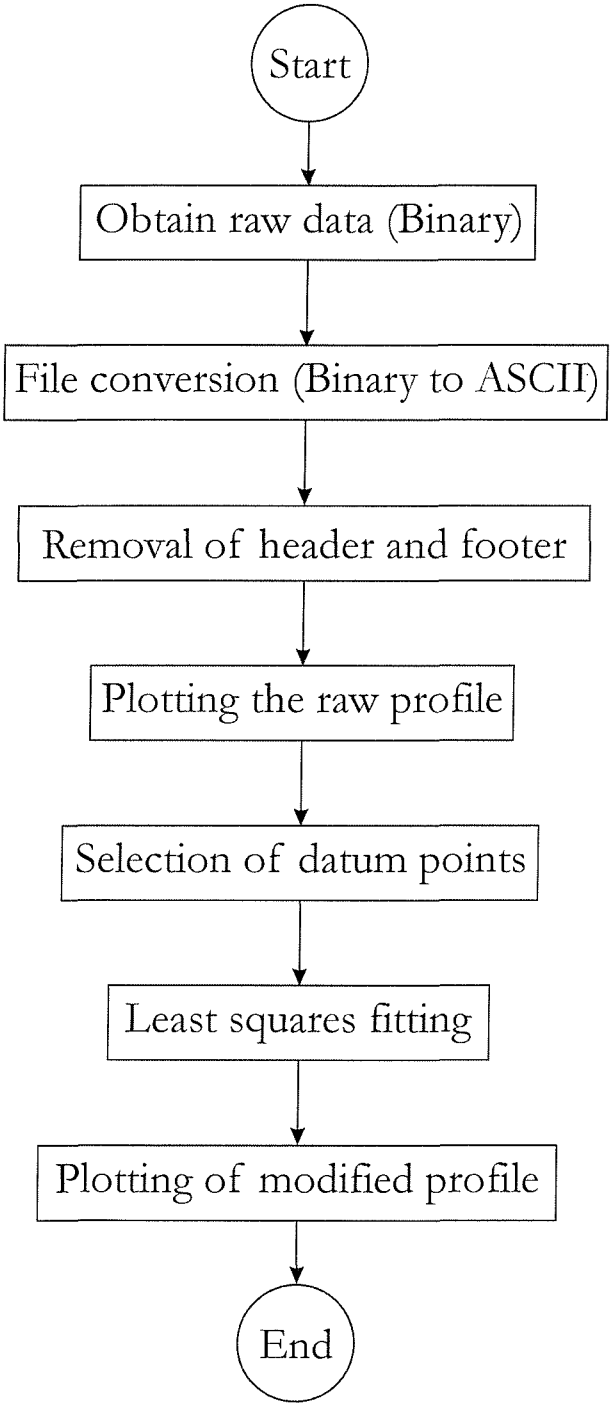

Figure B-1: Flow diagram showing the procedures for obtaining the 2D profiles for erosion, flow corrosion and erosion-corrosion specimens.

Appendix C – Estimation of synergy by calculation of electrochemical standard deviation

Under low kinetic energy conditions, negative synergy values were obtained, indicating reduced mass loss under erosion-corrosion or mass gain under flow corrosion.

$T = E + C - S$ *Equation D-1*

and $S = \Delta E + \Delta C$ *Equation D-2*

From Figure 7-12, it is shown that when $\sigma T / \sigma C$ approaches zero, the contribution of erosion enhanced corrosion (ΔC) is nearly zero as well. This corresponded with low kinetic energy of the sand particles.

$\sigma T / \sigma C \rightarrow 0 \; ; \; \Delta C \rightarrow 0$ *Equation D-3*

This indicates that under low kinetic energy,

$S = - \Delta E$ *Equation D-4*

Hence

$T = E + C - \Delta E$ *Equation D-5*

It is shown that in Equation D-4 negative corrosion enhanced erosion (ΔE) can occur under erosion-corrosion conditions. This is probably due to a highly efficient protective layer that acts as an interface between the target material surface and the impinging sand particles at low kinetic energies, reducing the rate of material removal.

At high kinetic energy conditions, positive synergy value was obtained:

$T = E + C + S$ *Equation D-6*

and high standard deviation ratio was obtained, indicating increased contributions of ΔC. As the system is actively corroding, ΔE will be positive as well.

$T = E + C + \Delta E + \Delta C$ *Equation D-7*

It was shown by Equation D-5 and Equation D-7 that the material loss under erosion-corrosion is variable and dependent on the sand particle kinetic energy and corrosion behaviour of the target material. If a stable protective layer can be sustained under sand particle impingement, the E/T mass loss ratio (Figure 7-2) will be large (based on variable T values). As the kinetic energy is increased, T values will be greater and E/T ratio will be reduced, moving the system towards a positive synergy regime.

Appendix D – Processing of electrochemical current noise signals with the discrete wavelet transform (DWT) and empirical mode decomposition (EMD) methods.

The discrete wavelets transform (DWT)

A relatively new technique for electrochemical noise analysis, the DWT decomposition, was also carried out on the ECN signals. Motard *et al.* first used it for analysing crevice and pitting corrosion of mild and stainless steels [186]. Subsequent work was carried out on the corrosion of aluminium specimens in NaCl solution [127,128,187]. As previously described in Section 2.5.5, Chapter 2, the process involves convolving the original ECN signal with a predetermined 'wavelet function' – containing an average value of zero and average squared value of unity. By changing the scale of the individual wavelet function and shifting it along the original ECN signal, a set of coefficients containing both time and frequency information can be obtained. The frequency and scale functions are then used to describe the ECN signals in a qualitative manner.

The DWT was carried out on the ECN signals using the MATLAB Wavelets Toolbox. It was applied to flow corrosion and erosion-corrosion conditions to investigate the following:

- The evolution of individual experiments, assessing the protective film growth and dissolution processes. These signals were obtained from experiments using constant velocity and sand concentration.
- The corrosion behaviour of the specimens when the jet velocity was altered. These signals were obtained from experiments using constant sand concentrations.

The Haar wavelet was used for the DWT analysis because it is the simplest wavelet and it is orthogonal. Furthermore, comparisons can also be made with recent work carried out by Speyer [125].

DWT analysis of the ECN signals resulted in a series of wavelet coefficients, each one of them corresponding to a frequency. The initial decomposition is associated with the Nyquist

frequency (i.e. 5 Hz and a period of 0.2 s). Subsequent decomposition follows the dyadic scale, meaning that following decompositions will have periods of 0.4 s, 0.8 s, 1.6 s and so on [126]. ECN signals were sampled at 10 Hz for 16.4 seconds, resulting in 164 data points. Seven wavelet scales were used, with the largest scale corresponding to a period of 12.8 s (providing frequency information of 0.08 Hz).

Figure D-1 shows DWT coefficients obtained from the ECN signal under erosion-corrosion at 5.0 ms^{-1}. The x-axis shows experimental progress (time), the y-axis shows the wavelet scales used, and the z-axis shows the power (variance) obtained from each DWT coefficients. The power of the coefficients lies generally at about 0.005, fluctuations were present at all frequencies and time, they were small in magnitude (~ 0.005). These fluctuations in the DWT coefficients are related to the effects of solid particle impingement on the corrosion of the NAB coating surface. A typical ECN signal obtained from erosion-corrosion of the NAB coating is shown in Figure D-2. As seen in the figure, the ECN signal experienced high levels of random fluctuations due to sudden depassivation and repassivation processes. As the 10 Hz acquisition frequency was not sufficient to resolve individual particle impacts, the fluctuations and subsequent DWT coefficients observed show the effects of averaged electrochemical activity on the specimen surface.

A variance peak is observed at the beginning of the experiment, in the low frequency region. This fluctuation can be associated with the initial instability caused by sudden exposure of a dry specimen to erosion-corrosion conditions. The low frequency process was probably caused by the sudden removal/modification of the pre-existent air-formed film when the surface was exposed to erosion-corrosion conditions. This will cease as the specimen surface acquires equilibrium under erosion-corrosion conditions.

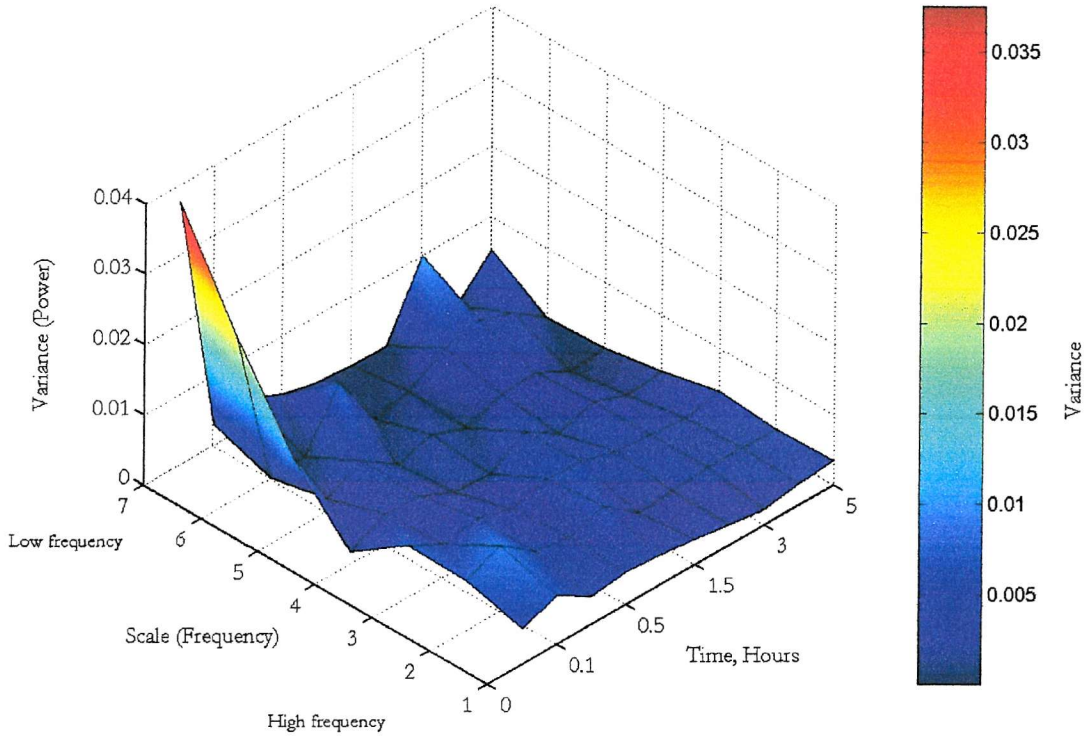

Figure D-1: DWT decomposition of ECN, NAB coating on steel substrate, erosion-corrosion at 6.7 ms^{-1}, 235 μm mean sand particle diameter, 25 °C.

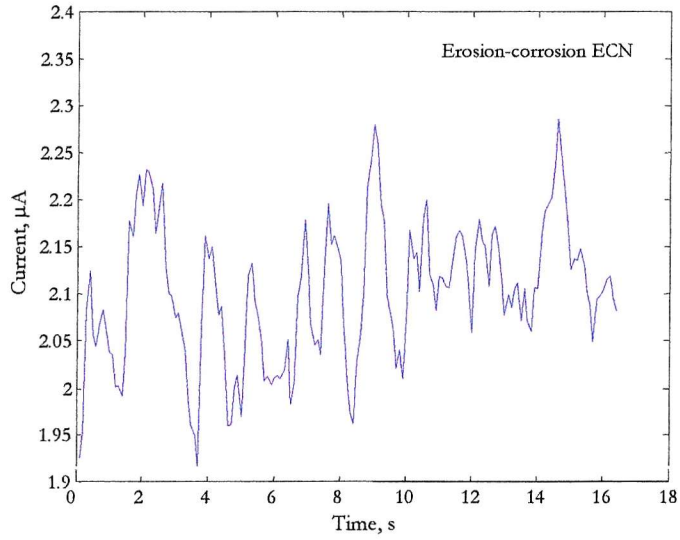

Figure D-2: A typical ECN signal obtained from erosion-corrosion of the NAB coating

Figure D-3 shows the DWT decompositions carried out on the ECN under flow corrosion conditions. The z-axis was expanded to accommodate the lower coefficient values under flow corrosion condition (nearly zero), compared to much higher values under erosion-corrosion

conditions (~ 0.005). The DWT coefficients revealed more uniformly distributed values throughout the experiment. This reflects the presence of a protective film on the coating surface. The protective film forms a barrier between the coating surface and the electrolyte, resulting in lower corrosion activity and less ECN fluctuations. A typical ECN signal obtained under flow corrosion conditions is shown in Figure D-4, showing the lower ECN fluctuations when compared to EC conditions (Figure D-2).

A variance peak (~ 0.005) was also observed at the beginning of the experiment, at the low frequency region. This can also be associated with the initial instability when the air-formed film was exposed to the flowing electrolyte. The process acquires an equilibrium when a stable film is formed on the specimen surface under jet impingement.

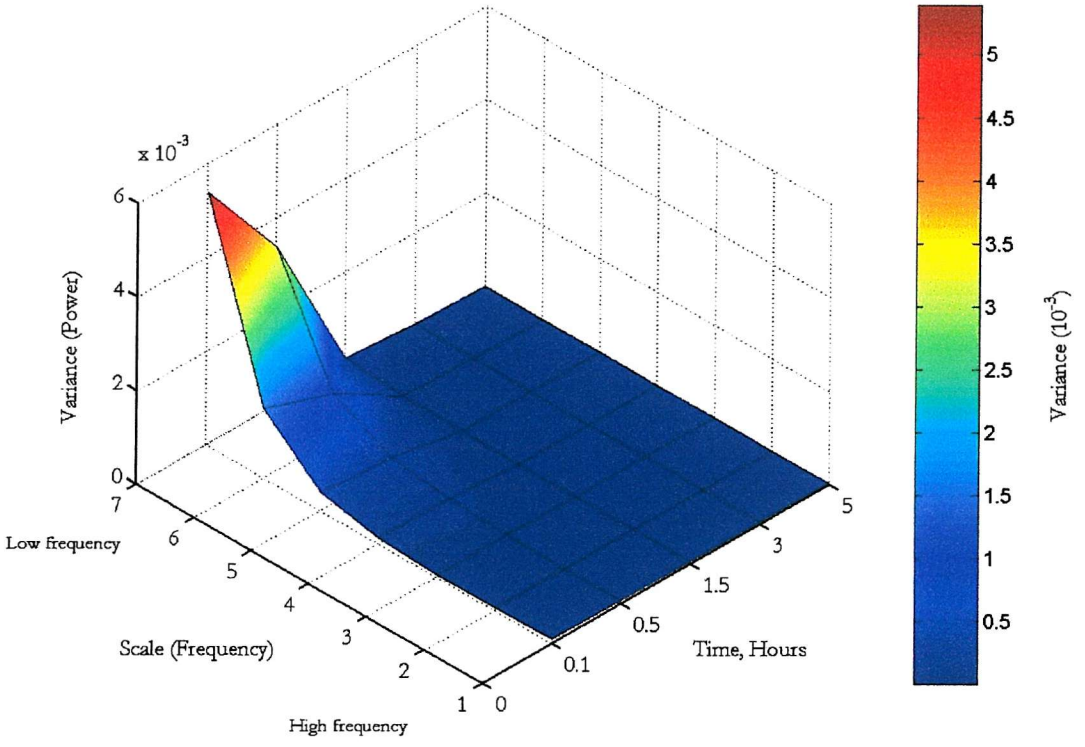

Figure D-3: DWT decomposition of ECN, NAB coating on steel substrate, flow corrosion at 6.7 ms^{-1}, 25 °C.

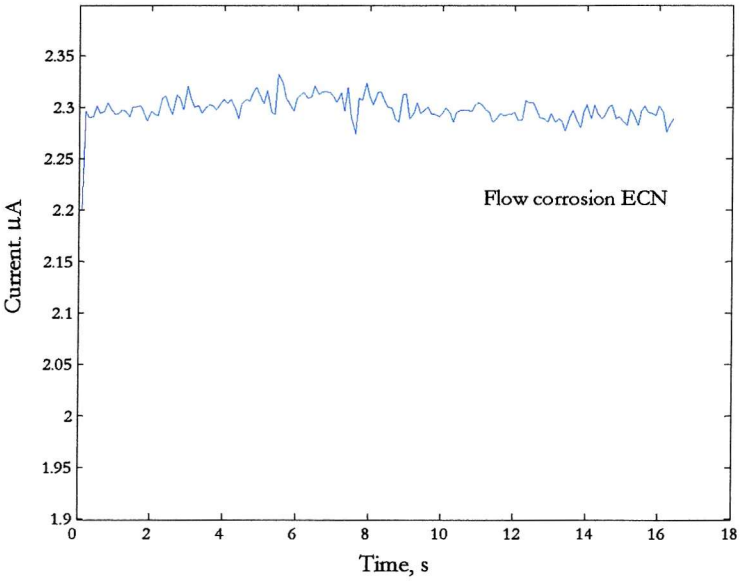

Figurer D-4: A typical ECN signal obtained from flow corrosion of the NAB coating

The DWT decomposition method has demonstrated that distinctions can be made between erosion-corrosion and flow corrosion processes, it is done by measurement of the absolute power of the coefficients and its uniformity.

In order to visualise the differences in the erosion-corrosion and flow corrosion coefficients, raw signals for both processes are plotted and shown in Figure D-5. The signals show ECN records at the beginning of the experiment (red) and the end of the experiment (blue). For both EC and FC conditions, the beginning of data acquisition revealed a DC trend, associated with initial instability as discussed earlier. The DC trend resulted in the variance peak observed at the high wavelet scales of the DWT decomposition.

ECN traces obtained towards the end of EC and C experiments show stable electrochemical noise signals without any obvious trends. Higher levels of current noise fluctuations associated with sand particle impingement [125,183,188] (Section 7.4). The amount of active surface area exposed during erosion-corrosion is random, it is related to the kinetic energy of individual sand particles and its contact angle during impact, generating a random ECN signal. This type of noise signal is observed as random fluctuations in the DWT coefficients (seen in Figure D-1). No characteristic frequencies were found in the EC noise signals.

For FC conditions, a downward drift in the ECN was observed at the beginning of the experiment. This indicated that the air formed film is slowly being replaced by a liquid-

formed film, reducing the dissolution rate of the coating. Under EC conditions, an upward drift in the positive direction was observed, showing increasing corrosion rates at the beginning of the experiment. The increasing dissolution rate was caused by the removal of the previous air formed film by the sand particles. As the stable liquid-formed film cannot be formed under solid particle impingement, increasing corrosion rates resulted in the upward drift in the ECN.

The absolute current noise level under FC conditions was higher at the end of the experiment. As discussed previously in Chapter 5, it is possible for the electrolyte to permeate the coating through the pore network during the experiment. The electrolyte situated within the pore network will react with the surrounding coating and further increase the corrosion rate. As corrosion proceeds, it is possible for the electrolyte to become more acidic, further enhancing corrosion rates.

For EC, the current noise level was found to be lower at the end of the experiment. This indicated lower corrosion rates, which is not possible under sand particle impingement conditions. Dissolution rates are higher initially when the air formed film was replaced by the liquid formed protective layer, producing higher current levels. As erosion-corrosion proceeds, the area directly under the jet stream (stagnation region) becomes anodic while the outer region (free jet region) in highly cathodic [167]. This surface polarisation can lead to a short circuit between the localised anode and cathode, resulting in lower current flow to the platinum counter electrode and subsequently lower current noise levels [177].

(a) (b)

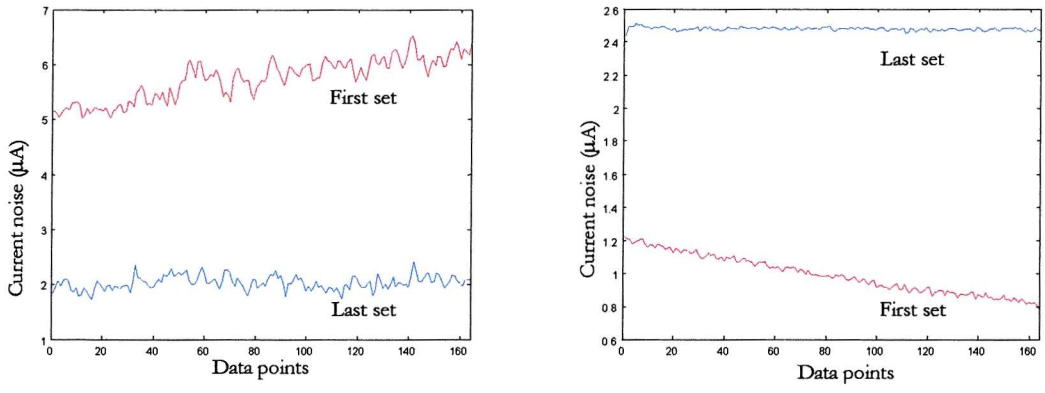

Figure D-5: Current noise signals for (a) erosion-corrosion, first and last time series and (b) flow corrosion, first and last time series

DWT decompositions were also carried out on the ECN signals that are obtained from experiments using various jet velocities. Current noise was recorded to show the severity of corrosion when the jet velocity/kinetic energy was increased.

Figure D-6 shows the DWT decomposition for the EC experiment, using 3.1 – 6.7 ms^{-1} jet velocities. Low variance values (nearly zero) were found at the low E_k conditions (E_k = 0.02 μJ, obtained by 3.1 ms^{-1} jet velocity and 135 μm diameter sand), indicating ECN signals that are similar to flow corrosion conditions due to the inability of the sand particles to impact the surface and cause protective film rupture or cut into the surface. As the kinetic energy is increased, the variances of the coefficients are shown to increase for all frequencies, up to values close to 0.02. This increase implies higher corrosion rates, probably associated with the removal of protective layers and increased mass transfer rates [165]. Variations were also observed in the coefficients, indicating depassivation/repassivation processes. A sudden transition between low (< 0.01) and high (> 0.01) variance is found at 5.0 ms^{-1}, indicating a sudden increase in ECN fluctuations (corrosion rate). The transition at 5.0ms^{-1} can be used as a kinetic energy threshold indication for the EC processes.

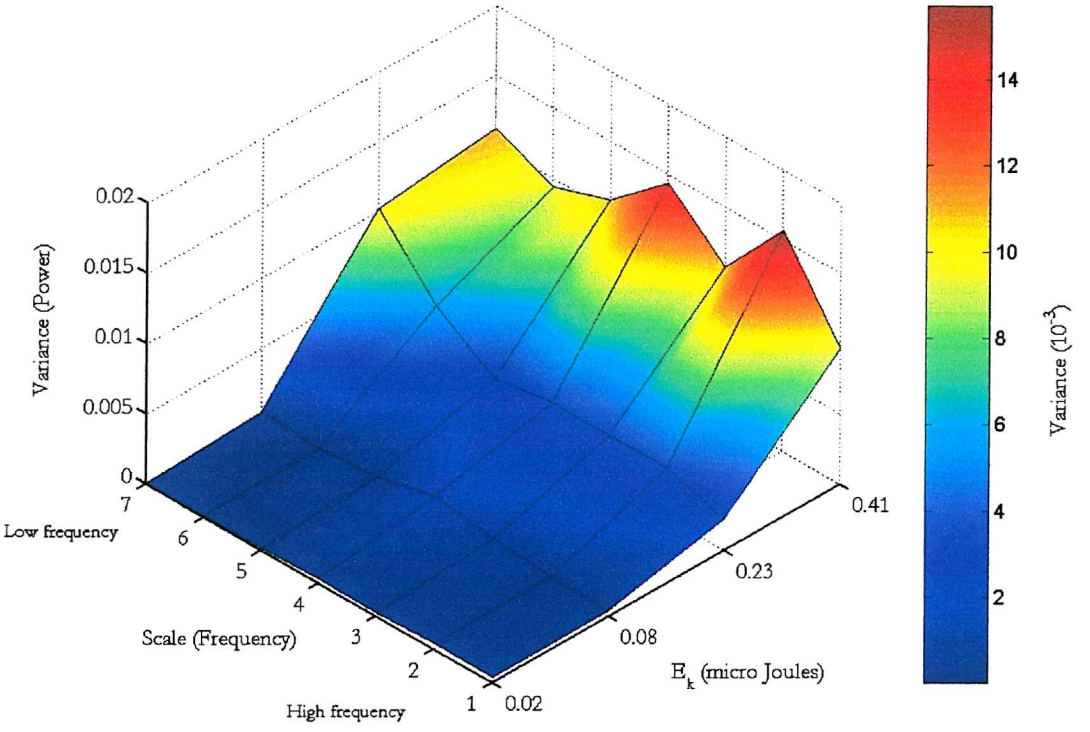

Figure D-6: DWT decomposition of ECN, NAB coating on steel substrate, erosion-corrosion, 25 °C. Kinetic energy, jet velocity and sand diameter: 0.41 μJ (6.7 ms^{-1} / 235 μm), 0.23 μJ (5.0 ms^{-1} / 235 μm), 0.08 μJ (3.1 ms^{-1} / 235 μm), 0.02 μJ (3.1 ms^{-1} / 135 μm)

Similar decompositions are also obtained from the FC experiments and the results shown inFigure D-7. The figure revealed that the decompositions have power values that are two orders lower than that obtained from EC experiments. This indicates that fewer current fluctuations are observed under FC conditions, the ECN signals are more uniform in nature. As discussed earlier, lower ECN fluctuations are found under FC because the surface is capable of forming a protective film when sand particles are absent.

Similar to the EC decompositions, a transition region was found under FC conditions, at around 5.0 ms^{-1}. At 6.7 ms^{-1}, the decompositions show high power at the low frequency region, indicating large-scale current fluctuations. This transition region can also be used to monitor the severity of flow corrosion for the NAB coating. At high jet velocities, the shear force and turbulence produced by the jet can possibly remove some of the protective film on the coating surface, increasing the mass transfer rate [51,180,189] and subsequently the anodic current [190].

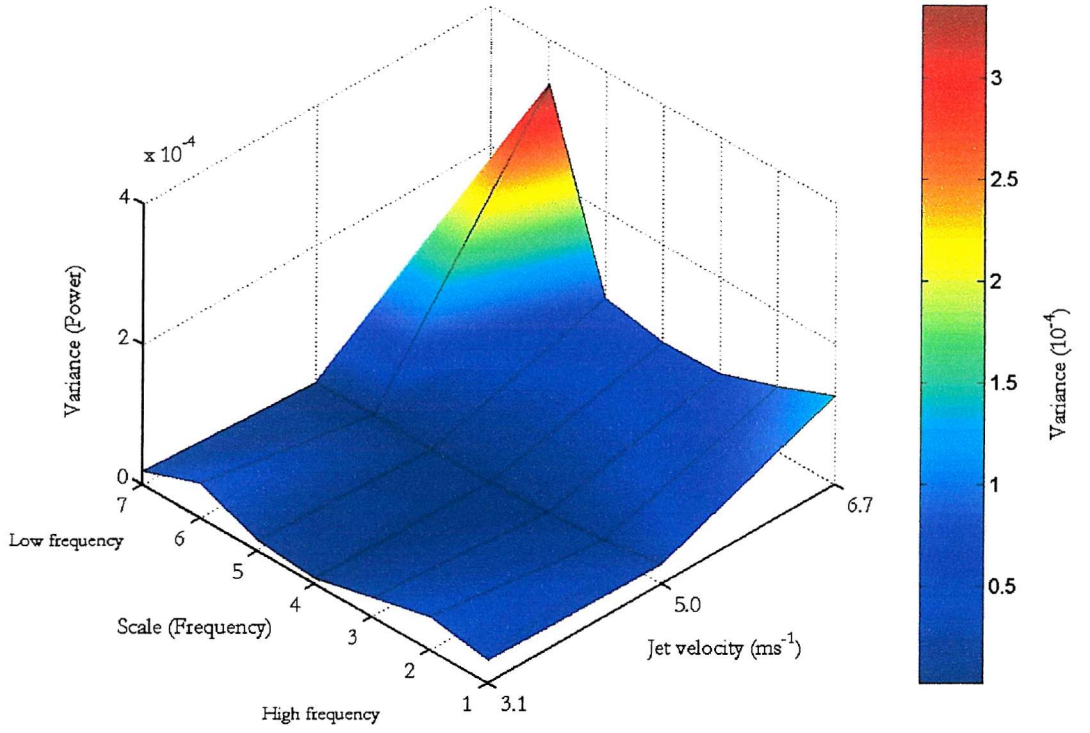

Figure D-7: DWT decomposition of ECN, NAB coating on steel substrate, flow corrosion, 25 °C.

The original ECN signals under EC and FC conditions are plotted in Figure D-8, so that the DWT decompositions can be associated with the current noise characteristics. For the EC and FC ECN traces, the highest jet velocity (6.7 ms^{-1}) condition is shown in red while the lowest jet velocity (3.1 ms^{-1}) condition is shown in blue.

Under EC conditions, mean current levels are 0.5 μA higher for the high velocity experiment. The current noise also revealed larger fluctuations, associated with higher corrosion rates at the coating surface. Higher velocity (sand particle kinetic energy) can increase the rate of protective film removal and mass transfer rates [180,189].

The ECN signals under FC conditions contain far fewer fluctuations than the EC experiments. The mean current levels are 1 μA higher at high kinetic energy conditions, due to higher rates of mass transport on the coating surface with increasing velocity [178,181]. Mean current for FC conditions (3.4 μA) was approximately 1 μA higher than that for EC condition (2.5 μA). This is probably a result of corrosion occurring at the pore network within the coating (Chapter 5).

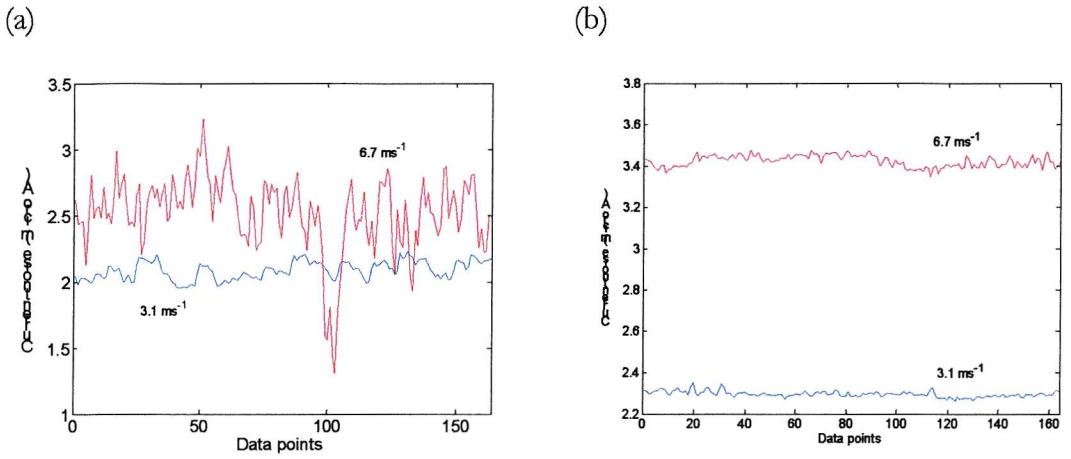

Figure D-8: Comparison of the current noise signals at low velocity (blue) and high velocity (red) conditions, under (a) EC conditions and (b) FC conditions

Previous DWT work by Speyer [125] used Haar wavelets for the analysis of HVOF aluminium coated specimens under flow corrosion and erosion-corrosion conditions. A higher sampling frequency of (100 Hz) was used, providing higher frequency information (three extra wavelet scales).

The author suggested that as corrosion processes were increased by either adding sand particles or NaCl, the maximum variance tends to shift towards lower frequencies (i.e. – lower frequency fluctuations become more prominent). He implied that depassivation and repassivation takes a longer time under a more corrosive environment. Similar types of results were obtained by Aballe *et al.* when aluminium was subjected to static immersion experiments in NaCl solution [127,128]. Comparisons with the present work show that this is true under low kinetic energy conditions, where passivation is still possible. However, this phenomenon was found to be reversed at high kinetic energy conditions with EC conditions revealing higher power at higher frequencies. This is probably due to the surface being constantly active, as sand particles cause more plastic deformation (work hardening and stress corrosion cracking) and more protective films were removed from the surface.

This observation showed that DWT analysis of erosion-corrosion processes in 2D (frequency-power) may not be sufficient. As shown in the 3D analysis (Figure D-1 and Figure D-3), frequency-power information varies with the experimental time. Small differences in the time where data was measured can result in variance peaks at different time scales under erosion-corrosion conditions. For a surface that is constantly under sand particle

impingement, depassivation / repassivation states can vary greatly throughout the experimental duration. The ECN signals can only resolve the averaged electrochemical response of the surface at the time it was measured. Hence, fluctuating variance values were observed at different time scales for the same experiment, the presence of such fluctuations depends on the local corrosion kinetics at the exact moment where ECN was measured.

The DWT method shows promise in analysing the ECN signals under EC and FC condition. However, some limitations were also found in this technique [129]:

- Leakage is generated by the limited length of the basic wavelet function – this makes quantification of energy-frequency-time distribution difficult.
- It is difficult to identify abrupt changes in the low frequency range by using with a large-scale wavelet.
- The wavelet technique is not adaptive, the same wavelet function has to be used throughout the analysis. It is not viable to change the wavelet functions as the need arises.
- The type of result obtained will depend on the wavelet functions chosen for the analysis

In order to compare the validity of the wavelet transform technique, the empirical mode decomposition (EMD) technique is also utilised for the current analysis.

Empirical mode decomposition (EMD)

The advantage of the EMD method over the wavelet transform is that this decomposition method is adaptive. The technique is based on the local characteristic time scale of the original signal and applicable to both non-linear and non-stationary processes. Further information on the EMD signal processing method can be obtained from Huang *et al.* [129], additional information on the EMD procedures can be found in Appendix E. Due to the non-stationary nature of the electrochemical noise collected from erosion-corrosion and flow corrosion processes, it can be useful to apply the EMD method to describe the characteristics of electrochemical noise signals from such systems.

Figure D-9 shows results obtained from the EMD method, for the erosion-corrosion specimen at 5.0 ms^{-1}. The graph shows experimental evolution on the x-axis, Intrinsic Mode Functions (IMF) on the y-axis and the power of individual IMF on the z-axis. The graph is similar to the one presented in Figure D-1 (DWT), except for the y-axis, where the wavelet scales are substituted with IMF. Although the algorithms of the DWT and EMD techniques are different, both expressions (wavelet scales and IMF) provide similar information – frequency. Out of the seven IMFs that are obtained, only six are shown in the figure. The seventh IMF, being a residual trend of the original signal, was not used in the analysis.

The graph revealed similar behaviour to the one shown in the DWT analysis with fluctuations in the IMF power at all frequencies throughout the duration of the experiment. These fluctuations are caused by the effects of sand particle impingement, involving sudden depassivation and repassivation processes (refer DWT section).

Generally, the IMF power is higher (between 0.004 and 0.006) at the high frequency range (low IMF numbers), and closer to zero at the low frequency end. The graph indicates that the EMD technique is sensitive to both high and low frequency fluctuations in the original current noise signal. The sensitivity is shown to be higher than the DWT technique, the DWT technique showed an almost equal distribution of power at all frequency range. The lower power at the low frequency range from the EMD method shows that the technique is adaptive to the DC trend of the original signal. The DWT technique, in this case the Haar wavelet, was not as sensitive to the low frequency DC trends. At low frequencies (large scale wavelets), the Haar wavelet will probably estimate higher variance values when convoluted with the original ECN signal.

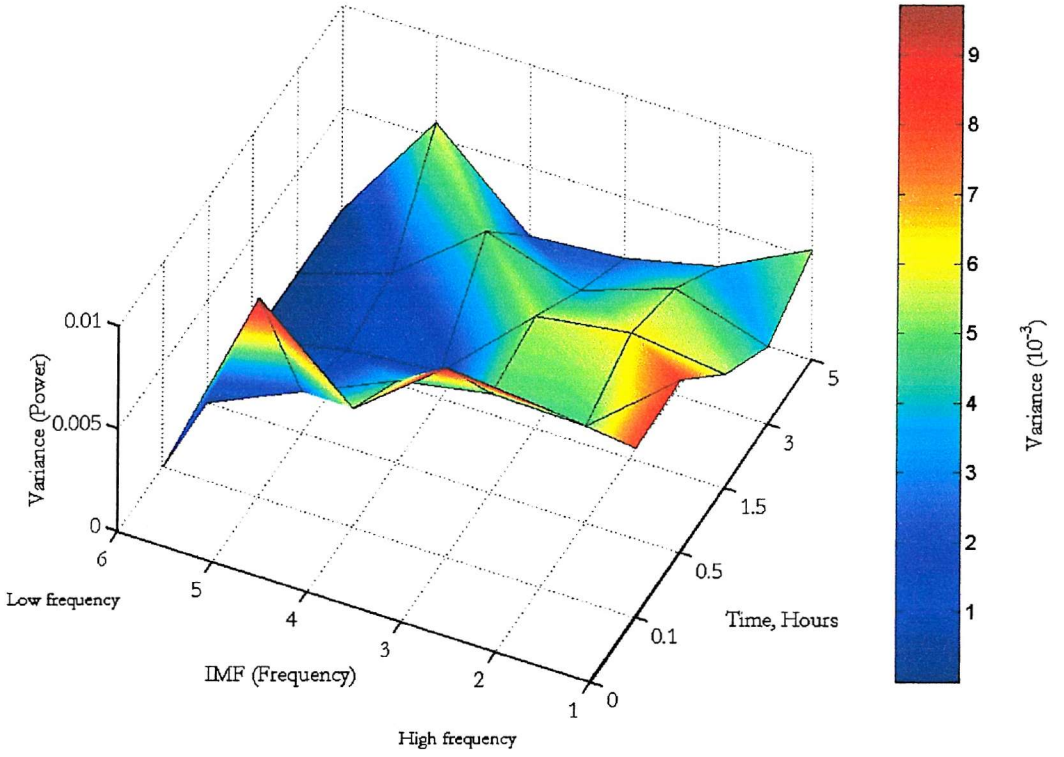

Figure D-9: EMD of ECN, NAB coating on steel substrate, erosion-corrosion at 6.7 ms^{-1}, 235 μm mean sand particle diameter, 25 °C.

Figure D-10 shows EMD results obtained from flow corrosion of the NAB coating at 5.0 ms^{-1}. Similar to the DWT analysis, the IMF power for flow corrosion conditions are found to be much lower than that under erosion-corrosion. This reflects that the original ECN signals contain fewer fluctuations, as the protective film is not damaged on the surface under flow corrosion conditions. The variance peak at the beginning of experiment (shown by the DWT) was not observed in the EMD analysis, this is due to DC trend being excluded in the EMD analysis. Higher variance values are observed in the beginning of the experiment, in the high frequency range (0.0004), probably due to initial instability when the specimen is exposed to the electrolyte jet (see DWT section). This phenomenon was not observed in the previous DWT analysis, probably due to much higher variance values found in the low frequency end (0.006), its values were nearly 10 time higher than the one observed in EMD analysis.

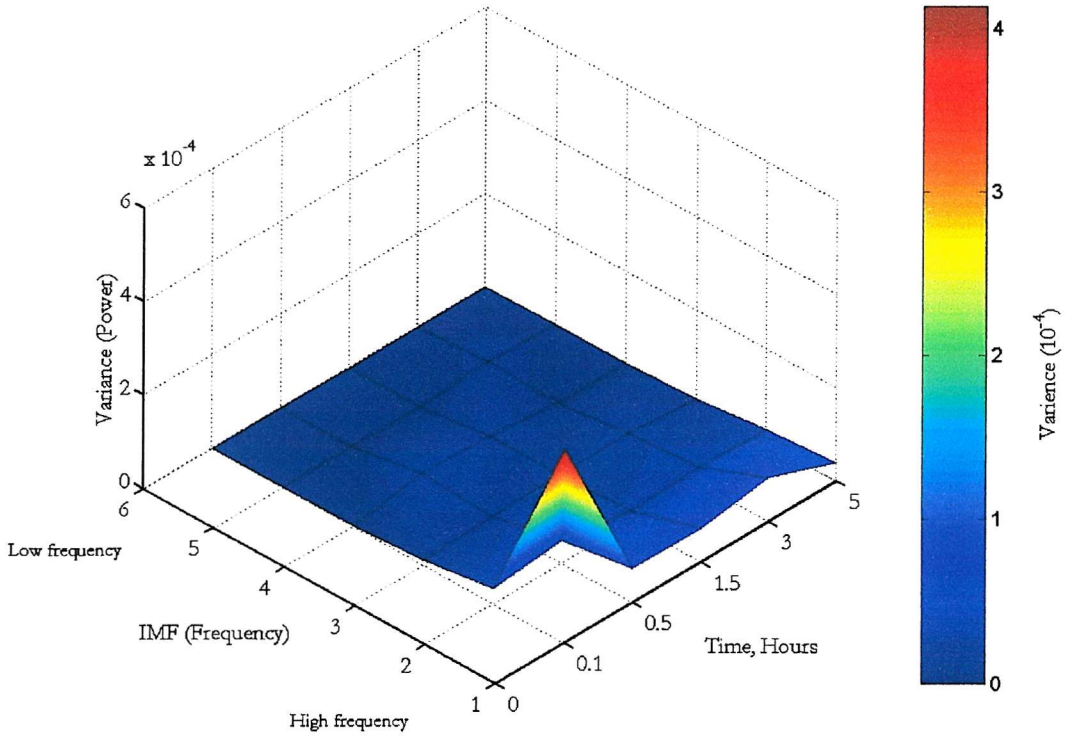

Figure D-10: EMD of ECN, NAB coating on steel substrate, flow corrosion at 6.7 ms^{-1}, 25 °C.

Figure D-11 and Figure D-12 show the EMD analysis for erosion-corrosion and flow corrosion of the NAB coating. As with the DWT analysis, the figures aim to elucidate the effects of jet velocity on the measured ECN signals.

Results between the EMD and DWT techniques are similar. Transition regions are found under EC and FC conditions, where the IMF shows a sudden increase in power, especially at the high velocity region (high kinetic energy). The power obtained from various frequencies for both EMD and DWT analyses were found to be similar, up to 0.06 for EC conditions and 0.0004 for FC conditions.

The transition region was indicated by a sudden shift in the signal power at all frequencies. As discussed earlier, it is associated with the higher fluctuations in the ECN. With the transition region, a 'low' and 'high' corrosive region can be defined, with the separation occurring at about 5.0 ms^{-1} (i.e. E_k = 0.23μJ). As the jet velocity crosses this separation region, both mass transfer effects and protective film removal is greatly enhanced. More work is required to accurately quantify the exposed surface and its subsequent increase in corrosion rate.

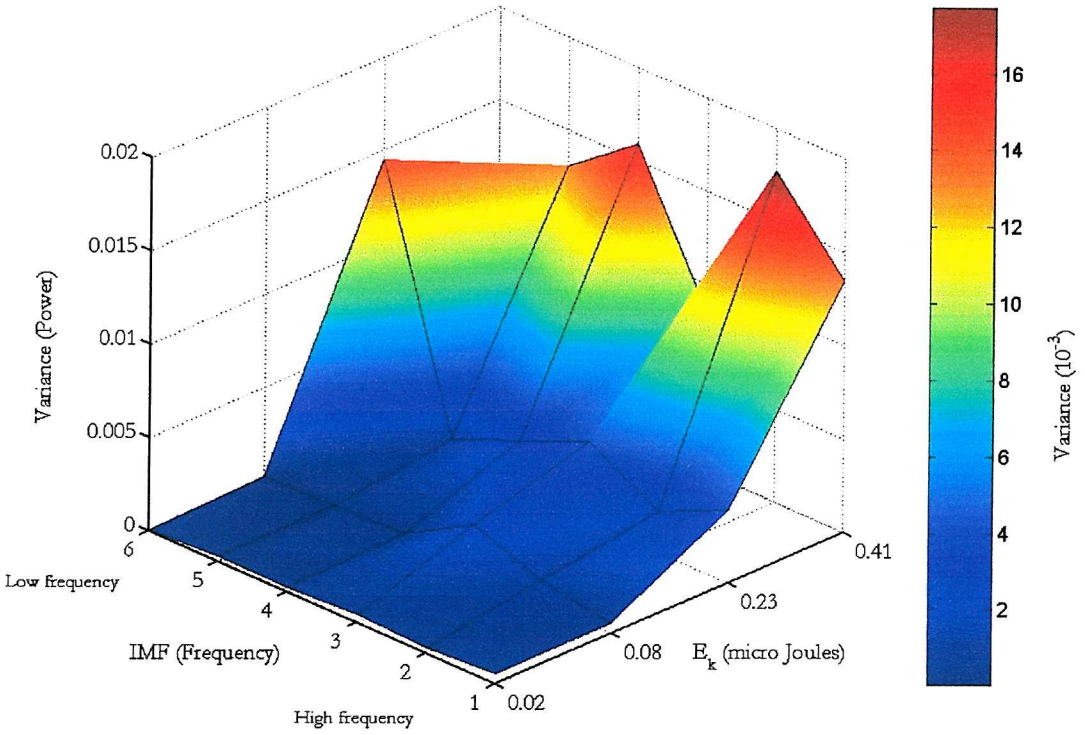

Figure D-11: EMD of ECN, NAB coating on steel substrate, erosion-corrosion, 25 °C. Kinetic energy, jet velocity and sand diameter: 0.41 μJ (6.7 ms^{-1} / 235 μm), 0.23 μJ (5.0 ms^{-1} / 235 μm), 0.08 μJ (3.1 ms^{-1} / 235 μm), 0.02 μJ (3.1 ms^{-1} / 135 μm)

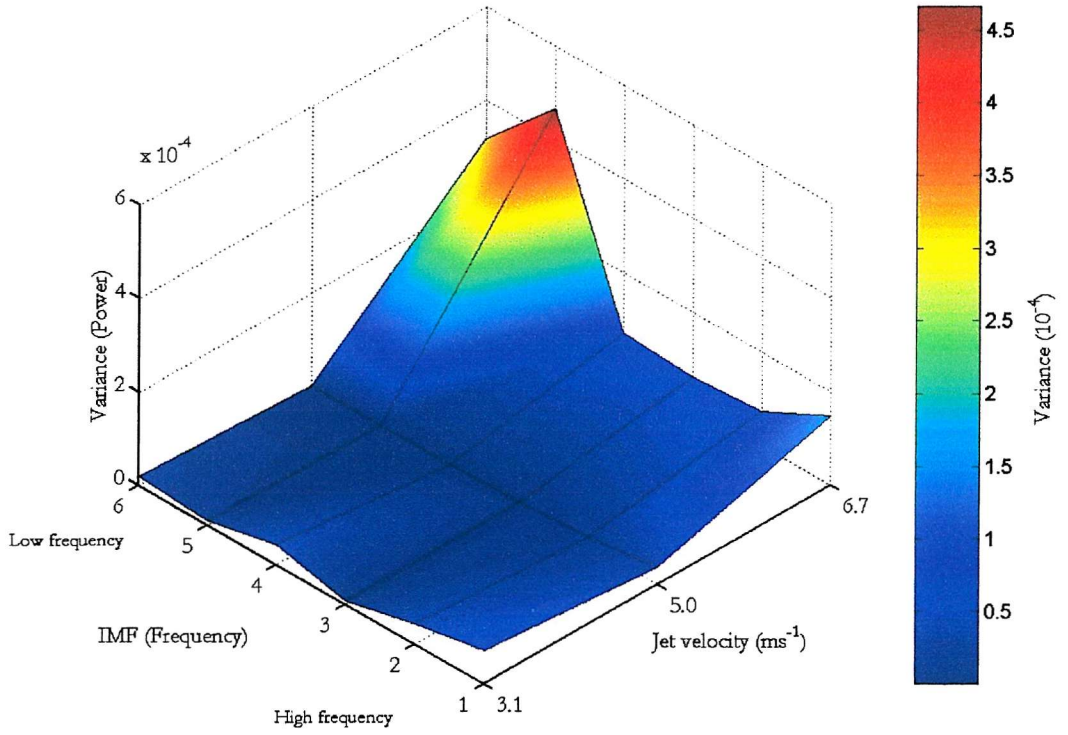

Figure D-12: EMD of ECN, NAB coating on steel substrate, flow corrosion, 25 °C.

The transition region was also observed in the standard deviation analysis (in Figure 7-12). It was shown that beyond E_k = 0.23 μJ, positive synergy will occur, indicating the effects of corrosion and erosion enhancements on the erosion-corrosion system. Processing ECN signals by DWT and EMD methods provides added information in terms of frequency-power distribution, which might be useful in determining the time scales of occurrences in corrosion processes such as depassivation and repassivation. This type of processes are not apparent for the current work as the acquisition rate was not able to resolve individual particle impacts.

Preliminary conclusions from the DWT and EMD techniques:

(a) The DWT and EMD techniques were able to distinguish the difference between erosion-corrosion and flow corrosion processes. Fluctuations were found in the EC decompositions while the FC decompositions revealed relatively uniform characteristics. The higher ECN fluctuations are probably due to sand particle impingement removing the protective film and exposing fresh surfaces, leading to higher corrosion rates.

(b) For both EC and FC conditions, high power was found at the low frequency decompositions, indicating instability when the dry specimen was exposed to the EC/FC jet. This is associated with the air-formed film being transformed into a liquid formed protective layer.

(c) A transition region was found for EC and FC decompositions, at around 5.0 ms^{-1} (0.23 μJ), where the variance experienced a sudden increase. The transition region agrees with that observed in the standard deviation calculations. The variance increase can be attributed to the removal of protective film or increased mass transport reactions.

(d) 3D mapping of erosion-corrosion processes by DWT and EMD revealed the stochastic nature of the electrochemistry on the target material surface that was linked to sand particle impingement. 2D DWT have been used for investigation of static corrosion ECN and the characteristic frequencies were associated with depassivation and repassivation phenomenon. Current results show that the 2D DWT technique may not be adequate for analysing the erosion-corrosion electrochemistry as the activity on the surface is constantly changing with time.

(e) The EMD method appears to be more sensitive than the DWT technique (Haar wavelet), especially at the low frequency region. Estimations of variance with EMD, under erosion-corrosion conditions, are more sensitive at both high and low frequency signals, indicating that the technique is more adaptive than the DWT technique.

Appendix E – Signal analysis by discrete wavelet transform (DWT) and empirical mode detection

Electrochemical current noise (ECN) signal analysis was carried out in the time-frequency domain by both DWT and EMD techniques. The DWT algorithms can be obtained from MATLAB by typing 'help dwt' in the MATLAB command window. The EMD analysis was carried out based on the MATLAB code provided by Huang *et al.* [130] and presented below:

```
% The empirical mode detection method

function [imf,ort,nbits] = emd(x,t,stop,tst);

% EMD (Empirical Mode Decomposition) according to:
% N. E. Huang et al., "The empirical mode decomposition and the
% Hilbert spectrum for non-linear and non stationary time series analysis,"
% Proc. Royal Soc. London A, Vol. 454, pp. 903-995, 1998.
%
% stopping criterion for sifting :
%  at each point : mean amplitude < threshold2*envelope amplitude
%  &
%  mean of boolean array ((mean amplitude)/(envelope amplitude) > threshold) < tolerance
%  &
%  |#zeros-#extrema|<=1

%[imf,ort,nbits] = emd(x,t,stop,tst)
% inputs:
%       - x : analysed signal (line vector)
%       - t (optional) : sampling times (line vector) (default : 1:length(x))
%       - stop (optional) : threshold, threshold2 and tolerance (optional)
%                       for sifting stopping criterion
%                       default : [0.05,0.5,0.05]
%       - tst (optional) : if equals to 1 shows sifting steps with pause
%                       if equals to 2 no pause

% outputs:
%       - imf : intrinsic mode functions (last line = residual)
%       - ort : index of orthogonality
%       - nbits : number of iterations for each mode

% calls:
%       - extr (finds extrema and zero-crossings)
%       - io : computes the index of orthogonality
%
% G. Rilling, July 2002

% default for stopping
defstop = [0.05,0.5,0.05];

if(nargin==1)
 t = 1:length(x);
 stop = defstop;
 tst = 0;
```

```
 end

 if(nargin==2)
   stop = defstop;
   tst = 0;
 end

 if (nargin==3)
   tst=0;
 end

 S = size(x);
 if ((S(1) > 1) & (S(2) > 1)) | (length(S) > 2)
   error('x must have only one row or one column')
 end

 if S(1) > 1
   x = x';
 end

 S = size(t);
 if ((S(1) > 1) & (S(2) > 1)) | (length(S) > 2)
   error('t must have only one row or one column')
 end

 if S(1) > 1
   t = t';
 end

 if (length(t)~=length(x))
   error('x and t must have the same length')
 end

 S = size(stop);
 if ((S(1) > 1) & (S(2) > 1)) | (S(1) > 3) | (S(2) > 3) | (length(S) > 2)
   error('stop must have only one row or one column of max three elements')
 end

 if S(1) > 1
   stop = stop';
   S = size(stop);
 end

 if S(2) < 3
   stop(3)=defstop(3);
 end

 if S(2) < 2
   stop(2)=defstop(2);
 end

 sd = stop(1);
 sd2 = stop(2);
 tol = stop(3);

 if tst

   figure
 end

 % maximum number of iterations
 MAXITERATIONS=2000;
```

```
% maximum number of symmetrized points for interpolations
NBSYM = 2;

lx = length(x);

sdt(lx) = 0;
sdt = sdt+sd;
sd2t(lx) = 0;
sd2t = sd2t+sd2;

% maximum number of extrema and zero-crossings in residual
ner = lx;
nzr = lx;

r = x;
imf = [];
k = 1;

% iterations counter for extraction of 1 mode
nbit=0;

% total iterations counter
NbIt=0;

while ner > 2

 % current mode
 m = r;

 % mode at previous iteration
 mp = m;

 sx = sd+1;

 % tests if enough extrema to proceed
 test = 0;

 [indmin,indmax,indzer] = extr(m);
 lm=length(indmin);
 lM=length(indmax);
 nem=lm + lM;
 nzm=length(indzer);

 j=1;

 % sifting loop
 while ( mean(sx > sd) > tol | any(sx > sd2) | (abs(nzm-nem)>1)) & (test == 0) & nbit<MAXITERATIONS

  if(nbit>MAXITERATIONS/5 & mod(nbit,floor(MAXITERATIONS/10))==0)
    disp(['mode ',int2str(k),' nombre d iterations : ',int2str(nbit)])
    disp(['stop parameter mean value : ',num2str(s)])
  end


  % boundary conditions for interpolations :

  if indmax(1) < indmin(1)
   if m(1) > m(indmin(1))
     lmax = fliplr(indmax(2:min(end,NBSYM+1)));
     lmin = fliplr(indmin(1:min(end,NBSYM)));
     lsym = indmax(1);
```

```
    else
      lmax = fliplr(indmax(1:min(end,NBSYM)));
      lmin = [fliplr(indmin(1:min(end,NBSYM-1))),1];
      lsym = 1;
    end
  else

    if m(1) < m(indmax(1))
      lmax = fliplr(indmax(1:min(end,NBSYM)));
      lmin = fliplr(indmin(2:min(end,NBSYM+1)));
      lsym = indmin(1);
    else
      lmax = [fliplr(indmax(1:min(end,NBSYM-1))),1];
      lmin = fliplr(indmin(1:min(end,NBSYM)));
      lsym = 1;
    end
  end

  if indmax(end) < indmin(end)
    if m(end) < m(indmax(end))
      rmax = fliplr(indmax(max(end-NBSYM+1,1):end));
      rmin = fliplr(indmin(max(end-NBSYM,1):end-1));
      rsym = indmin(end);
    else
      rmax = [lx,fliplr(indmax(max(end-NBSYM+2,1):end))];
      rmin = fliplr(indmin(max(end-NBSYM+1,1):end));
      rsym = lx;
    end
  else
    if m(end) > m(indmin(end))
      rmax = fliplr(indmax(max(end-NBSYM,1):end-1));
      rmin = fliplr(indmin(max(end-NBSYM+1,1):end));
      rsym = indmax(end);
    else
      rmax = fliplr(indmax(max(end-NBSYM+1,1):end));
      rmin = [lx,fliplr(indmin(max(end-NBSYM+2,1):end))];
      rsym = lx;
    end
  end

  tlmin = 2*t(lsym)-t(lmin);
  tlmax = 2*t(lsym)-t(lmax);
  trmin = 2*t(rsym)-t(rmin);
  trmax = 2*t(rsym)-t(rmax);


  % in case symmetrized parts do not extend enough
  if tlmin(1) > t(1) | tlmax(1) > t(1)
    if lsym == indmax(1)
      lmax = fliplr(indmax(1:min(end,NBSYM)));
    else
      lmin = fliplr(indmin(1:min(end,NBSYM)));
    end
    if lsym == 1
      error('bug')
    end
    lsym = 1;
    tlmin = 2*t(lsym)-t(lmin);
    tlmax = 2*t(lsym)-t(lmax);
  end

  if trmin(end) < t(lx) | trmax(end) < t(lx)
```

```
  if rsym == indmax(end)
    rmax = fliplr(indmax(max(end-NBSYM+1,1):end));
  else
    rmin = fliplr(indmin(max(end-NBSYM+1,1):end));
  end
  if rsym == lx
    error('bug')
  end
  rsym = lx;
  trmin = 2*t(rsym)-t(rmin);
  trmax = 2*t(rsym)-t(rmax);
end


mlmax =m(lmax);
mlmin =m(lmin);
mrmax =m(rmax);
mrmin =m(rmin);


% definition of envelopes from interpolation

envmax = interp1([tlmax t(indmax) trmax],[mlmax m(indmax) mrmax],t,'spline');
envmin = interp1([tlmin t(indmin) trmin],[mlmin m(indmin) mrmin],t,'spline');

envmoy = (envmax + envmin)/2;

m = m - envmoy;

[indmin,indmax,indzer] = extr(m);
lm=length(indmin);
lM=length(indmax);
nem = lm + lM;
nzm = length(indzer);

% evaluation of mean zero
sx=2*(abs(envmoy))./(abs(envmax-envmin));
s = mean(sx);

% display

if tst
 subplot(4,1,1)
 plot(t,mp);hold on;
 plot(t,envmax,'--k');plot(t,envmin,'--k');plot(t,envmoy,'r');

 title(['IMF ',int2str(k),';   iteration ',int2str(nbit),' before sifting']);
 set(gca,'XTick',[])
 hold  off

 subplot(4,1,2)
 plot(t,sx)
 hold on
 plot(t,sdt,'--r')
 plot(t,sd2t,':k')
 title('stop parameter')
 set(gca,'XTick',[])
 hold off

 subplot(4,1,3)
 plot(t,m)
 title(['IMF ',int2str(k),';   iteration ',int2str(nbit),' after sifting']);
```

```
      set(gca,'XTick',[])

      subplot(4,1,4);
      plot(t,r-m)
      title('residue');
      disp(['stop parameter mean value : ',num2str(s)])
      if tst == 2
        pause(0.01)
      else
        pause
      end

    end

    % end loop : stops if not enough extrema
    if nem < 3
      test = 1;
    end

    mp = m;
    nbit=nbit+1;
    NbIt=NbIt+1;

    if(nbit==(MAXITERATIONS-1))
      warning(['forced stop of sifting : too many iterations... mode ',int2str(k),'. stop parameter mean value :
',num2str(s)])
    end

  end
  imf(k,:) = m;
  if tst
    disp(['mode ',int2str(k),' enregistre'])
  end
  nbits(k) = nbit;
  k = k+1;
  r = r - m;
  [indmin,indmax,indzer] = extr(r);
  ner = length(indmin) + length(indmax);
  nzr = length(indzer);
  nbit=1;

  if (max(r) - min(r)) < (1e-10)*(max(x) - min(x))
    if ner > 2
      warning('forced stop of EMD : too small amplitude')
    else

      disp('forced stop of EMD : too small amplitude')
    end
    break
  end

end

imf(k,:) = r;

ort = io(x,imf);

if tst
  close
end
```

Both the DWT and EMD techniques involved obtaining 'Details' and 'IMF' respectively, providing frequency information. The magnitudes of these 'Details' and 'IMF' are related to the kinetics of corrosion, these magnitudes are subsequently quantified by obtaining its variance. The 3D graphs in Chapter 7 were obtained by plotting the variance of the 'Details' and 'IMF' against experimental parameters such as evolution or kinetic energy. A flow chart showing the procedures for signal analysis by DWT and EMD is shown in Figure C-1.

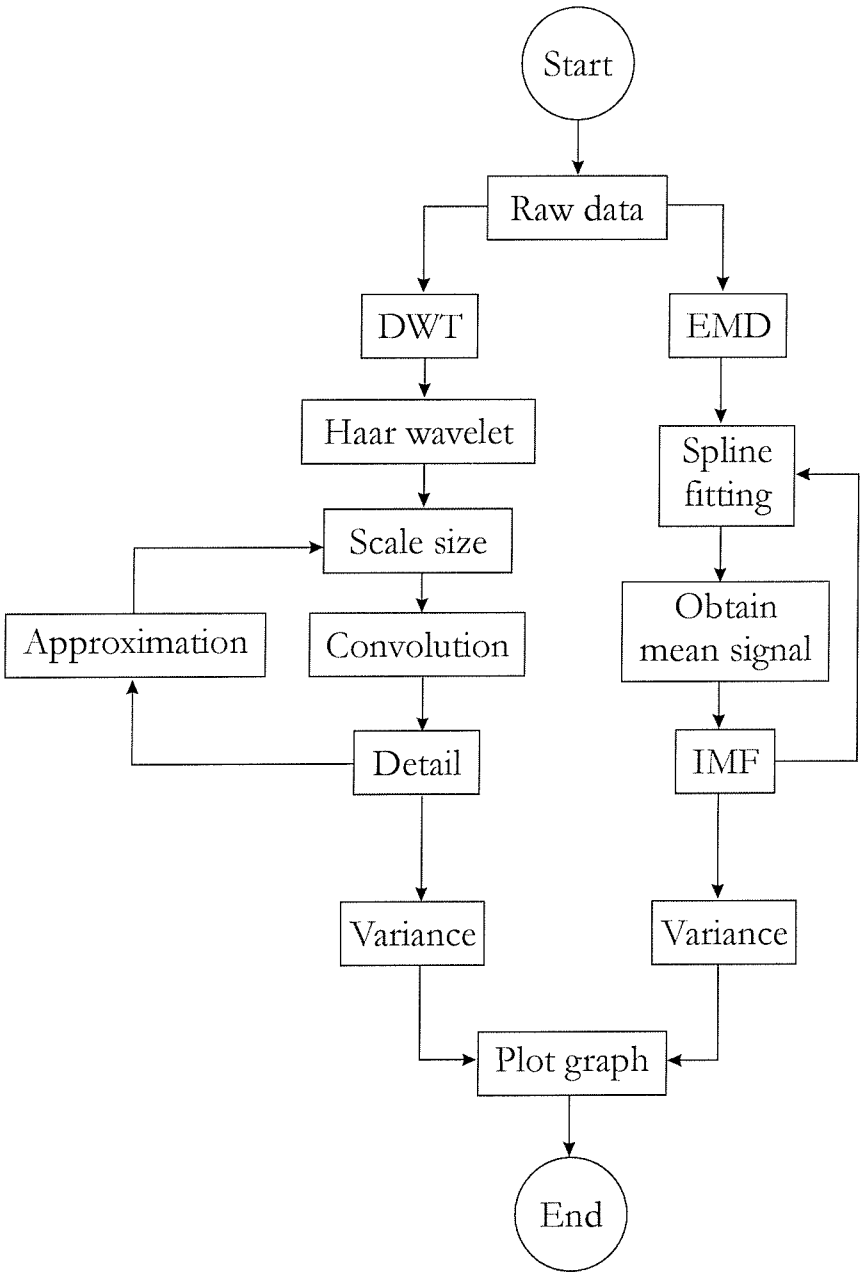

Figure C-1: A flow chart showing the procedures for signal analysis by DWT and EMD.

Acquisition of 'Details' by DWT have been well known and will not be discussed here. Figure C2 demonstrates the sifting process that was used in the EMD method to acquire 'IMFs'.

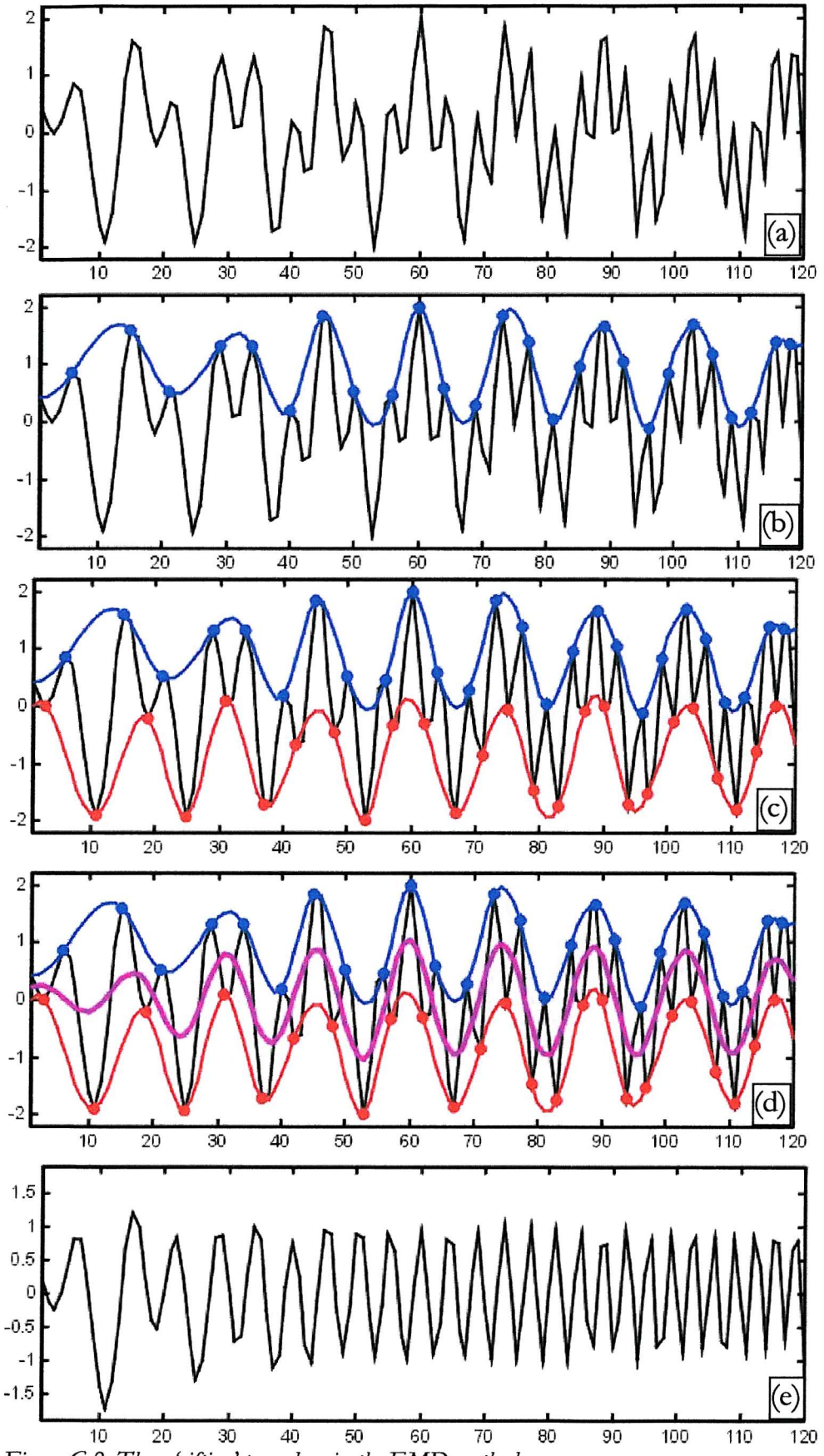

Figure C-2: Thew 'sifting' procedure in the EMD method, .

As seen in Figure C-2, the acquisition of IMF involves five fundamental steps:

(a) The original signal

(b) Identification of maxima points within the original signal, the maxima points were connected by a cubic spline line (shown in blue).

(c) Identification of minima points within the original signal, the minima points were connected by a cubic spline line (shown in red).

(d) A mean between the maxima spline line and minima spline line is obtained, shown in violet. The difference between the original signal and the mean line is the first 'component'.

(e) The first component.

This process is repeated until the standard deviation value between two successive 'components' are found to be 0.2 ~0.3, resulting in the last 'component'. The first IMF is obtained by obtaining the difference between the original signal and the last 'component'. The first 'IMF' is then 'sifted' again to obtain subsequent 'IMFs', this process is continued until the signal becomes a monotonic function from which no more IMF can be extracted.

Appendix F – Conference and journal publications

Conferences/symposiums attended

KS Tan, RJK Wood, JA Wharton, KR Stokes, 'Electrochemical investigation of HVOF aluminium bronze coatings under slurry erosion in saline environments', 41st Corrosion Science Symposium, September 2000, London, UK.

KS Tan, RJK Wood, JA Wharton, KR Stokes, 'Slurry erosion of high velocity oxy-fuel (HVOF) aluminium bronze coatings in saline environments', The Mission of Tribology Research 9, December 2000, ImechE, London, UK.

KS Tan, JA Wharton, RJK Wood, 'Electrochemical potential noise analysis on high velocity oxy-fuel aluminium bronze coatings', 42nd Corrosion Science Symposium, September 2001, Swansea, UK.

KS Tan, RJK Wood, JA Wharton, KR Stokes, 'Electrochemical investigation of high velocity oxy-fuel (HVOF) aluminium bronze coatings under slurry erosion in saline environments', Paper no. 02199, NACE Corrosion 2002, Denver, Colorado.

KS Tan, RJK Wood and JA Wharton, 'Erosion-corrosion related noise of HVOF aluminium bronze and nickel aluminium bronze coatings', Marine Corrosion Club Technical Presentation, January 2003, London, UK.

Journal publications

RJK Wood, JA Wharton, AJ Speyer, KS Tan, 'Investigation of erosion-corrosion processes using electrochemical noise measurements', Tribology International, Vol 35, (2002), pp 631-641.

KS Tan, RJK Wood, KR Stokes, 'The slurry erosion behaviour of high velocity oxy-fuel (HVOF) sprayed aluminium bronze coatings', accepted for publication in Wear, (2003)